UNIVERSITY OF CAMBRIDGE

Studies of urban air quality using electrochemical based sensor instruments

---

Olalekan Abdul Muiz Popoola

Queens' College

University of Cambridge

This dissertation is submitted for the degree of Doctor of Philosophy

Abstract

Poor air quality has been projected to be the world's top cause of environmental premature mortality by 2050 surpassing poor sanitation and dirty water (IGBP / IGAC press release, 2012[1]). One of the major challenges of air quality management is how to adequately quantify both the spatial and temporal variations of pollutants for the purpose of implementing necessary mitigation measures. The work described in this thesis aims to address this problem using novel electrochemical based air quality (AQ) sensors. These instruments are shown to provide cost effective, portable, reliable, indicative measurements for urban air quality assessment as well as for personal exposure studies.

Three principal pollutants CO, NO and NO_2 are simultaneously measured in each unit of the AQ instrument including temperature / RH measurements as well as GPS (for time and position) and GPRS for data transmission.

Laboratory studies showed that the electrochemical sensor nodes can be highly sensitive, showing linear response during calibration tests at ppb level (0-160 ppb). The instrumental detection limits were found to be < 4 ppb (CO and NO) and < 1 ppb for NO_2 with fast response time equivalent to t_{90} < 20 s.

Several field studies were carried out involving deployment of both the mobile and static electrochemical sensor nodes. Results from some short-term studies in four different cities including Cambridge (UK), London (UK), Valencia (Spain) and Lagos (Nigeria) are presented. The measurements in these cities represent snapshot of the pollution levels, the stark contrast between the pollution level especially CO (mean mixing ratio of 16 ppm over 3 hrs) in Lagos and the other three cities is a reflection of the poor air quality in that part of the world.

Results from long-term AQ monitoring using network of 46 static AQ sensors were used to characterise pollution in different environments ranging from urban to semi-urban and rural locations. By coupling meteorological information (wind measurements) with pollution data,

[1] International Geosphere-Bioshpere Programme (IGBP) / International Global Atmospheric Chemistry (IGAC) RELEASE STEMENT ON AIR POLLUTION AND CLIMATE CHANGE. Time to Act: The Opportunity to Simultaneously Mitigate Air Pollution and Climate Change. Tuesday 27th March, 2012. Available from: http://www.planetunderpressure2012.net/press_room.asp

pollution sources, and phenomena like the street canyon effect can be studied. Results from the long-term study also revealed that siting of the current fixed monitoring stations can fail to represent the actual air quality distribution and may therefore be unrepresentative.

This work has shown the capability of electrochemical based AQ sensors in complementing the existing fixed site monitors thus demonstrating an emerging measurement paradigm for air quality monitoring and regulation, source attribution and human exposure studies.

Declaration

This dissertation is my own work and contains nothing which is the outcome of work done in collaboration with others, except as specified in the text and Acknowledgements.

This dissertation has not been submitted, in whole or in part, for any other degree, diploma or other qualification at any other university.

The length of this thesis does not exceed 60,000 words.

Olalekan Abdul Muiz Popoola 15 June, 2012

Dedicated to my Creator, the most Gracious and the most Merciful.

Acknowledgements

I will like to express my deepest gratitude to my Supervisor, Rod Jones for offering me this opportunity to undergo my PhD research under his guided assistance. His words of encouragement have been very helpful throughout my research work. Iq Mead has been very helpful especially during the early development of the instruments. I am deeply grateful for his kind assistance in the course of my research. To Gregor Stewart, I say a big thank you for mutual assistance during most of the field campaigns.

I will like to appreciate the assistance of Mark Calleja and Mark Hayes for helping with most of the programming software used in the electrochemical sensor nodes in this research. In addition, I also like to acknowledge John Saffell and Ronan Baron for allowing me to carryout laboratory studies at Alphasense Ltd, UK. Thanks also go to Jo Dicks and Anita Lewis (Environmental Services, Cambridge City Council) for providing data for the intercomparison studies at the air quality stations in Cambridge. I will like to express my gratitude to Robin North (Imperial College) and Steve Wilkins (DUVAS technologies) for providing data for the field comparison study carried out in London, 2009. Appreciation also goes to Michael Bennett and Simon Christie (Manchester Metropolitan University) for providing lidar and Osiris data for the studies in Cranfield Airport. I will also like to thank Brian Jones for providing some of the meteorology data used in this work.

My sincere thanks to Francis Pope (now at University of Birmingham), Ailsa Benton (BAS), Bin Ouyang and Shehu Ibrahim for their constructive comments during my thesis write up. I will like to appreciate Ray Freshwaters, Neil Dickson, Matt McLeod, my best mate Oliver Kennedy, and all members of the 4th floor (Centre for Atmospheric Science). In addition, I will like to thank Isla Young for her encouraging words during the course of my study.

I wish to thank Cambridge Commonwealth Trust & Cambridge Overseas Trust and Dorothy Hodgkins Studentship for funding my PhD programme.

Finally, my utmost gratitude goes to my loving family, Mr and Mrs S.A. Popoola, my brothers: Layi, Lanre, Yinka and Niran and not forgetting my dearest cousin Lukman. I appreciate their words of encouragement throughout my study.

Table of Contents

Chapter 1 Introduction

Chapter Summary

This chapter will focus on brief review of air quality in term of history, effects and steps taken to mitigate against these effects. A brief description of the chemistry of some important tropospheric gas species especially those related to air quality will also be described. The implication of poor air quality in the UK will be discussed in addition to recent trends of some important air quality species. Finally, the outline of the remaining chapters will be presented.

1.1. Air Quality and Chemistry of the Troposphere

1.1.1. Introduction

The troposphere comprises the region of the atmosphere from ground level up to 8 - 17 km depending on the season and latitude being considered [1-3]. The troposphere can be divided into the planetary boundary layer and the free troposphere which extends from the boundary layer to the tropopause[2]. The planetary boundary layer is highly mixed and it extends about 1-2 km from the surface. The troposphere is the part of the atmosphere where life thrives and most of the weather phenomena occur in this region. The quality of air in this part of the atmosphere is therefore important to the sustenance of life on the planet. Ambient air quality (AQ) is defined as the conditions and quality of outdoor air in terms of selected pollutants of known negative effects on either human health or the environment at concentrations above normal ambient levels [1, 4]. These pollutants can be dust, toxic gases or odours, and can be from anthropogenic or biogenic sources. Important health related pollutants include carbon monoxide (CO), nitrogen monoxide (NO), nitrogen dioxide (NO_2), sulphur dioxide (SO_2), volatile organic compounds (VOCs) and particulate matter (size less than 2.5 μm, $PM_{2.5}$ or 10 μm, PM_{10}). The abundance of these pollutants is governed by the balance between sources and sinks. These sources can either be direct the emission (biogenic and anthropogenic) or via chemical reactions in the troposphere. In order to mitigate against negative effects on human health effects and / or the wider environment of poor or degraded ambient air quality, legislation and guidelines have been passed to help prevent, limit or eliminate emissions. For instance in the UK, legislation

[2] The tropopause is the boundary between the stratosphere and the troposphere

based on regional EU directive have been put in place to ensure good ambient air quality. Similarly, in the USA national air quality strategy is implemented by environmental protection agency (EPA). Meanwhile the World Health Organisation (WHO) has provided international guidelines for ambient air quality. This legislation provide guidelines on assessment criteria and specify the acceptable limits values (usually time dependant) for selected key pollutants as well as suggest action plans and management strategies for policy-makers.

1.2. Overview of Air Quality

The history of air quality dates back to period before human existed when natural disasters (e.g. volcanic eruptions, breaking waves, forest fires, dust and pollens [2]) were major sources of pollution and it have been reported that some of these events had devastating effects on life on the planet. There are documented reports linking natural events like volcanic eruptions have been linked to death of both humans and wildlife. Some of these episodes lead to the ejection of large volumes of highly concentrated toxic gases into the atmosphere. These gases include HCl, H_2S, SO_2 and CO in addition to large amount of ash accompanying eruption, all of which can have overwhelming impact on life and the environment [5]. For instance, the Laki eruption in Iceland (1783-1784 AD) had a significant negative environmental impact on both human and the environment across Europe but especially for Iceland. The toxic gas emissions were linked to the death of about 50% of local livestock and wider implications on air quality in some European countries including Sweden, Poland, England, Poland, Czech, Hungary, Russia and Germany [6, 7]. However in recent times, air quality has been influenced more by anthropogenic activities especially after the Industrial Revolution. The advent of the industrial revolution resulted in a significant increase in demand for energy which was satisfied in most cases by the burning of fossil fuels in industrial plants on an industrial scale. By-products such as soot / black carbon and SO_2 from industrial activity as well as the domestic burning of fossil fuels such as coal contributed to poor indoor and outdoor air quality across Europe. The impact of pollutants from these activities on air quality is particularly marked under calm and stable weather conditions which reduce the dispersion of the polluted air masses. Some of the earliest recorded anthropogenic air pollution events include the Meuse Valley fog in Belgium (December, 1930) and air pollution events in Donora, Pennsylvania, USA (October

1948) [4, 8]. Another notable example is the London smog[3] during the winter of December, 1952. It is estimated that more than 3000 people died as a direct consequence of the smog [9, 10]. In addition, there was a threefold increase in the mortality rate during the period of the smog [8]. This episode in London spurred the UK government to start considering ways of reducing / controlling pollutions related to human activities leading to the enactment of the Clean Air act of 1956 [11, 12]. This act culminated in the establishment in 1961 of the world's first national air pollution monitoring network which measured – in this case – the major species that were associated with smog (i.e.SO_2 and black smoke) [11]. More recently, anthropogenic related air pollution has been dominated by pollutants from road transport sources [2]. This is a direct consequence of previous control measures which were directed at pollution from industrial power plants [2]. In addition to direct emission of pollutants from traffic sources, a phenomenon involving secondary reactions of some primary pollutants (pollutant emitted directly from known sources e.g. NO and NO_2) initiated by sunlight resulting in the formation of secondary toxic gas species has been reported. One of the first recorded occurrences of this type of secondary air pollution was in Los Angeles, USA in late 1940's and early 1950's. Effects of pollutants associated with the smog include eye irritation and lethal effects on plants [12]. The environmental and health impacts of the events related to the 1950's Los Angeles smog led to the Clean Air Act in 1963. This act empowered the US Environmental Protection Agency (EPA) to develop regulations for the federal, state and local governments to limit pollution emissions from both stationary (industrial) and mobile (transport) sources [13].

1.3. Effects of Poor Air Quality

The effects of air pollution can be broadly classified into two categories: (a) effects on human health and (b) impacts on the environment. Environmental impacts include those on livestock and vegetation.

1.3.1. Human health effect

Several studies have investigated the impact of air pollution on human health. It has been shown that the association between poor human health and air pollution led to the establishment of legislations aimed at reducing anthropogenic related air pollution [9, 13].

[3] Smog was coined by Dr Des Voeux in 1905 to describe the combined effect of **sm**oke and natural f**og** that was prevalent in the city of London.

Recent WHO assessments show that more than 2 million premature deaths each year can be linked to both outdoor and indoor air pollution [14]. Some atmospheric species have become increasingly important as potent health hazards and are specifically targeted by legislations to help eliminate, prevent or reduce their emission. The species include CO, the oxides of nitrogen (NO and NO_2), SO_2, ozone (O_3) and particulates. The health impacts can range from acute effects e.g. nausea (due to short term exposure to very high levels) to chronic effects resulting from sustained long-term exposure to low concentrations of pollutants (e.g. increase risk of asthma).

1.3.1.1 Health implications of CO

In terms of absolute concentration, CO is the most prevalent outdoor pollutant. As a result, CO concentrations are often expressed in parts per million by volume (ppm) compared to other air quality species which are typically at parts per billion by volume (ppb) mixing ratios[4] [15]. The major exposure route of CO in humans / animals is via inhalation. It readily combines with the haemoglobin (Hb) (about 80-90% of the absorbed CO) to form carboxyhaemoglobin (COHb). The COHb complex limits the ability of blood to transfer oxygen because of the strong affinity between CO and Hb (approximately 200-300 times more than for oxygen). Although the binding process is reversible, the elimination binding half-life is reported to be between 2-6.5 hours depending on the initial COHb level in the blood [16]. The health effects of CO poisoning are often studied by monitoring COHb levels which serves as a biomarker for CO exposure. At high exposure levels, CO can also combine with other blood proteins like myoglobin, cytochrome oxidase and cytochrome P-450 which may affect the proper functioning of oxygen demanding organs and tissue such as the brain, heart and developing foetus [16].

There are several studies that have focused on the effects of CO exposure and the consequent elevated blood COHb on human neurological activity. It has been reported that CO exposure leading to a COHb rise of about 10% can result in headaches, and at levels slightly higher can cause dizziness, nausea and vomiting [17]. CO exposure that results in a 40% rise in COHb can lead to coma and 50-60% COHb rise can be fatal [17, 18]. Exposure to CO has been linked to several neurological effects. For instance, elevated COHb levels of 5-

[4] Mixing ratio is defined as amount of molecules present in the atmosphere. One ppm equals one molecule per million molecules of air and one ppb is equivalent to one molecule per billion molecules of air.

20% have been shown to negatively affect cognitive performance [19]. It has been reported that visual tracking ability was impaired with a 10% rise in COHb when the study subjects carried out heavy exercise [20]. Impaired cognitive responses such as reduced tracking and driving ability, reduced vigilance and impaired coordination have also been shown in double-blind tests for COHb increases as low as 5.1-8.2% [16].

Apart from neurological effects, exposure to CO has been linked to several adverse cardiovascular outcomes. For instance, exposure to CO resulting in a 6% COHb increase have been shown to cause ventricular ectopy in patients with existing coronary heart disease [17]. Existing heart conditions such as myocardial ischemia are negatively impacted by increased COHb levels as low as 2-4% resulting from CO exposure [17, 18]. Studies involving patients with ischaemic heart disease show that the time to onset of exercise induced chest pain were reduced due to increased COHb levels of 2.9-5.9% [16]. Epidemiological studies and clinical data have shown that CO from either smoking, environmental or occupational exposure can lead to increased cardiovascular mortality and is a major contributing factor to the early onset of myocardial infarction [18]. Studies have shown that lethal levels of COHb were between 10-30% in patients with severe heart disease compared to usual fatal level of 50-60% reported for healthy individuals [18].

Endogenous CO production occurs in humans due to catabolic reaction involving haemoglobin and some other haem proteins [18]. This can result in COHb level rise of 0.4-0.7% in healthy individuals at rest. However, this can rise to 4-6% due to hypermetabolism or the effects of certain drugs. In pregnant women, typical COHb levels are between 0.7-2.5% (about 20% higher compared to women who are not pregnant) [18]. Endogenous CO produced by the mother diffuses to the foetus and the level of COHb in foetus can be 10-15% higher than the mother [18, 21]. The foetus also has a stronger binding affinity for CO than adults and as a result elevated CO exposure pose greater health risks. COHb levels of 2-10% in the foetus of smoking mothers has been linked to low birth weight [21]. Recent study in California (USA) have also linked ambient CO exposure to lowered infant birth weights of -5.4 g (95% confidence interval -6.8 g, -4.1 g) per ppm of CO [22].

1.3.1.2 Health implications of oxides of nitrogen (NO and NO_2)

NO and NO_2 are two of the oxides of nitrogen that constitute pollutants of major health effects. NO_2 is the most ubiquitous of the two species due to the rapid oxidation of NO to NO_2 under ambient conditions. However direct emission of NO from road traffic sources can result in elevated exposure especially close to the source. Most health effect studies have primarily focused on NO_2. The primary entry route of NO_2 into human body is via the respiratory system. Health effects are due to oxidative damage resulting in the generation of free radicals [17]. Most of the health related effects of NO_2 in humans are related to respiratory system and people with histories of respiratory disease are more affected than healthy individuals. Both short-term and long-term health effects of exposure to NO_2 have been studied and reported in literature.

Short-term effects of exposure to high concentrations of NO_2 can lead to severe pulmonary damage in healthy people [23]. For instance, exposure to NO_2 concentrations more than 2.5 ppm for less than 2 hours resulted in decreased pulmonary function in healthy people while the exposure to concentrations less than 1 ppm resulted in no significant health effects in some healthy individuals [16, 24]. In contrast, 3.75 hr exposure to NO_2 concentrations of 0.3 ppm affected the lung functions in people with chronic obstructive disease [24]. Several studies have shown increased bronchial reactivity at NO_2 levels between 0.2-0.3 ppm [16]. However there are some studies that do not show same result at high NO_2 concentrations. This imply that the mechanism for the acute effects of NO_2 is not fully understood and further studies need to be carried out to understand the effect of NO_2 on bronchial activity [16].

Several studies in different countries have looked at the effect of outdoor exposure to NO_2 on human health. Results from these studies showed that NO_2 exposure had more health impact in children compared to adults. For instance, an elevated asthma risk of 2.28 was observed for NO_2 concentrations of 31-37 ppb in six year olds in Germany [25]. A recent study in Canada showed an increased risk of traffic related asthma in children of 1.12 ± 0.05 (95% confidence interval) for 5 ppb (10 $\mu m/m^3$) increase in NO_2 and risk of 1.08 ± 0.04 (95% confidence interval) for 8 ppb (10 $\mu m/m^3$) increase in NO [26]. A study in Taiwan in 2007 involving 5049 children revealed the adjusted risk odds of bronchitic symptoms with asthma was 1.81 per 8.79 ppb NO_2 [27]. A study in Ontario, Canada using sputum cell count as a

measure of respiratory activity showed evidence of strong correlation with mean monthly NO_2 concentrations [28]. A study of five cities in Germany revealed an increase of 28% in croup cases for increase in daily mean NO_2 from 5 ppb (10 μm/m^3) to 37 ppb (70 μm/m^3) [16]. Studies in Japan involving women showed increase in cases of chest cough, coughing, wheezing and phlegm in study subjects living close to roads with heavy traffic compared to individuals living several meters away. This was linked to traffic related NO_2 concentrations as there was no significant concentration change at 20, 50 and 150 m from the road compared to the high concentrations observed at kerbsides [29].

1.3.2. Effects on the environment

Ambient air quality also takes into account the effects of certain species on the ecosystem. Some of the important atmospheric species in this regard include O_3 and oxides of nitrogen (e.g. NO and NO_2). These gas species are absorbed by plant via the stomata during respiration. Species that undergo transformation (e.g. acidic transformation of oxides of nitrogen into nitric acids) can get into the natural ecosystem through wet deposition and subsequent absorption by plants.

O_3 is produced in the troposphere by photochemical reactions in the presence of sunlight and involving NO, NO_2 and VOC. Detailed review of the environmental impact of O_3 has been reported in the US EPA 2006 Air quality criteria for ozone and other photochemical oxidant [30]. In this review it was reported that current ambient O_3 concentrations in many countries impair growth of economically beneficial plant species. Effects are often observed at ambient concentrations greater than 80 ppb over few hours. The environmental impact of O_3 on growth of plants and trees is not always isolated and acts in synergy with other factors like insects, water, temperature and elevated CO_2 [30, 31]. Recent field based experiments like non-chambered free-air CO_2 exposure (FACE) systems have shown that O_3 can affect growth and cause foliage injuries in plants. These findings support previous chamber studies in open top chamber (OTC) systems [30]. FACE exposure study carried out in Illinois revealed a 15-25% reduction in soybean yield as a result of exposure to O_3. Decrease in ambient O_3 following legislation have been linked with improvement in forest recovery [30]. Several studies have been reported in the US that investigated the effect of ambient O_3 on plants in the ecosystem. These studies include vegetation studies in Valley of Mexico City, San Bernardino Mountains in Los Angeles, Sierra Nevada Mountains in

California and the Appalachian mountain in the eastern US [31]. Similarly, impacts of ambient O_3 concentrations on plant life have been studied in Europe. For instance, in UK the effects of O_3 were studied on the population of common plantain while impacts of O_3 on forest health were studied in Czech, Slovakia and Poland, Romania and Ukraine. In all studies elevated ambient O_3 was linked to reduced growths of the plant species in the different environment [31]. Although there is enough evidence indicating the effect of ambient O_3 on ecosystem, there is not enough data showing the degree of impact of O_3 on natural ecosystem [30].

Oxides of nitrogen (NO and NO_2) are other important species affecting the environment and thus constitute AQ problem. Necrosis, an acute damage in plants have been reported due to exposure to high concentrations of NO_2 [23]. Elevated concentrations of NO_X ($NO+NO_2$) have been reported to affect the most susceptible members of the ecosystem in terms of competing for abiotic components like nutrient, water, space and light [32]. These result in less plant biodiversity in the ecosystem. Some plant species can adapt to increasing NO_2 concentrations in the ambient air by increasing their nitrogen uptake however at certain critical level, the concentration of NO_2 becomes toxic and can reduce growth [23].

1.4. Air quality assessment and management

In the previous section the health and environmental implications of poor air quality has been reviewed. In order to mitigate against these effects, legislations and guidelines intended for air quality assessment and management has been developed at local, national, regional and global levels.

In recognition of the global implication of air quality, the WHO has produced a series of air quality guidelines (AQG) to guide policy-makers world-wide in addition to providing appropriate targets for wide range of air quality policies in different parts of the world [33]. The first edition of WHO AQG was established for Europe in 1987. This was revised in year 2000 to account for 37 common air pollutants [34]. In 2005 a global update of AQG was published by the WHO following new studies into the health effects of air pollutants. This update focused mainly on O_3, NO_2, SO_2 and particulate matters [33, 34].

In Europe, the European Commission Directive 2008/50/EC provide guidelines for ambient air quality pollutants which include setting national standards for Member States [35].

These standards are meant to avoid, prevent or reduce the human health effects and impacts on the environments of air pollutants. Some of the species considered in this legislation are CO, NO_X, SO_2, particulates matter ($PM_{2.5}$ and PM_{10}), O_3, lead (Pb) and benzene. The 2008 EU AQ directive replaced previous EU legislations on ambient air quality. This directive incorporated some of the WHO recommended standards, guidelines and programmes for air quality [35]. Recently attention has been paid to particulate matter especially $PM_{2.5}$ which has been implicated in much health effects yet has no identifiable standard threshold below which it has no health effect [33, 35]. Apart from establishing standards for pollutants, the legislation also requires member states of the EU to establish authorities and bodies within their territories to be responsible for:

- the assessment of ambient air quality;
- the approval of measurement systems (methods, equipment, network and laboratories);
- evaluating accuracy of measurements;
- the analysis of assessment methods;
- establishing cooperation with other Member States and the Commission;
- assist in the coordination of Community-wide quality assurance programmes are being organised by the commission within their territory [35].

The assessment of air quality based on fixed measurements is the recommended assessment techniques for areas where concentrations exceed the upper assessment threshold. Results from these fixed measurements can be supplemented by results from modelling techniques and indicative measurements. If however the concentrations are lower than upper assessment threshold then a combination of these measurements can be utilised for air quality assessment [35].

Meanwhile in the US following reported air quality events, the federal government passed the first legislation known as Clean Air Act in 1963, and this was subsequently amended in 1970, 1977 and 1990. The act empowered the United States Environmental Protection Agency (EPA) to establish national ambient air quality standards (NAAQS) for six ubiquitous pollutants including CO, NO_2, SO_2, particulate matter ($PM_{2.5}$ and PM_{10}), O_3 and lead [36]. The US-EPA has produced detailed air quality criteria documents for these pollutants [37]. These documents include details of health and ecological studies of air pollutants, the

standard assessment method, results from model studies and basis for the NAAQS standards [36]. A comparison of the air quality standards of the WHO, the EU and the US is shown in table 1.1. While the EU AQ standards aimed at the protection of vegetation is shown in table 1.2.

Table 1.1. Comparison of some air quality standards aimed at protection of human health.

Pollutant (unit)	Averaging time	WHO AQG 2005 [33]	EU 2008/50/EC [35]	NAAQS (US-EPA) [36]
CO (ppm)	1 h	30	—	35
	8 h	10	9	9
NO_2 (ppb)	1 h	106	106	100
	Annual	21	21	53
O_3 (ppb)	8 h	50	60	75
SO_2 (ppb)	10 min	188	—	—
	24 h	8	—	—
	1 h	—	131	75
	8 h	—	47	—
Lead (μgm^{-3})	Quarter	—	—	0.15
	Annual	0.5	0.5	—
PM_{10} (μgm^{-3})	24 h	50	50	150
	Annual	20	40	—
$PM_{2.5}$ (μgm^{-3})	24 h	25	—	35
	Annual	10	25	15

Table 1.2. EU AQ standards for O_3, NO_X and SO_2 aimed at protection of vegetation.

Pollutant	Averaging time	EU 2008/50/EC [35]
SO_2	Annual and winter	20 μgm^{-3}
	(1 October to 31 March)	
NO_X = NO+ NO_2	Annual	30 μgm^{-3}
O_3	AOT40[5] (calculated from 1 h values)	6000 μgm^{-3}.h
	May to July	

[5] AOT40 (in units of μgm^{-3}.h) is the sum of the differences hourly concentrations greater than 80 μgm^{-3} over a given period using only hourly measurements between 8:00 and 20:00 Central European Time (CET) each day.

1.5. Chemistry of Troposphere

1.5.1. Chemical Composition

The chemistry of the troposphere is complicated involving gas reactions sometimes initiated by light [1-3]. Some of the important species in the troposphere include hydroxyl radicals (OH), peroxy radicals (HO_2), nitrate radicals (NO_3), water vapour (H_2O) and pollutants like O_3, NO, CO, NO_2 and VOCs. The OH radical is a very important component initiating most of the day-time removal of pollutants from the troposphere. It is a product of photochemical reaction in the presence of sunlight involving photolysis of O_3 to $O(^1D)$ and subsequent reaction of this with H_2O as shown in reactions R1.1 and R1.2. Part of the excited oxygen atom $O(^1D)$ undergo quenching reaction to form ground state atomic oxygen, $O(^3P)$ by colliding with N_2 and O_2 molecules as shown in R1.3.

R1.1 $$O_3 + h\nu \xrightarrow{\lambda<320nm} O_2 + O\left(^1D\right)$$

R1.2 $$O\left(^1D\right) + H_2O \rightarrow 2OH \qquad (10\%)$$

R1.3 $$O\left(^1D\right) \xrightarrow{N_2 \& O_2} O\left(^3P\right) \qquad (90\%)$$

The concentration of OH reflects the oxidative capacity of the atmosphere during daylight. At night, NO_3 becomes more important as there is no OH formed during the night. NO_3 radicals are formed by the reaction of NO_2 with O_3. It readily establishes equilibrium with dinitrogen pentoxide (N_2O_5) by reacting with NO_2 as shown in reactions R1.4 and R1.5.

R1.4 $$NO_2 + O_3 \rightarrow NO_3 + O_2$$

R1.5 $$NO_2 + NO_3 \xleftrightarrow{N_2 \& O_2} N_2O_5$$

Although these reactions occur both during the day and night, NO_3 is rapidly photolysed during the day (R1.6a and R1.6b) resulting in low daytime concentrations with noon-time life time of approximately 5 s [1-3].

R1.6a $$NO_3 + h\nu \rightarrow NO + O_2 \qquad (10\%)$$

R1.6b $$NO_3 + h\nu \rightarrow NO_2 + O\left(^3P\right) \qquad (90\%)$$

Typical atmospheric oxidising reaction of OH radical is shown by the reaction depicted by R1.7.

R1.7 $$OH + A \xrightarrow{k_A} P$$

where *A* is a trace gas species like CO, NO_2, SO_2, CH_4 and VOC. *P* represents the oxidative product and k_A is the rate constant of the reaction between *OH* and *A*. If reaction R1.7 is assumed to be pseudo-first order such that the concentration of A >> concentration of OH, then the rate equation is given by E1.1 with atmospheric lifetime (the e-folding time) τ equal to 1/k'. The solution of E1.1 gives a time-dependent concentration for A as shown in E1.2.

E1.1 $$-\frac{d[A]}{dt} = k_A[A][OH] = k'[OH]$$

E1.2 $$[A] = [A]_0 \exp -k't$$

where k' = k_A[A]. Similar oxidative reaction can be written for atmospheric oxidants like Cl, NO_3, and Br. For example the atmospheric lifetimes for the removal of ethene are 33 hours, 230 days, 3.8 months and 1.8 years via reactions with OH, NO_3, Cl and Br radicals respectively [38].

1.5.2. Sources and Sinks

In this section sources and sinks of some important atmospheric pollutants will be reviewed. These species include CO, NO, NO_2 and O_3. Both natural and anthropogenic sources have been identified for these gas species. Removal of these species via sinks can either be through physical processes like dry and wet deposition or via chemical processes which proceed naturally or can be induced by activities of man [1, 2].

1.5.2.1 Ozone (O_3)

The main source of tropospheric O_3 is the photochemical reaction of oxides of nitrogen with VOC in the presence of sunlight [2]. This reaction can be natural or induced by activities of human [2]. Details of the chemical reaction will be discussed in the following section. Another natural source of O_3 is through downward transport of stratospheric O_3 [3]. Depending on the level of NO_X and VOCs, there can be net production or removal of O_3 via chemical processes. A natural sink for ozone is the uptake by vegetation in the ecosystem

although this has been shown not to be beneficial as it has a health implication at high concentrations. Ozone can also be lost by dry deposition onto earth surface [2].

1.5.2.2 Carbon monoxide (CO)

CO is a colourless, odourless and tasteless gas with low water solubility. It is an important air quality pollutant because of the health effects it has in humans as discussed earlier. Most of the ambient CO results from anthropogenic activities like the incomplete, low-temperature combustion of carbonaceous (fossil) fuels [39]. It has been reported that the annual global estimation of CO into the atmosphere is 2600 million tonnes (teragrams), 60% of which is due to anthropogenic activities and 40% from natural sources.

Table 1.3. Annual estimates of global CO sources and sinks (teragrams per year) based on values reported by Dignon et al [40].

	teragrams / year	Percentage (%)
CO sources		
Fossil fuel combustion	600	23.6
Biomass burning	600	23.6
Natural non-methane hydrocarbon (NMHC) oxidation	300	11.8
Anthropogenic NMHC oxidation	200	7.9
Methane oxidation	600	23.6
Oceans	10	0.4
Soils	30	1.2
Vegetation	200	7.9
Total	2540	100
CO sinks		
Soils	300	11.5
OH reaction	2300	88.5
Total	2600	100

Some of the anthropogenic activities include mobile sources like internal combustion engines (mostly vehicles) and stationary sources like power plants, coal burning in power plants and waste incinerators [16]. It has been estimated that vehicle emission account for approximately 90-95% of CO found in urban environment with high traffic density [39]. Natural sources include biological sources like plants and non-biological sources like oceans, wildfires (or biomass burning) and oxidation of hydrocarbon (see section 1.5.3) a major source of background CO outside urban areas [16, 18]. Some of the natural sinks of CO include soil microorganism and chemical destruction involving OH radical (see section 1.5.3). A summary of sources and sinks of CO is shown in table 1.3 [18].

1.5.2.3 Oxides of nitrogen (NO and NO_2)

Oxides of nitrogen are important air quality species because of their implication on human health and the environment, particularly the impact they have on the oxidising capacity of the troposphere [16]. NO is a colourless, odourless gas with slight solubility in water (0.006 g / 100 g of water at 24^o C and 1 atmospheric pressure) [41]. Most of the anthropogenic NO are products of high temperature combustion processes involving the oxidation of molecular nitrogen present in air (N_2) or those from nitrogen containing fuels [41]. The set of reactions defining the oxidation process resulting in the formation of NO are known as extended Zeldovitch mechanism and summarised by reactions R1.8 to R1.11. The amount of NO formed from the oxidation of N_2 depends on parameters like peak flame temperature, quantity of combustion air and gas residue time in the combustion chamber [41].

R1.8 $$O_2 + M \rightarrow 2O + M$$

R1.9 $$N_2 + O \rightarrow NO + N$$

R1.10 $$N + O_2 \rightarrow NO + O$$

R1.11 $$N + OH \rightarrow NO + H$$

NO_2 on the other hand is a reddish-orange-brown, water soluble gas with characteristic pungent smell. It is a highly oxidising gas and also corrosive [41]. It is formed as part of the products in the internal combustion engine via the termolecular reaction involving the oxidation of two molecules of NO by O_2 as shown in reaction R1.12.

R1.12 $2NO + O_2 \rightarrow NO_2$

This reaction does not occur under ambient conditions because there are other faster reactions involving NO that are kinetically favoured (see section 1.5.3). It has been estimated that about 5-10% of NO_X from internal combustion is emitted as NO_2. However recent studies have suggested that the percentage of primary NO_2 emitted from combustion engines for vehicles fitted with catalytic diesel particulate filter (CDPF) could range between 20-70% [42]. This is because the CDPF also oxidise NO to NO_2 in addition to oxidising CO and particulates. The NO_2 produced is further utilised in the oxidation of trapped particles [43]. Other anthropogenic sources of NO_2 include stationary sources like power plants and industrial combustion processes. Natural sources of NO_2 include intrusion from the stratosphere, bacteria activities (nitrification process) and volcanic eruption and lightning [16]. Chemical transformation of NO to NO_2 by O_3 is also a major source of atmospheric NO_2. It has been reported that 50% conversion can be achieved in less than 1 minute for NO and O_3 mixing ratios of 100 ppb [16]. Table 1.4 shows a summary of the global tropospheric NO_X sources in teragrams nitrogen per annum [44].

Table 1.4. Annual estimates of global NO_X sources (teragrams N per year).

NO_X sources	**Emissions, teragrams N / year**
Fossil fuel combustion	33
Aircraft	0.7
Biomass burning	7.1
Soils	5.6
Ammonia oxidation	–
Lightning	5.0
Stratosphere	<0.5
Total	51.9

NO_X are removed by physical processes and chemical process. Details of some of the chemical processes leading to the removal of NO_X will be discussed in section 1.5.3. Atmospheric NO_X are removed by physical process like dry and wet deposition. Wet

deposition relies on the water solubility of NO_X and consequent atmospheric washout following rainfall. NO_X can also be removed from the atmosphere by assimilation of nitrites and nitrates formed during wet deposition [1].

1.5.3. Chemistry of selected gas species in the troposphere

1.5.3.1. Daytime chemistry

The daytime reactions involving important AQ gases in the troposphere are mainly driven by the HO_X (OH + HO_2) reactive species especially OH which is produced during the day by photochemical reaction under UV light with H_2O (as discussed in section 1.5.1).

(A) Chemistry of unpolluted troposphere

Unpolluted troposphere is defined as the condition under which the concentration of atmospheric gas species like CO, NO and NO_2 are very low in parts per trillion volume (ppt) to few tens of ppb. Such conditions are characterised by the absence of local sources of the atmospheric gas species as found in areas around remote marine environments and rural tropical forests. The chemistry of NO_X under this condition is quite unique.

(i) Chemistry of CO and O_3

One major source of background CO is the oxidation of methane (CH_4). The reactions leading to the formation of CO are summarised in the following reactions [1, 18].

$$CH_4 + OH \rightarrow CH_3 + H_2O$$

$$CH_3 + O_2 \xrightarrow{N_2 \& O_2} CH_3O_2$$

$$CH_3O_2 + NO \rightarrow CH_3O + NO_2$$

$$CH_3O + O_2 \rightarrow CH_2O + HO_2$$

$$CH_2O + h\nu \rightarrow H_2 + CO \qquad (50\%)$$

or $\quad CH_2O + h\nu \rightarrow HCO + H \qquad (45\%)$

or $\quad CH_2O + OH \rightarrow HCO + H_2O$

$$HCO + O_2 \rightarrow CO + HO_2$$

In these reactions, CH_4 gets oxidised to methyl (CH_3) radical and H_2O. The CH_3 radical is then oxidised to form methyl peroxy (CH_3O_2) radical in the presence of molecules like N_2 and O_2. CH_3O_2 is then reduced to methoxy (CH_3O) radical by NO, which in turn is oxidised to formaldehyde (CH_2O) by O_2. The CH_2O is photolysed to form CO or formyl (CHO) radical. It can also be oxidised by OH to form HCO radical which in turn reacts with O_2 to give CO. Oxidation of other saturated hydrocarbons through similar reaction schemes can also result in the formation of CO although the yield may differ. For instance, atmospheric model results show that the yield of CO from CH_4 is 0.9 compared to 0.4 from ethane (C_2H_6) and propane (C_3H_8) [18]. The chemistry of CO and O_3 are connected and the destruction of one species can result in production of the other depending on the availability of NO_X species. One major sink for CO is the reaction with the OH radical.

In an unpolluted atmosphere with low NO_X environment (concentration of NO < 10 ppt), this reaction results in the destruction of O_3 thereby constituting a sink for atmospheric O_3 as shown by the sequence of reactions depicted in reactions R1.13 – R1.15 below. The net reaction is actually the OH-catalytic oxidation of CO to CO_2 by O_3. It has been estimated that 70% OH radical reacts with CO and 30% with CH_4 in the unpolluted troposphere [2].

R1.13 $$CO + OH \rightarrow CO_2 + H$$

R1.14 $$H + O_2 \xrightarrow{M=N_2} HO_2$$

R1.15 $$HO_2 + O_3 \rightarrow 2O_2 + OH$$

Net reaction $$CO + O_3 \xrightarrow{OH\&M} CO_2 + O_2$$ ***(sink for CO and O_3)***

(ii) Chemistry of NO_X (NO and NO_2)

In an idealised atmosphere which contains only the species NO and NO_2, the photolysis of NO_2 during the day in the absence of other oxidants results in the formation of NO and O(^{3}P) which reacts with O_2 to form O_3. The NO is subsequently oxidised by O_3 to produce NO_2 and O_2 as shown in reactions R1.16 to R1.18.

R1.16 $$NO_2 + h\nu \xrightarrow{J_{NO_2}} NO + O$$

R1.17 $$O + O_2 \xrightarrow{M} O_3$$

R1.18 $$NO + O_3 \xrightarrow{k_{1.18}} NO_2 + O_2$$

Reaction R1.17 is relatively fast compared to reactions R1.16 and R1.18 which are therefore considered in the rate equations for the three species. After some time, the reactions approach a steady state and this is often referred to as the photostationary state define by the Leighton relationship (equation E1.3).

E1.3 $$[O_3] = \frac{J_{NO_2}[NO_2]}{k_{1.18}[NO]}$$

where J_{NO2} is the photolysis rate of NO_2, and $k_{1.18}$ is the second order rate constant for the reaction between NO and O_3. The relaxation time to steady state for this coupled reaction is defined by the life time of the reaction of O_3 with NO (R1.18). Based on this the relaxation time τ is defined by the expression:

$$\tau = \frac{1}{k_{1.18}[NO]}$$

For [NO] = 1 ppb (equivalent to $1 \times 10^{-9} \times 2.46 \times 10^{19}$ molecules cm^{-3}) at a pressure of 1 atmosphere and $k_{1.18}$ of 1.9×10^{-14} cm^3 $molecule^{-1}$ s^{-1}, $\tau \cong 35.7$ min [1].

A key feature of this reaction scheme is that there is no net production or destruction of O_3 but a steady concentration is achieved over time. Note that R1.18 is actually O_3 oxidation of NO to NO_2, thus resulting in O_3 destruction. If however, NO_2 can be produced from NO via a different oxidation route there will be net production of O_3.

(B) Chemistry of polluted troposphere

Reactions considered under this section will affect the abundance of O_3 species more than other pollutants. Depending on the time of the day, the abundance of pollutants and availability of oxidising species, a net production or destruction of O_3 can occur. The reaction of CO with OH in the absence of NO_X has been considered and it has been shown to lead to a net destruction of O_3. In the real troposphere the reactions are complex and the

chemistry is not as simple as idealised for the NO_X reactions discussed earlier. In the presence of CO, the ensuing reactions are shown below.

R1.16 $NO_2 + h\nu \xrightarrow{J_{NO_2}} NO + O$

R1.17 $O + O_2 \xrightarrow{M} O_3$

R1.13 $CO + OH \rightarrow CO_2 + H$

R1.14 $H + O_2 \xrightarrow{M=N_2} HO_2$

R1.19 $HO_2 + NO \rightarrow OH + NO_2$

Net reaction $CO + 2O_2 + h\nu \rightarrow CO_2 + O_3$ ***(sink for CO and source for O_3)***

Note the key reaction here is **R1.19** in which NO is converted to NO_2 without consumption of O_3 (compare to **R1.18**). These results in net production of O_3 and the regeneration of HO_X radicals which helps sustain the reactions. Similar reaction schemes can also occur from the oxidation of alkanes which produce RO_2 radicals (see chemistry of CO and O_3 above) that undergo reactions similar to the HO_X chemistry. Note the reaction scheme above only proceeds if [NO] / [O_3] ratio is above a certain critical value. Below this ratio, the destruction of O_3 via the reactions R1.13 - R1.15 dominates. Model prediction shows that O_3 production through the reaction with HO_2 or RO_2 equals or surpasses its destruction in the presence of CO for NO mixing ratio ≥ 30 ppt [2]. This explains why remote locations such as the Pacific acts as a net sink for O_3 due to low NO_X concentrations found in these areas [2]. It is worth pointing out that at high NO_X concentrations (as found in urban environments) NO_2 preferentially reacts with HO to form HNO_3 as shown in reaction R1.20 [3].

R1.20 $OH + NO_2 \xrightarrow{M} HNO_3$ ***(important daytime sink for NO_X)***

This reaction serves to terminate the free radical processes resulting in the formation of O_3 and also the formation of HO_X and NO_X species (in the form of HNO_3) which is water soluble and can readily undergo both wet and dry deposition. Note **R1.18** is responsible for the reduced O_3 concentrations observed near NO sources such as motorways especially at nighttime [3].

1.5.3.2. Nighttime chemistry of the troposphere

NO_X composition at nighttime is mostly in the form of NO_2 because there is no photolysis of NO_2 at night (R1.16 does not proceed) and any daytime NO left are rapidly converted to NO_2 by O_3 (R1.18).

R1.18 $$NO + O_3 \xrightarrow{k_{1.18}} NO_2 + O_2$$ (τ_{NO} at 50 ppb O_3 is 42 s)

In addition, the OH radical is no longer produced at night. Subsequently, another oxidizing species (NO_3) plays a more dominant role during the nighttime chemistry [1-3]. The main source of NO_3 in the troposphere is via the reaction of NO_2 with O_3 as shown in R1.4.

R1.4 $$NO_2 + O_3 \rightarrow NO_3 + O_2$$

Concentrations of NO_3 are low during the day because it is rapidly photolysed to NO_X via reactions R1.6a and R1.6b in addition to conversion to NO_2 by reacting with NO (R1.21). However NO_3 concentration reaches a maximum at night especially close to an urban environment where there is anthropogenic emission of NO_X because reactions R1.6a and R1.6b cease at night. Reaction R1.21 barely plays any role due to lack of daytime NO at night a direct consequence of R1.18 at nights.

R1.6a $$NO_3 + h\nu \rightarrow NO + O_2$$ (10%)

R1.6b $$NO_3 + h\nu \rightarrow NO_2 + O\left(^3P\right)$$ (90%)

R1.21 $$NO + NO_3 \rightarrow 2NO_2$$

NO_3 establishes equilibrium with N_2O_5 by reacting with NO_2 (R1.5).

R1.5 $$NO_2 + NO_3 \xleftrightarrow{N_2 \& O_2} N_2O_5$$

Oxidation reactions of NO_3 proceed by the reaction with hydrocarbons resulting in the formation of alkyl radical (R) which can combine with O_2 to form the RO_2 radical, a very potent oxidative species. HO_2 is also produced from the reaction of NO_3 with HCHO thus continuing the HO_X chemistry at night. A major sink for NO_X is the heterogeneous gas (aqueous aerosol) hydrolysis of N_2O_5 as shown in R1.22.

R1.22 $$N_2O_5 + H_2O_{(s)} \rightarrow 2HNO_3$$

1.6. Overview of air quality in the UK

As part of the response to the growing concerns of the effects of air quality on human health and the environment, the UK Government established the Environmental Act of 1995 which was intended to produce air quality strategy for improving ambient air quality [45]. In 1997, the UK Government published its first air quality strategy – the United Kingdom National Air Quality Strategy, based on the EU council Directive 96/62/EC. This strategy was replaced in 2000 by the Air Quality Strategy for England, Scotland, Wales and Northern Ireland. In July 2007, the UK Government published an updated Air Quality Strategy for England, Scotland, Wales and Northern Ireland [46]. This AQ strategy allow local authorities to carry out air quality Review and Assessments based on the Technical Guidance and Policy Guidance document provided by The Department for Environment, Food and Rural Affairs (DEFRA) [47]. If a local authority finds out that a zone may not meet the national air quality standards, an air quality management area (AQMA) is declared for that area. Once an AQMA is declared, a system for continuous monitoring of air pollutants has to be established. As at 2010 there were 179 national air quality monitoring sites across the UK. 127 of which are designated automated urban and rural network (AURN) and data from this network are used to prepare the obligatory EU Commission reports on the state of the ambient air [47]. Pollutants monitored across the network include CO, NO, NO_2, SO_2, O_3 and $PM_{2.5}$ / PM_{10}. Automated air quality networks operated by local councils which are not part of the AURN are called the local air quality networks (LAQN). The LAQN are used for air quality assessment in AQMA by local authorities. For the purpose of air quality assessment, the UK is divided into 43 zones: 28 of which are considered as agglomeration[6] zones while the remaining 15 zones are classified non-agglomeration zones in accordance to EU Directive 2008/50/EC [47].

1.6.1. Financial implication of poor air quality in the UK

It has been estimated that the effect of air quality on human health costs the UK government between £8.5 billion to £20.2 billion a year [48]. The actual cost may however

[6] Agglomeration refers to a zone with population in excess of 250 000 inhabitants or where the population is less than 250 000 with a given a given population density per km2 as defined by Member States.

be higher than this given the fact that the estimation ignores the impact on morbidity instead taking into account only mortality. In addition, the health effects of NO_2 are not included in the estimate because this species acts in synergy with other pollutants. The costs from environmental impact of air pollution also include reduced in certain crops yield due to high ambient O_3 concentrations. A 5% to 15% reduction in wheat yield was reported in southern UK resulting from the impact of elevated ambient O_3 concentrations [48]. The financial burden of poor air quality can also come in the form of fines if EU standards are not met within the specified target time. For instance, the inability of the UK to meet the EU recommended standard for NO_X will cost the Government £300 million pounds if the application by the UK Government for an extension in target time is not accepted by the European Court of Justice [48].

1.6.2. Trends in emission and measurements of CO, NO, O_3 and NO_X in the UK

The time series of average maximum 8-hour running mean CO measurements from all AURN sites in the UK from 1990 to 2010 shows a downward trend in ambient CO concentration (see figure 1.1).

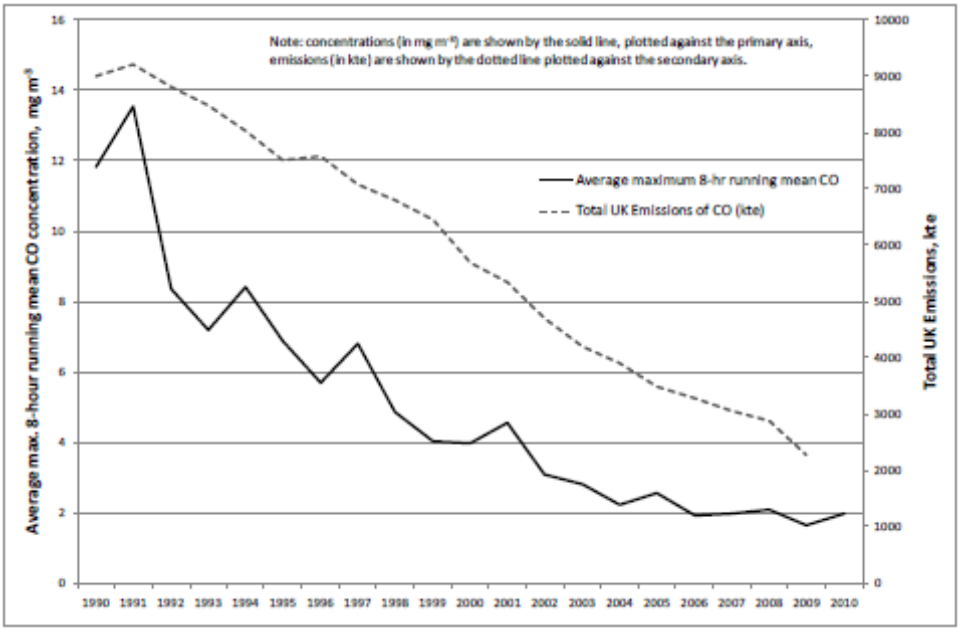

Figure 1.1. Time series of average maximum 8-hour running mean CO for all AURN sites and the NAEI CO emission estimate for UK from 1990 to 2010. Figure reproduced from the report on Air pollution in UK 2010 [47].

A rapid decrease in CO occurred in early 1990s and steadily decreasing in the last two decades. This is consistent with the National Atmospheric Emission Inventory (NAEI) emission estimates for this period which show steady decline in annual CO emission. It has been reported that CO emissions have decreased by 73% between 1970 and 2009 [47].

Unlike CO, the time series of annual maximum 8-hour running mean of O_3 from all AURN sites from 1990 to 2010 show there is no distinct upward or downward trend in the maximum 8-hour running mean O_3 concentrations. However, there are some annual variabilities in the in the concentrations. There is no emission data for O_3 as there is no significant source in the UK and the measured concentrations are the product of photochemical reactions involving NO_X species [47]. The implication of this steady pattern in O_3 concentrations is that zones currently at risk of target exceedence will most likely not meet the standard in the future [47]. At the end of 2010, 41 of the 43 zones in the UK exceeded the long-term target for human effect of O_3 while 3 exceeded the long-term target for the effect of O_3 on vegetation [47].

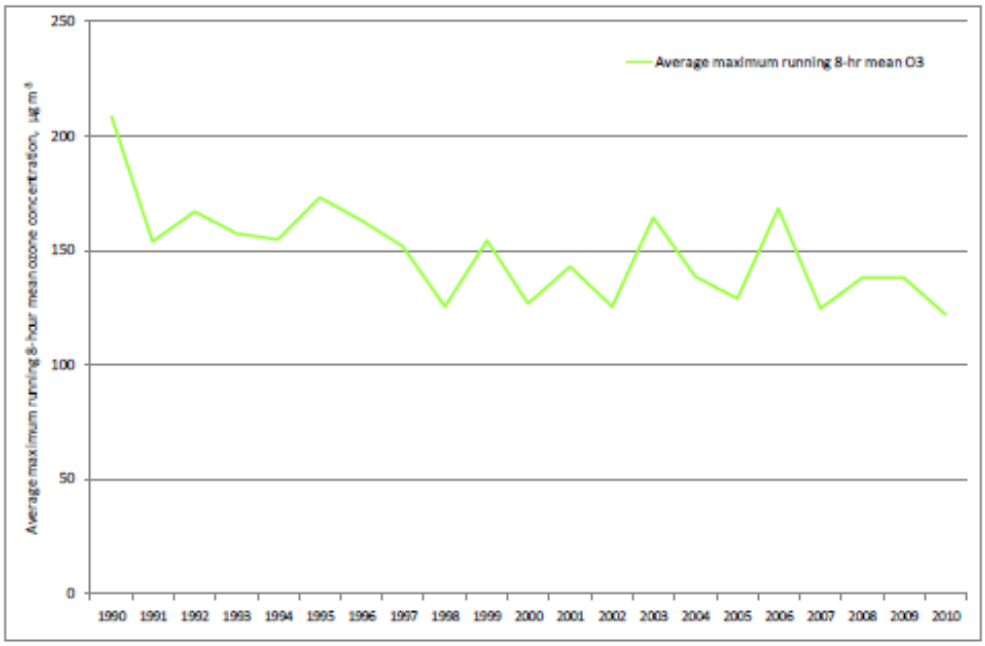

Figure 1.2. Time series of annual maximum 8-hour running mean[7] O_3 for all AURN sites (1990 – 2010). Figure reproduced from the report on Air pollution in UK 2010 [47].

[7] 8-Hour running means are calculated by summing mean concentrations from hourly measurements of previous eight hours for an hour in question. For instance, value for the first hour of each day (i.e. 01:00) will be the mean of the hourly measurements starting from 17:00 of the previous day to 01:00 of the day in

The NO_2 and NO_x measurements and emission show a different trend compared to the pattern observed in CO. Two patterns were noticed in the annual mean NO_2 concentrations for urban background measurements. There was steady decrease in NO_2 concentrations up to mid 2000s which was consistent with the decline observed in the NAEI NO_X emission estimates [47]. However the concentrations seem to level off after this period in a sharp departure from the emission estimates which still showed downward trend. Similar patterns have been reported in a recent study on trends in NO_X and NO_2 emissions and ambient measurements in the UK [49]. In this report two periods identified in the NO_2 and NO_X trend were 1999 to 2002/2004 and 2002/2004 to 2010. In the former the concentrations decreased rapidly while there was little change in the latter period. The annual percentage reduction in NO_2 was estimated to be $\approx$ 1.4% for rural sites and 0.5-1% close at motorway sites [47]. The deviation of the measurements from emission estimates from year 2002/2004 onwards was partly due to change in the primary NO_2 fraction (f-NO_2) in vehicle exhausts in the UK from 5-7% in 1996 to 15 – 16% in 2009. A larger range of 21-22% was estimated for London [49]. Other explanations are that older petrol vehicles (Euro 1-3) emit more NO_X than was previously thought and also that the Euro Standards failed to achieve a decrease in NO_X emission in diesel cars and lighter goods vehicles (LGV) [47].

1.7. Road transport emissions of CO and NO_X.

CO emissions in the UK are dominated by road sources and there has been a steady decrease in road traffic related sources over the past 20 years [50]. The reduction in CO emission from road sources was about 86% between 1990 and 2007 and was due mainly to improvements in exhaust treatment due to introduction of catalytic converters and in part to the increase in volume of diesel vehicles [50]. Based on European emission standards for vehicles referred to as Euro classes, diesel vehicles have lower CO emission standards compared to petrol vehicles. For instance, the CO emissions in Euro 3 cars introduced in January 2000 should be below 0.64 g km^{-1} in diesel fuel compared to 2.30 g km^{-1} in petrol fuel [51]. Similarly, road transport is the major source of NO_X. The European Environmental Agency reported a 40% reduction in road transport emissions of NO_X in the EU-27 between

interest and the last calculation will use hourly readings between 16:00 to 24:00 of each day. The annual maximum is thus the maximum 8-hour mean value obtained from five out of six months over the summer season (April to September) 35. *DIRECTIVE 2008/50/EC OF THE EUROPEAN PARLIAMENT AND OF THE COUNCIL.* Official Journal of the European Union, 2008. **L152**.

1990 and 2008 [52]. This value was based on emission estimates which are based on results from New European Driving Cycle (NEDC). However, recent findings have shown that estimates based on NEDC do not reflect real world driving. For instance, a recent study in the UK using remote sensing data (RSD) revealed higher absolute NO_X emission for Euro 0-6 diesel cars compared to estimates from UK/ EU emission standards [53]. A similar result was observed in Euro 3 & 4 diesel Light Good Vehicles (LGV) [53]. The study also revealed low estimation of NO_X emissions for Euro 1-2 petrol cars based on UK/ EU emission standards compared to result from RSD. This was attributed to poor representation of the catalyst-degradation in the EU/UK inventories [53].

With the increasing concern albeit the impact of fossil fuel consumption on the climate, it is important to look at the implication of renewable fuel on the emission of regulated air quality pollutants. The EU directive 2009/28/EC stipulated that by 2020 at least 10% of fuel in the transport sector must be based on renewable fuel which is mostly met by adoption of biofuels [54]. In the UK, a combination of this directive and the national Renewable Transport Fuel Obligation (RTFO) targets led to an increase in volume of sales of fuel from renewable sources (bioethanols and biodiesel), with bioethanol making up 1.4% petrol sales and biodiesel 4.2% in diesel fuel sales in 2009 [55]. With this recommended future change in fuel composition in mind, the NAEI has simulated the effect of biofuels on emissions of regulated pollutants including CO and NO_X. It found that a scenario involving equal uptake of bioethanol and Rapeseed Methyl Ester (RME) biodiesel, will lead to a -22% reduction in CO emissions and 0.5% increase in NO_X emissions [55].

1.8. Outline of the thesis

The work described in this thesis will review established measurement techniques for some selected AQ pollutants (chapter 2). This will be followed by a detailed description of the development of novel electrochemical based portable air quality (AQ) sensors. The principles of operation, electronic design of two variants of the AQ sensors (mobile AQ and static AQ sensors) and establishment of AQ network based on these instruments including data management / online utility will be discussed (chapter 3).

Much of the hardware work described in chapter 3 was based on work by Iq Mead (Chemistry Department, University of Cambridge) in collaboration with an industrial partner,

Alphasense[8] UK while the data management and online functionality is based on work carried out by research colleagues from the Cambridge eScience Centre and Centre for Mathematical Science, Departments, University of Cambridge. My contributions to the research described in this thesis are presented in chapters 4, 5, 6 and 7.

The characterisation of the AQ sensor instruments will be discussed in detail. Firstly, laboratory performance of the instruments will be described these including laboratory calibration tests using standard gases and tests for interfering gas species. Secondly, intercomparison tests involving: (a) reference (chemiluminescence) instrument and (b) an optical instrument (differential ultraviolet absorption spectroscopy, DUVAS) will be discussed (chapter 4). Finally, the influence of environmental factors such as temperature on the sensor performance and the method developed to account for this factor will be described in detail (chapter 5).

Following successful laboratory and intercomparison studies with other instruments under ambient conditions, some field studies involving the use of the AQ sensors will be presented. The first set of studies involved field deployments of mobile AQ sensors in different environments. Results from deployments in urban environments in parts of UK (London and Cambridge), at an airport (Cranfield airport, UK), urban area in Valencia (Spain) and coastal / urban roadside in Lagos (Nigeria) will be described (chapter 6). In addition, some short-term network deployment (lasting few hours) of mobile AQ and a long-term network deployment (for about two and half months) of static AQ sensors will be presented in this thesis (chapter 7).

Finally, suggestions for future work aimed at incorporating more air quality species into the present AQ instrument design will be discussed including a plan for the deployment of these modified AQ instruments for ambient pollution monitoring at London Heathrow Airport (UK).

[8] Alphasense Ltd, UK is the industrial partner that manufactures the electrochemical sensors used in this research work.

Chapter 2 Overview of Air Quality Monitoring Techniques

Chapter Summary

The most practical approach to air quality assessment is the measurements of pollutants in areas where pollution is suspected. These measurements are often used to validate model data and form part of the requirements for standard air quality assessment. This chapter will review some of the techniques currently used for air pollution studies. In addition, some of the desirable selection criteria for consideration in the choice of measuring techniques will be discussed. Focus will be on the principles of operation and comparing the advantages and disadvantages of each technique in relation to the selection criteria.

2.1. Examples of measuring techniques

2.1.1. Chemiluminescence technique

This technique works by measuring light emission (UV, IR or visible) resulting from the deactivation of a chemically excited product molecule resulting from the reaction between the analyte molecule and reactant species as shown in the reactions R2.1-R2.2.

R2.1 $$A + R \rightarrow P^*$$

R2.2 $$P^* \rightarrow P + h\nu$$

Where *A* is the ground state of the analyte molecule, P^* is the excited state of the product molecule, *P* is the ground state of the product molecule and *R* is molecule of the reactant that resulted in the chemiluminescence reaction. Quantitative analysis is based on the proportional dependence of the intensity of the emitted light to the concentration of the excited analyte molecules. The emitted light is detected with the aid of photomultipliers [12]. A calibration plot of known gas concentrations of analyte against the intensities of emitted light is used to characterise chemiluminescence instruments. This is one of the widely used technique for the analyses of nitrogen containing compounds and it is the recommended standard technique for determining NO and NO_2 by both EU Commission and US-EPA [35, 41]. It directly measures NO and other species such as NO_2, HONO, HNO_3, N_2O_5, peroxyacetyl nitrate (PAN), NO_X, ammonia, and NO_3 by first converting them to NO and estimating their contribution to the total NO measured. In this instrument NO reacts with O_3

to form excited NO_2* which subsequently deactivates to ground state NO_2 with the emission of light at wavelengths between 590 nm and 2800 nm [12]. The emitted light is detected using red-sensitive photomultipliers fitted with optical filters which remove photons of wavelength below 600 nm thereby preventing interference from light emitted from products of other reactive gas species [41]. This technique can be used for monitoring NO_2 by first reducing it to NO by passing it through hot molybdenum chips at a temperature of 315^{o}C. The equivalent NO_2 is thereafter determined from the NO concentrations measured. Interference from other nitrogen species is negligible at ambient concentrations. Direct NO_2 measurement without the need for reduction can be achieved by reacting NO_2 with luminal resulting in chemiluminescence reaction with emitted light of wavelength around 424 nm [56]. Chemiluminescence has also been used for determining O_3 concentration by reacting O_3 with ethene resulting in exited product which emits characteristic light with wavelength centred at 440 nm [57].

2.1.2. Spectroscopic techniques

Spectroscopic techniques are based on changes in the properties of light after interaction with the analyte molecules. An example is the absorption spectroscopy in which the intensity of the original light is altered due to absorption by an analyte over a given path length. Analytical techniques based on absorption spectroscopy include fluorescence techniques, tunable diode laser absorption spectroscopy (TDLAS), non-dispersive infrared spectroscopy (NDIR), ultraviolet photometry and differential optical absorption spectroscopy (DOAS).

2.1.2.1. Fluorescence technique

This technique relies on the molecules of the analyte having an excited state with short enough life-time relative to the collision deactivation life time [58]. Once excited by a light source, the excited molecules decay from excited state to a more stable and lower energy state by the emission of light of different wavelength from that of the original light (fluorescence). Fluorescence can be induced by a laser beam and this form of fluorescence is known as laser induced fluorescence (LIF). The fluorescence light is observed using a photomultiplier tubes. Depending on the number of photon type present in the laser beam, there can be either single photon (SP), double photon (DP) or triple photon laser induced

fluorescence (TP). LIF has been used to monitor ambient concentrations of NO using pulsed ultraviolet (UV) and infrared (IR) laser light sources [41]. The resulting fluorescence is observed at wavelengths between 187 and 220 nm. Ambient SO_2 can also be measured using a zinc (213.8 nm) or cadmium (228.8 nm) light source and observing the resulting fluorescence between 200-400 nm [12].

2.1.2.2. Tunable diode laser absorption spectroscopy (TDLAS)

TDLAS is a form of absorption spectroscopy similar to Fourier transform infrared spectroscopy (FTIR) in which the analyte molecules absorb light of particular wavelength in the infrared region. However unlike FTIR which utilise a light source with continuous wavelength and so scans the entire wavelength spectrum, TDLAS utilise a laser light source with very narrow line width which can be tuned over a smaller wavelength range (e.g. 100 to 200 cm^{-1}). The ability to tune over a smaller wavelength range improves the resolution and sensitivity of TDLAS when compared to FTIR [12]. Quantitative analysis of TDLAS is based on comparing the relative light intensity (or power, P) of the transmitted light to the incident light (P_0) with the product of wavelength dependent absorption cross section (σ_λ in cm^2 $molecule^{-1}$), absorption path length (L in cm) and the concentration of the analyte (N in molecules cm^{-3}) as shown in Beer-Lambert relationship in equation E2.1. This technique has been used for measuring ambient concentrations of SO_2, NO, NO_2 and CO [12, 41, 59].

E2.1. $$\frac{P}{P_0} = \exp\left(-\sigma_\lambda . N . L\right)$$

2.1.2.3. Non-dispersive infrared spectroscopy (NDIR)

NDIR measures the infrared light absorption by infrared absorbing gas species without utilising dispersion radiation or Fourier transform technique. In operation, infrared light is passed through two cells: one containing the sample air (called sample cell) operated in continuous flow mode and the other holding a non-infrared-absorbing gas (called the reference cell) as shown in figure 2.1. A third cell (sensor cell) is filled with the gas of interest but the cell is also separated into two compartments (A and B) by a flexible metal diaphragm. One part of the sensor cell (labelled A) faces the reference cell and the other half (labelled B) faces the sample cell.

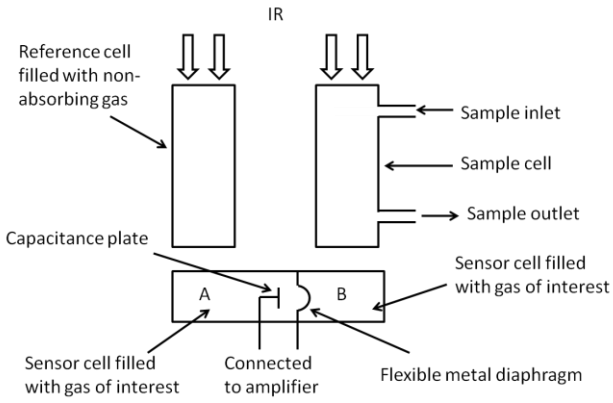

Figure 2.1. Schematics of nondispersive infrared instrument (adapted from Finlayson-Pitts [12])

If no absorbing gas is present in the sample cell, then the IR beam emerging from the reference and sample cells will heat up the compartments A and B in the sensor cell at the same rate causing equal gas expansion and no movement in the flexible metal diaphragm. However if the sample has an IR absorbing species, less IR beam will strike the compartment B of the sensor cell relative to compartment A, resulting in more heating in this compartment of the sensor cell. This different heating rate results in a pressure gradient due to the different expansion of the gas in the two compartments. This leads to a movement of the flexible metal diaphragm towards compartment B which in turn results in a change in the capacitance of the fixed capacitance plate connected to the diaphragm [12]. The degree of change in capacitance reflects the concentration of the analyte. This method has been used to monitor CO species in the atmosphere and is the recommended instrumentation by the EPA and the European Commission for the assessment of ambient CO concentrations [18, 35]. This instrumentation has the advantage that it is not sensitive to sample flow rate and changes in ambient temperature. They are also sensitive over a wide range of operational temperature [18].

2.1.2.4. Ultraviolet absorption spectroscopy (or ultraviolet photometry)

Ultraviolet photometry also uses Beer-Lambert relationship although the light source used in this method lies in the UV region of the electromagnetic spectrum. Practical application of this technique can vary depending on the optical path length of the instrument. It can either be short path length (typically 0.15 to 0.3 m) or long-path length (3 m). The technique has been successfully used in monitoring ambient O_3. Current O_3 UV photometry instruments

have improved sensitivity by comparing transmitted light (λ = 254 nm) from the sample air with light from air already scrubbed of any O_3 using manganese dioxide (MnO_2). The concentration of O_3 is determined using Beer-Lambert relationship because the absorption cross section of O_3 at wavelength of 254 nm is well characterised [60].

2.1.2.5. Differential optical absorption spectroscopy (DOAS)

DOAS measures absorption of light with two different but close wavelengths from an artificial source by an atmospheric species over a path range typically of 0.5 to 1.5 km. One of the wavelengths is characteristic of the absorption line of the target species while the other wavelength with slight offset is chosen to account for atmospheric interferences [60]. The differential optical absorption (*D'*) from these two wavelengths is related to the concentration (*N*) using the Beer-Lambert relationship shown in E2.2.

E2.2
$$D' = \ln\left(\frac{I_0'(\lambda)}{I'(\lambda)}\right) = L\left[\Sigma\sigma_\lambda' N\right]$$

Where $I'_0(\lambda)$ is the intensity of the light in ambient air in the absence of the absorbing species, $I'(\lambda)$ is the intensity of the light in ambient atmosphere due to the absorbing species, *L* is the optical path length and σ'_λ is the optical coefficient of the absorbing species. One advantage of this technique is that it is an absolute measurement because the differential optical coefficients of the target molecules are well known, hence eliminating the need for field calibration [12]. This technique has been used for the measurement of several atmospheric species including O_3, SO_2, NO_2, NO_3, nitrous acid (HONO), formaldehyde (HCHO) and free radicals like OH, BrO, ClO and IO [12]. DOAS is a technique suitable for remote sensing of pollutants in the ambient atmosphere providing both spatial distribution and temporal resolution of the target species. Other advantages of this technique include multi-species detection, high sensitivity and fast response time [60].

2.1.2.6. Light detection and ranging (LIDAR)

Lidar works using similar principles as radar except rather than using radio waves, a laser pulse is fired into the atmosphere and the characteristic scatter of the light is detected and time taken for the return is used to estimate the distance of the scatter species. This method has been applied in remote sensing of atmospheric species especially for vertical

profile studies of concentration distribution. Dual wavelength lidar (DIAL) has made it possible to measure gas species in the atmosphere. The technique is based on comparing the signal returned from the two different wavelengths: one located in a region of strong absorption by the target species and the other in a region of little or no absorption [61, 62]. Species measured using this technique include O_3, SO_2, NO_2 and benzene. DIAL has been successfully used in the vertical profiling of O_3 concentrations in both the troposphere and stratosphere [61].

2.1.3. Passive sensing techniques

Passive sensing technique is based on the principle of diffusion of the analyte unto a reactive substrate. It has the advantage that it is low cost, portable and very simple. It however cannot be used for temporal variation measurements as it only gives mean concentrations over the period of deployment. In addition, the devices based on this technique are analyses offsite in the laboratory. Other disadvantages of the technique include limited specificity (due to interference from other atmospheric species) and possibility of damage during transport or storage and as a result are not generally used as standard methods for ambient air quality monitoring [60]. These techniques are often used for personal exposure studies and for long-term measurement studies such as the evaluation of the impact of pollutants on the environment. They have also found application in remote locations like forests where standard techniques cannot be deployed [60]. Species monitored using passive sensing technique include O_3, NO, NO_2 and CO. Several commercial sampling devices are now available for these species. Palmes diffusion tubes have been used to measure ambient NO and NO_2 [41]. Examples of commercial O_3 passive sensing device (PSD) include ChromoSence^{TM}, Ogawa PSD and indigo carmine PSD. CO has been measured using PSD based on ion-exchange utilising Y-type zeolite and zinc adsorbent [18].

2.1.4. Electrochemical sensors

Electrochemical sensors have been widely used for personal exposure studies and recent advances in nanotechnology have helped improve the sensitivity and selectivity of this technique for application in low concentration measurements as found in ambient conditions. Electrochemical sensors used in gas species measurements are generally referred to as amperometric gas sensors (AGS). The principle of operation is based on

relating the concentration of the target gas to the current generated inside the cell. This current is limited by the rate of diffusion of the gas which in turn is proportional to the concentration gradient across the cell [63]. Detailed review of theory and principle of operation will be discussed in the next chapter. Electrochemical sensors are low-cost, selective, sensitive, and have fast response times. They are however affected by external parameters like temperature, RH and are also susceptible to cross interference. Species that can be detected using this technique include CO, NO, NO_2, O_3, H_2S and SO_2.

The work presented in this thesis shows that some of these shortcomings can be overcome by a combination of post-data processing and the use of simultaneous sensor measurements to account for cross interferences.

2.2. Criteria to be considered for choosing a measuring technique

Some of the criteria desirable in effective measuring technique for ambient pollutant measurements include:

- cost associated with technique including maintenance and operational costs,
- minimal response to environmental factors such as temperature and relative humidity.
- while being very sensitive to its target species, the technique should show little or no response to interfering gases.
- it should be easy to operate with little or no need of specialist training,
- it should be suitable for real time measurements with fast response times and reproducibility of measurements,
- it should be of low energy consumption,
- minimal changes in performance due to operational conditions like pressure and flow rates,
- easily incorporated into an automated monitoring network.

While it is difficult to find any particular technique that meets all the above criteria, recent developments in miniature sensor technology have made electrochemical sensors viable options for the purpose of air quality monitoring. Table 2.1 summarises the advantages and disadvantages of the various measuring techniques in terms of the criteria outlined above.

Table 2.1. Advantages and disadvantages of some techniques used for ambient pollution measurement.

Technique	Atmospheric species	Advantages	Disadvantages
Chemiluminescence	NO†, NO_2†, O_3‡	• High sensitivity. • Fast response time. • Multiple species detection. • Highly selective. • Online data acquisition.	• Expensive cost between £10,000 - £15,000 excluding maintenance [64]. • Requires mains power. • Cannot be deployed in remote locations. • Not cost effective for large network studies. • Requires accessory e.g. pumps. • Cannot be used for remote sensing.
UV spectroscopy	O_3†	• High sensitivity. • Fast response time. • Highly selective. • Good precision. • Online data acquisition.	• Expensive cost between £10,000 - £15,000 excluding maintenance [64]. • Requires mains power. • Cannot be deployed in remote locations. • Requires skilled operator.
NDIR†	CO†, HNO_3	• High sensitivity. • Fast response time. • Highly selective. • Not affected by air flow rate. • Online data acquisition.	• Expensive cost between £10,000 - £15,000 excluding maintenance [64]. • Requires mains power. • Cannot be deployed in remote locations. • Not cost effective for large network studies.
DOAS	O_3‡, SO_2‡, NO_2‡, NO_3, HONO, HCHO, OH, ClO, BrO, IO	• High sensitivity. • Fast response time. • Highly selective. • Multi-species analysis. • Suitable for remote sensing.	• Very expensive cost. • High power demand. • Cannot be deployed in remote locations. • Not cost effective for large network studies. • Requires skilled operator.
Passive sensing	CO, NO, NO_2	• Require no power. • Low cost. • Can be deployed as network. • No need for technical operator.	• No temporal resolution. • Possible interference. • Low precision. • Requires laboratory analysis.
LIDAR	Benzene, NO_2, O_3, SO_2	• High sensitivity. • Fast response time. • Highly selective. • Multi-species analysis. • Suitable for remote sensing.	• Very expensive cost.. • High power demand. • Cannot be deployed in remote locations. • Not cost effective for large network studies. • Requires skilled operator.
Fluorescence	NO, SO_2†	• High sensitivity. • Fast response time. • Highly selective. • Good precision. • Suitable for remote sensing.	• Expensive instrumentation. • Possible drift in background measurement. • Cannot be deployed in remote locations. • Not cost effective for large network studies. • Requires skilled operator.
TDLAS	SO_2, NO, NO_2, CO	• High sensitivity. • Fast response time. • Highly selective. • Multi-species analysis. • Suitable for remote sensing.	• Very expensive cost. • High power demand. • Cannot be deployed in remote locations. • Not cost effective for large network studies. • Requires skilled operator.
Electrochemical sensors	CO, NO, NO_2, O_3, SO_2, H_2S	• Low cost and low power. • High sensitivity (*ca* 2 years). • Fast response time. • Selective. • Multi-species analysis. • No need for technical operator.	• Loss of sensitivity over time. • Possible interference. • Affected by environmental factors like temperature & RH.

† Reference method recommended by EU Commission and U.S. Environmental protection Agency [12, 35].

‡ Equivalent methods recommended by U.S. Environmental Protection Agency.

2.3. Some applications of electrochemical sensors in air quality studies.

The main application of electrochemical sensors in pollution studies has been in the area of personal exposure studies. They are used as pervasive monitoring techniques with several studies reporting their application for gas species mostly CO and more recently NO_2 [65-68]. There is little literature on the application of electrochemical sensors for NO exposure studies and given that the most health and environmental effects of oxides of nitrogen are reported as NO_X (NO and NO_2), it becomes increasingly important to monitor NO in this case using electrochemical sensors. The limited measurements of ambient NO mixing ratio using electrochemical sensors was addressed in thesis by developing electrochemical sensor nodes which simultaneously monitored three important air quality pollutants, CO, NO and NO_2.

Although there have been recent studies attempting to deploy a network of electrochemical based sensors for the purpose of air quality assessment to complement existing fixed monitoring sites, these studies only provided data for limited gaseous pollutants. For instance, in a recent study in Gateshead, UK, only CO and NO_2 were monitored during the network deployment of motes sensors [69]. In addition, the data transmission during this study was via a multi-hop routing protocol utilizing Zigbee enabled mesh network. This data transmission method limits the spatial coverage in this type of sensor network because the sensors must be within certain distance from the relay gateway for optimal data transmission. In contrast, the static electrochemical nodes deployed as part of the air quality network in this thesis utilise GPRS for data transmission (details in chapter 3 and 7). The advantage is that the network design is not limited by the need to cluster the sensor nodes around data transmission hotspots as GPRS is ubiquitous in most cities across the globe. Without such limitation, an area of approximately 10 × 10 km was covered during the network deployment of static sensor nodes which is 50 times as large as the area (2 km^2) covered using the Zigbee data transmission at Gateshead [69, 70]. Although the GPRS module is power consuming, as will be discussed in chapter 3, sophisticated power management in the operational software programme used in the electrochemical sensor nodes helps reduce the power demand.

2.4. Summary and Conclusions.

In this chapter, some of the criteria to be considered in choice of measuring techniques have been reviewed. Some of the existing measuring techniques have been discussed in relation to some of these criteria as summarised in table 2.1. It has been shown that no particular technique satisfies all the requirements but depending on the purpose of the assessments one or more techniques may be suitable. In the absence of fixed measurements, indicative measurements can be used along with model data to characterise pollution in ambient environment [35]. Presently, passive sensing techniques are often used for this purpose although these methods do not provide time resolved measurement. A more suitable replacement for this technique will be electrochemical sensors which have all the advantages of the passive technique in addition to providing fast time resolved measurements. The next chapters will be focused on showing how electrochemical sensors can be utilised for ambient air quality measurements for the purpose of assessments and regulations as well as for personal exposure studies.

Chapter 3 Development of Low–Cost Electrochemical Sensor for Air Quality Monitoring

Chapter Summary

In this chapter, the principles of operation of electrochemical sensors are described together with the main features of the two designs of the electrochemical sensors used in the experiments discussed in subsequent chapters. In addition, the data management and online tool developed as part of network deployment of the electrochemical sensors are also discussed.

3.1. Electrochemical Sensors

Electrochemical sensors are a good example of a practical application of electrochemical techniques in quantitative and qualitative analysis. The application of electrochemical techniques requires an understanding of the principles of the electrochemical processes which govern changes within electrochemical cells. Electrochemical processes are unique in terms of the heterogeneity of interaction between different phases (e.g. solid-liquid) compared to other analytical techniques and this is a fundamental characteristic of all electrochemical cells. A typical electrochemical cell is made up of electrodes which are conductors and an electrolyte which acts as ionic conductor. Reactions can occur in the homogenous electrolyte component of the cell or at the heterogeneous electrode-electrolyte interface.

3.1.1. Theory and Principles of Operation

The principal classes of electrochemical sensors – based on their principle of operation – are conductometric, potentiometric and amperometric sensors. Conductometric sensors rely on the measurement of changes in conductivity of the electrochemical cell due to the reaction of the target species in the electrolyte when external voltage is applied across the cell. The conductance of the electrolyte is represented by the expression given in equation E3.1. G is the conductance (in Ω^{-1}), σ is specific conductivity of the electrolyte ($\Omega^{-1}cm^{-1}$), A is the surface area of the electrode (cm^2) and L (cm) is the distance between the two electrodes [71]. However, due to the nature of this type of electrochemical cell, a potential difference

can develop at the electrode-electrolyte interface either due to a Faradaic process[9] or the formation of a double layer which affects the conductance of electrolyte and accuracy of the measured conductance. This effect can be overcome by incorporating an ac (alternating current) circuit into the overall instrumental design. Although conductometric sensors can be used for quantitative measurements e.g. of ion concentrations, their primary application tends to be in conductometric titration and as detectors for ion chromatography [72].

E3.1 $$G = \frac{\sigma A}{L}$$

The potentiometric technique depends on the measurement of the cell potential in an open-circuit resulting from the reduction-oxidation (redox) reaction occurring at the electrode-electrolyte interface. It is a thermodynamic process governed by the Nernst relation. For instance, consider the redox reaction O + ne = R which occurs at the cathode of an electrochemical cell. This type of reaction is the reductive half cell reaction. The Nernst equation under thermodynamic condition is given in Eq E3.2.

E3.2 $$E = E^0 + \frac{RT}{nF}\ln\left(\frac{a_o}{a_R}\right)$$

Where E is the measured cell potential, E^0 is the standard cell potential at standard state of the species O and R, R is the gas constant, T is absolute temperature, n is number of moles of electrons involved in the reaction, F is the Faraday constant and a_O / a_R are the activity of species O and R respectively. The sensitivity of the potentiometric cell dependent on the gradient of the linear plot of E versus log of the activity ratio. It should be noted that equation E3.2 applies only to the half-cell reaction of the target species, to complete the electrochemical cell reaction a non-interfering half-cell reaction takes place at a reference/counter electrode [73].

Amperometric electrochemical sensors are governed by both kinetic and Faradaic processes and the current resulting from redox half-cell reaction are related to concentrations of the reacting species at the active electrode. As in the potentiometric sensors, a complementary non-interfering half-cell reaction takes place at a counter electrode. The measured current

[9] Faradaic process refers to current flow in an electrochemical cell resulting from redox process at the electrode-electrolyte interface

is directly proportional to the concentration of the active species provided kinetic processes such as mass transfer are controlled (this is usually incorporated into the electrochemical cell design). Recent advances in nanotechnology have made it possible to optimise sensor design to limit factors that would otherwise interfere with the measured current in amperometric electrochemical sensor cells. This has made it possible for the development of amperometric gas sensors which are operated using a three interface system (solid-liquid-gas (analyte) phase) at which fast redox reactions are achievable [63]. The teory and principles of operation of amperometric gas sensors are discussed in detail in the following section.

3.1.2. Amperometric gas sensors

Amperometric gas sensors are electrochemical sensors in which the current resulting from a redox reaction pair is driven across an external circuit under the influence of an external potential. They can be operated with both controlled or variable potential resulting in constant-potential and variable-potential amperometry respectively.

3.1.2.1 Electrochemical reactions

A simple electrochemical sensor is typically made up of two electrodes where redox reaction occur and an electrolyte for ionic transport. Reactions at the electrode-electrolyte interface are called half-cell reactions and are usually either oxidation or reduction reactions. Consider a primitive amperometric gas sensor as illustrated in figure 3.1 with corresponding half reactions occurring at the two electrodes represented by equations E3.3 and E3.4.

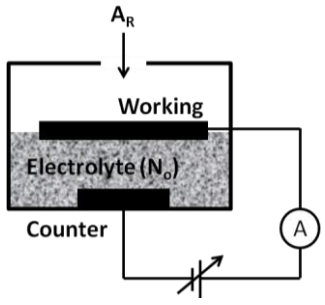

Figure 3.1. Schematic of a primitive amperometric gas sensor cell with two electrodes in contact with a mobile electrolyte with the working electrode exposed to the gas.

A_R represents the gaseous analyte and A_O its oxidised form, N_O the non-interfering species present in the electrolyte, N_R the reduced form of this species and n the stoichiometric number of moles of electrons involved in the redox reaction pair. In figure 3.1, the working electrode is positively biased relative to the external power supply consequently; it will favour oxidation at this electrode while the balancing reduction reaction takes place at the counter electrode.

E3.3 $A_R \rightarrow A_O + ne$ oxidation-half reaction at the anode (working electrode)

E3.4 $N_O + ne \rightarrow N_R$ reduction-half reaction at the cathode (counter electrode)

Generally in electrochemistry, the reduction half-reaction occurs at the cathode while the oxidation half-reaction occurs at the anode [74]; hence in this example the working electrode is the anode and the counter electrode the cathode. Depending on the analyte and the electrical bias of the cell, the oxidation or reduction reaction proceeds at the working electrode. In these types of cells the reaction at the counter electrode must balance that which occurs at the working electrode.

It is somewhat complicated to define the rate of the reactions in an amperometric sensor because of the heterogeneous nature of the chemical interaction occurring at the interface. The rate of these reactions depends on several processes including mass transfer, kinetic (or faradaic) processes arising from redox reactions and nonfaradaic processes (due to adsorption and desorption at the interface) [63, 72, 74]. The external current flowing in the cell is proportion to the rate of reaction at the interface which in turn depends on these competing processes. If the sensor is designed to limit the rate dependence to kinetics and mass transport processes, using a combination of Faraday's Law and mass transport relationships (Nernst-Planck equation), it is possible to define the current generated in terms of concentration of the analyte [74].

3.1.2.2 Theory of limiting current

The measured current in amperometric sensors can be related to concentration using simple mathematical expressions under special operational conditions called limiting conditions. These conditions depend on the two competing processes, the kinetic (rate = r_k) and the mass transport (rate = r_{mt}) of which one of the two rates (r_k or r_{mt}) is the rate

limiting process. The current measured under this specific set of conditions is referred to as limiting current [63].

If the net rate of the electrochemical reaction is limited by the kinetic process ($r_k < r_{mt}$), then the expression for the limiting current i_{lim} is shown in equation E3.5,

E3.5 $$i_{\lim} = nFkA[C]\exp(\alpha nF\eta / RT)$$

where *n* is number mole of electrons involved in the redox reaction, *F* is Faraday's constant, *A* is the area of the electrode, *α* is transfer coefficient, *k* is the standard rate constant, *R* is the gas constant, *η* represents the overpotential, *[C]* is concentration of analyte and *T* is the absolute temperature. If all other variables are constant then the limiting current is directly proportional to *[C]*. It has been reported that the limiting current obtained under this condition is highly unstable thus limiting the practical application of the amperometric sensor [63].

However, if the limiting condition for the cell reaction depends on rate of mass transfer process ($r_{mt} < r_k$), it is possible to define the limiting current by equating Faraday's Law (E3.6) and Fick's Law of diffusion (E3.8) which is one of the three terms in the mass transport rate equation defined by the Nernst-Planck equation E3.7. It is assumed that the rate of mass transport (according to the Nernst-Planck equation) is dominated by the diffusion term ($-D\delta C_i(x)/\delta x$) with the migration ($[-ziF/RT]D_iC_i[\delta\varphi/\delta x]$) and the convection / hydrodynamic terms ($C_iv(x)$) eliminated by employing highly concentrated electrolyte and stable sensor design respectively [72, 74]. The concentration gradient profile under this condition is depicted in figure 3.2.

E3.6 $$\upsilon_{rx} = \frac{i}{nFA}$$

E3.7 $$\upsilon_{mt} = J_i(x) = -D_i\frac{\delta C_i(x)}{\delta x} - \frac{z_iF}{RT}D_iC_i\frac{\delta\phi(x)}{\delta x} + C_iv(x)$$

E3.8 $$\upsilon_{mt} = J_i(x) = -D_i\frac{\delta C_i(x)}{\delta x} = D_i\frac{([C]_\infty - [C]_0)}{\delta_0} = m_0[C]_\infty$$

Under the limiting condition *i* tend to i_{lim}, the overall rate, v_{rx} equal to the mass transport rate, v_{mt}. Consequently combining E3.6 and E3.8 gives an expression for the limiting current in terms of concentration as shown in equation E3.9.

E3.9 $$i_{\lim} = nFAm_0[C]_\infty$$

Note the rate of the kinetic process is faster than the mass transport process hence the concentration of the analyte at the electrode interface will be zero under this limiting condition.

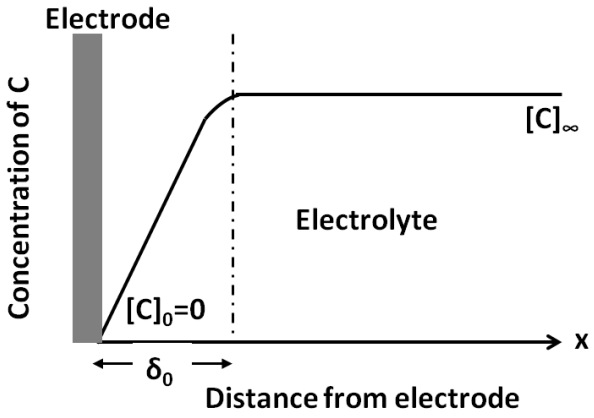

Figure 3.2. Concentration profile at the electrode-electrolyte interface for the limiting condition where the net electrochemical rate of reaction is dominated by the rate of mass transport of the analyte, of concentration C, to the electrode.

In equations E3.6 - E3.9 , C_i is concentration of species *i*, J_i is the flux of species i, *A* is the surface area of the electrode, *i* is the current, i_{lim} represents the limiting current, *n* is the number of moles of electrons, *F* is the Faraday's constant, $[C]_0$ is the concentration C at the electrode surface, $[C]_\infty$ is the concentration, *C* in the bulk solution, $\delta C_i(x)/\delta x$ is the concentration gradient at the distance *x* from the electrode, $\delta\varphi(x)/\delta x$ the potential gradient at distance x, δ_0 is the thickness of Nernst diffusion layer on electrode surface, and m_0 is the mass transfer coefficient which is the Fick's diffusion term D_i per unit length [74].

Amperometric sensors have a successful practical application as the current-concentration plot is linear over a wide concentration range (ppbv to ppmv) [63]. To achieve this desired operating condition, the working electrode is maintained at a constant potential by

introducing a third electrode which is connected to a balancing potentiostatic circuit as discussed in the following section.

3.1.2.3 Components of amperometric gas sensors

A typical amperometric gas sensor with three electrodes connected to an external power supply is shown in figure 3.3.

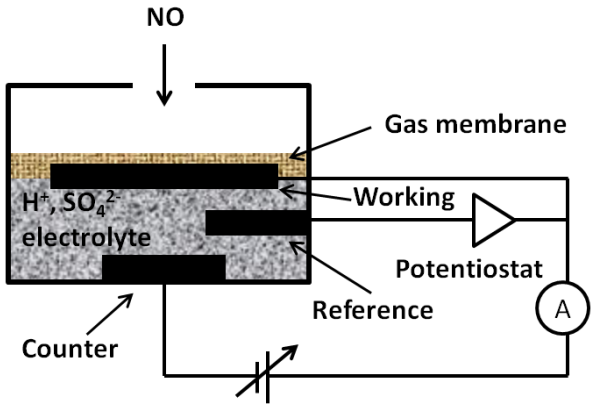

Figure 3.3. Schematic of an amperometric NO gas sensors showing the basic components including three electrodes, electrolyte and gas membrane.

A. Electrodes

Figure 3.3 shows the three electrodes that make up a typical NO amperometric gas sensor. The electrode where the desired reaction occurs is referred to as the working electrode, while the counter electrode is the location of the complementary non-interfering reaction. A third electrode called the reference electrode helps keep the working electrode at a fixed potential under which the measured current is mass transport limited. The half cell reactions proceeding at the electrodes are represented by equations E3.9 and E3.10.

E3.9 $NO + H_2O \rightarrow NO_2 + 2H^+ + 2e$ oxidation-half reaction at working electrode

E3.10 $1/2O_2 + 2H^+ + 2e \rightarrow H_2O$ reduction-half reaction at counter electrode

Typically the working electrode is made up of a highly porous material to maximise its surface area thereby increasing the potential for solid-liquid-gas interface interaction. It is desirable that the working electrode be stable to an applied potential and will be advantageous if it can also serve as catalyst to increase selectivity of the sensors. As a result

typical materials used for making this electrode include noble metals such as platinum, gold, carbon forms like graphite and glassy carbon [63]. In the NO sensor shown in figure 3.3, NO is reduced to NO_2 at the working electrode (see E3.9) and the resulting current is due to the flow of electrons measured in the external circuit.

The counter electrode is often made from platinum and must be stable to the electrolyte solution while serving as the surface for the complementary reaction [63]. In the example of the sensor shown in figure 3.2, the complementary reaction is the reduction of oxygen to a single water molecule at the counter electrode-electrolyte interface (as shown in equation E3.10). It must also be physically separated in the cell from the other electrodes. This is achieved by employing wetting filters which provide ionic connection between the three electrodes by allowing current to flow through the cell through ions present in the wetting filters.

As discussed earlier it is desirable to maintain the working electrode at a potential where the measured current is proportional to the concentration of the reacting analyte species. This is achieved through the use of the reference electrode which is connected to a potentiostat and is in contact with the working electrode (figure 3.3). Good examples of references electrodes include Ag/AgCl and Pt/air electrodes [63].

B. Electrolyte

Electrolytes are ionic conductors used in electrochemical sensors and are in physical contact with both electrodes. They can either be made up of aqueous solutions (e.g. sodium chloride, sulphuric acids, and sodium hydroxide), molten salt (NaCl-KCl eutectic), ionically conducting polymers (e.g. Nafion, polyethylene oxide-$LiClO_4$) or even solid materials like sodium, β-alumina [74]. In the NO sensor shown in figure 3.3, the electrolyte material is concentrated sulphuric acid and it provides the medium for the redox reaction which for the sensor in figure 3.3 proceeds under acidic condition as indicated by the presence of H^+ ion in the half cell equations in E3.9 and E3.10. The concentrated form of the acid is used to ensure the limiting condition for the net rate of the reaction will be diffusion limited as discussed in section 3.1.2.2.

C. Gas Membrane

The gas membrane serves several functions in gas sensors, it helps prevent leakage of electrolyte solution from the sensor, improves selectivity by allowing only the analyte of interest to diffuse through it, and allows products of redox reaction diffuse out of the sensor. The choice of material for the membrane therefore depends on these factors plus the durability and manufacturability of the membrane materials, and on the sensor physical size. Examples of materials used include thin solid Teflon films, silicon membranes and microporous Teflon films [63]. It is the first component of the sensor which the analyte comes in contact with (figure 3.3), therefore the rate of diffusion of the analyte through the membrane will be dominate the diffusion rate and hence the limiting current.

3.1.3. Alphasense toxic gas sensors

Commercial cells used in the air quality sensors described in this thesis are manufactured by Alphasense (Alphasense Ltd, UK). They are either part of the industrial toxic gas sensor product line available from the company or variants of these sensors developed in partnership with the University of Cambridge specifically for air quality applications. These sensors are all amperometric gas sensors and are made up of three working electrodes in electrical contact with the electrolyte (3 – 7 M concentrated sulphuric acid) via wetting filters as shown in fig. 3.4.

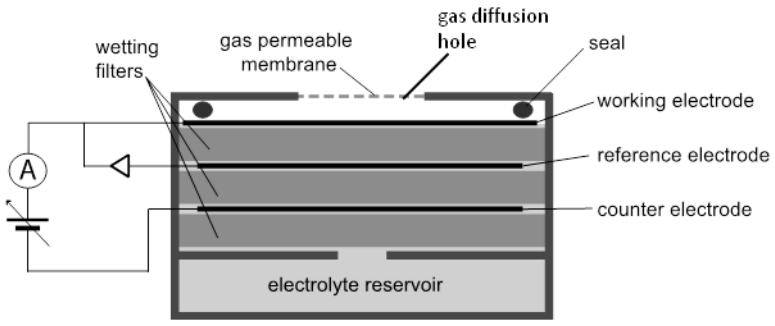

Figure 3.4. Schematic of a typical Alphasense toxic gas sensor showing the major components including the three electrodes, the electrolyte solution reservoir, the gas membrane and wetting filters.

The gas sensors are designed to operate under limiting conditions where the measured current is directly proportional to the concentration of the target gas species [75]. This is

achieved by maintaining the working electrode at fixed potential via the reference electrode as discussed in 3.1.2.

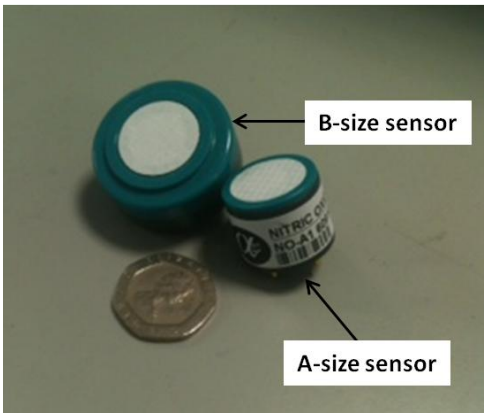

Figure 3.5. Size comparison of Alphasense A-size and B-size sensors relative to a 20 pence coin.

Two sizes of toxic gas sensors were used: the 20mm diameter sensor ("A-size) and 32 mm diameter sensors ("B"-size) as depicted in figure 3.5. These are standard sizes and are used widely in the industrial sector. Both sensors are made up of similar components differing in size/volume and outer shell, specifically the aperture for gas diffusion which affects sensitivity and concentration range. A small aperture in the shell results in lower sensitivity and a larger concentration range whilst a larger aperture leads to a higher sensitivity but relatively smaller concentration range [75].

3.2. Design of electrochemical sensor nodes[10]

The original motivation behind the development of mobile electrochemical sensor nodes was to fulfil part of the research objective of the MESSAGE (Mobile Environmental Sensing System Across Grid Environments) project. It was a three-year project (starting October, 2009) involving collaboration between leading UK Universities and consortium of Industrial partners [76]. The University of Cambridge developed portable handheld (or mobile) air quality sensor instruments monitoring CO, NO and NO_2 for personal exposure studies. Further developments and modifications have been made to the original sensor instruments used in the MESSAGE project details of will be discussed in this section.

[10] In this thesis electrochemical sensor node refers to a air pollution instrument made up of toxic gas sensors, temperature / RH sensors, electronics and weather proof enclosure.

The electrochemical sensor nodes used in this research were designed to take advantage of recent advances in toxic gas sensor developments. Improved sensitivity of gas sensors, low power requirement and portability were some of the key factors considered in the design of the electrochemical sensor nodes. For portability the mobile sensor nodes employed the relatively smaller A-size sensors while the static sensor nodess due to their relatively larger size can be designed to incorporate the B-size sensors. Although practical application of the sensor involves measuring very small currents (nanoampere, nA), the electronic design of the air quality sensor instruments amplifies this signal, converts it to digital outputs which are then converted to concentration units (ppb) using known calibration factors generated for each sensor. These data are then stored onboard the sensor unit or transmitted to a remote server which can either serve as a historical database or provide live visual data updates in the form of time series and spatial KML[11] plots.

3.2.1. Hardware design

The common hardware features of both the mobile and static sensors instruments are the electrochemical sensors, temperature sensors GPS (Global Positioning System) and GPRS (Global Packet Radio Service) transmitter, controlling electronics (with slight modifications) and batteries (of different sizes).

3.2.1.1. Mobile sensor nodes

Two generations of mobile sensor nodes were used in this research: the first generation mobile sensor nodes (called type A's) required mobile phone for data storage and transmission and the second generation mobile sensor nodes (referred to as type C's) which had onboard data storage and transmission functionality and thus did not need a paired mobile phone.

Both generations of mobile sensor nodes incorporated three Alphasense A-size electrochemical sensors (measuring CO, NO and NO_2), a temperature sensor (platinum resistance thermometer) located close to the electrochemical sensors and a GPS antenna for accurate time and position data (figure 3.6). In addition, a PIC (Programmable Interface Controller) (PIC 18F67J10, Microchip Technology Inc., USA) with 128K byte FLASH, 4 K byte

[11] KML refers to Keyhole Markup Language which is used to generate geographic and visualised annotations in two or three dimensional internet based Google earth maps.

RAM and 128 byte programmable EEPROM was used as the microcontroller for the sensor node. An operational programme in Intellec Hex format was stored on the FLASH while operational parameters written in C were stored in the EEPROM.

In the first generation (type A) sensors measurement data are stored onboard the mobile phone and data transmission is via GPRS functionality onboard the phone. In contrast in the second generation sensor instruments, measurement data are stored on a 128K byte memory external to the PIC while data are transmitted using the onboard GPS-GSM module (Telit GM862-GPS, Telit Wireless Solutions Inc, USA) with GPRS antenna (Isis 900/1800/1900 MHz internal antenna). This design modification was necessitated by the fact that deployment time of the first generation mobile sensor unit was limited by the battery life of the mobile phone which lasted about four hours (when operated with Bluetooth active with data transmission via GPRS) although the sensor unit itself can be operated for about eighteen hours on fully charged batteries. The sensors instruments are powered by four standard AA rechargeable batteries except for long-term studies where they can be powered by mains using a DC power adaptor.

All components are housed in a 18.5 × 9 × 3 cm enclosure (H-75-4AA, Serpac Electronic Enclosures, USA) with a protective mesh opening at the end close to the electrochemical sensors (figure 3.6).

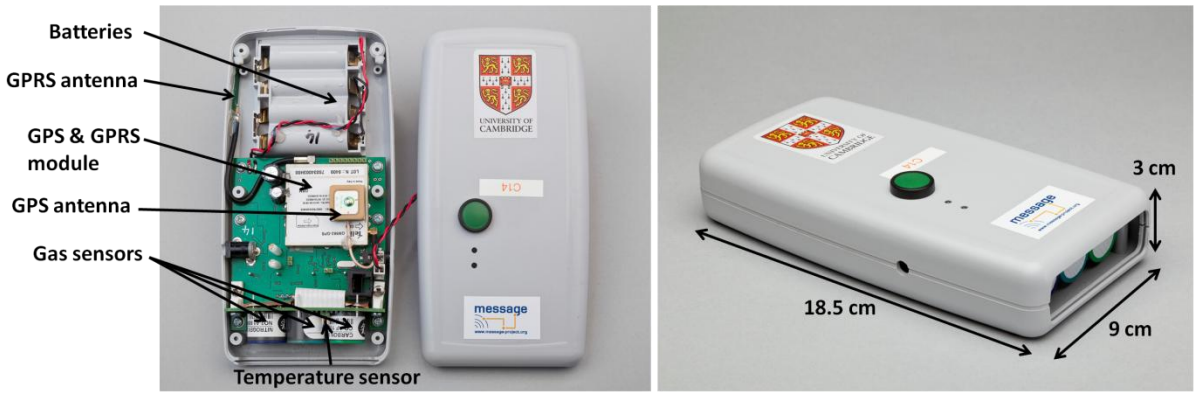

Figure 3.6. Mobile sensor node (type C) incorporating three electrochemical sensors (for CO, NO and NO_2 in this case). Components (GPS/GPRS module, batteries etc.) are identified in the left panel. For clarity, the unit is shown without its protective wire mesh, which, during operation, is located in front of the sensors.

The mobile AQ sensors have a gross weight of <300g and are operated by single button on the sensor enclosure. Data are sampled at 1 s intervals (1 Hz) for the type A instruments and at 5s intervals (i.e. 0.2 Hz) for the type C instruments. Internal communication with the type C instruments is via the RS232 protocol with data sent in the NMEA0183 v2.2 format while this is achieved via Bluetooth connection for the type A. Although another variant of the type C sensors (second generation mobile AQ instruments) which incorporated CO_2, total VOC and one electrochemical sensor were also developed. Results from these sensor instruments are not presented in this thesis.

3.2.1.1. Static sensor nodes

Static sensor nodes based on successful deployment and application of the mobile sensor nodes were designed for long-term (months), autonomous and maintenance-free operation (see Figure 3.7). Like the mobile AQ instruments, three electrochemical sensors measuring CO, NO and NO_2 were incorporated into the design but, as the hand-held constraint had been removed, larger sensors (Alphasense B-size sensors see figure 3.4) were used for increased long-term baseline stability. Data were collected at 10 second intervals and transmitted every 2 hours (data frequency and transmission periods can be changed straightforwardly in the firmware see section 3.2.2.).

The static sensor nodes incorporate temperature (platinum resistance thermometer) and humidity (Honeywell 4000 series humidity sensor, Automatic and Control Solutions, USA) probes in addition to the electrochemical sensors. The temperature and humidity probes are located in a modified IP66-rated through connector with a gas-permeable, hydrophobic membrane covering the open end. This configuration allows measurement of conditions outside the sensor unit enclosure rather than internal measurements, without compromising robustness and weather proofing.

Position and accurate times are collected via GPS and GPRS modem (The GPS unit is internal to the GPRS module (Telit GM862-GPS, Telit Wireless Solutions Inc, USA)), which has its antenna (low profile, combined GPS patch and GSM unit with a 26dB gain) mounted on the top of the sensor node for maximum satellite visibility. Like the mobile instruments, the microcontroller used is a PIC (PIC 18F67J10, Microchip Technology Inc., USA) with 128 byte programmable EEPROM onto which operational parameters are stored and 128 K byte

FLASH onto which the sensor operational programme (Intellec Hex files) are stored. Measurement data were stored on an additional 16 M byte onboard memory which is external to the PIC memory. The GPRS module incorporates a mobile phone SIM card (Subscriber Identity Module, “Mini” format). Internal communication is via the RS232 protocol with data sent in the NMEA0183 v2.2 format.

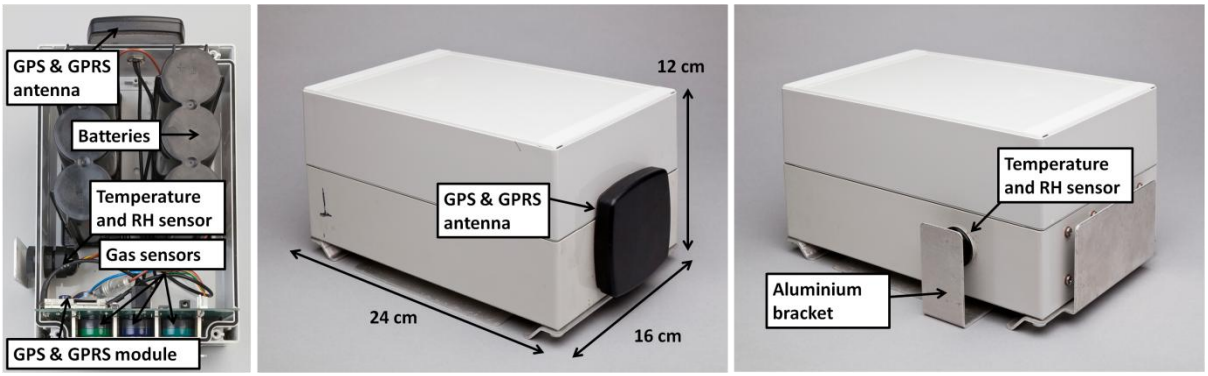

Figure 3.7. Static sensor node showing three electrochemical sensors (for CO, NO and NO_2), RH & temperature sensor, GPS & GPRS unit and batteries (left panel). The middle and right panels show the closed sensor unit with the protective aluminium bracket.

Power is supplied by 2 sets of 3-cell lead-acid battery monoblocs running in series (Hawker Cyclon, 6 V, 8 Ah, EnerSys Europe, Switzerland) as shown in figure 3.7. If the instruments are operated with the sampling and transmitting times described above then it will have sufficient power to operate for approximately 3 months (this varied slightly depending on GPS and GPRS field strength, and also on operation of the tip sensor functionality). The static sensor may be securely attached to suitable street furniture such as a lamp-post using a formed aluminum bracket attached to an IP66 enclosure, which is bound using two Tamtorque tamperproof bands (Tamtorque, JCS Hi-Torque LTD, UK). To minimise the visual impact on the installation location, the enclosure is neutral in colour and has no external indicator lights or control buttons. To ensure that the static sensor installation is correct, the instruments are set up and sealed in a standby mode with an external magnetic reed preventing early activation. This standby mode is left in operation until the sensor unit is correctly installed, at which point the magnet is removed and normal sensor operation commences. The gross weight of a typical static AQ sensor unit is 3.5kg with external dimensions of 24 × 16 × 12 cm (see figure 3.7).

3.2.2. Operational software of sensors nodes

As discussed in section 3.2.1, the sensor operation is controlled by a PIC programme while the higher functionality such as the GPS and GPRS modules are controlled by code written in the Python programming [77]. In the case of the mobile sensor instruments, this code is installed on the mobile phone for the type A sensors and is stored on the GPS-GSM module (Telit GM862-GPS) for the type C's and the static sensor nodes. It is desirable to keep higher functionality commands to a minimum to reduce power consumption especially by the GPS and GPRS antennae. To achieve this, data are stacked in batches before being transmitted as a single set to the data base.

Three different command routines (setup command, data command and tilt command) can be activated in the static sensor instruments. Each command routine involves interaction between the PIC code and the Python code with different output resulting from return for each query. This output can alter the frequency of data transmission or power cycling the GPS/GPRS modules to help conserve battery life. Each of the three different command routine is discussed in detail below.

3.2.2.1. Setup command routine

This is the first command routine that is executed once the sensor is powered on for operation. Essentially the PIC code switches on the GPRS module then waits for a response signal from the Python script in this case a "G" character. If it does not receive this after a given time interval it times out from the routine. If a positive response is received, the PIC sends the sensor details (the sensor ID and a command line "setup") to the Python. Once the Python code receives the "setup" it sends <cr> to the PIC and thereafter switches on the GPS module, if a GPS fix is acquired it sends the GPS data to the PIC which will otherwise timeout after 8 minutes. The PIC then writes the time to the onboard clock and also saves the location information. The PIC then sets the timer to wait for 6 minutes whilst continuing to log data. At this point the GPS is switched off and line of code (RI=1) is sent to the PIC to power off the GPRS module, if the PIC does not receive a command line to power off the GPRS module, then the 6 minutes timer takes effect (it automatically powers down GPRS module). Shown in figure 3.8 is a flow chart that summarises the setup command routine.

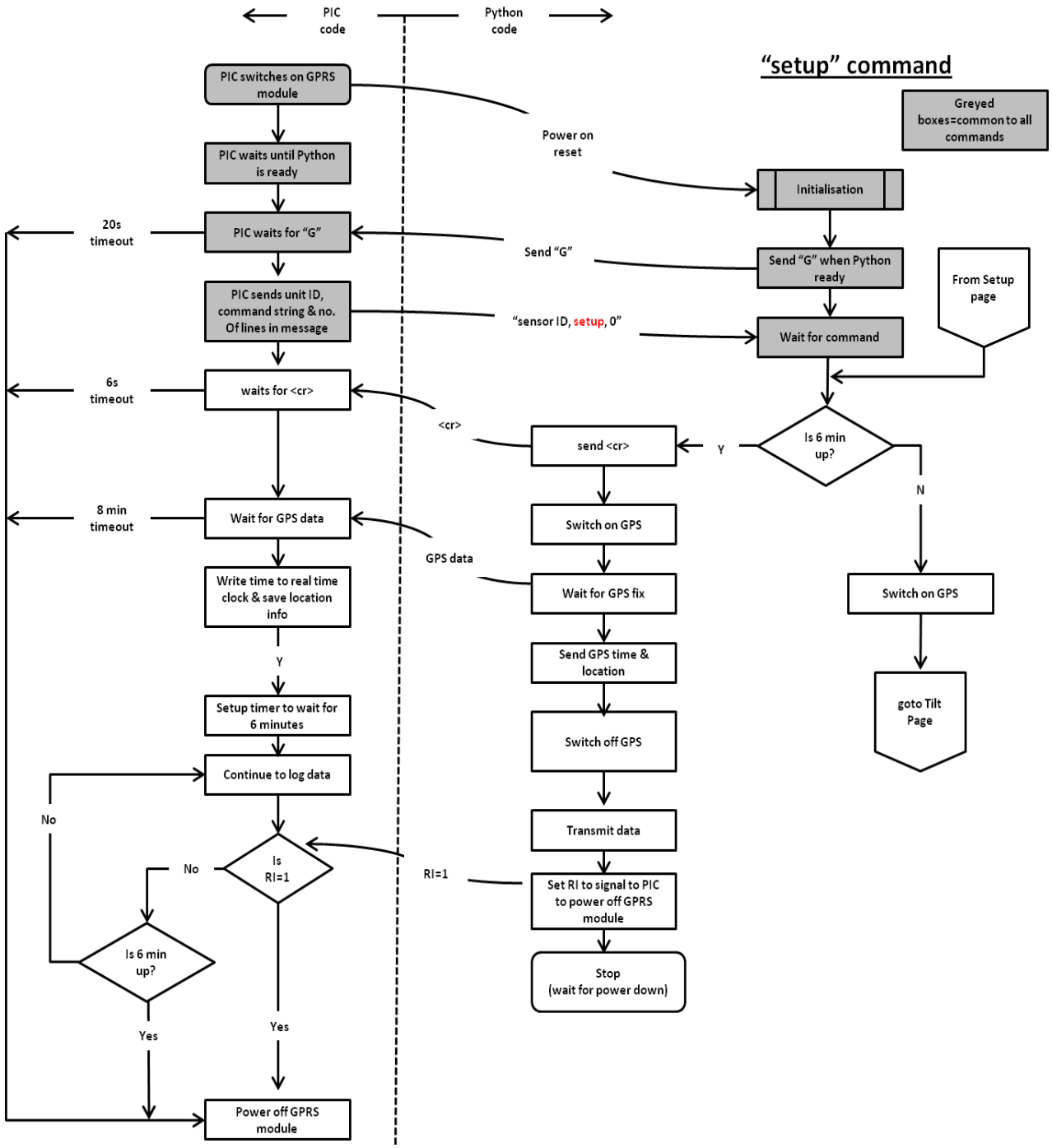

Figure 3.8. Flow chart showing the setup command routine for the static sensor nodes.

3.2.2.2. Data command routine

This routine is initiated after the setup mode, and it functions mainly to log data and also transmit data. This is the primary operational routine. Note the greyed boxes in figure 3.9 are common to all command routines. In this command routine the PIC sends a data message to the Python rather than a setup message which in turn sends a <cr> message to

the PIC. This triggers a data line to be sent from the PIC to the Python with the first line of the data being time record (which was registered in the setup routine). The Python then sends a message (another line of command <cr>) to the PIC which the PIC interprets as a request for more data. Note the PIC times out from executing this if it does not receive the <cr> command from the Python modules. The size of a data message depends on the acquisition time set in the operational parameters on the PIC. The default operational routine of the static sensor instruments has a two-hour data acquisition time, thus the loop before the decision command in both the PIC and Python code will be repeated until 2 hours of data is stacked. This results in a completed response in both the Python and PIC code execution. The Python then initiates data transmission while the PIC activates the 6 minutes timer and continues logging data. With the end of data transmission, the Python sends a message to the PIC to power off the GPRS module. A summary of this command routine is depicted in figure 3.9.

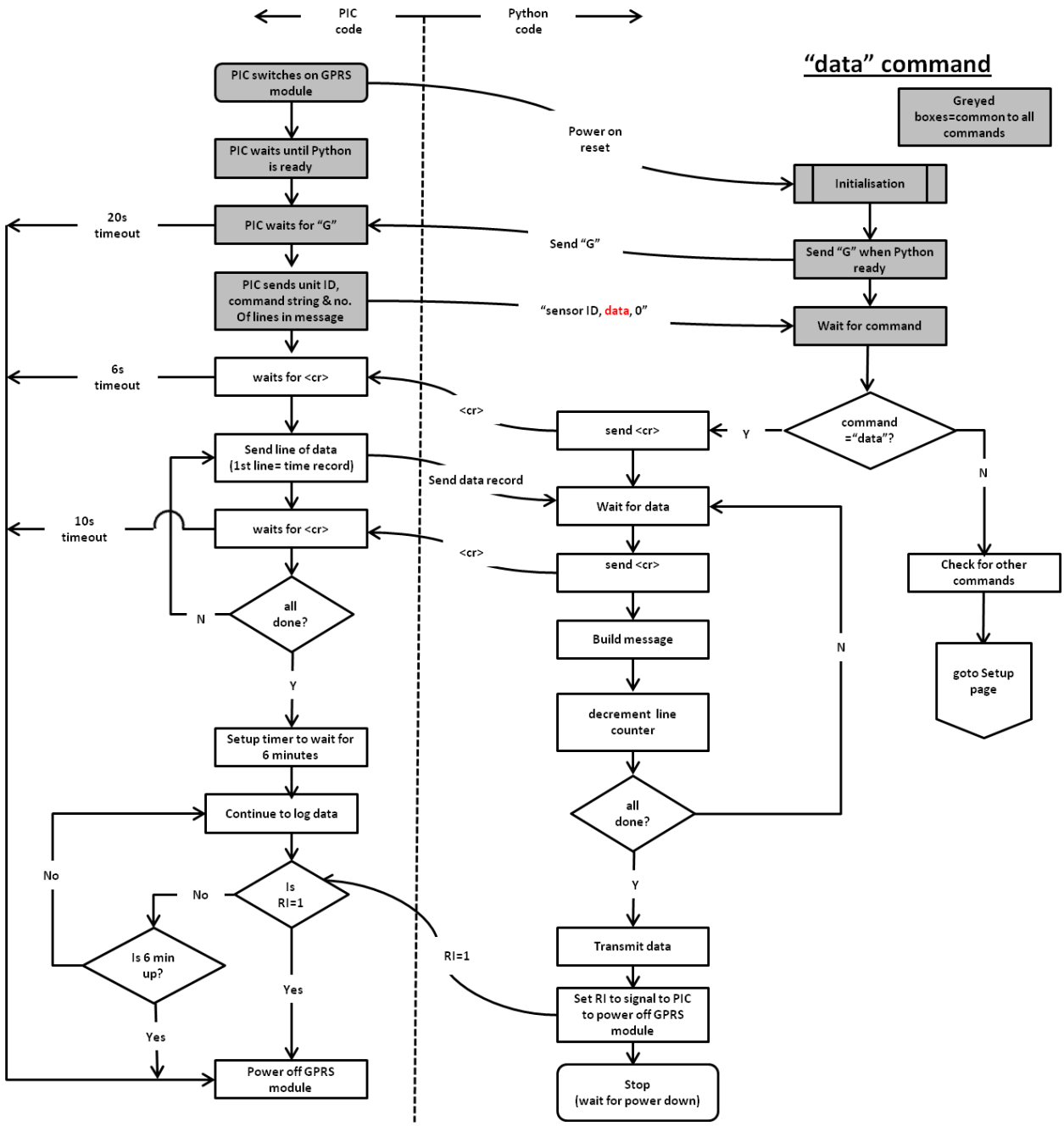

Figure 3.9. Flow chart showing the data command routine for the static sensor nodes.

3.2.2.1. Tilt command routine

Figure 3.10 shows a flow chart summarising the tilt command routine. This is non-standard operational routine which is only activated if the sensor is tilted more than 15 degrees from normal indicating that there is an issue with the installation of the sensor unit. One of the key differences in this routine compared to the data command routine is the activation of the GPS module which is a power draining component (which is not live under normal operational conditions i.e. data command routine). If the tilt command routine is triggered

the PIC sends a tilt message to the Python module which in turn activates the GPS module after 30 attempts with a 30 s interval between each attempt. If a fix is acquired, positional data is transmitted otherwise it transmits position data from the startup routine. Data continues to be acquired and logged in this mode. Note in this command routine the battery life of the sensor instruments will not last for the estimated three month period as there is a significantly greater demand for power due to frequent position acquisition and transmission.

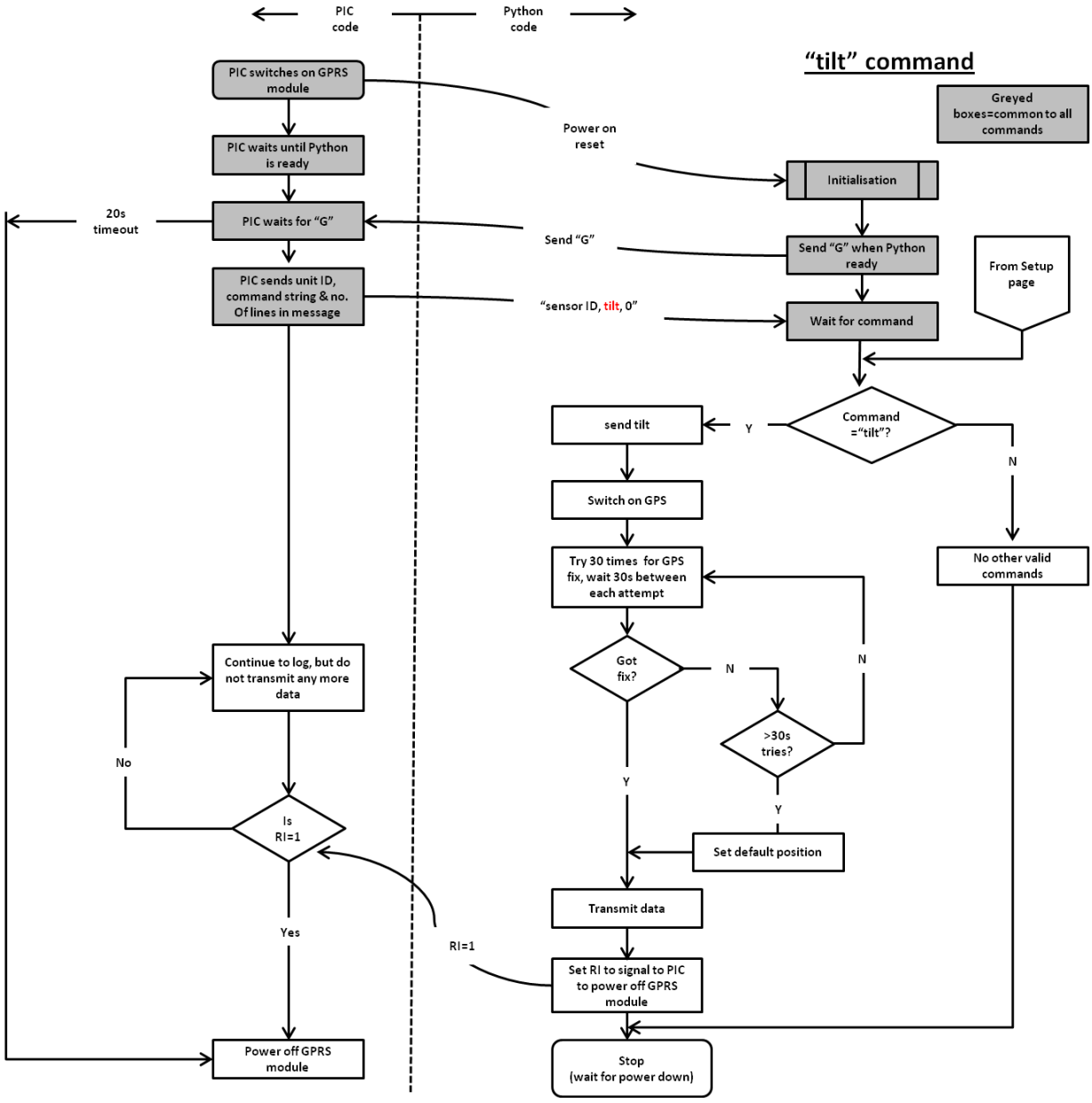

Figure 3.10. Flow chart showing the tilt command routine for the static sensor nodes.

3.3. Network and data management

During the MESSAGE project, an online data management facility was developed for real time interrogation and storage of data. The database was managed by project partner from Cambridge eScience Centre and The Cavendish Laboratory, University of Cambridge.

3.3.1. Online data storage and management

Data is transmitted by the sensor instruments using the HTTP (Hypertext Transfer Protocol) over a GPRS data network (for this research the O_2 network was primarily used) to an

Apache 2 web server [78]. This web server hosts a number of Computer Generated Imagery (CGI) scripts which inject the data into relevant PostgreSQL [79] database running on the same physical host. Other scripts allow for data mining and visualisation of ingested data, either by retrieving the data in its raw form or presenting it in graphical form on a web browser.

3.3.2. Online data visualisation and processing

For the mobile sensor nodes, the visual display can be in the form of time series which can be displayed as either raw, smooth or rebased data as shown in figure 3.11(a) or as map-based plots embedded within the Google Earth plug-in as depicted in figure 3.11(b). The map based plots can either be in form of static (KML plots) or dynamic in the form of video display (as shown in figure 3.11b). The dynamic and static display provides quick qualitative information on the spatial variability of the monitored gas species. The lighter colour in the video indicates low mixing ratios and the darker colour implies high mixing ratios (right panel figure 3.11). In contrast, the relative mixing ratio levels are shown by height difference in the spatial plots (left panel figure 3.11b). This tool makes it possible to quickly identify sensor failure during mobile sensor network deployment and makes it faster to implement contingency plans (e.g. restarting sensor unit or replacing failed instruments with new ones) thereby improving data coverage during the deployment.

A different web interactive tool was developed for the static sensor nodes since by design they are not meant to be mobile. This tool provides display of the sensor network on either a Google Earth map or Google map interface as shown in figure 3.12. In addition to giving information on the coverage of the sensor network, an additional diagnostic tool (Inset plot figure 3.12) is available for each sensor within the network. This tool is used to check failure in terms of failed data transmission or for tilt events. If frequent tilt events are observed or there is failed data upload, the unit installation in question is inspected for possible damage. For instance, during the network deployment in Cambridge (March-May, 2010 details discussed in chapter 7), a sensor unit located close to bus stop failed to send data few days after installation, on inspection it was found that the unit had been hit by a bus and had to be replaced to re-establish the desired network coverage.

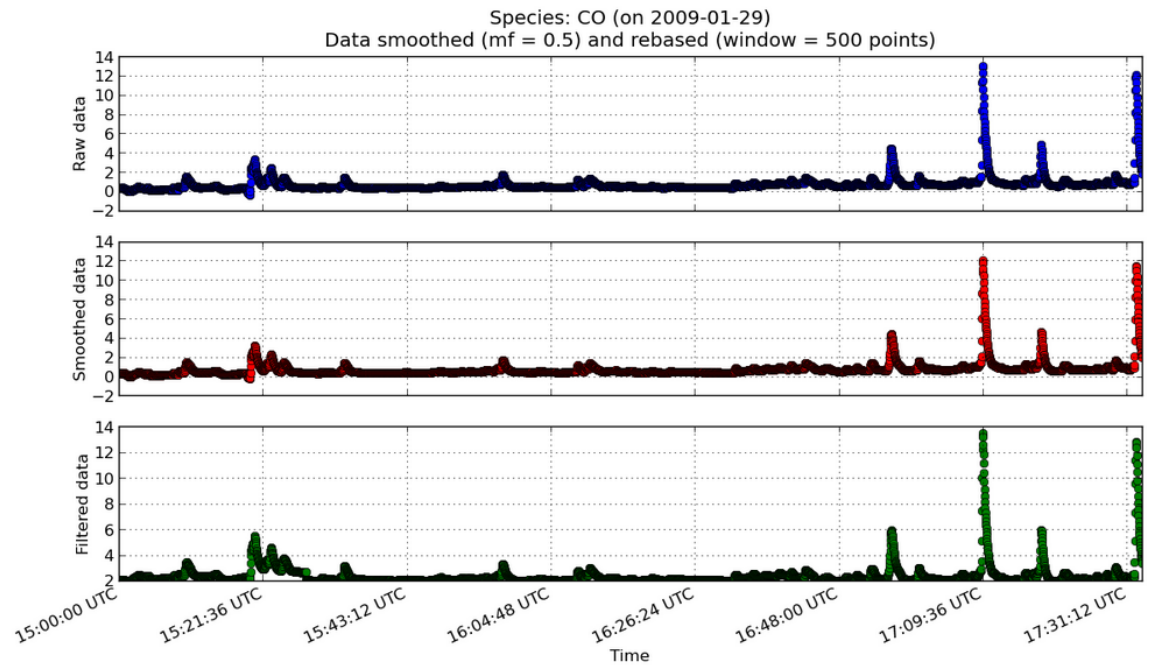

(a)

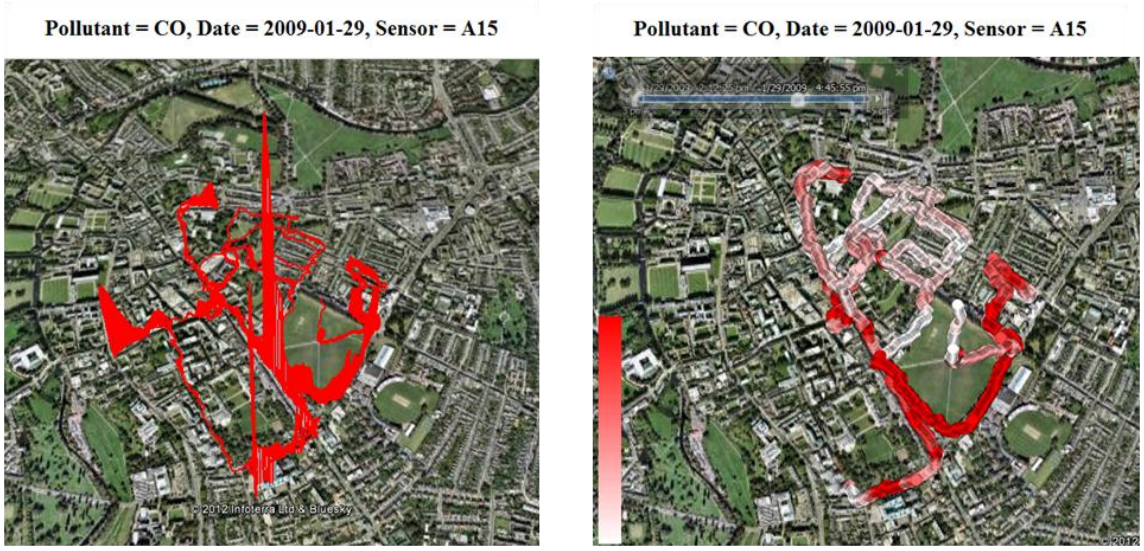

(b)

Figure 3.11. Screen shot of online visualisation tool for mobile sensor nodes. (a) Time series plot for sensor A15 for a two and half hour deployment in Cambridge, UK (29th January, 2009). (b) Static (spatial plot, left panel) and dynamic plot (video, right panel) showing spatial distribution of CO mixing ratios during the deployment. Note in the spatial plot, the heights of the trace are a proxy for mixing ratios. Maps courtesy Google Earth [80].

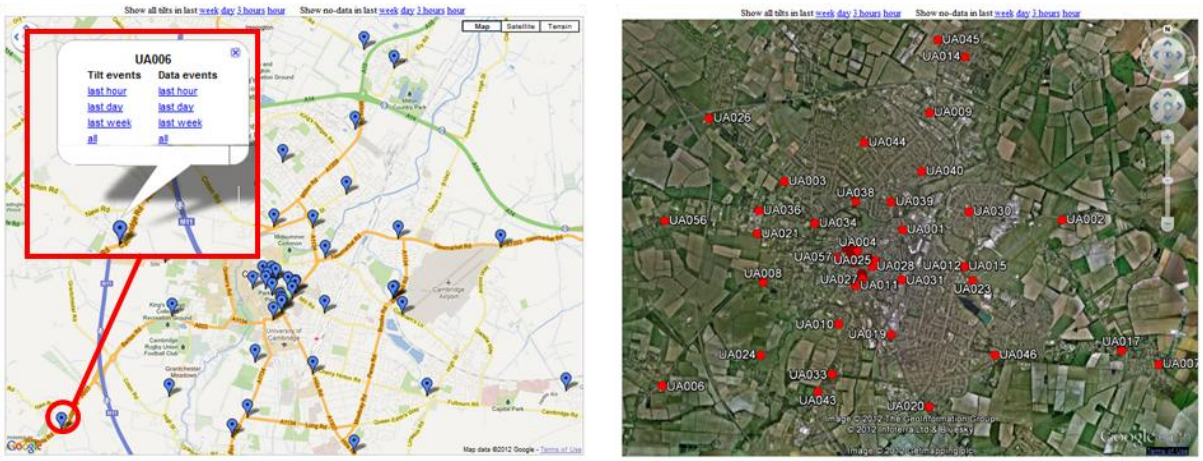

Figure 3.12. Online interactive map used for monitoring the network of static sensor nodes around Cambridge, UK for a three-month deployment covering an area of about 100 km^2 (March-May, 2010). (a) Map displayed on Google Map interface (Inset is additional interactive tool used to access data transmission or failure for each sensor). (b) Map displayed on Google Earth interface. Map courtesy Google Map and Google earth [80, 81].

3.4. Summary and conclusions

Some of the fundamentals and principles of operation of electrochemical sensors have been discussed including the properties of the electrochemical sensors used in this thesis.

The design details of the two variations of air quality sensor (mobile and static senor nodes) developed at the Chemistry Department, University of Cambridge with Alphasense have been explained in terms of their physical components and operational software. Qualitative assessments of the sensor nodes are discussed in chapter four.

Data management and visualisation tools developed as part of the Cambridge AQ monitoring system have also been discussed. Although this facility was developed and successfully implemented as part of the MESSAGE project, it has been subsequently modified for network deployments of mobile and static sensor nodes (chapter 7) as well as for the upcoming research project involving pollution monitoring in and around London Heathrow Airport (chapter 8).

Chapter 4 Characterisation of Electrochemical Sensor Nodes

Chapter Summary

Discussed in this chapter are the procedures used for characterising, calibrating and validating the performance of the electrochemical sensor nodes. This involved carrying out a series of laboratory tests to assess sensor response, selectivity and reproducibility. Also described in this chapter are two intercomparison studies with different measuring techniques used for monitoring air quality in the urban environment. In addition, sources of interference and how these can be accounted for are discussed in detail. This chapter is structured such that there are conclusions for sections where field measurement data are presented.

4.1. Calibration of electrochemical sensor nodes

A series of laboratory tests were carried out at Alphasense UK using known gas mixing ratios at parts per billion by volume (ppb) levels. These tests were done at relatively low mixing ratios (< 200 ppb) compared to the standard tests done by the manufacture which were often in the parts per million by volume (ppm) range as the sensors were originally designed for alarming and warning applications in industrial environment.

4.2. Laboratory tests

4.2.1. Experimental section

4.2.1.1. Apparatus and test setup

For the laboratory tests, eight mobile sensor nodes (five for simultaneous CO and NO_2 and three for NO mixing ratio measurements) were used. First generation mobile sensor nodes (type A's) were used for the CO and NO_2 test while second generation mobile sensor nodes (type C) were selected for the NO tests. The reason for using different sensor nodes for the NO test was because of the lower noise characteristics (< 1 ppb). The CO and NO_2 sensor nodes logged data onboard a mobile phone whereas NO data were stored on an internal memory. Eight of the nine sensor nodes were placed in a Perspex chamber with an approximate internal volume capacity of 16 litres (see figure 4.1). Two fans (80 × 80 × 32cm,

ebm W2G076-BF13-01, DC fan) were fitted inside the chamber to facilitate rapid mixing of the gas mixture. The reason for using multiple sensor nodes for this test is to verify reproducibility in sensor performance across different nodes.

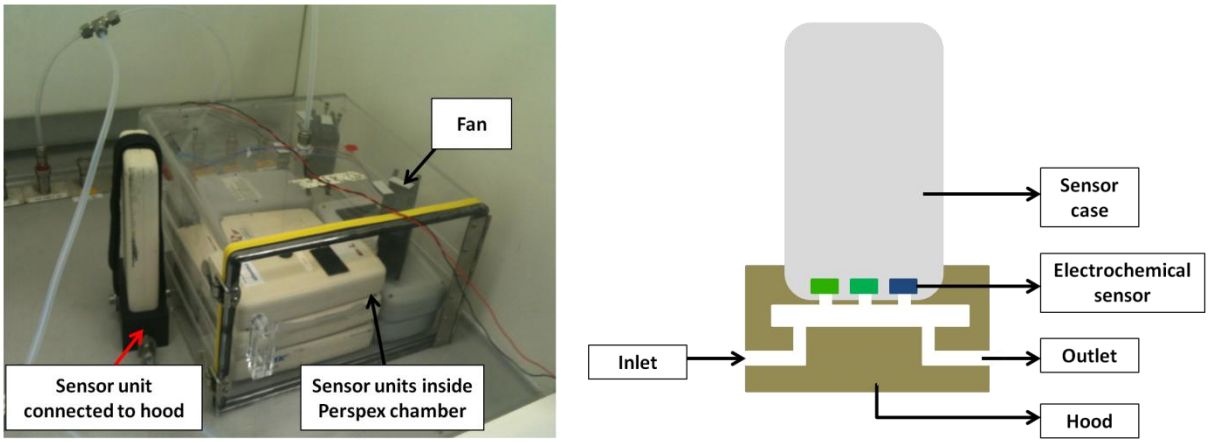

Figure 4.1. Experimental setup for the laboratory calibration experiments at Alphasense UK. The figure on the right shows setup for response time test using a specially designed gas hood.

The last electrochemical sensor unit (A27) was used to evaluate the response time[12] (t_{90}) of electrochemical sensor nodes during the NO_2 calibration tests. It was connected in series to the Perspex chamber (via a specially designed gas hood) as depicted in figure 4.1. This hood is designed to fit across the mobile sensor unit and it provides a small dead–volume compared to the sensors in the chamber.

4.2.1.2. Calibration gas generation

Gas standards were generated by blending high mixing ratio standard gases with high purity zero air using a system of DMFC[13] setup to give a total flow of 5,000 sccm[14]. The zero air used was generated from ambient air by passing it through particulate filter (to remove particles) and subsequently through a catalytic purification system (Whatman zero air generator, Model 765-818, 18 Lpm, Parker Hannifin, Cleveland USA). This was then passed through another set of particulate filters to ensure any artefacts resulting from the zero-air generator were removed before being flown through a dehydration bed and stored for later

[12] t_{90} is time taken (usually measured in seconds) for sensor to reach 90% of change in mixing ratio.
[13] DMFC refers to Digital Mass Flow Controller.
[14] sccm implies standard cubic centimetre per minute.

use. A simple dilution formula (E4.1) was used to calculate the volume of the standard gas that is needed to be mixed with zero air to give the desired diluted mixing ratio.

E4.1 $$V_{STANDARD} = \frac{(C_{DILUTED} \times V_{TOTAL})}{C_{STANDARD}}$$

$V_{STANDARD}$ is the flow rate in sccm of the standard gas, $C_{DILUTED}$ is the standard mixing ratio desired in ppb, V_{TOTAL} is the total flow rate which is always 5,000 sccm for the test and $C_{STANDARD}$ represents the mixing ratio of the standard gas bottle in ppb. For instance, for the CO test the standard gas used was 20 ppm (20,000 ppb) which translates to $C_{STANDARD}$ =20,000 ppb. If a dilute mixing ratio (C_{DILUTE}) of 160 ppb was desired using E4.1 above the flow rate ($V_{STANDARD}$) required from the CO gas standard line will be 40 sccm. Gas standards used for the test were Air products Speciality Gases: CO 20.04 ppm (±1%), NO 21 ppm (±2%) and NO_2 9.94 ppm (±2%).

4.2.2. Results and discussion

4.2.2.1. Chamber tests

The raw data retrieved from the sensor nodes are shown in figure 4.2. Note data between 11:03:00 and 11:15:59 in the CO plots are not shown because there was a spike in the sensor response. This measurement artefact was due to the opening of the valve connected to the standard gas line. There are drifts in the baseline of the sensor measurements for three gas species. This was due to the sensors stabilising after they were switched on. The drifts were removed by fitting appropriate functions (quadratic for NO and exponential for CO and NO_2) using periods when zero gas was flowing through the system. It is important to use these regions for the fit to avoid removing actual signal resulting from sensor response to calibration gas. Shown in figure 4.3 are fitted lines for CO, NO and NO_2 sensors response. The de-trend data shown in figure 4.4 were obtained by removing these fitted lines (fig 4.3) from the raw data. The final data processing involves smoothing the de-trend data. This was done by using a 30 point moving average for the 1 Hz CO and NO_2 measurements and a 6 points moving average for the 0.2 Hz NO data both of which gave 30 s running average data (figure 4.5).

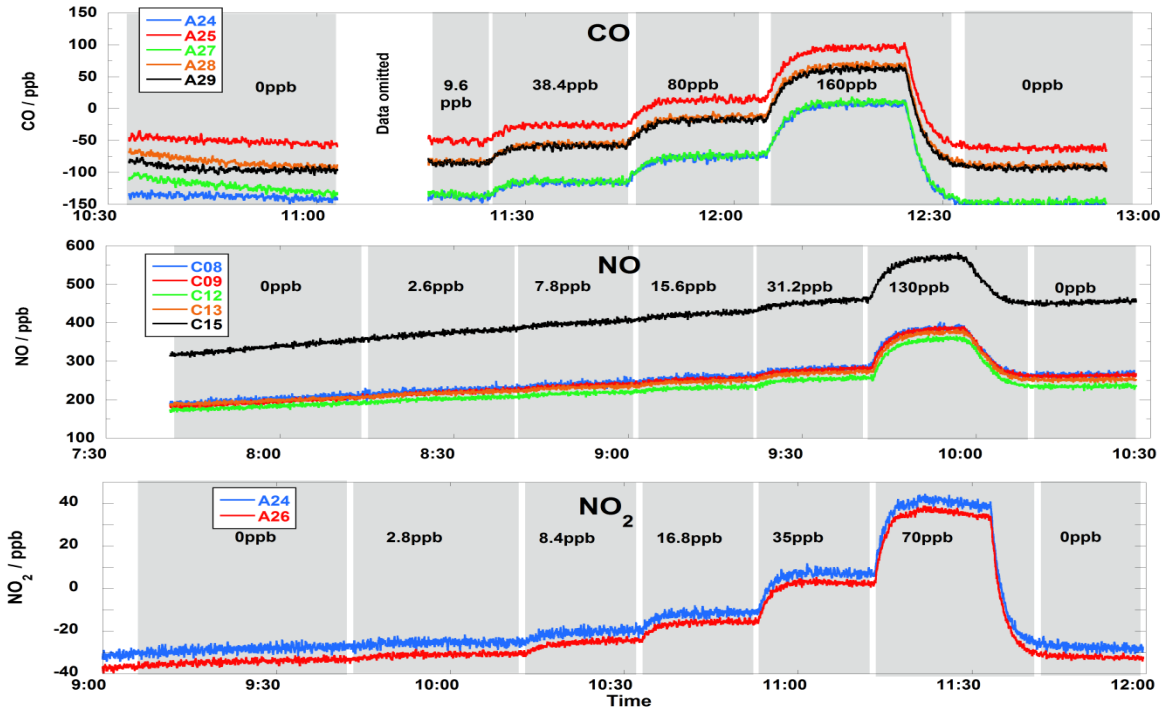

Figure 4.2. Time series of raw CO, NO and NO_2 data for all sensor nodes used in the standard gas calibration tests.

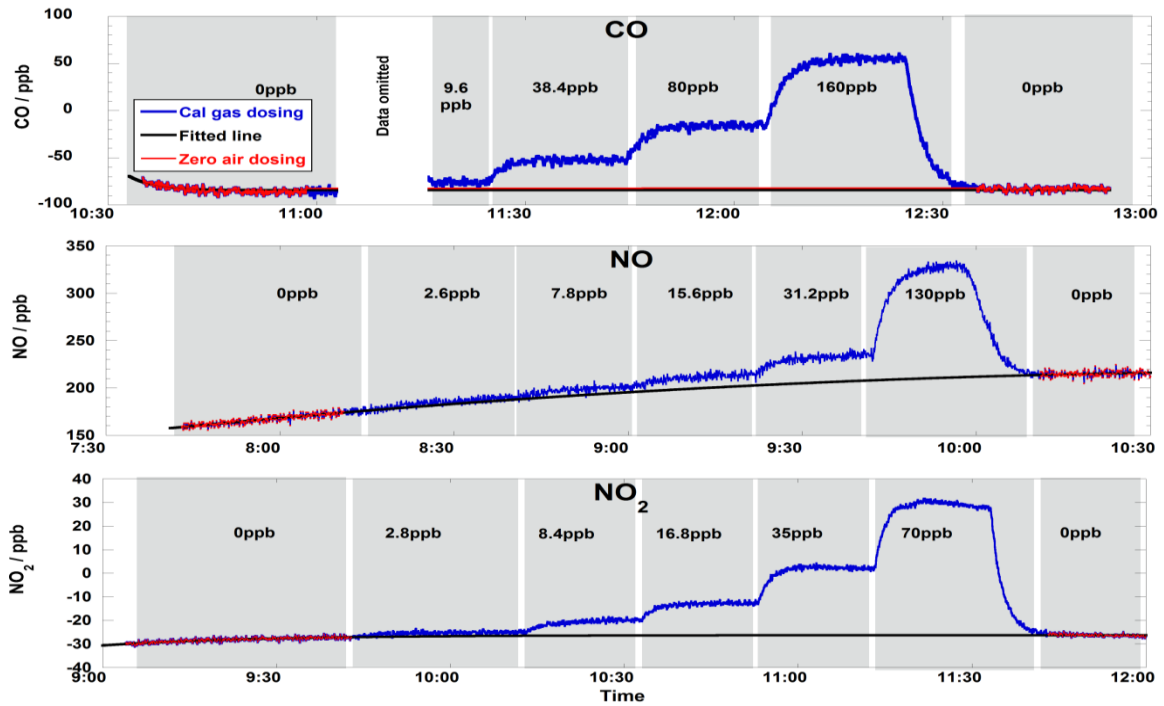

Figure 4.3. Time series showing fitted lines onto raw CO, NO and NO_2 data from one sensor node used in the standard gas calibration tests.

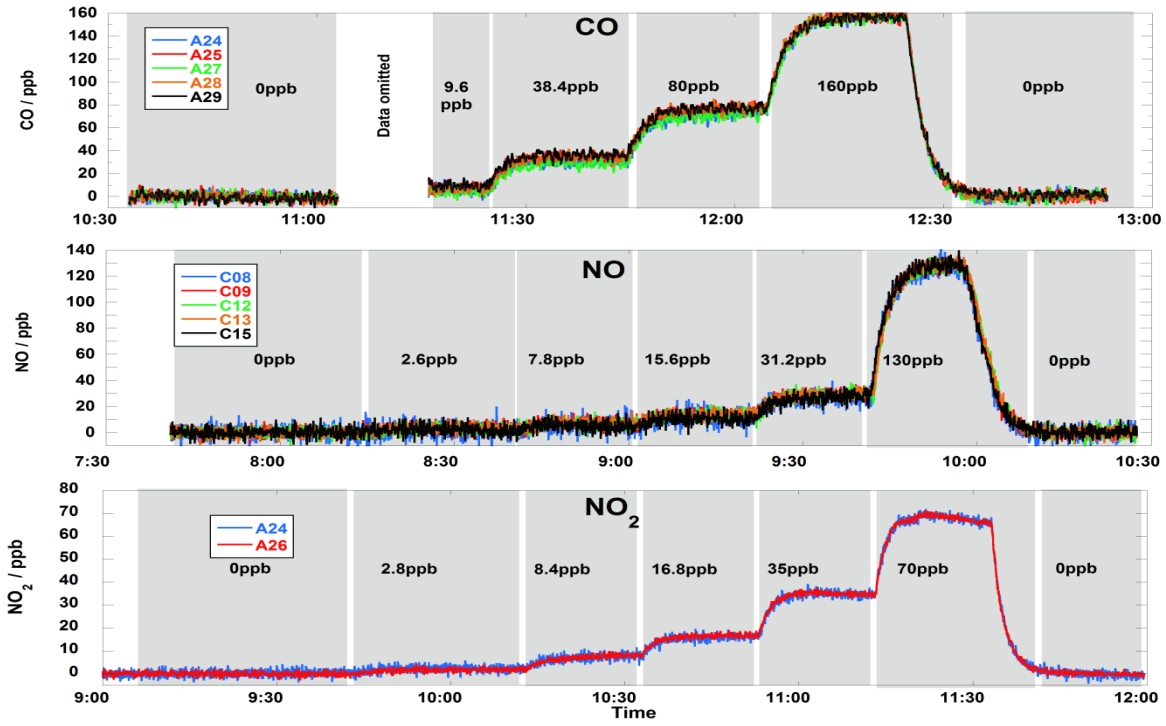

Figure 4.4. Time series of de-trend CO, NO and NO_2 data for all sensor nodes used in the standard gas calibration tests.

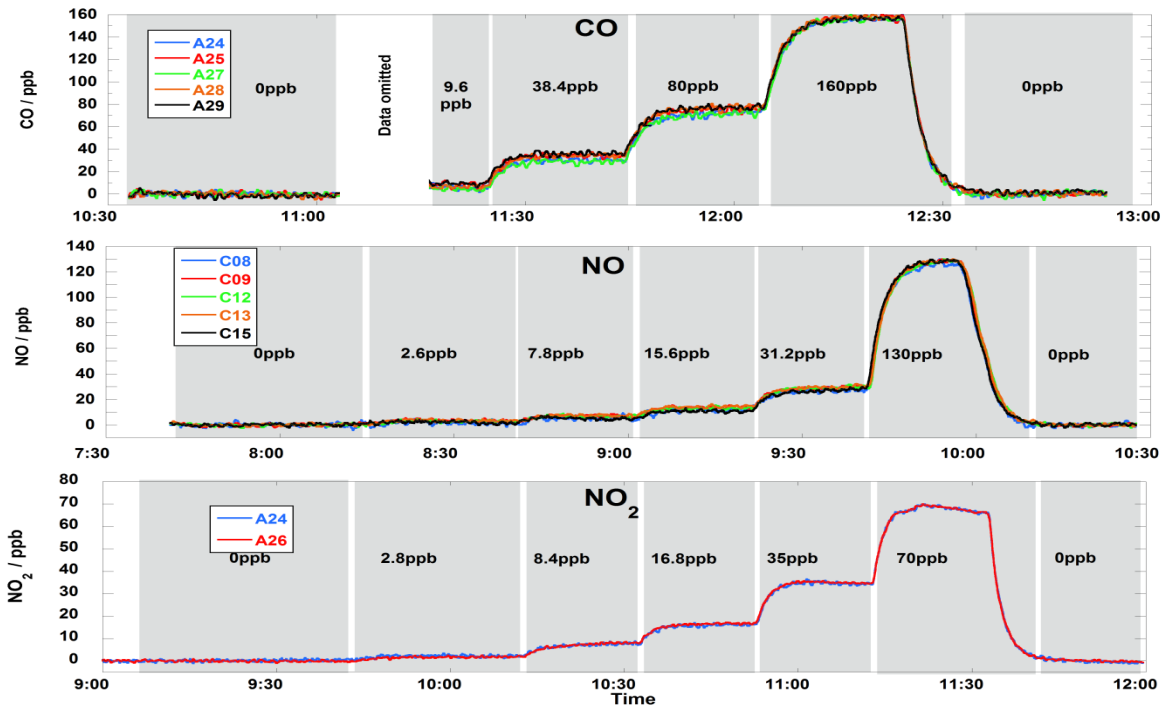

Figure 4.5. Time series of smooth (30 s running average data) for CO, NO and NO_2 data for all sensor nodes used in the standard gas calibration tests.

Shown in fig. 4.6 is the time series of the mean of the 30 s running data for CO, NO and NO_2 response of all the sensor nodes used for calibration tests. Distinct step changes at different test mixing ratios can be seen clearly in these plots. Table 4.1 summarises the results of the average measured and actual mixing ratios used for these tests. Figure 4.7 shows the correlation plot between the standard gases mixing ratios and mixing ratios measured by each of the sensor nodes. This plot shows that there is good linear response of the sensors to the test mixing ratios confirming the potential application of these sensor nodes at low mixing ratios (ppb levels).

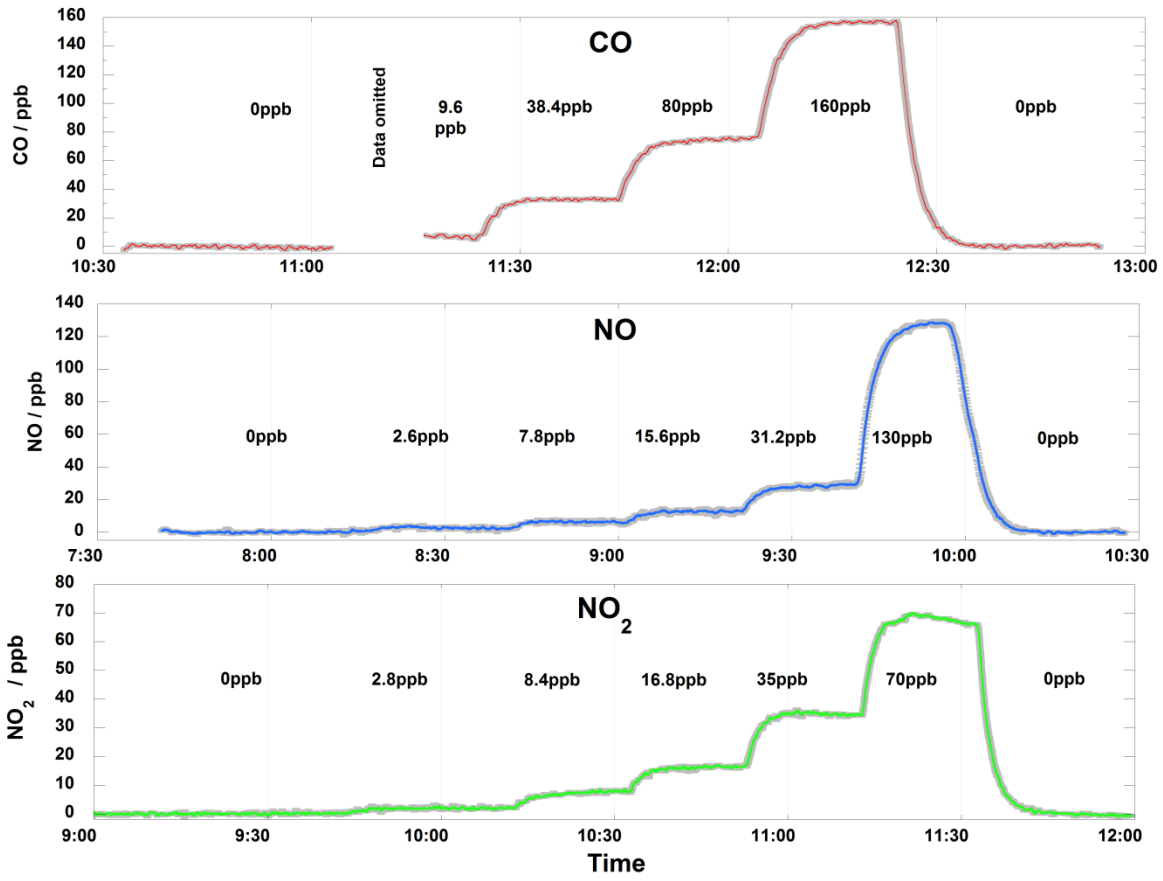

Figure 4.6. Time series of CO, NO and NO_2 sensors response during the standard gas calibration tests. The red, blue and green lines represent average mixing ratios of 1 second (CO and NO_2) and 5 seconds (NO) measurements respectively for all the sensor nodes used in the calibration test while the grey shade is the ± 1σ about the mean measurements. The plots shown above are from tests carried out inside the chamber.

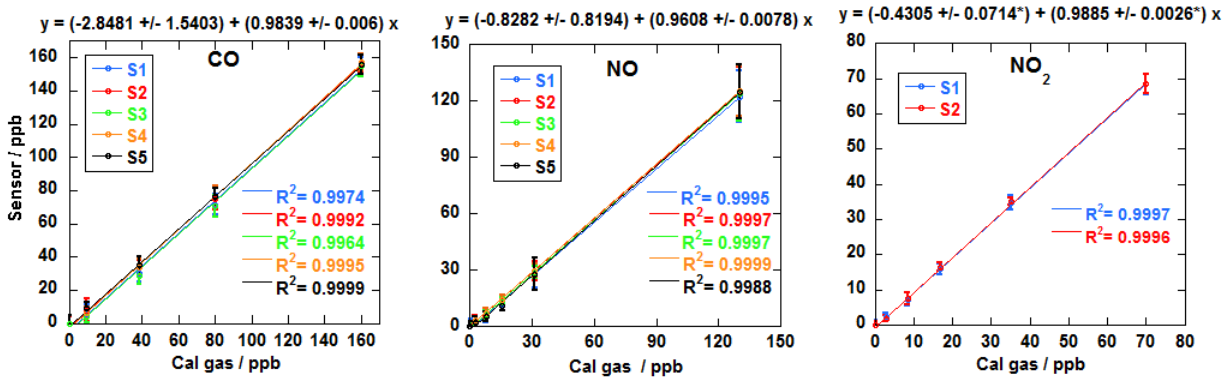

Figure 4.7. Correlation plots with ±3σ error for CO, NO and NO_2, where the x and y axes are mixing ratios in ppb. The mean line fit equations are shown above each plot with 1 sigma error for the fit parameters. Note * in the linear fit equation of the NO_2 plot represents error generated by taking the difference between the maximum and minimum of the fit parameters for the two sensors (S1 & S2) used for the test.

Table 4.1. Table summarising the actual and mean measured mixing ratios with the corresponding 95% confidence intervals (CI) for calibration tests for all three gaseous species.

CO			**NO**			**NO_2**		
Cal (ppb)	**EC (mean)**	**± 95% CI**	**Cal (ppb)**	**EC (mean)**	**± 95% CI**	**Cal (ppb)**	**EC (mean)**	**± 95% CI**
0	-0.2	0.04	**0**	0.1	0.06	**0**	0.0	0.02
9.6	7.0	0.09	**2.6**	3.0	0.07	**2.8**	2.0	0.015
38.4	32	0.07	**7.8**	6.0	0.06	**8.4**	7.4	0.04
80	74	0.09	**15.6**	13	0.07	**16.8**	16	0.03
160	156	0.10	**31.2**	29	0.24	**35**	35	0.03
			130	124	0.72	**70**	69	0.08

To illustrate the intrinsic sensor and instrumental noise, the probability density[15] function plots for CO, NO and NO_2 were generated. This plot used data for two test conditions: (a) at known gas mixing ratios (160 ppb for CO, 130 ppb for NO and 70 ppb for NO_2)

[15] Where the density function is the fraction of the values in each bin divided by the bin width i.e. the probability divided by bin width.

representative of typical levels in ambient urban environment and (b) at zero mixing ratios. Note in figure 4.8, the distribution plots at known mixing ratios have been centred on zero to show similarity in distribution under the two test conditions. The data shown represents 1 Hz measurements for the three species. The noise of the instrument for each gas species is defined as ±1σ under these test conditions. Defining the instrumental detection limit (IDL) as signal to noise ratio of 3, the IDL (3σ) were estimated to < 4 ppb, < 4 ppb and < 1 ppb for CO, NO and NO_2 respectively.

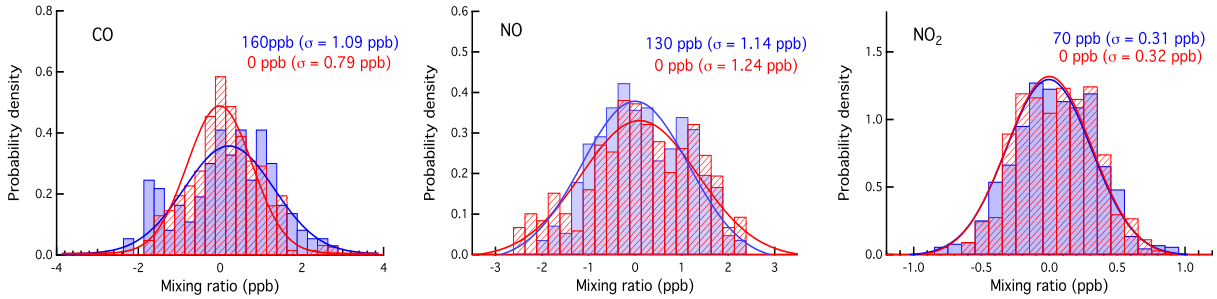

Figure 4.8. Probability density plots of the CO, NO and NO_2 sensor responses in clean (zero) air (red) and at mixing ratios representative of those found in the urban environment (blue) with their respective Gaussian fits. Gas mixing ratios are those of the calibrant gas.

4.2.2.2. Gas hood tests

Although figure 4.6 suggests approximate response times of (200 – 240 s) for CO, NO and NO_2, results from the hood test indicates much faster sensor response times. Comparing the high resolution plot for the NO_2 gas calibration test from 8.4 to 16.8 ppb for the test in the chamber and the hood, a much faster response was observed for test done in the hood compared to those in the chamber (figure 4.9). This large difference is due to a relatively larger dead–volume inside the chamber compared to the hood. The total volume occupied by the sensor nodes inside the 16 litres chamber is approximately 5 litres (calculation was based on number of sensor nodes and their dimensions). However, the percentage void volume inside each sensor unit is approximately 60%, hence; the true volume occupied by the sensors in the chamber is approximately 2 litres (40% of 5 litres). From these calculations, the dead–volume inside the sensor filled chamber is approximately 14 litres. Since the total flow during the experiment was 5,000 sccm (5 litres per minute), the time required to fill the chamber will be approximately 2.8 minutes (168 s). This does not take

into account the actual sensor response time and if this is considered, the observed t_{90} will be greater than 168 s. This clearly explains the large t_{90} observed for the test carried out in the chamber as shown in fig. 4.9. In contrast, the specially designed gas hood fig. 4.1, provides a relatively small dead–volume (< 0.02 litres) and the time delay in sensor response to test gas approximates to the true t_{90}.

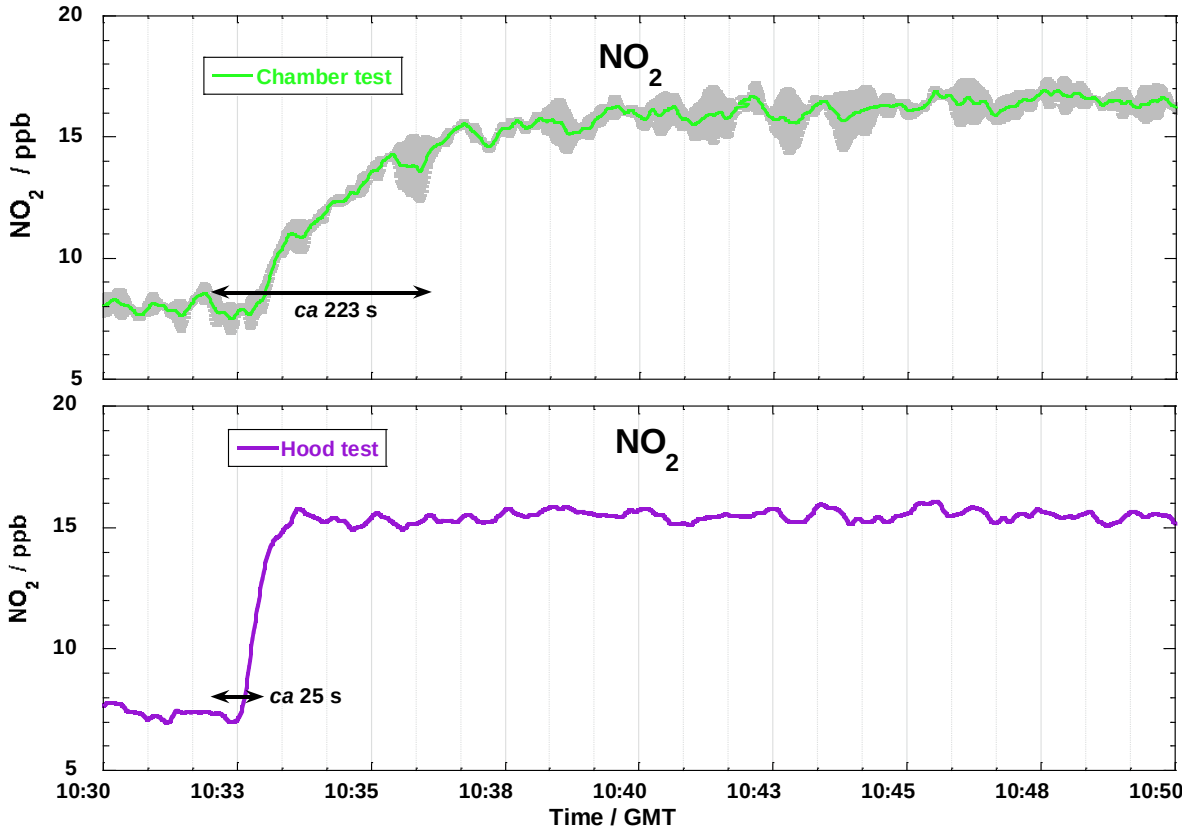

Figure 4.9. A high resolution time series showing time of response of NO_2 electrochemical sensors to step change in NO_2 standard gas mixing ratio from 8.4 ppb to 16.8 ppb. Top plot shows mean response of sensors in chamber and the bottom plot result of sensor connected to hood.

If the sensor response to each of the five-step NO_2 gas calibration tests in the hood is normalized to unity and an exponential function fitted to this output, then a 1/e response time of 9.21 s is observed for the NO_2 electrochemical sensor as depicted in figure 4.10. This corresponds to t_{90} of 21 s which is within the value quoted by the sensor manufacture (t_{90} < 40s) for this type of electrochemical sensor [82].

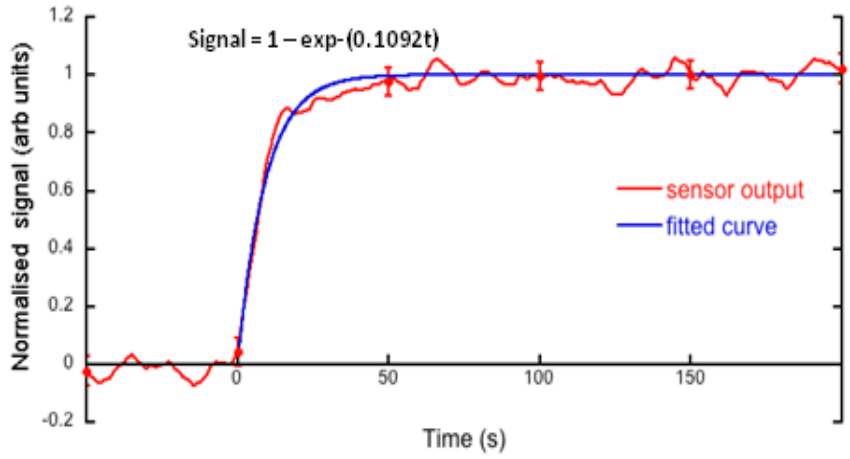

Figure 4.10. Response of an NO_2 sensor to step changes in target gas concentration. The data (red) are normalised signals obtained at 1 Hz, averaged over several step changes in calibrant gas mixing ratio. Also shown is the fitted exponential relationship (blue). Error is ±1σ for the mean data of the five-step runs.

4.3. Field comparison of electrochemical sensor nodes with other measurement techniques.

As discussed in section 4.2, it has been shown that the electrochemical sensor nodes perform well under laboratory conditions. As the sensor nodes were intended for ambient monitoring of toxic gas species, field performance was studied by comparing measurements with other instruments under ambient conditions. These studies involved comparing the electrochemical sensors with two different instruments: a traditional chemiluminescence instrument [83] used at most air quality monitoring stations across UK for ambient outdoor measurement of mixing ratios of NO and NO_2 species and an optical instrument based on the principle of Differential Ultraviolet Visible Absorption Spectroscopy (DUVAS) developed at Imperial College, UK.

Although the DUVAS instrument is considered portable (measures approximately 800 × 20 × 15 cm and weighs <15 kg) it is considerable larger than the electrochemical sensor nodes (approximately 18.5 × 9 × 3 cm and 325 g) and cannot be easily deployed on multiple platforms (e.g. bicycles) like the electrochemical devices. Similarly chemiluminescence analysers because of their physical size, infrastructural requirements (e.g. power supply, pumps) can best be used as static AQ monitors.

4.3.1. Intercomparison with chemiluminescence Instrument.

An intercomparison study between electrochemical sensor nodes and chemiluminescence instrument was carried out over a period of one week in January, 2009 at the Automated Urban and Rural Network (AURN) site located on Regent Street in Cambridge (fig 4.11). Gaseous species measured at this site by the Department of Environmental Health and Protection of the Cambridge City Council include CO, NO, NO_2, O_3 (UV spectroscopic instrument) and particulates (PM_{10}). Although the electrochemical sensor nodes measure three species (CO, NO and NO_2), in this study only the NO and NO_2 data were used as there was no CO data available from the AURN station for the period of the experiment.

Figure 4.11. Location of AURN monitoring station on Regent Street Cambridge, UK. Inset is the sampling inlet of the monitoring station at the first floor of Cambridge City Council Building. Image courtesy Cambridge City Council. Map courtesy Google Maps [81].

4.3.1.1. Site description

The AURN station at Regent Street in Cambridge (52.202189 N, 0.124283 E) is one of the five monitoring stations within the Air Quality Management Area (AQMA) declared by the CCC council. It is located along a busy urban road in the city centre and as such designated a roadside station. Air is sampled at a height of 4 m and a distance of 2.5 m from the kerbside.

The monitoring station is located on the first floor of the Council building where both the chemiluminescence instrument (Thermo Environmental Model 42C NO-NO_2-NO_X) and the pair of electrochemical sensor nodes used for this study were housed. As the instruments are located indoors, the air sample is adjusted to room temperature before being analysed by the NO instruments. This is significant because this eliminated the need for correction of temperature–baseline drift on the electrochemical sensors especially for the NO sensor, an issue that will further discussed in chapter 5.

4.3.1.2. Experimental setup

Two mobile electrochemical sensor nodes (EC1 and EC2[16]) were used for this study and were housed in a single sealed case with air drawn by means of small pumps into the shared airspace between the two sensor nodes from a spare sample inlet available at this site. The sensor nodes and mobile phones were powered from the mains supply in the monitoring room. Data were logged both locally on mobile phones and also uploaded onto a server. EC1 ran for a longer period because EC2 failed two days to the end of the deployment. For the purpose of data intercomparison, we generated hourly averaged data from the fast response (2 s measurements) made with EC1 and EC2 as the ratified NO and NO_2 mixing ratios from the chemiluminescence instrument are always reported as hourly averages. Data was missing between 1200 hrs (26, January) and 0600 hrs (27, January) due to loss of Bluetooth connection between the sensors nodes and the mobile phones.

4.3.1.3. Results and discussion

The NO_2 electrochemical sensors used for this study are cross sensitive to ozone (O_3). However since the AURN station also measured O_3 at this station, the NO_2 measurements from the electrochemical sensors were corrected for interference by subtracting the hourly O_3 measurements from the NO_2 mixing ratios for the duration of the deployment. Results of NO_2 presented here have therefore been corrected for the O_3 interference. Details of this correction are discussed in section 4.4.1.

[16] EC1 and EC2 represent electrochemical sensor instruments 1 and 2 respectively.

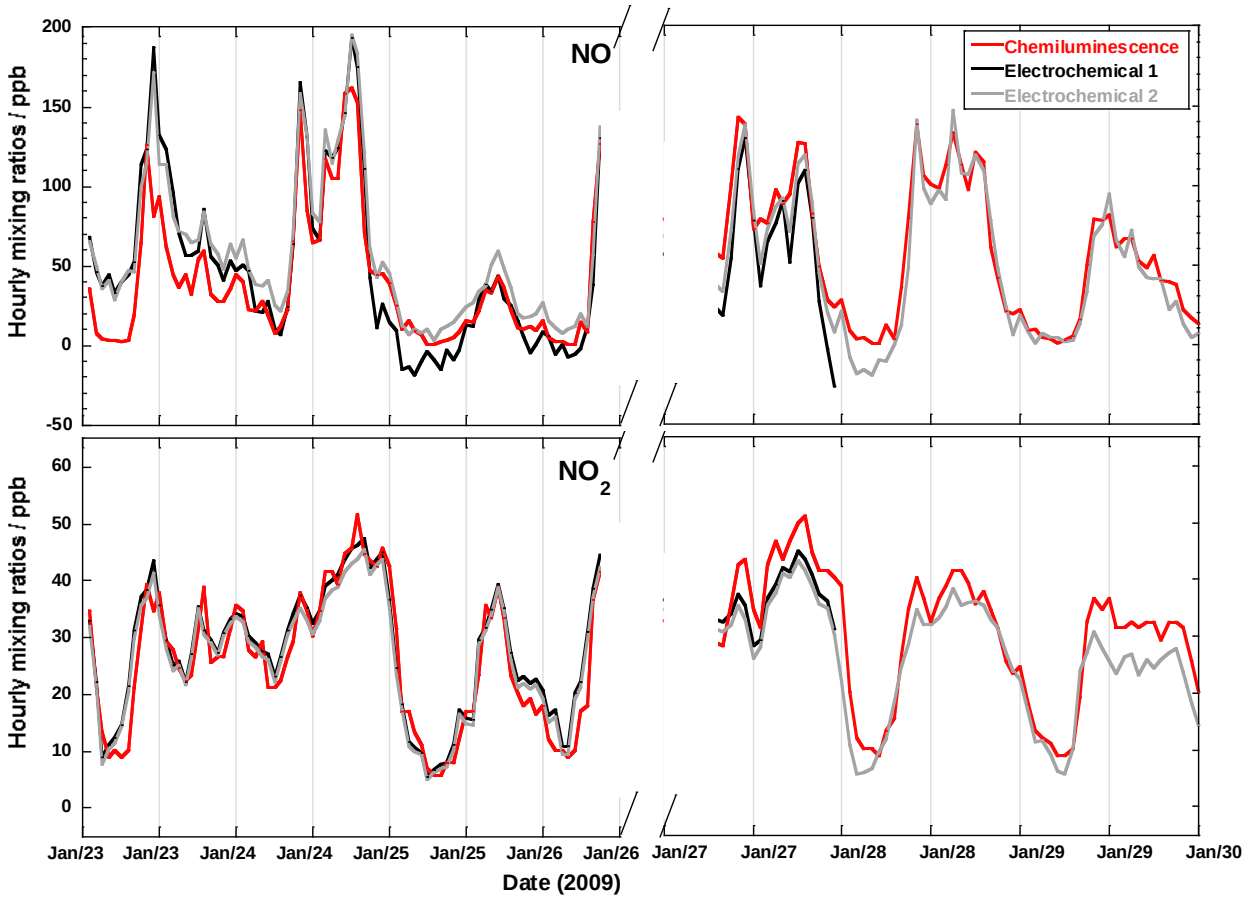

Figure 4.12. Time series of hourly mean mixing ratios of NO and NO_2 for both the pair of electrochemical sensor nodes and the chemiluminescence instrument at the AURN station on Regent Street (23 – 29 January, 2009). The NO_2 data has been corrected for known O_3 interference see section 4.4.1.

Fig 4.12 shows the time series of hourly mean mixing ratios of NO and NO_2 for both the pair of electrochemical sensor nodes and the chemiluminescence instrument at the AURN station on Regent Street (23 – 29 January, 2009). From this figure it can be seen that similar trend were observed for the measurements between the two instruments for both species being compared. A plot of the correlation between the two different measuring techniques (fig 4.13a) indicate a good agreement exist for both NO and NO_2. For NO species correlation coefficients (R^2) of 0.74 and 0.83 were observed between the chemiluminescence and electrochemical sensor 1 and 2 respectively. Similarly statistically significant R^2 values of 0.88 (electrochemical 1) and 0.85 (electrochemical 2) were observed for NO_2 between the two different instruments. A summary of the correlation coefficients and the first order equation of fits for NO and NO_2 is presented in table 4.2.

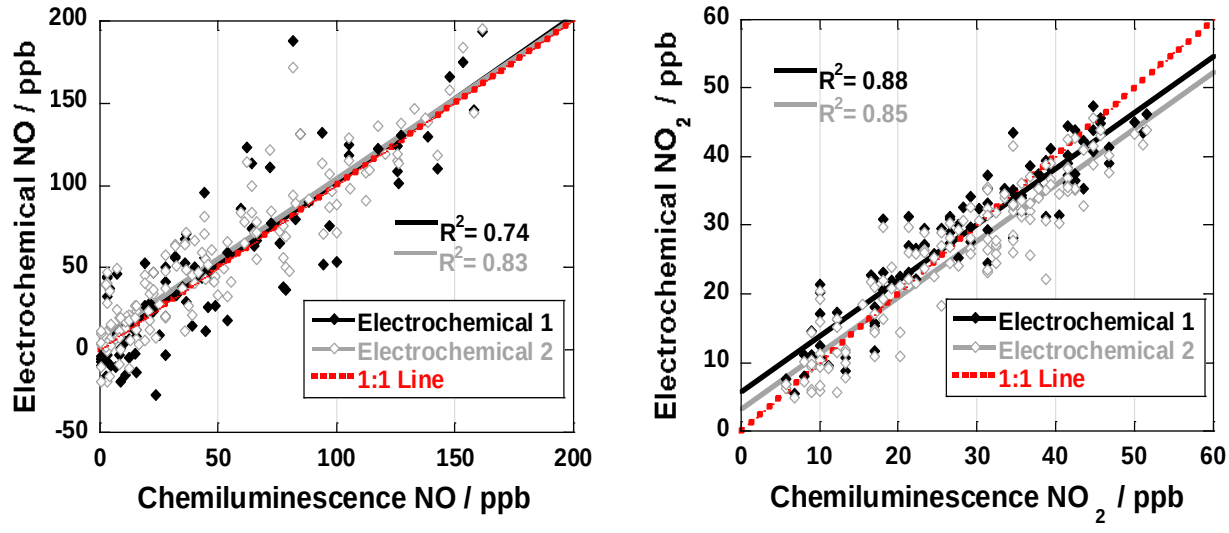

(a)

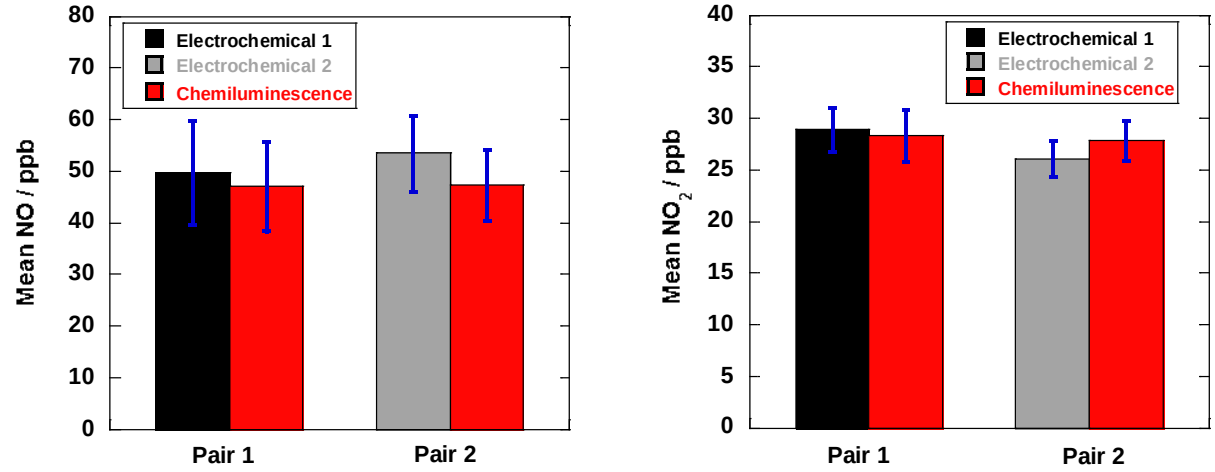

(b)

Figure 4.13. (a) Scatter plots of hourly mean mixing ratios of NO and NO_2 for both the pair of electrochemical sensor nodes and the chemiluminescence instrument at the AURN station on Regent Street (23 – 29 January, 2009). (b) Bar chart of the weighted mean mixing ratios for both NO and NO_2 for the duration of deployment. The error bar is the 95% confidence interval about these mean values.

Table 4.2. Table showing the first order equations of fit for NO and NO_2 mixing ratios between chemiluminescence and the pair of electrochemical sensors at Regent Street (23 – 29 January, 2009). The error represents the 95% confidence interval for the corresponding equation estimator.

Species	Pairs	First order equation	No of points	R^2	P value
NO	EC1 & CHL[17]	$NO_{(CHL)} = (1.00 \pm 0.12) \times NO_{(EC1)} + (2.35 \pm 7.67)$	97	0.74	<0.01
	EC2 & CHL	$NO_{(CHL)} = (0.97 \pm 0.07) \times NO_{(EC1)} + (7.76 \pm 4.53)$	146	0.83	<0.01
NO_2	EC1 & CHL	$NO_{2(CHL)} = (0.81 \pm 0.06) \times NO_{2(EC1)} + (5.83 \pm 1.89)$	97	0.88	<0.01
	EC2 & CHL	$NO_{2(CHL)} = (0.82 \pm 0.05) \times NO_{2(EC2)} + (3.35 \pm 1.66)$	146	0.85	<0.01

Figure 4.13b shows bar chart of the weighted mean for both NO and NO_2 for the duration of deployment. The mean values of NO were 50 ± 10 ppb and 54 ± 7.4 ppb respectively for EC1 and EC2 and these were in close agreement with (within the 95% confidence intervals of) the corresponding NO mean mixing ratios (47 ± 8.7 ppb and 47 ± 6.9 ppb) from the chemiluminescence instrument. Good agreement also existed between the NO_2 mean measurements with values of 30 ± 2.2 ppb (EC1) compared to 28 ± 2.5 ppb (CHL) and 26 ± 1.7 ppb (EC2) compared to 28 ± 1.9 ppb (CHL) over similar length of time.

4.3.1.4. Conclusions

It has been shown that the sensor readings are not only reliable in short–term but also long–term deployment (1 week data presented from January, 2009). Statistical comparison of measurements between the chemiluminescence and pairs of electrochemical sensors revealed good agreement between the two techniques. R^2 values of 0.74 – 0.88 (NO) and 0.83 – 0.85 (NO_2) were obtained from this study. There is excellent agreement (within the

[17] CHL, EC1 and EC2 stands for chemiluminescence, electrochemical 1 and electrochemical 2 instruments respectively.

error limits) for overall weight mean mixing ratios for both NO and NO_2 for measurements made by the two techniques (figure 4.13b).

These excellent results from the intercomparison study with a standard monitoring instrument for NO and NO_2 has demonstrated the practical application of electrochemical based sensors for ambient measurement of NO and NO_2.

4.3.2. Comparison with optical instrument (DUVAS)

An intercomparison study under outdoor conditions was carried out in London in June, 2009 as part of the Mobile Environmental Sensing System Across Grid Environment (MESSAGE)[84]. This study involved the deployment of an electrochemical sensor node and an optical instrument (DUVAS) developed originally at Imperial College, London as part of MESSAGE Project (but now part of Imperial College spin out company called DUVAS technologies Ltd). The electrochemical sensors measured CO, NO and NO_2 while the DUVAS instrument monitored NO, NO_2, O_3, benzene and SO_2[85]. However during this study, the DUVAS unit was still in its development stage and only NO and NO_2 were compared as these were the only species common to both instruments. The electrochemical sensor nodes used (type A's) do not have the latest low noise sensors and the NO sensor channels in the instruments were noisier than current instruments now in use. The NO_2 measurement from the electrochemical sensor node was not corrected for O_3 interference because there was no independent O_3 measurement during this study.

4.3.2.1. Introduction

The scientific aim of the University of Cambridge (UCAM) aspect of the MESSAGE[84] consortium program was to develop and deploy low–cost sensors suitable for sensing selected air quality gases at mixing ratios typical of the urban environment (in sub ppm levels). These sensors are designed to be simple to use and are operated by a single button (with two indicator LEDs) with no detailed knowledge required for their deployment. Details of the UCAM sensor design, operation and performance are discussed in chapter 3 and section 4.2. In the case of the DUVAS instrument it uses the principle of Beer–Lambert where light (in this case UV) specific to the desired species is passed through a sample cell and the intensity of light absorbed is related to the mixing ratio of the gaseous species. The

instrument has a fast response time and a built-in software algorithm used to generate the mixing ratios of measured species[85].

4.3.2.2. Methodology

This study involved co-location of the instruments (sensor node and DUVAS) over a selected pedestrian route in South Kensington, London in June 2009. The route was planned to include a monitoring site operated by the London Air Quality Network, LAQN (the site is designated a roadside station [86]) located in the grounds of the Natural History Museum near the junction between Cromwell road and Exhibition roads (see figure 4.14). For the duration of the study the electrochemical sensor unit was strapped next to the sampling inlet of the DUVAS unit to achieve as close a co–location as possible as shown in fig. 4.15. The study lasted approximately sixty minutes with stationary periods of approximately ten minutes at selected sites (traffic island, LAQN site and background site which is located in the garden of the Natural History Museum).

Figure 4.14. Map showing route walked during the study in June 2009 in London. Sites of interest are also indicated. Map courtesy of Google Maps [81].

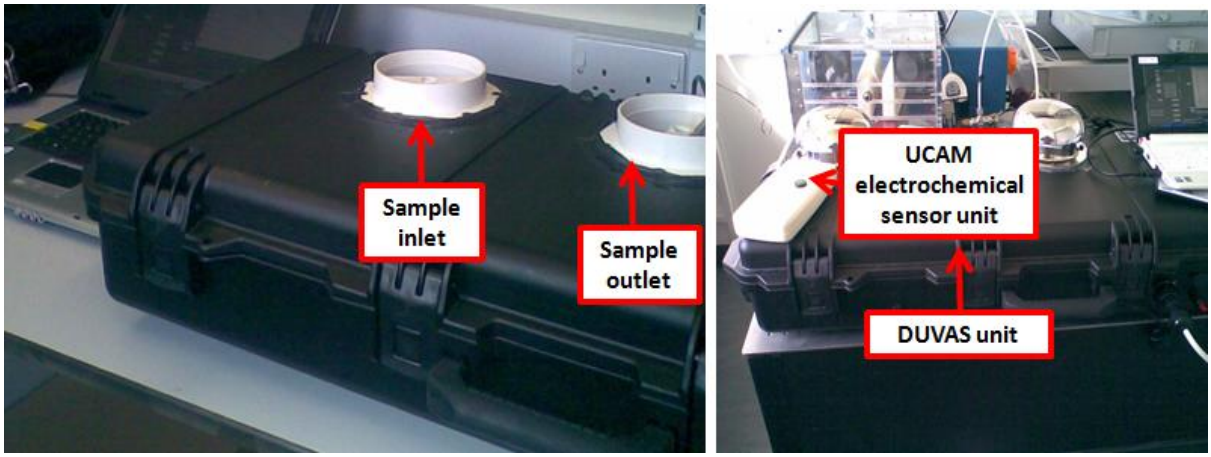

Figure 4.15. DUVAS instrument with sample inlet and outlet uncovered (left) and co-located DUVAS and UCAM electrochemical instruments (right). Note the relative size difference between the two instruments.

Both instruments were logging at a rate of 1 Hz. However due to difference in the response time of the instruments, 10 seconds averaged data were used for data comparison. The DUVAS data has been processed such that all data below zero are disregarded and set to zero. This processing was done by our collaborating partners at Imperial College and one of the reasons giving was that the instrument was still in development at time of this study.

4.3.2.3. Results and discussion

Overall results

Table 4.3 and 4.4 show statistical summary of the comparison of the two systems for the entire period of the study and 10 minutes period at the traffic island respectively. The maximum mixing ratio reading from the two instruments for both NO (1.20×10^3 ppb for electrochemical and DUVAS respectively) and NO_2 (280 & 200 ppb for electrochemical and DUVAS respectively) was observed when the instruments were stationed at the traffic island (between 12:32 – 12:42). It was noted that at the time of the study that there was a significant amount of static traffic built up around this point. The observed fleet composition was mixed and included cars, light duty industrial vehicles and buses. The instruments tracked each other very well for the duration of the co–location (figure 4.16) and were especially good at higher mixing ratios (see figure 4.17). As expected low values were

recorded at the background site between 12:50 – 13:00 where the instruments were away from primary road sources. In addition there was little variation in NO and NO_2 measurements at this site as can be seen in figure 4.16. Slight differences were recorded between the instruments at low mixing ratios especially for NO (minimum values of 26 and 0.6 ppb for electrochemical and DUVAS instruments respectively). This is due in part to differences in the detection limits between the two instruments for the two species and also from the fact that the DUVAS data supplied for this study assumed all negative values to be zero. Hourly averaged NO mixing ratio recorded at the LAQN between 12:00 – 13:00 hr was 31 ppb further supporting the conclusion that the minimum recordable mixing ratio during this study cannot be as low as indicated by the DUVAS instrument. However statistically significant agreement was observed at high mixing ratios, with mean mixing ratios between the electrochemical and DUVAS instruments for NO being (300 ± 57 ppb & 300 ± 61 ppb respectively) and (56 ± 12 ppb & 64 ± 11 ppb respectively) for NO_2 (see table 4.4).

Table 4.3. A summary of the statistical parameters for NO and NO_2 species measured by the electrochemical sensor node and DUVAS in London in June, 2009 for the entire duration of the deployment. All measurements are in ppb.

	Electrochemical sensor		DUVAS	
	NO	NO_2	NO	NO_2
Mean (ppb)	160	23	92	30
SD (ppb)	150	31	170	33
Max (ppb)	1.20×10^3	280	1.20×10^3	200
Median (ppb)	110	13	19	18
Min (ppb)	26	0.5	0.6	0.9
N	308	308	308	308
95% C.I. of mean	±17	±3.4	±19	±3.7

Table 4.4. Summary of the statistical parameters for NO and NO_2 species measured by the electrochemical sensor node and DUVAS in London in June, 2009 for period at traffic island.

	Electrochemical sensor		DUVAS	
	NO	NO_2	NO	NO_2
Mean (ppb)	300	56	300	64
SD (ppb)	240	50	250	45
Max (ppb)	1.20×10^3	280	1.20×10^3	200
Median (ppb)	240	40.0	240	61
Min (ppb)	45	1.6	30	2.2
N	66	66	66	66
95% C.I. of mean	±57	±12	±61	±12

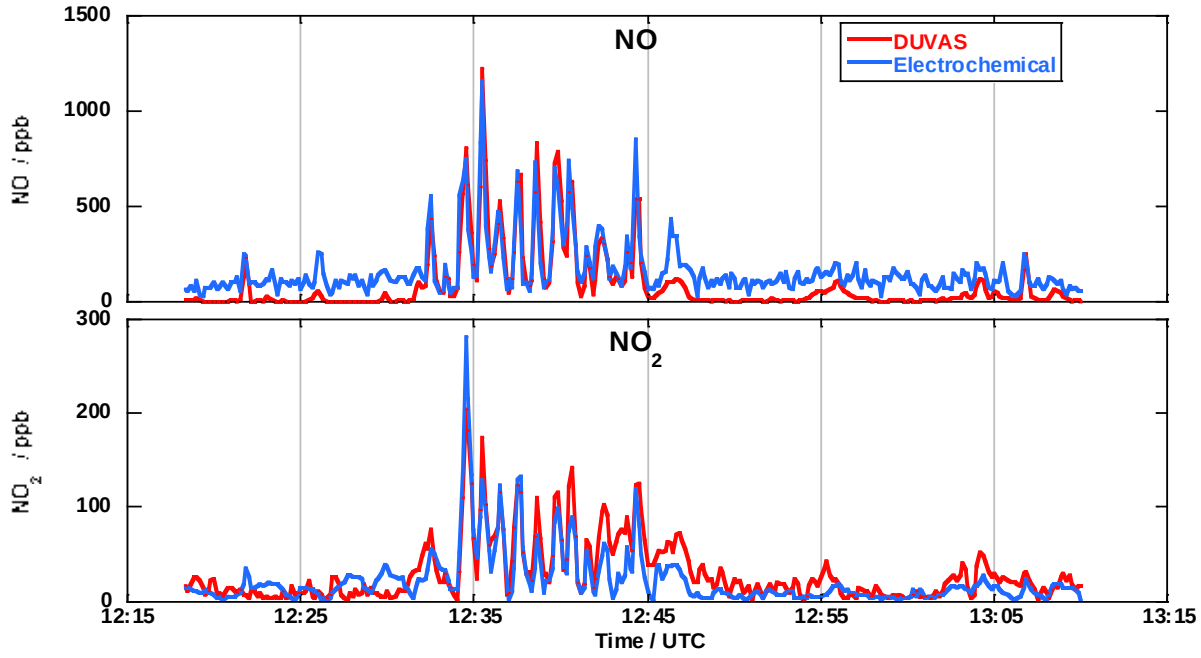

Figure 4.16. Time series of NO and NO_2 mixing ratios for the electrochemical sensor node and DUVAS for the entire deployment in London, 2009.

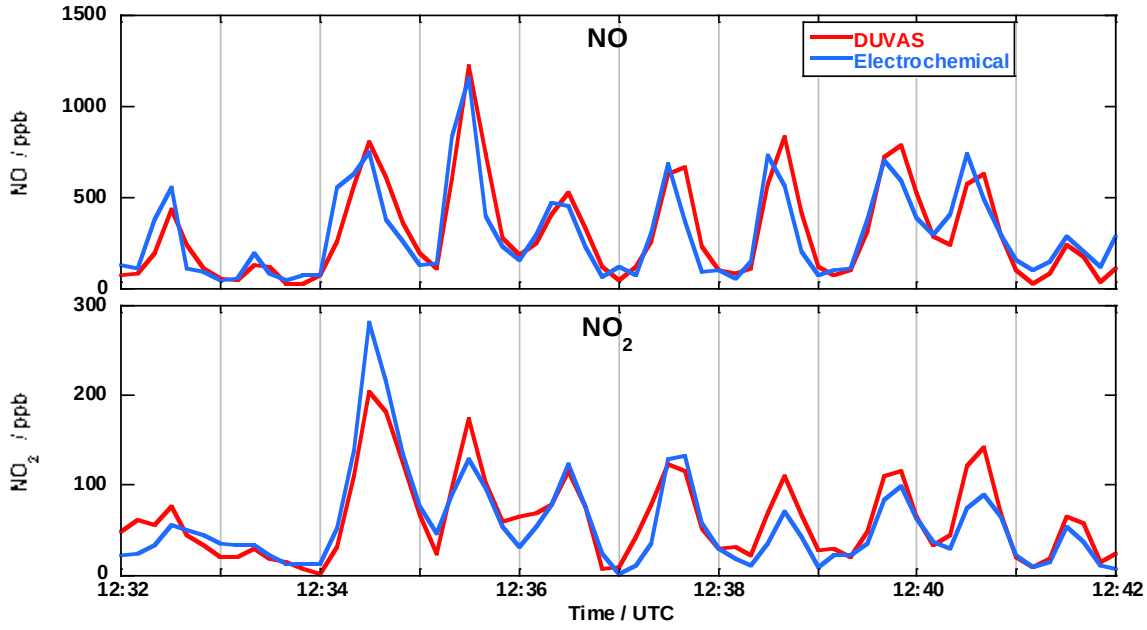

Figure 4.17. Time series of NO and NO_2 mixing ratios for the electrochemical sensor node and DUVAS for period when instruments were located at the traffic island.

Compatibility of data sets between the electrochemical and DUVAS instruments.

A regression analysis using a least squares method was performed on the data for two periods: (1) the entire duration of the deployment (12:18 – 13:11) and (2) for period when the instruments were located on the traffic island (12:32 – 12:42). Tables 4.5 and 4.6 show the summary of the regression analysis between the electrochemical sensor node and DUVAS with the scatter plots shown in figure 4.18. From the values of the regression coefficients, 0.78 and 0.73 (figure 4.18a) for NO and NO_2 respectively, a statistically good correlation exist between the two systems.

Table 4.5. Summary of the regression analysis parameters for the two species measured during the campaign in June, 2009. Errors are 95% C.I. for the equation parameters.

Species	First Order Equation	R^2	Data points	P value
NO	$NO_{(ELECTROCHEMICAL)}=(0.77 \pm 0.05) \times NO_{(DUVAS)} + (90.74 \pm 7.84)$	0.78	308	<0.01
NO_2	$NO_{2(ELECTROCHEMICAL)}=(0.81 \pm 0.05) \times NO_{2(DUVAS)} - (1.44 \pm 2.34)$	0.73	308	<0.01

Table 4.6. Summary of the regression analysis parameters for NO and NO_2 from 11:32 – 11:42 (traffic island).

Species	First Order Equation	R^2	Data points	P value
NO	$NO_{(ELECTROCHEMICAL)}=(0.83 \pm 0.11) \times NO_{(DUVAS)} + (49.27 \pm 41.74)$	0.79	66	<0.01
NO_2	$NO_{2(ELECTROCHEMICAL)}=(0.97 \pm 0.13) \times NO_{2(DUVAS)} - (6.74 \pm 9.8)$	0.78	66	<0.01

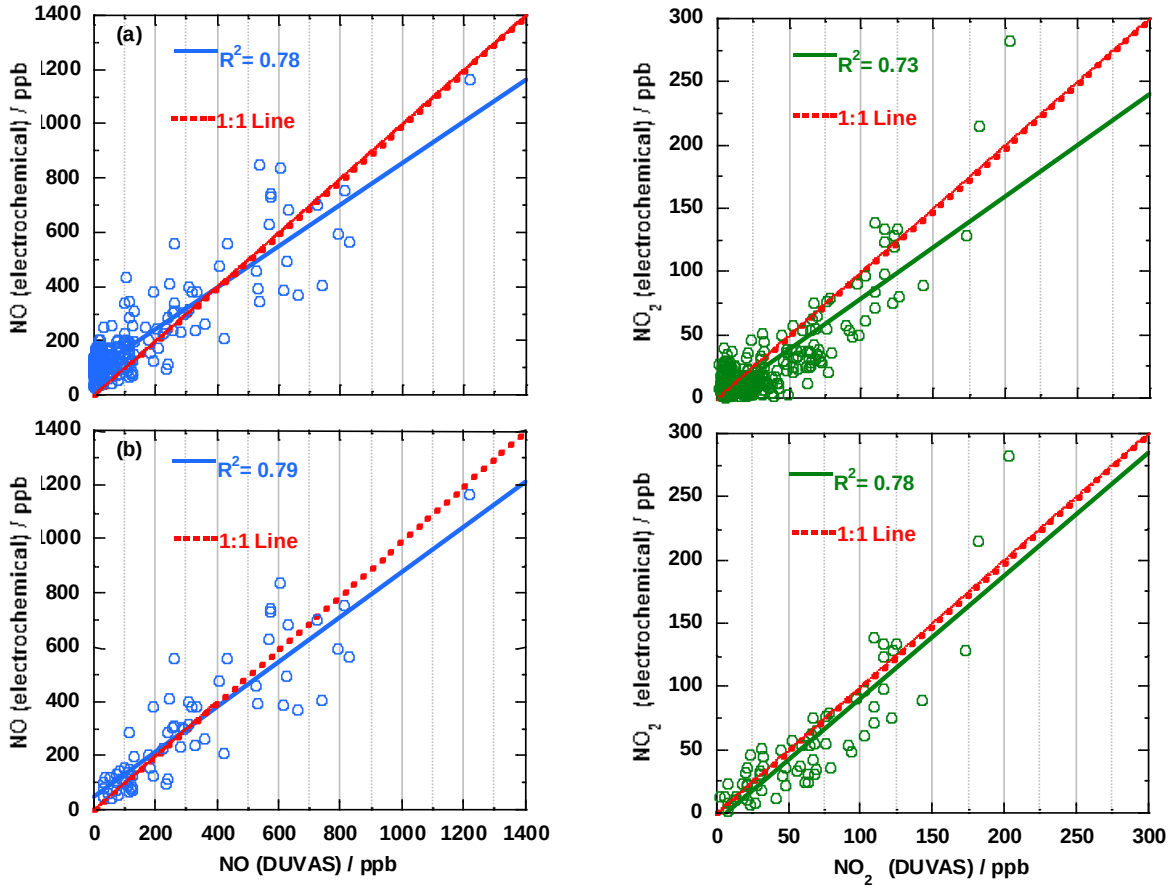

Figure 4.18. (a) Scatter plots of NO and NO_2 mixing ratios showing correlation between the electrochemical sensor node and DUVAS for the entire duration of deployment in London, 2009. (b) Scatter plots of NO and NO_2 mixing ratios showing correlation between the two instruments for period when they were stationed at the traffic island.

This conclusion is confirmed by the gradient values 0.77 and 0.81 for NO and NO_2 respectively (table 4.6). These values represent the ratio between the electrochemical

sensor node and the DUVAS instrument readings (measure of sensitivity ratio) and indicate that the instruments are in fairly close agreement. Small variations between the two instruments are expected due to imperfect co–location of the inlets. The inlet to the DUVAS instrument is fan driven. This fan passes ambient air through the measurement cell before it exhausts from the system. The electrochemical sensor nodes in contrast are purely passive diffusion driven. The CO, NO and NO_2 electrochemical sensors are located behind a mesh on the bottom face of the sensor node. This face was located as near to the vanes of the fan of the DUVAS unit as possible (see figure 4.15).

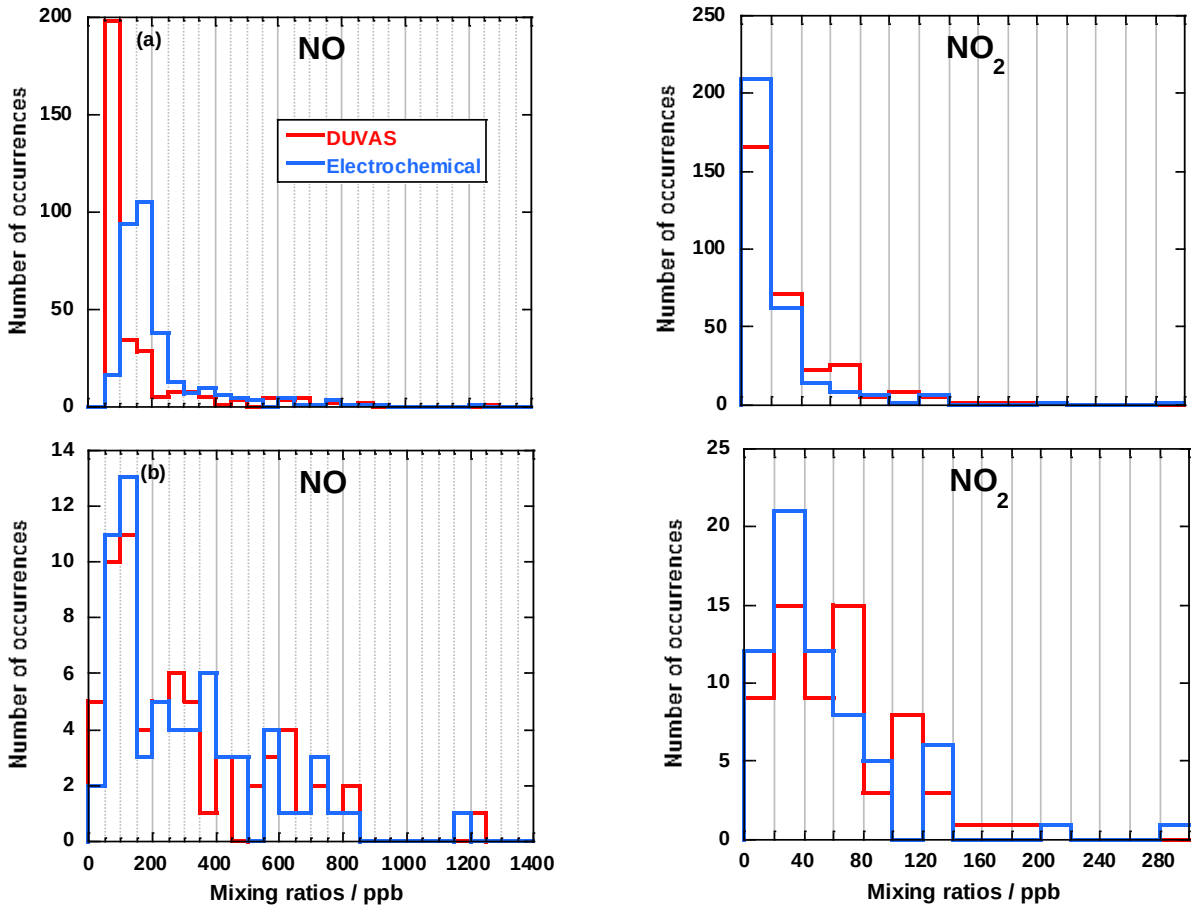

Figure 4.19. (a) Histogram depicting the distribution pattern and bias of NO and NO_2 mixing ratios between the two instruments for the entire duration of deployment in London, 2009. (b) Histogram depicting the distribution pattern and bias of NO and NO_2 mixing ratios between the two instruments for period when they were stationed at the traffic island.

From the results of the traffic island analysis (table 4.5), a small intercept value for NO_2 (-1.44 ± 2.35 ppb) implies that the slope of the line (0.81 ± 0.05) can be taken to represent the $NO_{2\ (ELECTROCHEMICAL)}/NO_{2\ (DUVAS)}$ ratio and as the R^2 value is large (0.73) it can be inferred that there is good agreement between the two instruments in terms of NO_2 mixing ratio across the whole range of values measured during the experiment. However in the case of NO, this ratio is only important if $NO_{(DUVAS)}$ is above 100 ppb at which the value of the large intercept (90.73±7.84 ppb) becomes relatively insignificant showing that the two instruments are in agreement above this mixing ratio as can be seen in the table 4.6 and figure 4.18b. This further confirms the earlier observation of poor agreement at low mixing ratios.

From the slopes of NO and NO_2 in table 4.5 it can be inferred that the readings from the DUVAS instrument were always higher than from the electrochemical sensor node, a pattern seen in the NO_2 histogram plot shown in figure 4.19. This however is not the case for NO as a relatively large intercept value (90.73 ± 7.84) indicates that the reading from the electrochemical sensor node is often higher than the DUVAS instrument (see figure 4.18a). The NO_2 distribution pattern is similar between the two systems with a peak number of occurrence centred within 0 – 20 ppb (see figure 4.19a). In contrast, the distribution pattern of the NO data is quite different between the two instruments and this is largely attributed to the relatively poor agreement at very low mixing ratios (< 100 ppb) seen in the time series (see figure 4.16). However there were significantly better agreements at relatively high mixing ratios as observed when the two different instruments were located at the traffic island (figures 4.17, 4.18b and 4.19b). At these high mixing ratios, the distribution pattern between the two instruments (figure 4.19b) is in fact similar for both species with modes in the range 100 – 150 ppb for NO and 20 – 40 ppb for NO_2.

Assessment of bias between the electrochemical sensor and DUVAS instruments

The percentage difference (PD) [87] were calculated for the two species over the time window 12:32 – 12:42 when the two systems were co–located on the traffic island. These PD values were used as estimator for the bias between the two systems. Shown in figure

4.20 is histogram depicting the PD values for both NO and NO_2. The PD was calculated using the mathematical expression shown in equation E4.2.

$$PD = \left(\frac{(C_{DUVAS} - C_{ELECTROCHEMICAL})}{C_{DUVAS}} \right) x100\% \quad \text{E4.2}$$

Where C_{DUVAS} represents the measurements from the DUVAS instrument, $C_{ELECTROCHEMICAL}$ is the measurement from the electrochemical sensor unit and *PD* is the percentage difference.

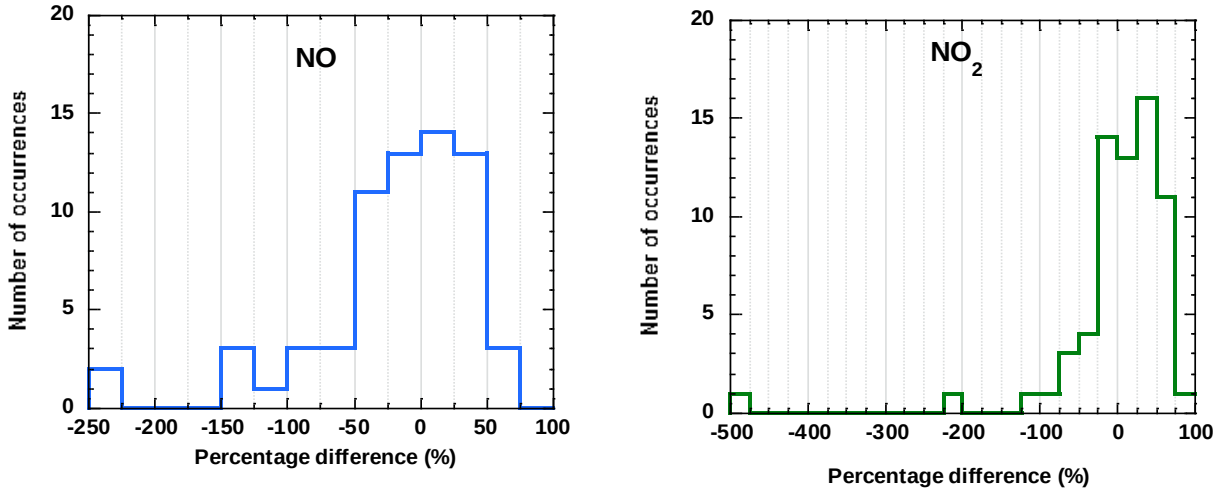

Figure 4.20. Histogram showing percentage difference of NO and NO_2 mixing ratios between the electrochemical sensor node and the DUVAS instrument for period when they were stationed at the traffic island.

A PD value between -500 and 90 % corresponds to a $C_{ELECTROCHEMICAL}/C_{DUVAS}$ ratio of 6 and 0.1 respectively. From the NO plot in figure 4.12, most of the PD data (81.81%) lie between -50 and +50 corresponding to $C_{ELECTROCHEMICAL}/C_{DUVAS}$ ratio of 1.5 and 0.5 respectively. However, 93.94% of the PD values of NO_2 lie between -75 and +75 corresponding to $C_{ELECTROCHEMICAL}/C_{DUVAS}$ ratio of 1.75 and 0.25 respectively. The modes of the PD for NO and NO_2 data which lie between (0 – 25 and 25 – 50 % respectively) indicates that the two systems agree well at high mixing ratio because these values correspond to $C_{ELECTROCHEMICAL}/C_{DUVAS}$ ratio in the range $0.75 \leq C_{ELECTROCHEMICAL}/C_{DUVAS} \leq 1$ and $0.5 \leq C_{ELECTROCHEMICAL}/C_{DUVAS} \leq 0.75$ for NO and NO_2 respectively.

4.3.2.4. Conclusions

This field study demonstrates that there was good agreement between the electrochemical sensor node and the DUVAS spectroscopic instrument, especially for NO_2. The lower correlation between the two different instruments at lower mixing ratios (less than 100 ppb) is due to the difference between the detection limits of the two instruments and also the way the DUVAS data were processed for this deployment. As the readings from the DUVAS instrument tend to less than 1 ppb even in a NO source rich urban environment (with NO_2 varying between 10–20 ppb), the readings from the electrochemical sensor node are considered to be real atmospheric variations in NO levels. In the urban environment where relatively high mixing ratios of NO are routinely recorded this difference becomes less significant if not negligible as shown by the good statistical correlation between the two instruments for both NO and NO_2 for period when stationed at the traffic island. The low–cost and portability of the UCAM electrochemical sensor nodes means that it is feasible for a high density network of these systems to be deployed for monitoring of air quality.

4.4. Interferences

The major sources of interference to application of electrochemical sensors in AQ monitoring include cross–sensitivity to other gases and temperature effect on sensor performance.

4.4.1. Cross–sensitivity to other gases

Since the sensors are intended to be used in ambient conditions where they will be exposed to a variety of gaseous species, it is imperative to see if there is any cross-sensitivity to other species and if so to estimate this amount and subsequently correct for this effect.

As part of the standard manufacturing procedure, the sensor manufacturer carries out series of cross–sensitivity tests in the laboratory of the toxic gas sensors to other gaseous species [88]. In this thesis I will be reporting data for CO, NO and NO_2 which are toxic gas electrochemical sensors used in my research.

Shown in table 4.7 is percentage cross–sensitivity of CO, NO and NO_2 electrochemical sensors to important gaseous species. These tests were carried out at constant interfering

gas mixing ratios and at very high mixing ratios in ppm range. From the table the most important cross–sensitive gas to the CO sensor is hydrogen with 52.5% cross sensitivity. Although direct emissions of H_2 is minimal from vehicles it has been reported to be present in urban environment [89], based on this study H_2/CO emission ratio of 0.53 was reported. By using the expression in equation E4.3 the actual CO mixing ratio can be estimated.

Table 4.7. Percentage cross-sensitivity (% CS) of Alphasense toxic electrochemical sensors.

Interfering gases	ppm applied	Typical ambient mixing ratios / ppm	% CS of CO-AF (ambient CS ppb)	% CS of NO-A1 (ambient CS ppb)	% CS of NO_2-A1 (ambient CS ppb)
CO	400	0.2 – 3		0.1 (< 3 ppb)	0.1 (< 3 ppb)
NO	50	0 – 1	5 (50 ppb)		0.5 (< 5 ppb)
NO_2	10	< 0.2	0.1 (< 0.2 ppb)	5 (< 10 ppb)	
SO_2	20	< 0.002 [90]	0.1 (< 0.002 ppb)	3 (< 0.06ppb)	-2.5 (< -0.05 ppb)
Cl_2	10	~0 [91]	0.1 (~ 0 ppb)	15 (~0 ppb)	100 (~0 ppb)
H_2	400	0.6 [89]	60 (360 ppb)	0.1	0.1
C_2H_4	400	0.00067 [2]	25 (< 0.17 ppb)	0	0.1 (~0)
NH_3	20	< 0 [90]	0.1	0.1	0.1
H_2S	20	< 0 ppb	0.1	30	-40

E4.3 $$[X]_{REAL} = [X]_{EC} - (\alpha \times [CS])$$

Where $[X]_{EC}$ represents the mixing ratio measured by electrochemical sensor for gas species *X*, $[X]_{REAL}$ is the real ambient mixing ratio of this species, *[CS]* stands for ambient mixing ratio of the cross–sensitive gas CS and α is the % cross–sensitivity of the electrochemical sensor (measuring X) to CS. In the absence of a simultaneous measurement of the CS (in this case H_2), the emission ratio H_2/CO was used to express the amount of H_2 present under ambient condition, thus if CS equals H_2 and X equals CO, then [H_2] equals $0.53*[CO]_{REAL}$. By substituting this expression for [H_2] in E4.3 and on rearranging, the true ambient CO can be estimated using the expression in equation E4.4.

E4.4 $$[CO]_{REAL} = \frac{[CO]_{EC}}{1 + (\alpha \times 0.53)}$$

Using α of 60% (0.6) from table 4.7, the true CO mixing ratio is estimated to be 0.78 of the amount measured by the CO electrochemical sensor i.e. 0.76 of $[CO]_{EC}$. In the case of NO_2 sensor the most important interfering gas is Cl_2 (100%). However this is not important under

the urban environment as there are no primary sources for Cl_2. Table 4.7 also shows that cross sensitivity to most of these gas species are negligible at the ambient mixing ratios of these species.

Table 4.8. Cross-sensitivities of CO, NO and NO_2 electrochemical sensors to applied mixing ratios of CO, NO and NO_2 at typical ambient levels. Quoted errors are ±1σ, with manufacturer's specifications from ppm measurements shown in brackets.

	Electrochemical Sensor		
Interferent gas	**CO**	**NO**	**NO_2**
CO	-	+0.10 ± 0.08% (0.1%)	-0.02 ± 0.03% (0.1%)
NO	+0.24 ± 0.05% (5%)	-	+1.2 ± 0.11% (0.5%)
NO_2	+0.20 ± 0.08% (0.1%)	+0.45 ± 0.2% (5%)	-

The cross–sensitivity results presented so far are based on values supplied by the sensor manufacturer. The configuration of the mobile sensor which measures three gas species (CO, NO and NO_2) simultaneously made it possible to study cross-sensitivity of electrochemical sensors to the applied standard gas during the calibration tests. The result of the cross-sensitivity of CO, NO, and NO_2 during the calibration tests is shown in table 4.8. Although the result shows that several of the cross-sensitivities are statistically significant (< 1%), and are generally better than the sensor manufacture's specification. These relatively small interferences are readily accountable for during data analysis.

One gas that has significant interference on NO_2 sensor and is relatively abundant in the urban environment is O_3. Laboratory studies conducted in conjunction with the sensor manufacturer showed that NO_2 sensors currently used in both the mobile and static sensor nodes are +100% cross sensitive to O_3. This was evident in the results from the NO_2 intercomparison study between electrochemical sensor nodes and the chemiluminescence instrument at Regent Street (23 – 29 January, 2009). During this study O_3 data was obtained from UV instrument used at the AURN site. Figure 4.21(a) shows the time series (for uncorrected NO_2 data from the electrochemical sensor nodes, NO_2 data from the

chemiluminescence system and O_3 data from the UV instrument) and the correlation plot for hourly mean NO_2 from the two NO_2 instruments. R^2 values of 0.78 and 0.64 were obtained for NO_2 data between the two electrochemical sensors and the chemiluminescence instrument.

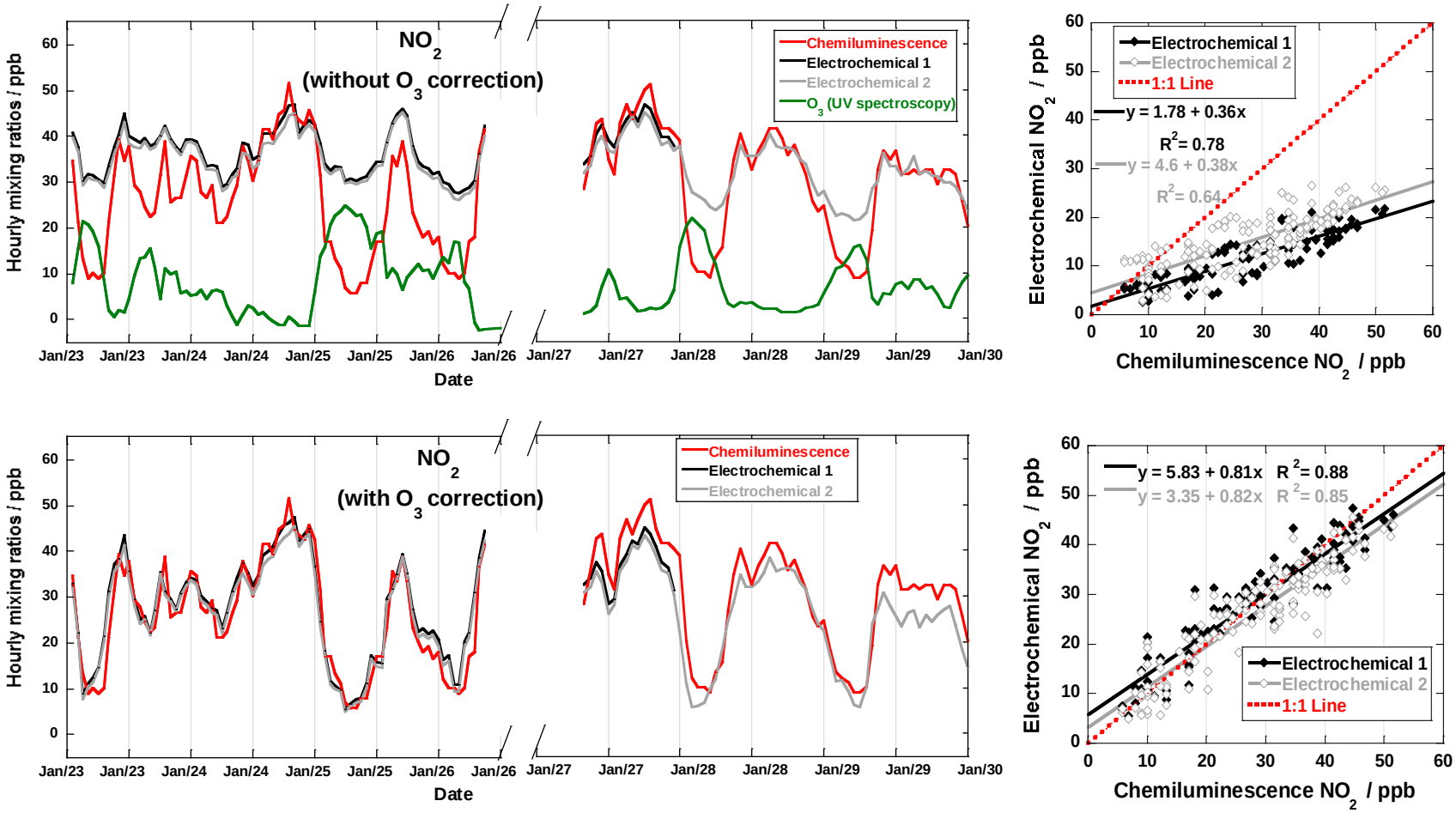

Figure 4.21. (a) Time series of uncorrected hourly mean NO_2 mixing ratio measurements of two electrochemical sensor nodes and NO_2 measurements of chemiluminescence instrument at the AURN station on Regent Street (23 – 29 January, 2009). The green line represents hourly mean O_3 measurements from a UV spectroscopic instrument at the AURN site. (b) Time series of O_3 – corrected hourly NO_2 mixing ratio measurements of two electrochemical sensor nodes and NO_2 measurements of chemiluminescence instrument at the AURN station on Regent Street (23 – 29 January, 2009).

However, the correlations between the two different techniques improved to 0.88 and 0.85 (fig. 4.21(b)) after effecting O_3 correction on the NO_2 data from the electrochemical sensor nodes. Shown in fig 4.21(b) is time series after effecting O_3 correction. This plot shows the two systems agree far better than prior to O_3 correction as shown in fig. 4.21(a).

Although cross–sensitivity is not a desirable attribute in electrochemical sensors, it can be a useful property in determining the actual mixing ratio (if measurement is desirable) of the interfering gas in the environment. This is achieved by using two electrochemical sensors with different cross sensitivities to same interfering gas. For two electrochemical sensors E1 and E2 measuring gas X and with respective cross sensitivities of $\alpha 1$ and $\alpha 2$ to the gas species CS, two equations (E4.5 and E4.6) can be written for the two sensors based on equation E4.3.

E4.5 $$[X]_{REAL} = [X]_{E1} - (\alpha 1 \times [CS])$$

E4.6 $$[X]_{REAL} = [X]_{E2} - (\alpha 2 \times [CS])$$

By solving the simultaneous equations E4.5 and E4.6, the mixing ratio of CS can be calculated using E4.7.

E4.7 $$[CS] = \frac{([X]_{E1} - [X]_{E2})}{(\alpha 1 - \alpha 2)}$$

This approach is currently been developed for measuring O_3 which is an interfering species on NO_2 sensor. This will be achieved by deploying two NO_2 sensors with significantly different cross – sensitivity to O_3 and solving equation E4.7.

4.4.2. Effect of temperature on sensor performance

Another possible source of interference is the effect of temperature on electrochemical sensors. This effect manifests itself in two ways: (1) Temperature effect on the sensitivity of sensors and (2) zero – baseline change (or baseline drift) due to temperature. The sensor manufacturer supplied data that can be used to correct for both of these effects. However, although these data can be used for sensitivity–dependant temperature correction, results from long–term deployment (especially when daily diurnal cycles are observed) show it was not effective for correction of temperature–dependent baseline change. Consequently,

independent corrections for the temperature–dependent baseline drift had to be developed and applied for long–term measurements. Details of this correction methodology will be discussed in chapter 5.

4.4.2.1. Sensitivity temperature correction

For all the toxic gas sensors manufactured at Alphasense changes in sensitivity were checked between -30 and +50^{o} C at 10^{o} C intervals. This change is expressed as a percentage and referenced to sensitivity reading at 20^{o} C (which is taken to be 100%) because this is the test condition used by the manufacturer during sensor calibration tests. An interpolation fit is generated between temperature and the corresponding sensitivity change for the temperature ranges -30 to + 50^{o} C (figure 4.22). These fits relate temperature to percentage sensitivity change. By using temperature measurements made by temperature probe present in the sensor instruments, the sensitivity–dependent temperature change can be corrected. Although there are relatively large changes in sensitivity at extreme temperature conditions (<-10^{o} C and > 40^{o} C), this is not a source of concern as the ambient temperature conditions under which these electrochemical sensors have been deployed never exceeded these extremes. For instance, in the UK, the 1970–2000 averages gives a minimum temperature of -2^{o} C [92] (Scotland) and a maximum is 20.6^{o} C (England)[93]. This correction approach was used for sensitivity–temperature correction for all data presented in this thesis.

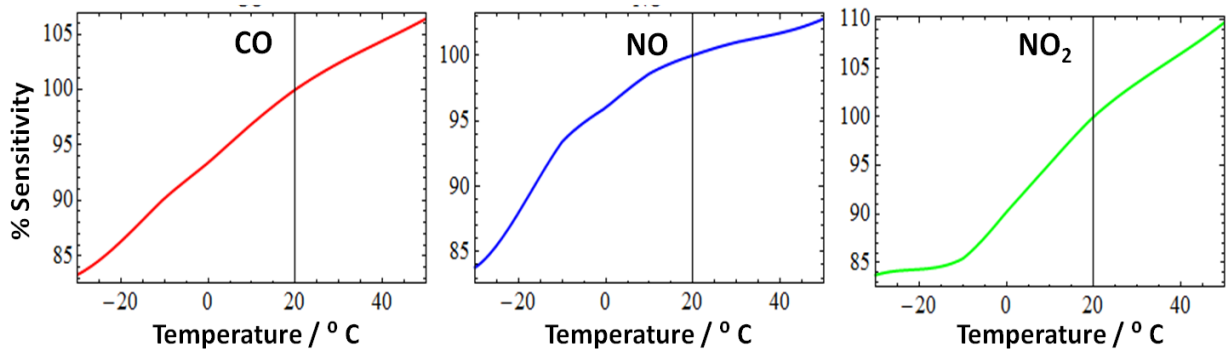

Figure 4.22. Plot showing sensitivity – temperature dependent correction fit for CO, NO and NO_2.

4.5. Uncertainty associated with the electrochemical sensors.

The precision of the instrument was obtained from the spread (1σ) of repeated measurements at known calibrant mixing ratios, and was ≈ 2 ppb for the 5 × CO, 5 × NO sensors and ≈ 1 ppb for the 2 × NO_2 sensors used for the calibration tests.

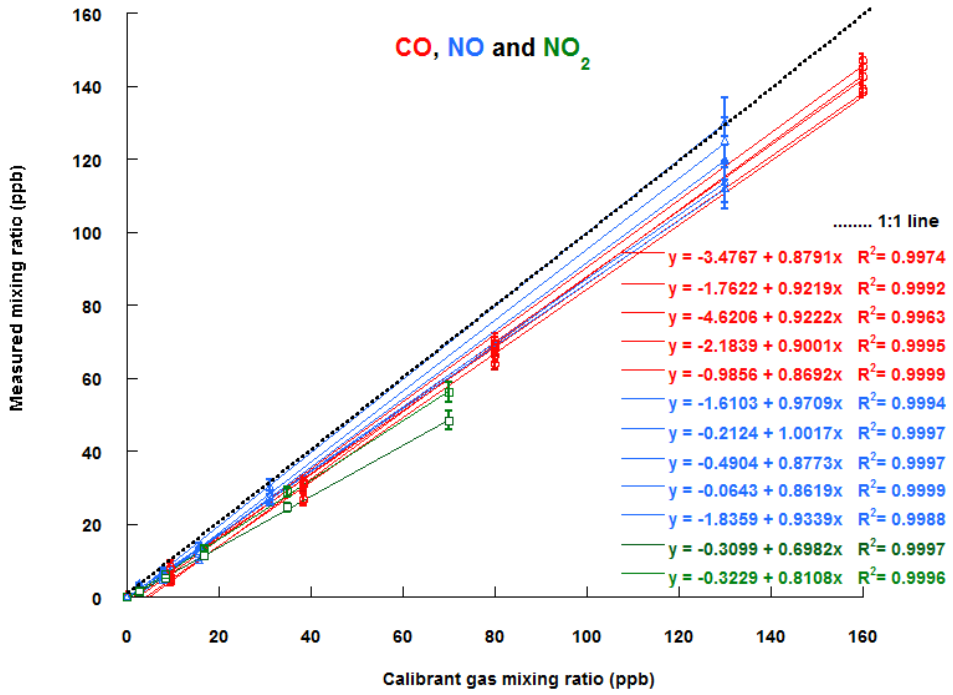

Figure 4.23. Correlation plots of mixing ratios of CO (red), NO (blue) and NO_2 (green) measured using the electrochemical sensors for different calibrated gas mixing ratios (abscissae). The plot was generated using gains provided by the manufacturer for the batch of sensors. Error bars shown are ±1σ. Linear regression lines and fit parameters are shown in each plot. In all cases the regression coefficients were 0.9996 or better and are same before and after recalibration.

Using the off-the-shelf gain conversions provided by the manufacturer, the sensor underestimated the true mixing ratios (plot fig. 4.23). The mean gradients of 0.90 ± 0.02 for CO, 0.93 ± 0.06 for NO and 0.75 ± 0.06 for NO_2 (table 4.9). This implies that under laboratory conditions using gain factors provided by the manufacturer, the uncertainty associated with every measurement is 10% ± 2 ppb for CO, 7% ± 2 ppb for NO and 25% ± 1 ppb for NO_2. However, when the sensors were recalibrated using specific gain conversions at ppb mixing ratios, the uncertainty in each measurement were limited to the precision of the sensors and were ± 2 ppb for CO, ± 2 ppb for NO and ± 1 ppb for NO_2.

Table 4.9. Statistics comparing the gradients of the linear fits for the correlation plots between calibrant gas and different sensors using generic gain conversions. * The standard deviation (SD) was not calculated for NO_2 because only two sensors were used during the NO_2 tests.

	Gradient (generic gain)		
	CO	NO	NO_2*
Mean	0.90	0.93	0.75
Max	0.92	1.00	0.81
Min	0.87	0.86	0.70
SD	0.02	0.06	—

The performance of the electrochemical sensors under field conditions is quite different compared to laboratory conditions. In a comparative study using early prototype sensor nodes and a reference instrument (a chemiluminescence instrument discussed in section 4.3.1), the electrochemical sensor nodes agreed to within < 5% for NO and < 20% for O_3 corrected NO_2 at ppb ambient mixing ratios (0-200 ppb NO and 0-50 ppb for NO_2). Similarly, comparison with a spectroscopic instrument (DUVAS see section 4.3.2) shows an accuracy to within 5% at high mixing ratios (ppm of NO and 100s of ppb of NO_2), typical of pollution levels observed at traffic islands in urban centres.

4.6. Summary and conclusions

Laboratory tests of electrochemical sensors (CO, NO and NO_2) have shown excellent linear response at ppb levels to standard gas mixing ratios. The sensor nodes are not only sensitive (with instrumental detection limits of < 4 ppb (CO and NO) and < 1 ppb for NO_2) but also reproducible showing good sensor-to sensor agreement ($R^2 \approx 0.9$). In addition, results from the NO_2 test carried out using a specially designed gas hood showed the electrochemical sensors have fast response time ($t_{90} \leq 20$ s). The sensors are also very selective as shown by little cross–sensitivity to other gaseous species (e.g. CO, NO and NO_2). Although there are some interferences e.g. with O_3, this can be corrected as long as the mixing ratio and percentage cross sensitivity is known. A good example of this correction approach is shown

for the NO_2 cross–sensitivity to O_3 for the NO / NO_2 intercomparison study at the AURN station in Cambridge.

The reliability of these electrochemical sensor nodes has also been shown by the good agreement observed with other measurement technique. Results from co–deployment studies with both chemiluminescence and DUVAS instruments show statistically significant agreement between these different techniques. R^2 values of 0.74 – 0.88 (NO) and 0.83 – 0.85 (NO_2) were obtained from comparison with chemiluminescence and while studies with the DUVAS instrument gave R^2 of 0.78 and for NO and NO_2 respectively.

One major source of interference is temperature which has a dual effect on sensitivity and zero–baseline. While the former can be corrected using data provided by the sensor manufacture, an independent correction was developed to correct the effect of temperature–dependent baseline drift.

In summary, the results presented in this chapter have shown effectiveness of electrochemical based sensors for use in ambient measurements of CO, NO and NO_2 and consequently implying their potential wider application in a network for air quality monitoring.

Chapter 5 Development of Baseline-Temperature Correction Methodology and Implication of this Correction on the Long-Term Stability of Electrochemical Sensors

Chapter Summary

As discussed in the last chapter, the baseline drift due to temperature is a source of error in the practical application of electrochemical sensors under ambient conditions. Results from field studies showed this effect is most pronounced for NO sensors. This chapter will focus on the correction methodology developed to remove this effect. Results from two intercomparison studies in Cambridge will be presented in this chapter, one of which is used to validate the correction methodology. In addition, the long-term stability of temperature corrected electrochemical sensor data in relation to other meteorology parameters will be discussed.

5.1. Fundamental temperature effect on electrochemical sensors

The electrochemical sensors used in sensor nodes employed in this study are designed to work as an amperometric device tuned such that the output current is limited by diffusion of gases into the sensor. This is achieved by applying a voltage across the working electrode. Under this mode of operation, the overall current is defined by the combination of individual current resulting from diffusion across four regions, electrolyte–electrode, membrane, gas space and sensor hole as shown in figure 5.1 [94]. For each region, the diffusion flux can be expressed in terms Fick's first law as shown in E5.1.

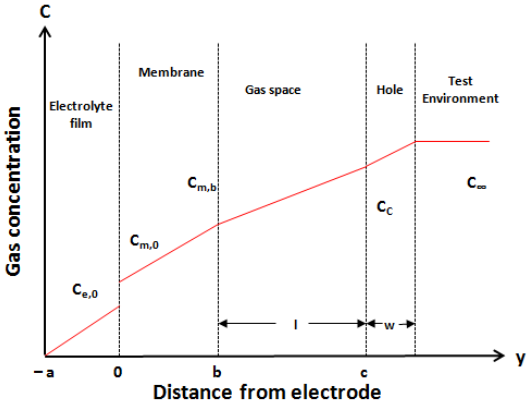

Figure 5.1. Diffusion barriers and mixing ratio profile for membrane covered electrochemical sensor. Modified from Hitchman et al 1997 [94].

E5.1
$$j = -\frac{D\Delta C}{\Delta y}$$

Where *D* is the diffusion constant, *ΔC* is the difference in mixing ratio of the diffusing species at the edges of the barrier, *Δy* is the distance across the barrier in the y direction (this can be a, b, l or w as shown in fig 5.1) and *j* is diffusion flux across the barrier. The negative sign is due to the fact that flow is opposite to the direction y. The total current generated by the sensor is related to *j* by the expression *I=nFAj*, where *n* is number of electrons involved in the redox reaction, *F* is Faraday constant and *A* is area of the barrier in context [94]. By replacing j with E5.1, the total current is given by the expression in E5.2.

E5.2
$$I = -\frac{nFAD\Delta C}{\Delta y}$$

The diffusion coefficient *D* can either be Fickian, Knudsen or surface diffusion depending on the type of diffusion occurring across the barrier. Studies have shown that for Fick's diffusion, current is proportional to $T^{1/2}$ whereas the current is proportional to $T^{-1/2}$ for Knudsen diffusion [94]. In addition, an exponential dependence of dissolved gas to temperature has also been reported [95]. If one considers the complex interactions at various barriers, it becomes increasingly unrealistic to have one single expression relating temperature to current for an electrochemical sensor.

5.2. Methodology

The pair of electrochemical sensor nodes installed at site 2 (described in section 5.2.1 below) measured CO, NO and NO_2. It was observed that the ambient temperature mainly affected the NO measurements compared to CO and NO_2 measurements as indicated in figure 5.2. The NO sensor measurements showed exponential correlation with temperature with R^2 = 0.97 compared to R^2 of 0.07 and 0.15 observed for CO and NO_2 respectively. As a result, the rest of this chapter will focus on temperature correction of NO electrochemical sensor with the assumption that this correction methodology can be used for other electrochemical sensors that also show strong temperature dependence.

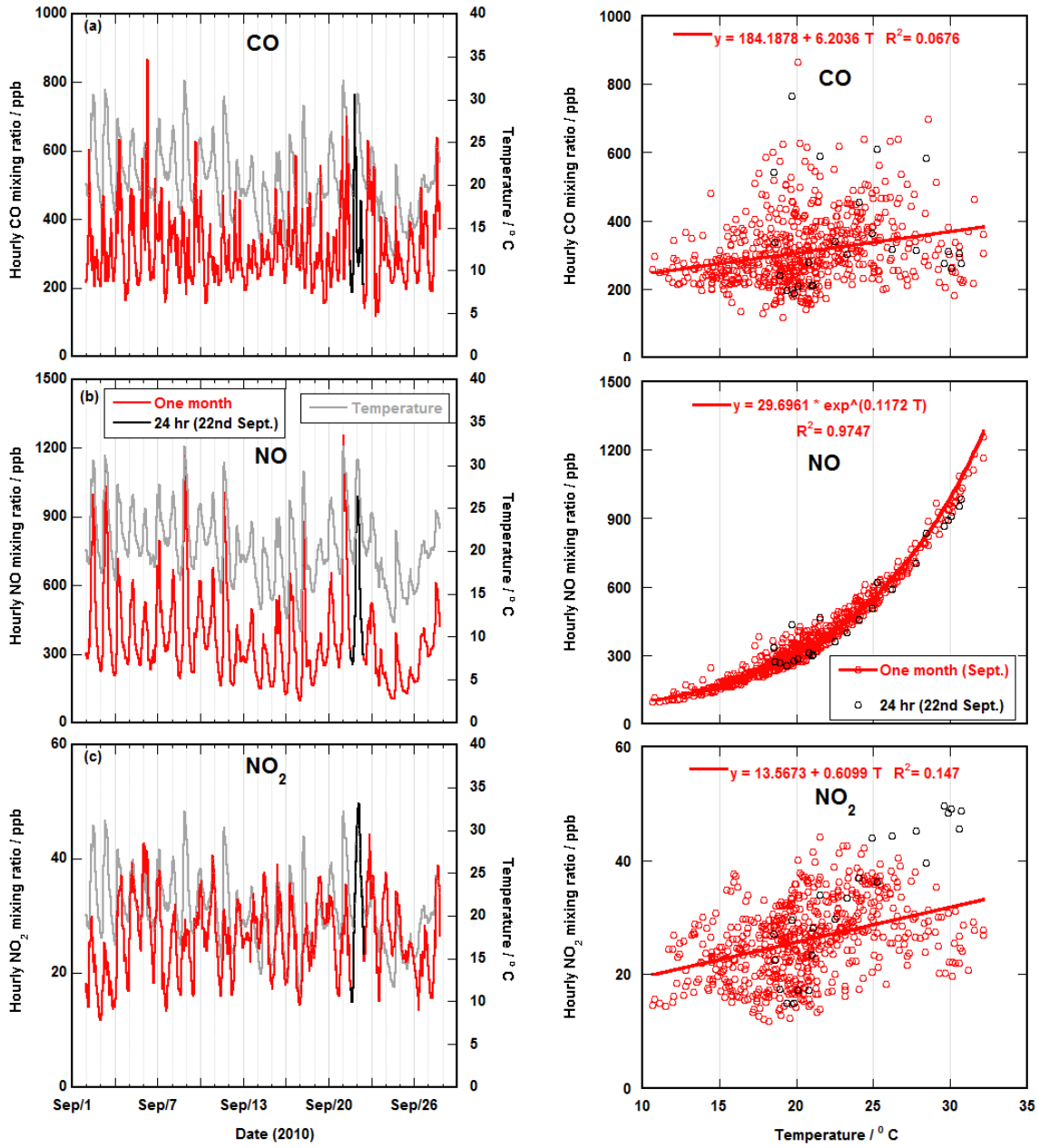

Figure 5.2. Time series and scatter plot of hourly mean mixing ratios of raw data during the long-term deployment at the LAQN station in Gonville Place, Cambridge (February-December 2010). (a) A month-long NO measurement (2-29, September 2010) (b) A month-long NO measurement (2-29, September 2010). (c) A month-long NO_2 measurement (2-29, September 2010).

5.2.1 Deployment areas

This section describes ambient conditions at two sites where intercomparison studies were carried out. The most significant environmental factor that differs between these sites was temperature. This provided an excellent opportunity to investigate effect of temperature on

NO electrochemical sensors which were used for measuring outdoor NO mixing ratios at the sites (the other instrument was chemiluminescence analyser).

Ambient NO mixing ratios were measured using a pair of closely co–located electrochemical sensor nodes at the Gonville Place LAQN station (site 1) in Cambridge, UK (52.199957 N, 0.127719 E) continuously for approximately six months between February and December 2010. In addition, NO mixing ratios were measured for a period of one week at an AURN station (site 2) on Regent Street (52.202189 N, 0.124283 E) in January 2009 (fig. 5.3). Site 1 is close to a busy junction linking four major roads (Gonville Place, Hills Road, Regent Street and Lensfield Road) as seen in fig 5.3. In contrast, site 2 is located along Regent Street, however it is also the major route (fig. 5.3) to the bus station in Cambridge city centre and has been designated a roadside station by the environmental department at the Cambridge City Council.

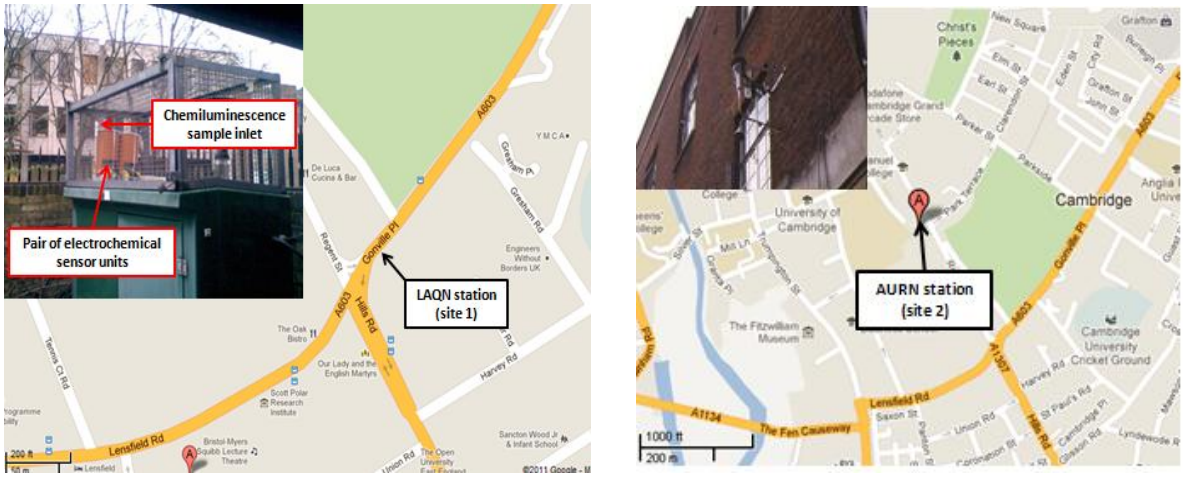

Figure 5.3. Locations of the two co-location test sites at Cambridge UK. The left panel shows the LAQN station (site 1) in Gonville Place, Cambridge UK. Inset is the co–location of two electrochemical sensor instruments (housed in weather proof enclosures) with the chemiluminescence unit at the LAQN station. In the right panel is the AURN monitoring station (site 2) in Regent Street, Cambridge, UK. Inset is the sampling inlet of the monitoring station located on the first floor of Cambridge City Council Building. Image courtesy Cambridge City Council. Map courtesy Google Map [81].

At site 2, air is sampled at a height of 4 m (figure 5.3) and adjusted to room temperature before NO analysis by the electrochemical sensor nodes and the chemiluminescence instrument. This site has an advantage in that there was little variation in temperature for the duration of the study. In contrast, site 1 is a typical roadside station and the entire deployment was under outdoor conditions (fig. 5.3) with large variations in daily temperatures.

5.2.2 Correction approach

5.2.2.1. Baseline extraction

A mathematical approach was developed to extract the daily baseline change due to temperature. The correction approach was applied to the fast response NO data (5 s data collected at AURN station in Gonville Place) and this was achieved using a function to extract the minimum value over a specified window for every 24 hours (this correction assumes the background NO mixing ratio approaches zero). This extracted minimum is referred to as the extracted baseline. This extracted baseline was then correlated with temperature measurement for the same period using an exponential fit. The coefficient of correlation R^2 between these two variables was then obtained. This process was repeated for varying windows (10, 50, 100, 150, 200, 250, 300 and 350). Note each window correspond to a time scale of x 5 seconds such that a window of 10 imply minimum values over 50 s intervals. By making a plot of R^2 against *the* windows, an optimal window was obtained which corresponds to the turning point of the plot which gives maximum R^2 as shown in figure 5.4(a). This optimal window was then used to generate the extracted (temperature dependent) baseline which can be seen in figure 5.4(b).

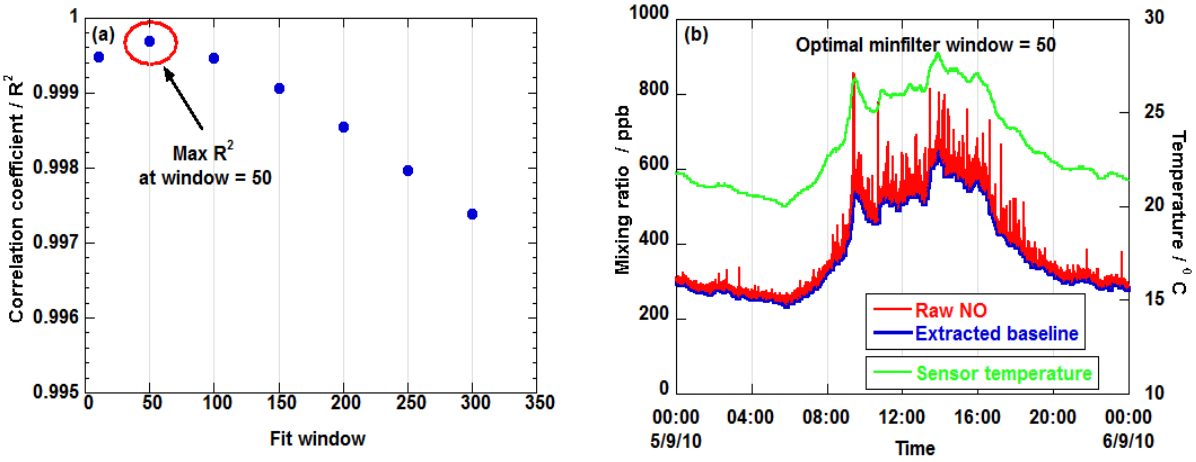

Figure 5.4. (a) A typical plot of varying fit windows against R^2 for a 24 hour period. (b) Time series of NO mixing ratio from electrochemical sensor with extracted baseline derived from optimal MinFilter window. Note: The optimal window is the turning point of the points in the Fig. 5 (a); in this case it was 50 corresponding to 250 s intervals.

5.2.2.2. Temperature correction

A fit was generated between the extracted baseline and the temperature measurement using an exponential function as depicted in figure 5.5(a), and from the values of the fit parameters, a temperature–dependent baseline was generated from actual sensor temperature measurements as shown in figure 5.5(b). This was then subtracted from the raw NO measurements and the resulting output gives the temperature corrected data as shown in figure 5.6. This correction methodology was repeated in steps of 24 hours for the entire dataset. The rational for choosing 24 hours interval is based on the fact that it is long enough time interval to observe diurnal profile in temperature and short enough to get good fit between the extracted baseline and temperature.

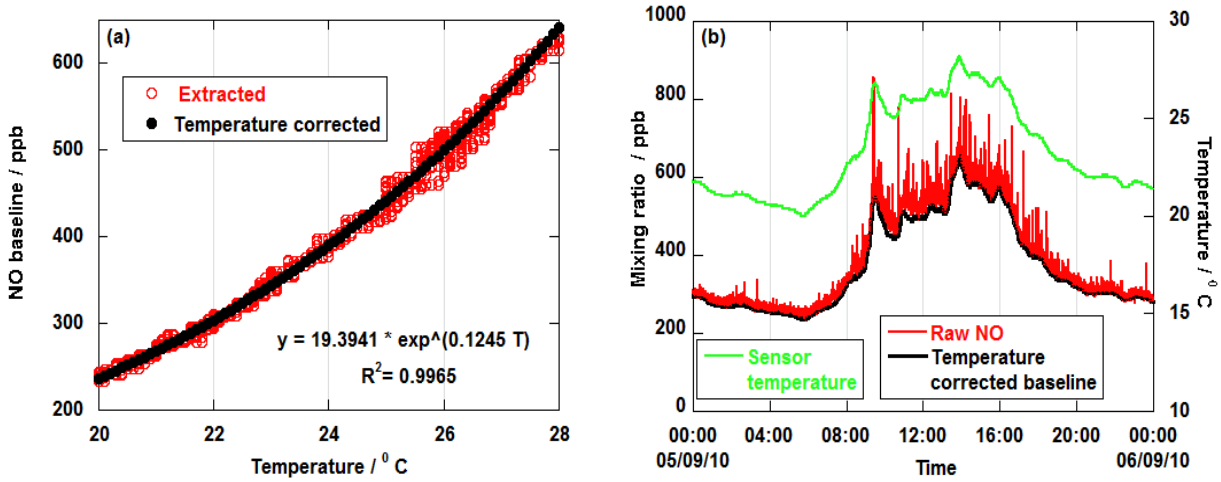

Figure 5.5. (a) A typical scatter plot of temperature and temperature–baseline change (red is extracted and black is fitted). (b) Time series of uncorrected NO mixing ratio (raw) and fitted baseline for a typical 24 hour period.

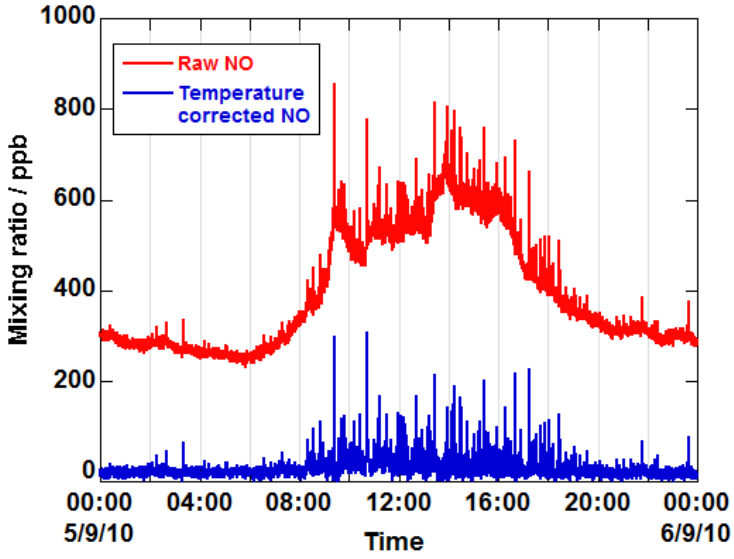

Figure 5.6. Time series of uncorrected (red) and temperature corrected (blue) NO mixing ratio from electrochemical sensor for a 24 hours period.

5.3. Results and discussion

5.3.1 Observed temperature effect on NO baseline

The hourly temperature ranges recorded for site 1 and site 2 are summarized in table 5.1. While the hourly temperature ranges between 23.3 – 24.0^{o}C at site 2, it was between 0.6 – 36.0 ^{o}C for the entire duration of the deployment at site 1. In addition, the expected diurnal

variation in temperature was not seen at site 2 while these were clearly visible from results of the study at site 1 as shown in figure 5.7(b).

Table 5.1. Summary of hourly mean temperature statistics for AQ stations in Regent Street and Gonville Place.

Site	Temperature range / ° C	Maximum temperature / ° C	Minimum temperature / ° C	Duration of study
Gonville Place (site 1)	36.2	36.0	-0.1	Feb. – Dec. 2010
Regent Street (site 2)	0.6	24.0	23.3	23 – 29, Jan. 2009

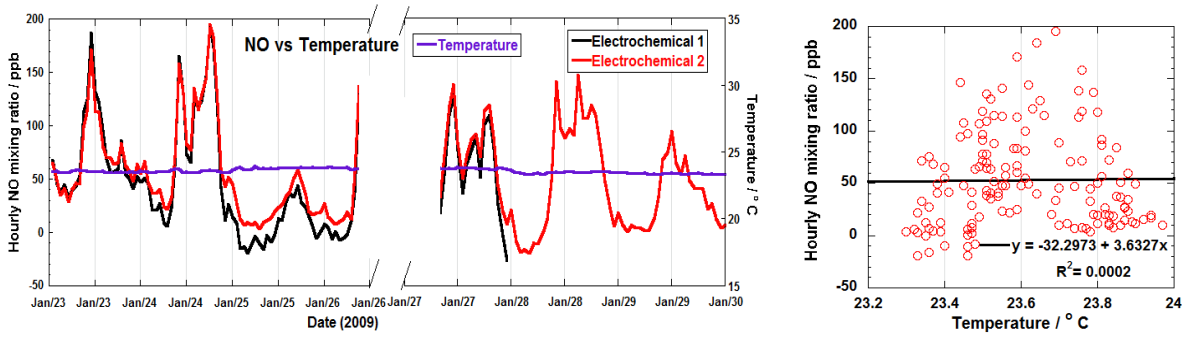

(a)

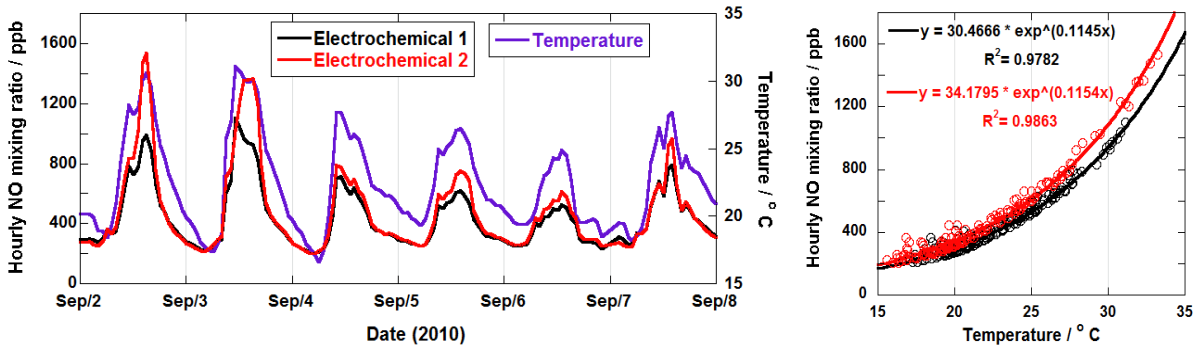

(b)

Figure 5.7. Time series and correlation plots of hourly NO mixing ratios and temperatures for the two sites in Cambridge. (a) Controlled environment (room conditions) at the AURN site (site 2) in Regent Street, Cambridge (23 – 29 January, 2009). (b) Ambient conditions (uncontrolled environment) at the LAQN station (site 1) in Gonville Place, Cambridge (2 – 8 September, 2010).

NO measurements at site 1 correlated exponentially with temperature (this relationship is consistent for both long–term and short–term datasets as shown in fig 5.8) in contrast to site 2 where there was no visible correlation as depicted figure 5.7(a). The variations seen in NO measurement made at site 2 were due only to changing ambient NO mixing ratios. This is confirmed by the good correlation of NO measurements from the electrochemical and chemiluminescence instruments located at this site (figure 5.9).

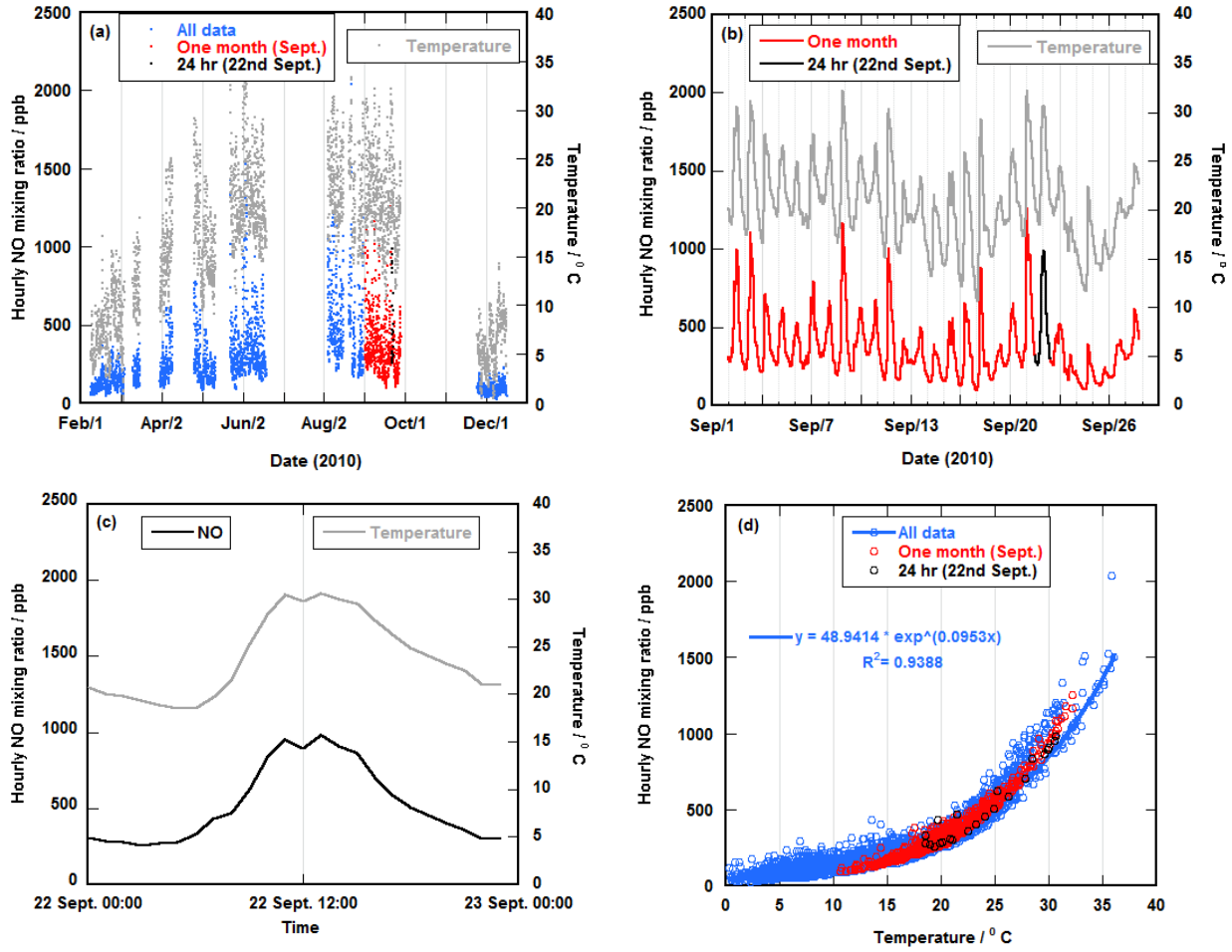

Figure 5.8. Hourly mean temperature and measured NO mixing ratios using electrochemical sensor nodes at Gonville Place, site 1. (a) For the whole duration of the deployment (February–December 2010). (b) A month during the deployment (2 – 29, September 2010). (c) For a 24 hour period during the deployment (22 September, 2010). (d) Correlation plot of hourly mean temperature and measured NO mixing ratios using electrochemical sensor colour coded based on length of data set.

These results show that a rise in temperature therefore has a direct effect on the NO baseline value for measurements made using electrochemical sensors. It is therefore

imperative for the temperature dependant baseline to be extracted and used to correct for measured signal.

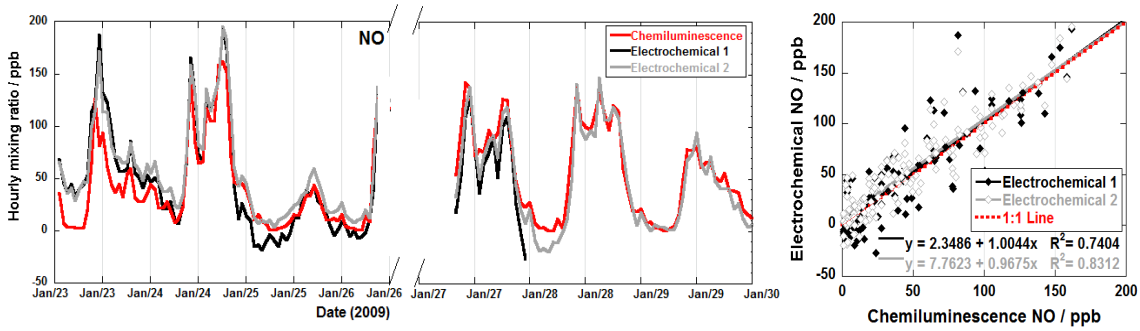

Figure 5.9. Time series and correlation plots of hourly NO measurements using two different techniques at site 2, Regent Street (23 – 29 January, 2009).

5.3.2 Reproducibility of correction methodology

The reproducibility of this correction methodology was validated by comparing results from corrected NO data from these two electrochemical sensor nodes deployed at the LAQN station in site 2 (fig. 5.2). Shown in figure 5.10 are the time series and correlation plots for hourly average NO measurements for one month during the deployment (2 – 28 September, 2010). A correlation coefficient of 0.96 was obtained for the pair of sensors showing that the correction method is reproducible. In addition, the mean NO mixing ratios over this period were 30.0 ± 2.3 ppb and 31.0 ± 2.2 ppb for electrochemical sensor 1 and 2 respectively. The summary of the statistics for the NO measurements of the two electrochemical sensor nodes is shown in table 5.2. The differences in NO mixing ratios between the two sensor nodes were also calculated. Shown in figure 5.11 are the time series and histogram plots for these differences. Note the distribution pattern for both the fast response (5 s) and hourly mean data are similar (figure 5.11(c)) indicating that the overall trend in NO mixing ratio was not lost in the hourly averaged data. The mode of the distribution lies between -5 and 0 ppb and is consistent with the mean value of the NO difference which was -1.5 ± 0.4 ppb (table 5.2) which lies within the modal range.

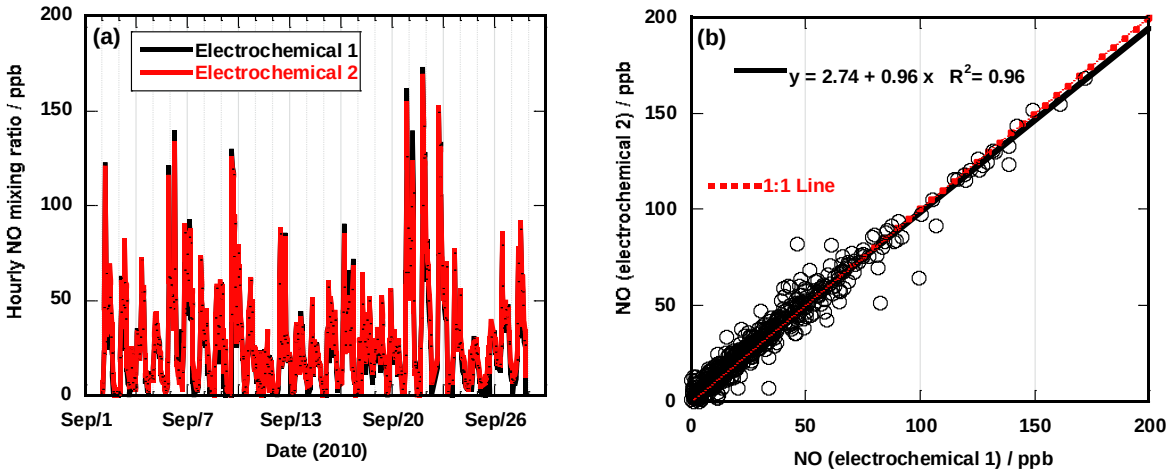

Figure 5.10. (a) Time series of hourly temperature corrected measured NO mixing ratios of a pair of co-located electrochemical sensor nodes at Gonville Place (2 – 28 September, 2010). (b) Scatter plot showing correlation between the pair of temperature–corrected NO electrochemical sensor at Gonville Place (2 – 28 September, 2010).

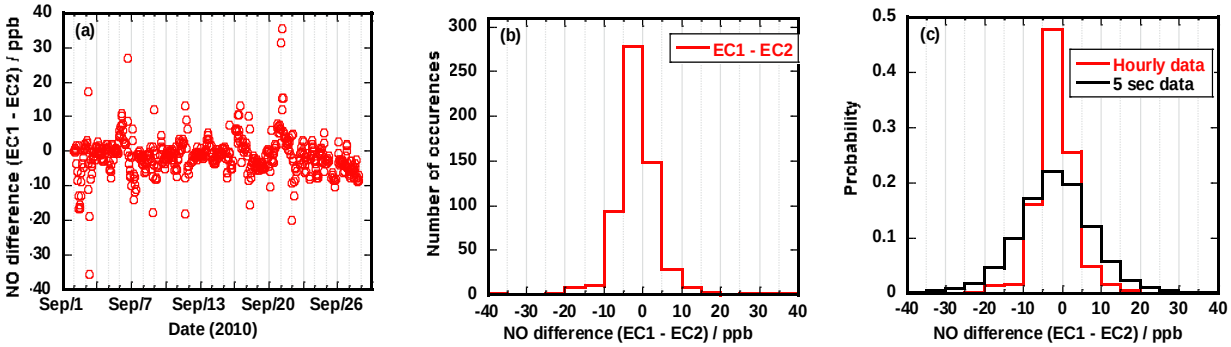

Figure 5.11. Differences between temperature-corrected NO mixing ratios of a pair co-located electrochemical sensor nodes in Gonville Place (2 – 28 September, 2010). (a) Time series of the difference (hourly data). (b) Histogram showing the distribution of the differences (hourly data). (c) Histogram showing the distribution of the differences for both hourly data (red line) and 5 seconds data (black line).

Table 5.2. Statistical table of temperature–corrected NO measurements from two electrochemical sensor nodes for the period 2 – 28 September, 2010 at the LAQN station on Gonville Place. Also shown is the statistics for the difference between these sensors. CI represents confidence interval.

Sensor (s)	Mean / ppb	95 % CI / ppb	SD / ppb	Max / ppb	N
Electrochemical 1 (EC1)	30.0	±2.3	28.0	170	585
Electrochemical 2 (EC2)	31.0	±2.2	27.0	170	585
EC1–EC2	-1.0	±0.4	5.4	35.0	585

5.3.3. Validation of correction methodology

5.3.3.1. Statistical comparison with LAQN data

The correction methodology was tested by comparing hourly mean NO mixing ratios before and after temperature correction with those from the chemiluminescence instrument [96] used at the LAQN station at Gonville Place (site 1). The time series of the comparison between the uncorrected electrochemical NO and the chemiluminescence instrument show that the two instruments do not track each other for the duration of the study especially during the warmer months (figure 5.12). In addition, poor correlation was observed between the two instruments (pair of electrochemical sensors and chemiluminescence) for the uncorrected NO data with R^2 of 0.02 (for electrochemical 1 and 2 respectively) for the entire dataset shown in figure 5.12(a). Correlation coefficients of 0.12 (electrochemical 1) and 0.10 (electrochemical 2) were obtained for a month long dataset as shown in figure 5.12(b). However, after implementing temperature correction, there was better agreement between the two instruments (electrochemical sensors and chemiluminescence) with R^2 of 0.78 (electrochemical 1) and 0.71 (electrochemical 2) for the full dataset and 0.87 (electrochemical 1) and 0.84 (electrochemical 2) for a month dataset as presented in figures 5.13(a) and 5.13(b). This improved correlation is easily seen in the time series of the two different instruments (figure 5.13). A summary of the correlation coefficient between

chemiluminescence and the pair of electrochemical sensors for the uncorrected and temperature corrected NO measurements is presented in table 5.3.

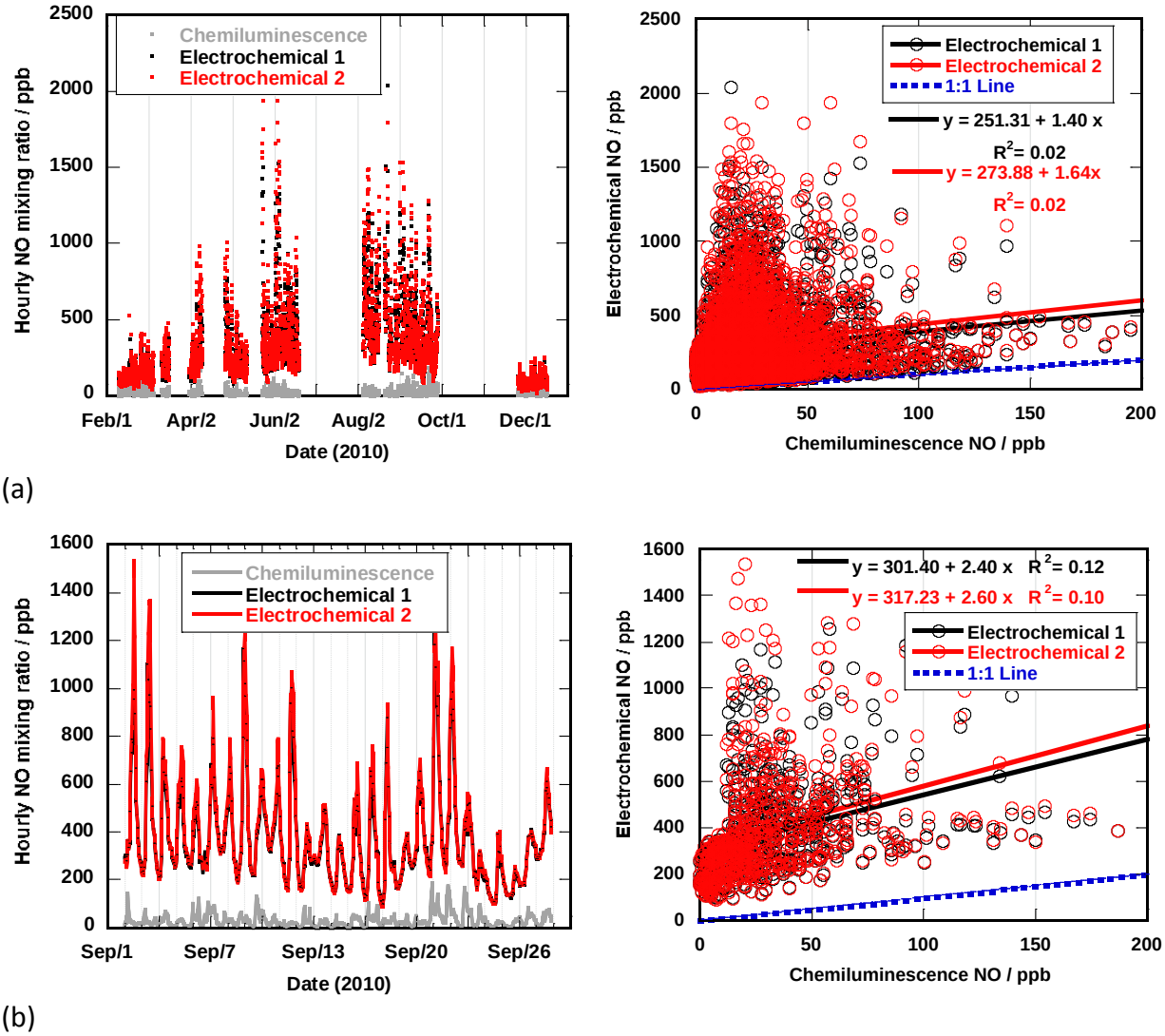

Figure 5.12. Time series and correlation plots between uncorrected NO measurements from the pair of electrochemical sensor nodes and chemiluminescence instrument. (a) The entire duration of the deployment (February – December, 2010) at AURN site in Gonville Place, Cambridge. Hourly mean measured NO mixing ratios using electrochemical and chemiluminescence instruments in Gonville Place (February – December 2010). (b) One month during the deployment (2 – 28th September, 2010) at LAQN site in Gonville Place, Cambridge.

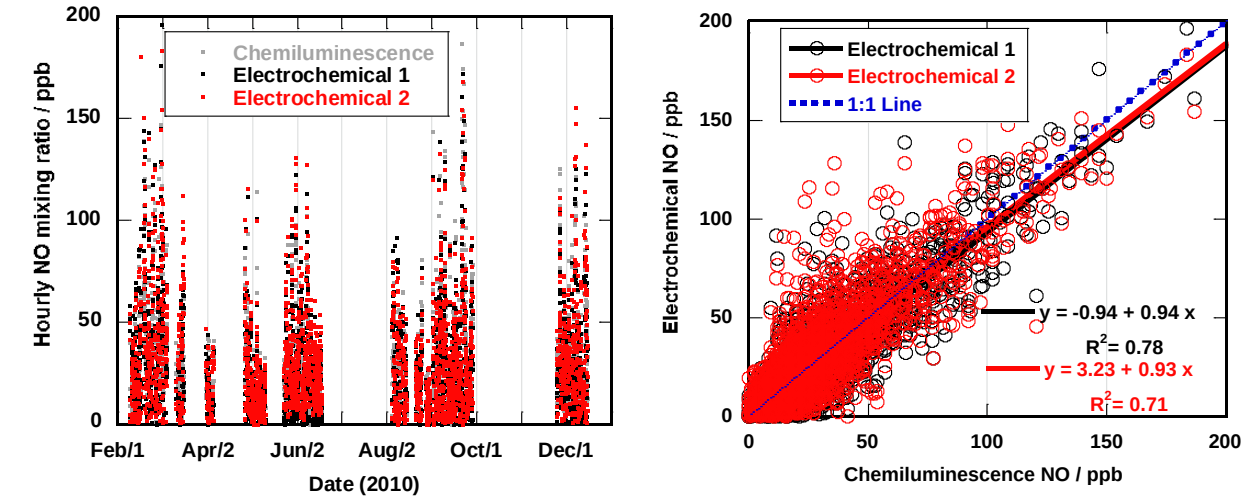

(a)

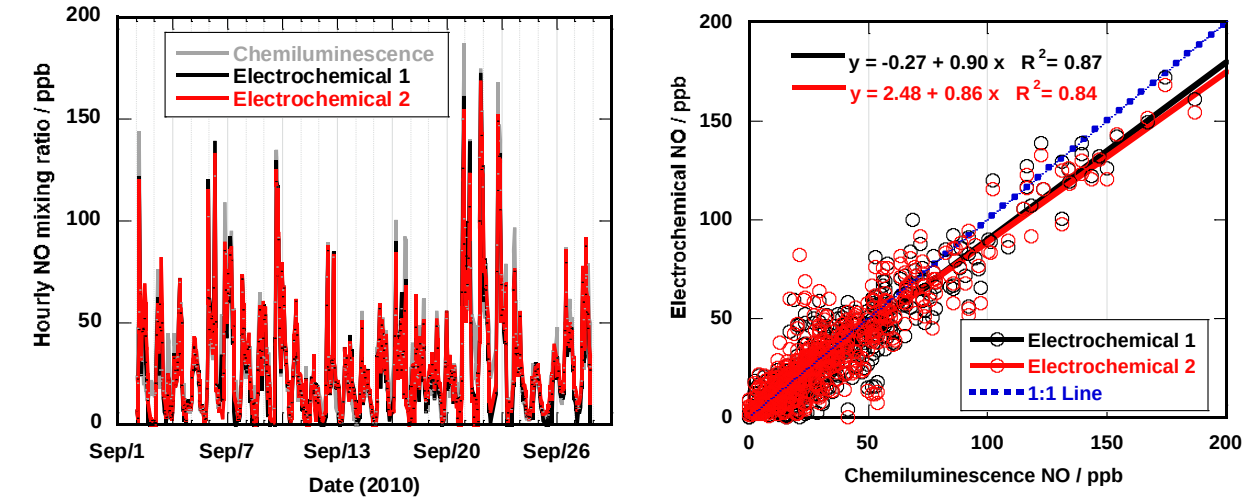

(b)

Figure 5.13. Time series and correlation plots between temperature–corrected NO measurements from the pair of electrochemical sensor nodes and chemiluminescence instrument. (a) The entire duration of the deployment (February – December, 2010) at AURN site in Gonville Place, Cambridge. Hourly mean measured NO mixing ratios using electrochemical and chemiluminescence instruments in Gonville Place (February – December 2010). (b) One month during the deployment (2 – 28th September, 2010) at LAQN site in Gonville Place, Cambridge.

Table 5.3. Statistical summary of correlation coefficient between the electrochemical sensor nodes and chemiluminescence instrument for uncorrected and temperature corrected NO data for the entire duration of the deployment.

Species	First Order Equation	R^2
Uncorrected NO	$NO_{(ELECTROCHEMICAL\ 1)} = (1.40 \times NO_{(CHEMILUMINESCENCE)}) + 251.31$	0.02
	$NO_{(ELECTROCHEMICAL\ 2)} = (1.64 \times NO_{(CHEMILUMINESCENCE)}) + 273.88$	0.02
Temperature corrected NO	$NO_{(ELECTROCHEMICAL\ 1)} = (0.94 \times NO_{(CHEMILUMINESCENCE)}) - 0.94$	0.78
	$NO_{(ELECTROCHEMICAL\ 2)} = (0.93 \times NO_{(CHEMILUMINESCENCE)}) + 3.23$	0.71

5.3.3.1. Correlation of NO measurements with measured temperature

In addition to comparing NO measurements between the two instruments, the correction methodology was also validated by checking the correlation between temperature and NO measurements (before and after the temperature correction). Results of the temperature corrected data show that majority of the temperature dependence has been removed as shown in figure 5.14 (b) and the strong exponentially correlation (fig. 5.14 (a)) observed prior to temperature correction no longer exist between the NO and temperature measurements. This indicates that temperature-baseline effect on the electrochemical NO data has been removed thereby validating the correction methodology.

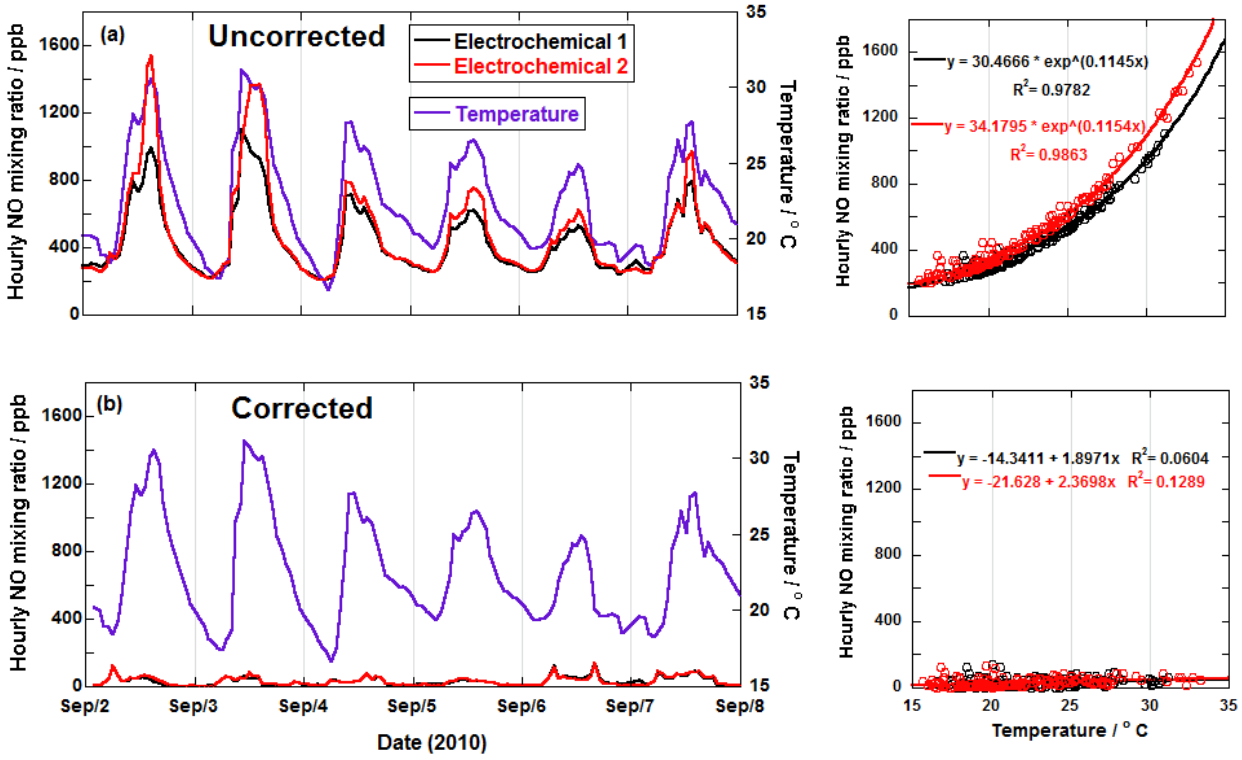

Figure 5.14. Time series and correlation plots of: (a) uncorrected hourly NO mixing ratios against temperatures for the LAQN station in Gonville Place, Cambridge (2 – 8 September, 2010) (b) temperature corrected hourly NO mixing ratios against temperatures for the LAQN station at Gonville Place, Cambridge (2 – 8 September, 2010).

5.3.4. Bias between the electrochemical sensor nodes and the chemiluminescence instrument

In order to evaluate the overall performance of the electrochemical sensor nodes in measuring ambient NO relative to the chemiluminescence instrument, the differences in measured NO between the two instruments were calculated. In addition, the differences in NO measurements from the pair of electrochemical sensors were also determined and a summary of the results statistics for 2 – 28, September 2010 is shown in table 5.4. The value of the difference between the two different instruments (electrochemical 1 and chemiluminescence) range from -38.0 to +41.0 ppb. Although this appears to be a large variation, the bulk of the values (the mode) lie between -5 and +5 ppb as shown in figure 5.15. This is similar to the difference observed between the pair of electrochemical sensors where the mode falls between -5 and 0 ppb (fig 5.15). In addition, the mean of the differences which were calculated to be -4.0 ppb (EC1 and chemiluminescence) and -2.0 ppb

(EC1 and EC2) both lie within these modal values. Since the mean of the difference between the two instrument is small (-4.0 ppb), it was concluded that temperature–corrected NO electrochemical sensor is suitable for measuring ambient NO mixing ratios.

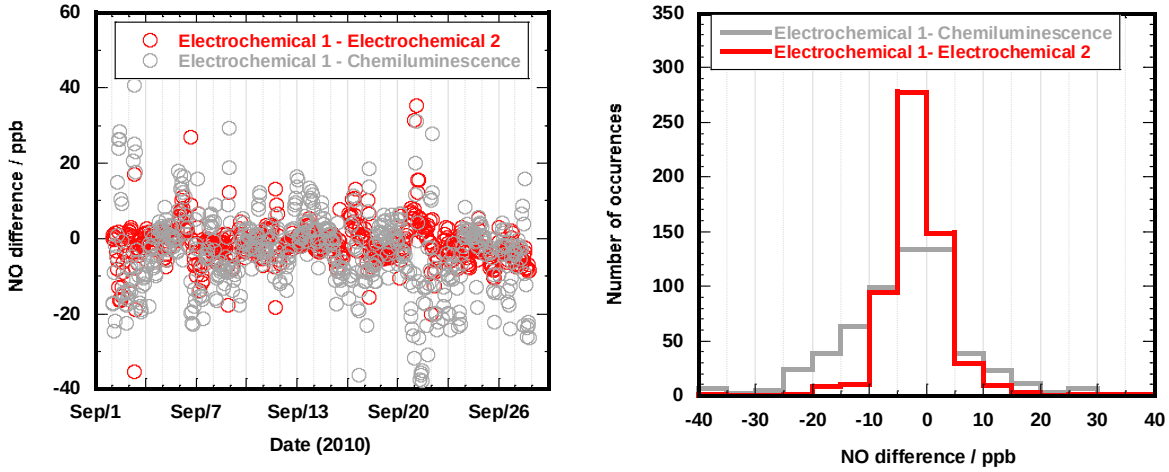

Figure 5.15. Time series and histogram plots of the differences between temperature–corrected NO mixing ratios from a pair of electrochemical sensor nodes (red line) against NO differences between chemiluminescence and temperature corrected–NO electrochemical sensor (grey line).

Table 5.4. Statistics showing summary of the differences in NO measurements between chemiluminescence and temperature corrected NO electrochemical sensors for the period 2 – 28 September, 2010 at the LAQN station in Gonville Place. Also shown is the statistics for the NO difference between pair of electrochemical sensors (temperature corrected data).

Sensor (s)	Mean / ppb	95 % CI / ppb	SD / ppb	Range / ppb	N
EC1–Chemiluminescence	-4.0	±0.8	10.0	-38.0 to 41.0	585
EC1–EC2	-2.0	±0.4	5.0	-36.0 to 35.0	585

5.4. Long-term stability of electrochemical sensors

Long-term measurements made at the LAQN station in Gonville Place, Cambridge made it possible to assess the long-term stability of the temperature-corrected NO electrochemical sensors. The sensitivity (or gain) change with time was determined by calculating the ratios

of (temperature-corrected) NO measurements made with the electrochemical sensor to that from the chemiluminescence instrument for different periods during the deployment. The chemiluminescence instrument was used as a reference because it was assumed that it has stable gain. This was based on the fact that ratified NO data were used for this comparison and any instrumental drift in the chemiluminescence instrument will have been accounted for during quality assurance and quality control (QA & QC) of the raw chemiluminescence data. Figure 5.16 shows the time series of the relative gain change of the NO electrochemical measurements for different periods between February and December, 2010 at the LAQN station on Gonville Place in Cambridge. The slope of the trend line ($4.25 \times 10^{-9} \pm 4.13 \times 10^{-9}$ per second) corresponds to gain change of -13 % ± 13 % per annum. This shows that the electrochemical sensor has no statistically significant drift in gain over a year.

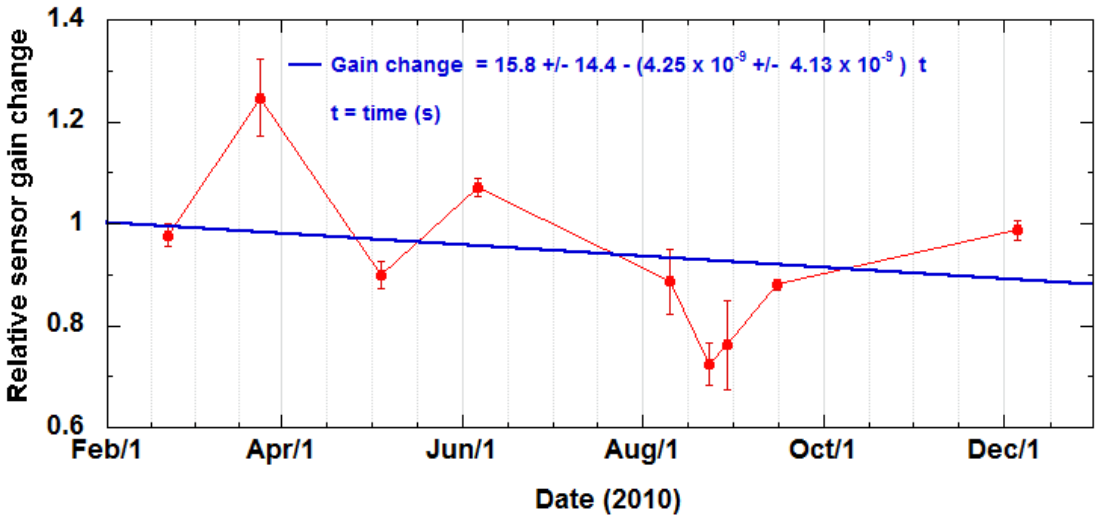

Figure 5.16. Time series of the relative gain changes of NO measurements from electrochemical sensor node with respect to chemiluminescence instrument for different periods between February and December, 2010 at the LAQN station on Gonville Place in Cambridge. The error bars represent ± 1σ of the mean ratio estimate for each period.

Apart from the drift in gain analysis, the relative gain change of the NO electrochemical sensor with temperature was also studied (see figure 5.17). There was no significant change in gain with temperature as indicated by the small gradient associated with the trend line ($4.55 \times 10^{-3} \pm 5.15 \times 10^{-3}$ per ^{o} C). This result further validates the temperature correction methodology described in section 5.2.

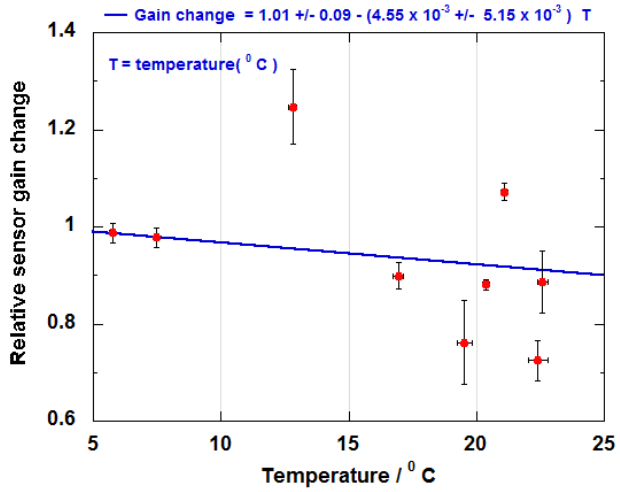

Figure 5.17. Correlation plot of mean temperature against relative gain changes of NO measurements from electrochemical sensor with respect to chemiluminescence instrument for different periods between February and December, 2010 at the LAQN station on Gonville Place in Cambridge. The error bars represent ± 1σ of the mean ratio estimate for each period.

The effects of other meteorological parameters on long-term stability of temperature corrected NO electrochemical sensors were also evaluated using a similar analysis as described above for both time dependent and temperature change. A summary of the relative gain change in relation to some meteorological parameters are shown in table 5.5. As observed for temperature, there was no statistically significant change in gain with respect to RH change. This implies that the temperature correction also accounted for the RH change as the absolute humidity does not vary much over the day. There was no significant dependence of sensitivity on pressure although there seems to be a small apparent (negative) dependence on wind. The origin of the latter is unclear.

Table 5.5. Correlations of NO sensor with some meteorological variables. Errors shown are 1σ.

Variable	Gain change dependence
Pressure	$-4.4 \times 10^{-3} \pm 9.0 \times 10^{-3}$ / hPa
RH	$-1.2 \times 10^{-3} \pm 5.2 \times 10^{-3}$ / %RH
Wind speed	-0.12 ± 0.046 / ms^{-1}

5.5. Summary and conclusions

Deployment of NO electrochemical sensors under different ambient condition has shown that temperature changes can result in baseline changes which invariably affect the sensor performance. In order to correct for temperature-dependent effects on gas mixing ratio measurements made using electrochemical sensor nodes, a correction methodology has been developed, implemented and validated. The correction approach has been shown to be reproducible for the NO electrochemical sensor nodes used in this study. In addition, the results presented in this chapter show that the effect of temperature on the baseline of NO electrochemical sensors has been successfully removed as indicated by (1) much improved correlation with NO measurements from chemiluminescence instrument (R^2 = 0.78 compared to 0.02 before correction) and (2) lack of correlation between the corrected NO measurement and temperature. Therefore, the most dominant external factor affecting the NO measurement, in this case temperature, has been successfully removed. The small mean value (-4.0 ppb) of the difference between temperature–corrected NO electrochemical sensor and the chemiluminescence instrument indicate that the measurements from the electrochemical sensors now truly reflect true ambient mixing ratios.

It has been shown that temperature-corrected NO electrochemical sensors do not show statistically significant drift in gain over a year. This makes them suitable for use in extended studies. There was no significant change in gain due to meteorological parameters like pressure, RH and temperature after implementing the baseline-temperature correction. However, a small negative dependence gain change due to wind speed was observed.

In conclusion, for practical applications of electrochemical sensors under ambient conditions, simultaneous ambient temperature measurements are required. By implementing the temperature correction methodology described in this chapter, limitations of electrochemical sensors in monitoring ambient gas species mixing ratio (in this case NO species) have been greatly reduced. In effect this means they can provide reliable, cost–effective monitoring technique to existing standard air quality infrastructures.

Chapter 6 Field Deployments of Mobile Electrochemical Sensor Nodes

Chapter Summary

This chapter presents results from several field studies using the mobile electrochemical sensor nodes described in previous chapters. These studies range from short-term deployments which lasted just a few hours to long-term measurements lasting several months. The field trials were conducted at different urban areas, both within and outside the UK. Finally, details of the deployments of mobile air quality sensors at Cranfield airport (UK) will be presented.

6.1. Field deployments of mobile sensor nodes in urban areas

A number of short-term (2-3 hours) outdoor deployments of mobile sensor nodes were conducted in urban centres in Cambridge and London (UK), Valencia (Spain) and Lagos (Nigeria). These studies aimed at measuring air quality gaseous species (CO, NO and NO_2) related to road transport sources. This section will focus mainly on studies conducted in Cambridge and Lagos.

6.1.1. Short-term studies of pollution from road transport sources in Cambridge, UK

In this section two outdoor deployments involving the use of CO, NO and NO_2 mobile electrochemical sensor nodes in Cambridge will be discussed. The first trial involves monitoring the pollutant exposure levels of pedestrians walking along selected routes in city centre in Cambridge, while the other study involves assessing the typical pollution exposure of a cyclist along certain routes in Cambridge city centre.

6.1.1.1. Cambridge mobile sensor study (CASE 1): measurement of CO, NO and NO_2 mixing ratios along pedestrian route.

Overview of deployment

This field trial was aimed at evaluating the field performance of the sensor nodes in addition to quantifying the target gas species along the study area. Two pairs of sensor nodes (pair 1 include sensors S1 & S2 while pair 2 include sensors S3 & S4) at waist height were carried by two volunteers walking along the kerbside in Cambridge city centre. The journey route was

designed to cover quiet road, busy roads and also the bus station (fig. 6.1). The experiment lasted one hour (09:36-10:36) during which each sensor pair journeyed along different routes for most of the deployment except for a short 10 minutes period (09:56-10:06) where the two pairs were co-located (the volunteers were walking together).

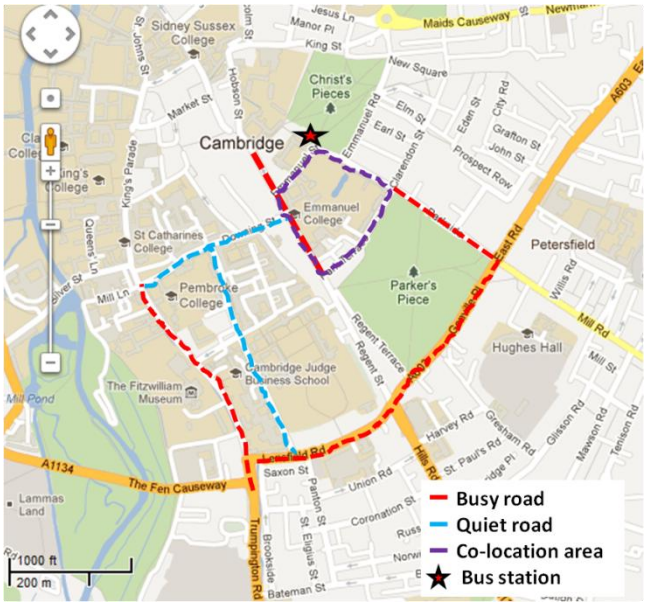

Figure 6.1. Map showing part of Cambridge city centre with routes colour coded to show the traffic activity and also co-location area (which encompass the bus station, busy road and part of a quiet street). Map courtesy Google Map [81]

Results and discussion

Figure 6.2 shows the time series and correlation mixing ratio plots of all four sensor nodes for CO, NO and NO_2. There is good reproducibility in measurement for pairs 1 and 2 for the entire duration of the deployment. Sensor S2 stopped logging data 10 minutes before the end of the deployment due to failure of the Bluetooth connection between the sensor unit and the mobile phone. Consequently the data for pair 1 (S1 & S2) has been trimmed for the period when the two sensors had measurements.

The results of the correlation plots of S3 and S4 (pair 2) showed good agreement for all three species with R^2 of 0.95 (CO), 0.95 (NO) and 0.94 (NO_2) in addition to close sensor sensitivities which are inferred from the gradients of the linear fits 0.94 (CO), 0.97 (NO) and 1.15 (NO_2). In contrast, only the NO (R^2 = 0.97, gradient = 0.92) and NO_2 (R^2 = 0.95, gradient = 1.01) measurements from pair 1 (S1 and S2) show similar correlation statistics (fig. 6.2).

Although a R^2 = 0.86 for CO from pair 1 (fig 6.2) indicates statistically significant correlation between CO measurements of S1 and S2, the gradient of 0.58 at the p = 0.00 level suggest significant difference in sensitivities between the two sensors. However, careful inspection of the time series (fig 6.2) revealed that this large sensitivity difference was due to two pollution events at about 09:40 and 10:08. The sensors response to these high pollution events were not same possibly due to the fact that they were hanging on either side (left and right) of the volunteer waist and were exposed to different mixing ratios away from the primary source (vehicle exhaust). For instance, the first peak in the CO measurements at 09:40 was observed when the volunteer was crossing a busy road at a traffic light. At this instance, one sensor (S1) was facing the static traffic relative to S2 and might detect elevated mixing ratios due to its proximity to the source(s). This seems to be the most plausible explanation as the sensors agreed well for most of the duration of the deployment. When the correlation analysis were recalculated excluding the two peak events in the CO (which skewed the statistical parameters), better values of R^2 = 0.95 and gradient = 0.88 at the p = 0.00 level were obtained as seen in figure 6.3.

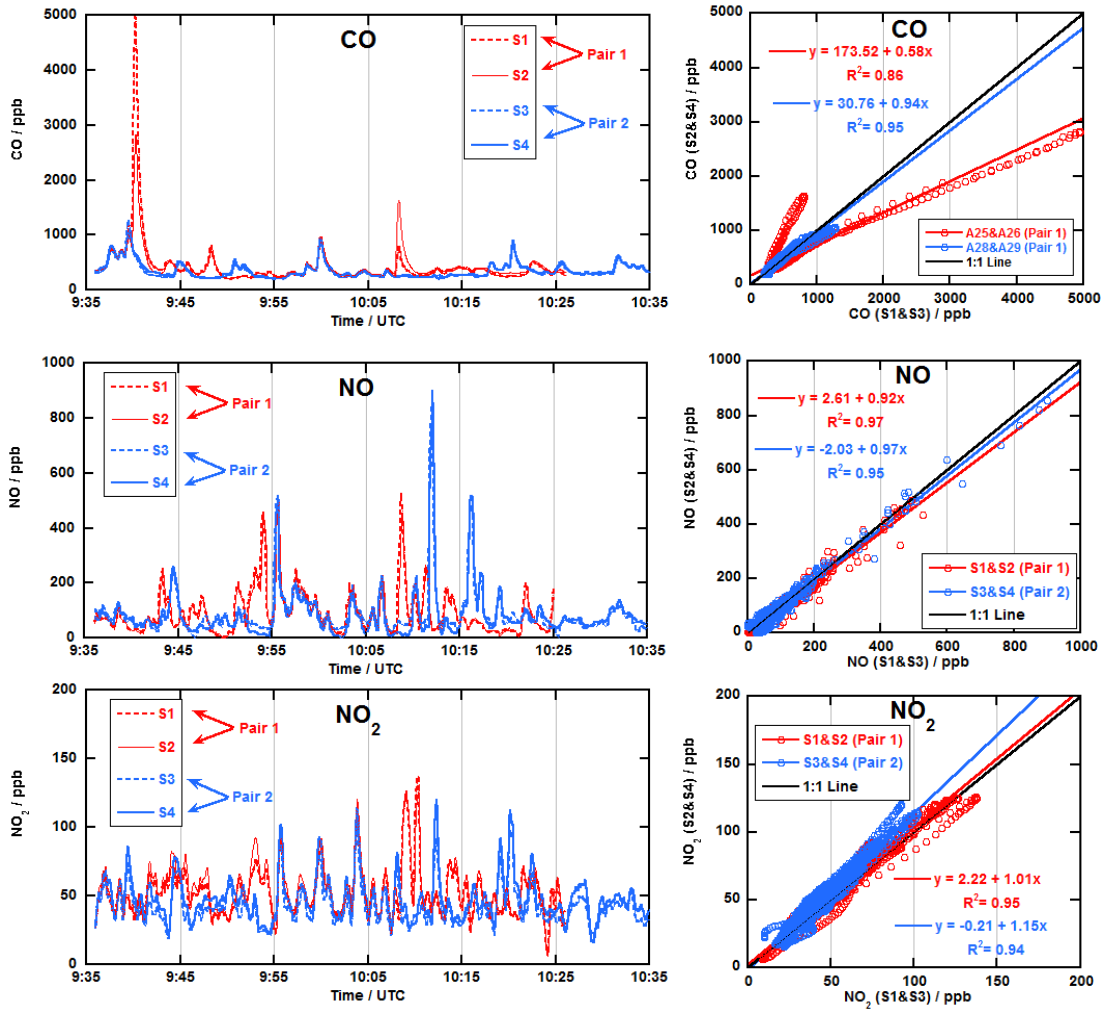

Figure 6.2. Time series and correlation plots of CO, NO and NO_2 mixing ratios for the two pairs of mobile sensors deployed in part of central Cambridge city centre.

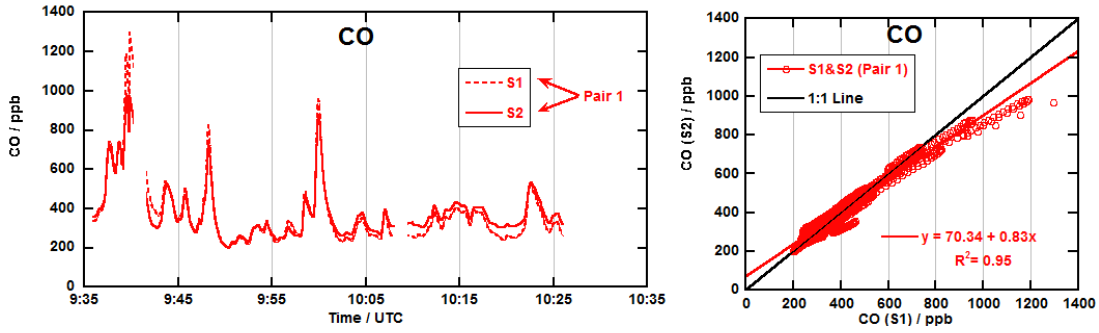

Figure 6.3. Time series and correlation plots of CO mixing ratios for pair 1 (S1 and S3) mobile sensor nodes deployed in part of central Cambridge city centre. Note the two peak events around 09:40 and 10:08 has been removed from these plots (cf. CO plots in figure 6.2)

The varying mixing ratios of CO, NO and NO_2 are related to proximity of the sensor nodes to different traffic sources along the deployment route. This spatial variability is represented in the KML[18] plot in figure 6.4. Elevated mixing ratios were observed close to cross-roads where there is often a build-up of static traffic. Also noticeable in fig 6.4 is the high NO mixing ratios around the bus station which might be related to different vehicle sources in this case high volume of buses and coaches in this area.

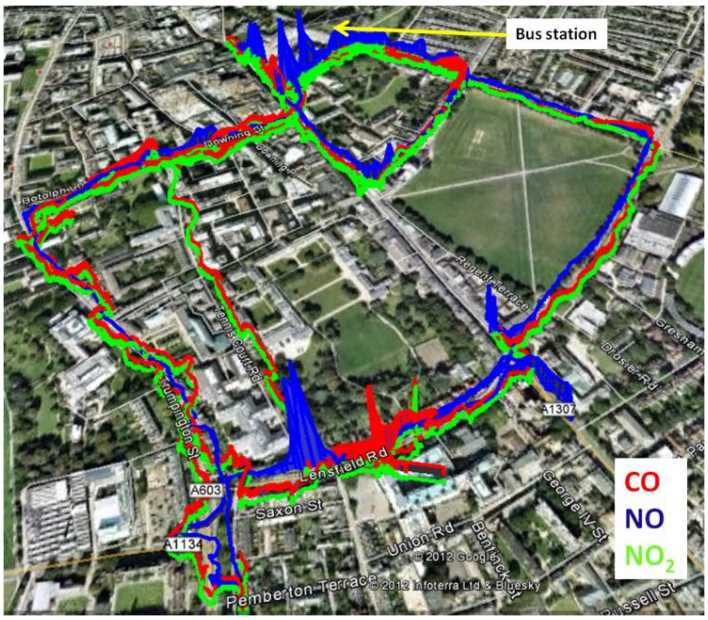

Figure 6.4. Plot showing spatial variability in mixing ratio of CO, NO and NO_2 in Cambridge part of city centre for all four mobile sensors. Heights of the trace are proxy for mixing ratios. Note the elevated NO_X mixing ratios around the bus station and junctions between busy roads. Map courtesy Google Earth [80].

[18] KML refers to Keyhole Markup Language which is used to generate geographic and visualised annotations in two or three dimensional internet based Google earth maps.

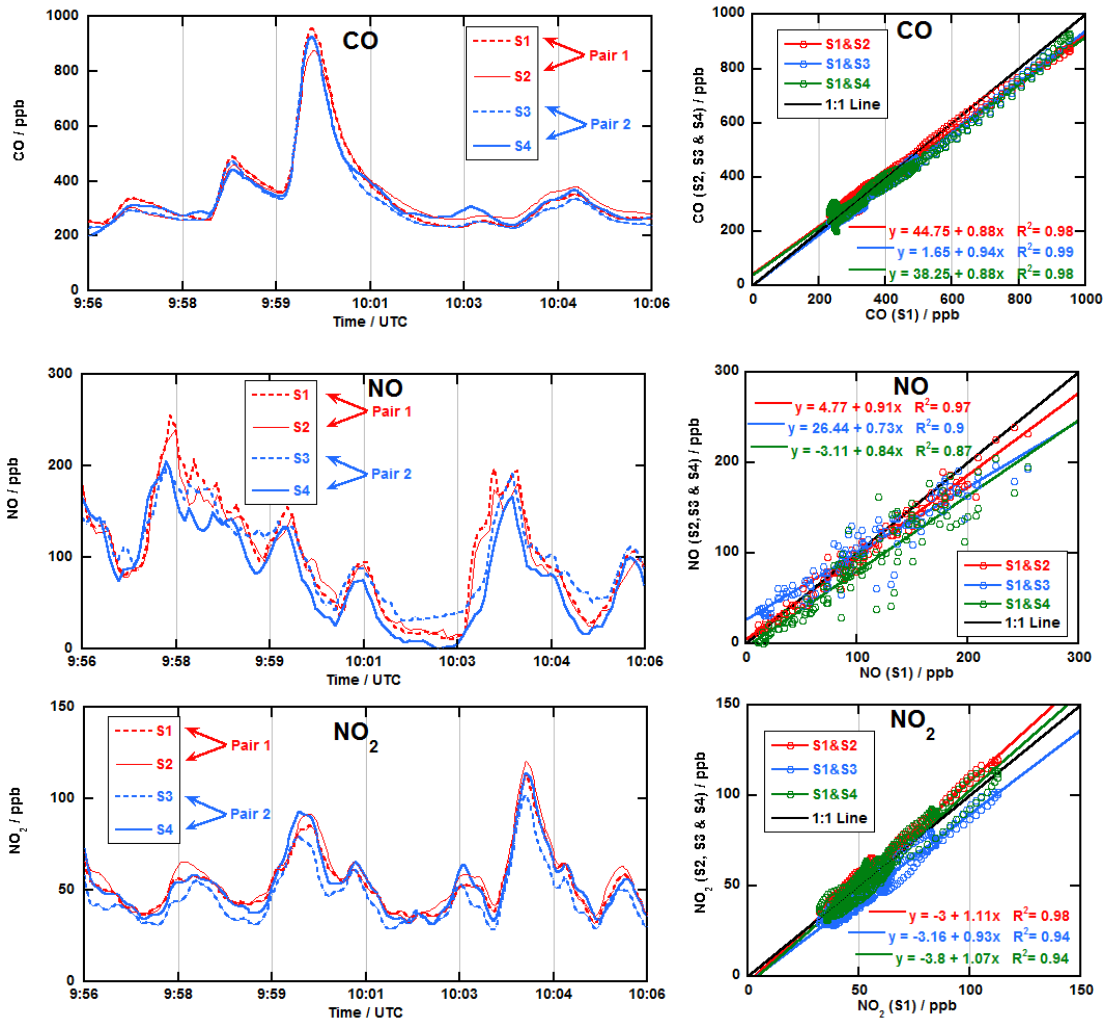

Figure 6.5. Time series and correlation plots of CO, NO and NO_2 mixing ratios for the co-location period (09:56–10:06) all mobile sensor nodes deployed in part of Cambridge city centre.

Figure 6.5 shows results of the co-location period when both pairs of sensor nodes were along the same route (purple track in figure 6.1). From the correlation plots, there is remarkable agreement between the similar pair (S1 & S2) and the different pair (S1 & S3, S1 & S4) for all three gas species (R^2 of 0.98-0.99 for CO, 0.87-0.97 for NO and 0.94-0.98 for CO). Though the two pairs of sensor nodes were carried by two pedestrians, they all detected changing mixing ratios of CO, NO and NO_2 over small time scale with good agreement.

Conclusions

The results from this study showed the field performance under ambient conditions (in terms of reproducibility, sensitivity and selectivity) of the CO, NO and NO_2 electrochemical sensor nodes was the same as observed under laboratory conditions (see chapter 4).

Spatial variability in air quality over short-time scales (seconds to minutes) was captured during this experiment and this is only possible because of the portability of the instruments. This trial indicated that targeted experiments like exposure studies can be planned using these electrochemical sensors because they can be easily deployed and the precision (sensor- to-sensor agreement) is very good.

6.1.1.2. Cambridge mobile sensor study (CASE 2): measurement of CO, NO and NO_2 mixing ratios along cyclist route.

Overview of deployment

The previous mobile field campaign has demonstrated the practical application of the mobile electrochemical sensor nodes for monitoring air quality gas species like CO, NO and NO_2. While spatial variability of the air quality was observed during the campaign, source attribution was difficult as there was no video or picture record during the deployment. This deployment was aimed at identifying roadside pollution sources in addition to quantifying typical air pollution exposure experienced by a cyclist. Two mobile sensor nodes monitoring CO, NO and NO_2 were used for this study. One was strapped onto a backpack representing shoulder-high level (1.5-1.6 m) measurements (typical exposure height of an adult cyclist) while the other sensor node were secured at waist-height (1 m) (representing the exposure height of a young child cyclist). The vertical distance between the two sensors was about 50-60 cm. In addition to the sensor nodes, a video camera was also deployed during the campaign. The entire deployment which lasted an hour and twenty minutes (08:32-09:55), was designed to include the morning rush hour. The cycle route was planned to include major roads, streets and green parks within Cambridge city centre as depicted in figure 6.6.

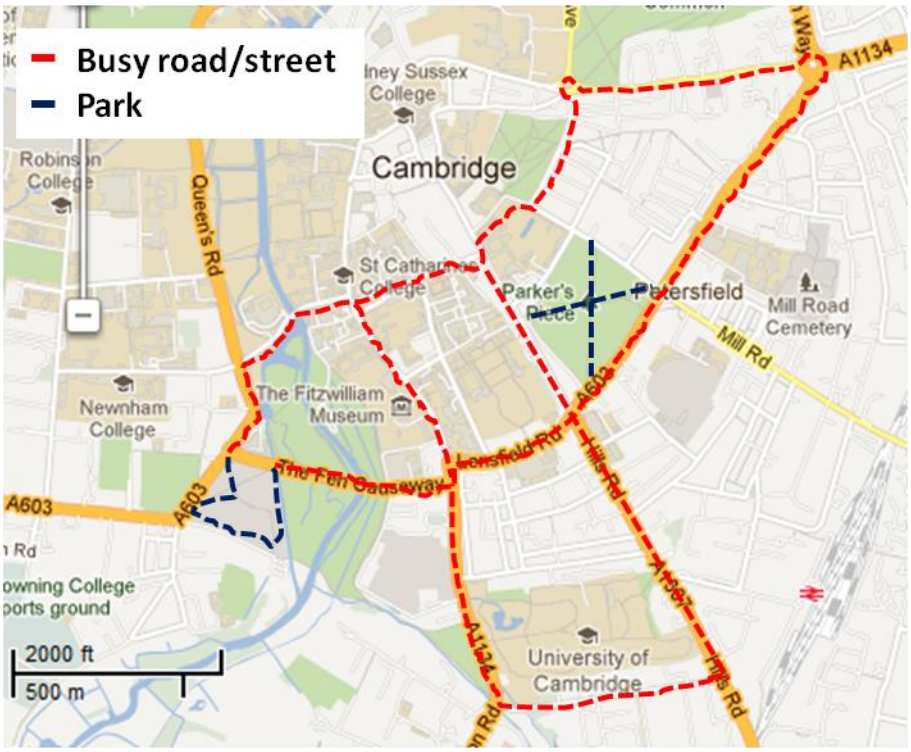

Figure 6.6. Map of Cambridge city centre showing cycle route for the cyclist pollution exposure experiment at Cambridge, UK. Map courtesy Google Map [81]

Results and discussion

Time series of the CO, NO and NO_2 measurement during the experiment are shown in figure 6.7. There is large scale variability in mixing ratios of the gaseous species which are due to traffic volume and in some cases specific pollution events due to particular vehicle type. The purple area in the plot represents pollution due to static traffic. This event was observed in CO, NO and NO_2 measurements. In contrast, the second high pollution event in CO around 08:50 was not recorded in the NO, NO_2 measurements. From the video log, this was likely due to the sampling of the exhaust of a particular car (fig. 6.7). Similarly, the maximum NO event (at 09:25) was recorded when the cyclist went past a bus. This event was therefore likely to be due to sampling of primary NO in the exhaust of the bus and since there were no peak measurements in the other pollution gases being monitored (CO and NO_2), it therefore appears to be particular to this kind of vehicle (fig 6.7). The peak measurement in NO_2 at 09:40 coincides with the period when the sensor nodes were behind a white van at a traffic junction (see fig 6.7). Low CO, NO and NO_2 mixing ratios were recorded when the cyclist was away from local pollution sources in this case at parks (green shades figure 6.7) and the

fact that this was noticed in all three gas species further links the pollution events to traffic sources.

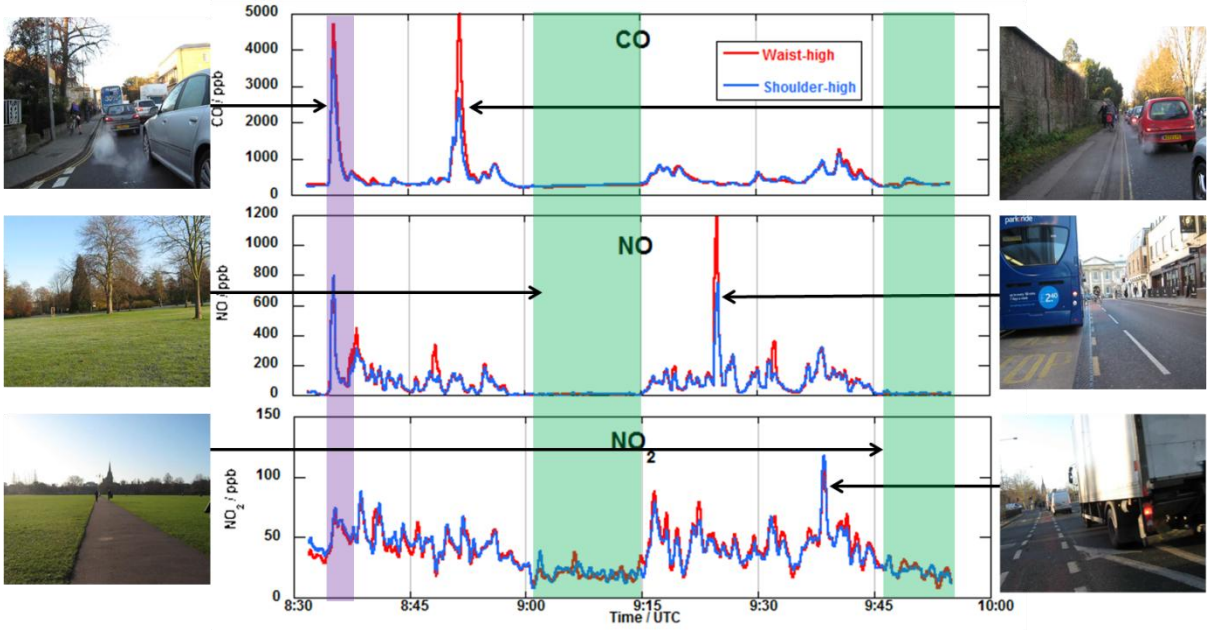

Figure 6.7. Time series of the CO, NO and NO_2 mixing ratios for the cyclist pollution exposure experiment at Cambridge, UK. Some key pollution events and their sources are also shown.

The exposure levels at different heights (waist and shoulder level) were also determined for this deployment. Shown in figure 6.8 is histogram of the distribution for the sensor at waist and shoulder heights. The probability distribution plots for CO, NO and NO_2 were similar for the two sensor nodes. Although two modes can be seen in the NO_2 probability plot for the two sensor nodes, the modal mixing ratio for the waist-high sensor was between 15-20 ppb compared to a range of 20-25 ppb for the shoulder-high sensor. This plot shows that the height difference has little effect on the most likely exposure level (modal range) for a cyclist at the low mixing ratio region of the probability distribution. If however the high mixing ratio regions are considered (an indication of short-term exposure to elevated mixing ratios of these gas species), then the height difference becomes very significant.

Table 6.1 summaries the statistics for the two sensor nodes deployed based on height. Except for NO_2 species that has similar mean mixing ratios for the two sensor nodes (38.1 ppb for waist-high and 38.0 ppb for shoulder-high sensor), the values were 500 ppb for CO and 84.0 ppb for NO (waist-high sensor) compared to 460 ppb for CO and 77.0 ppb for NO

(shoulder-high sensor). This comparison shows that for the entire duration of the deployment, the waist-high sensor recorded higher mean mixing ratios compared to the shoulder-high sensor especially for CO and NO species. The percentage difference between the waist-high and shoulder-high sensors for the mean mixing ratios was ≈ 10% for both CO and NO and insignificant for NO_2. Although this value appears small it becomes relatively important when high pollution events are experienced. By using the maximum mixing ratios events as proxy for high pollution events, the percentage difference between the waist- and shoulder-high sensors were 20% for CO and 30% for NO. A negative percentage difference (-10%) was observed for the NO_2 difference and this is small relative to the values obtained for CO and NO. The result shows that NO_2 was the least varying species in terms of mixing ratios at the height distance considered in this study. The standard deviation of NO_2 mixing ratios was 16.4 ppb (waist-high) and 16.0 ppb (shoulder-high) compared to CO of 540 ppb & NO of 116 ppb (waist-high) and values of 381 ppb (CO) & 93 ppb (NO) at shoulder heights.

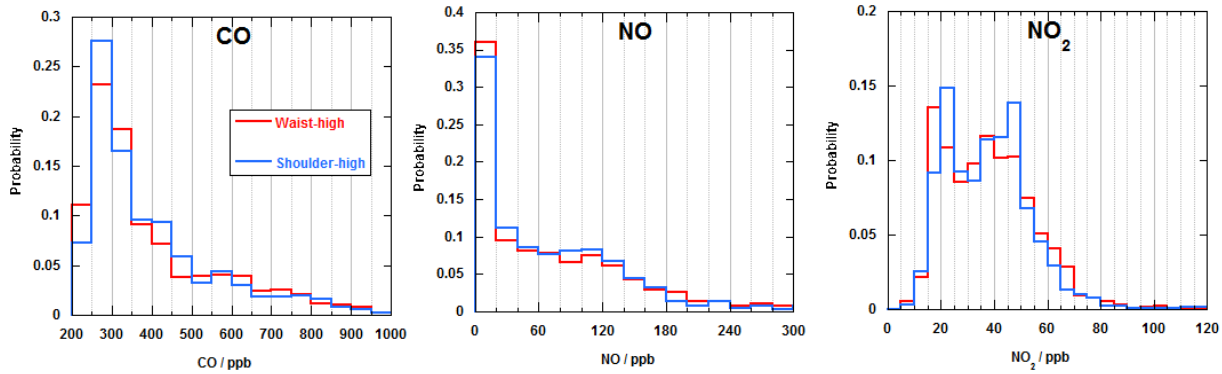

Figure 6.8. Probability distribution plots of CO, NO and NO_2 for the two sensor nodes used during the cyclist pollution exposure experiment at Cambridge, UK. Very high mixing ratio data of CO (> 1000 ppb) and NO (> 300) are not shown in this plot as there are few data for these events.

Table 6.1. Statistics table for the exposure study at different heights for the entire deployment.

	Waist-high sensor			**Shoulder-high sensor**		
	CO	NO	NO_2	CO	NO	NO_2
Mean / ppb	500	84.0	38.1	460	77.0	38.0
Max / ppb	5.00×10^3	1.2×10^3	106	4.00×10^3	0.80×10^3	117
Standard deviation / ppb	540	116	16.4	381	93.0	16.0
95% CI	15.1	7.21	0.46	10.8	5.84	0.44

Conclusions

The application of electrochemical sensors in studying personal exposure of a cyclist under different environment has been shown in this section. There is significant difference in measurements along the road and along cycle parts in parks. Certain routes can also potentially leave the cyclist exposed to elevated mixing ratios of certain gas species which are emitted as primary source in exhaust of the vehicle. For instance, elevated NO mixing ratios were recorded when the cyclist went past a bus.

This experiment was also used to quantify the level of pollution exposure experienced by a cyclist at different heights (waist-high and shoulder-high levels). While the probability distribution pattern for the CO, NO and NO_2 species during the experiment are similar for both waist and shoulder height levels, the overall mean mixing ratios show significant higher exposure level (at 95% confidence interval) at waist height especially for CO and NO compared to shoulder height. This is expected given the proximity of the waist-high sensor to the exhaust plumes of vehicles during the deployment.

6.1.2. Measurement of primary CO, NO and NO_2 from road sources in Lagos, Nigeria

6.1.2.1. Introduction

This section describes the campaign conducted in November 2010 in Lagos, Nigeria (Sub-Saharan Africa) using novel low-cost electrochemical sensor nodes to characterise the air quality in one of the world's fastest growing mega-cities. The study show results from two zones in the city: (1) a background site on an island and (2) city centres at this site and on a mainland location in Lagos.

6.1.2.2. Background

Air quality is increasingly becoming the major problem in developing countries where there is increasing population residing in city centre. Therefore more people are at the risk of being exposed to air pollution and subsequently suffer from related health effects. In response to this growing concern on poor AQ, the Nigerian federal government through a decree in 1988 established the Federal Environmental Protection Agency (FEPA) Act which was responsible for establishing air quality standard across the country. The FEPA Act was replaced by the NESREA Act [97] through the establishing of the National Environmental Standard and Regulation Enforcement Agency (NESREA) in 2007 and all functions of FEPA was transferred to this agency. However ambient air quality standards put in place by FEPA and subsequently NESREA only take into account pollutions from stationary sources and do are not apply to mobile sources, a major source of poor air quality in cities. Even with these regulations there is no established air quality monitoring network in any of the cities across the Country. Following the smog event of 12th October 2005 in Lagos [98], the local authorities in Lagos state through LAMATA (Lagos Metropolitan Area Transport Authority) facilitated the LAQMS (Lagos Air Quality Management Study) between February, 2007 and April, 2008. Although selected air pollution related studies have been conducted in some parts of the country like Calabar in the South East of Nigeria [99] and also in South-Western States (including Lagos) looking at environmental impact of road transportation [100], there are no record of studies looking at fine scale temporal and spatial variability of air quality within a city. This is partly due to the cost associated with conducting such studies (need of

expensive analytical instruments) and also the lack of high resolution portable air quality instruments.

Lagos is the largest city in Sub-Sahara Africa and the sixth largest in the world [101], with an estimated annual growth rate of 6 %. Road transportation is the main form of commuting within the city and this is made up of both public and privately owned vehicles. The fleet of vehicles ranges from petrol run cars to diesel operated duty vehicles, van and trucks [102]. Poor vehicle documentation means vehicles unfit for the environment (high pollution emitting vehicles) still end up as part of the transport network in the city. A large percentage of the population reside in the city centre and this number keeps increasing [103]. As a result, a large proportion of the population are facing increasing health risks resulting from road transport related pollution.

This field campaign was aimed at characterising air quality by measuring mixing ratios of CO, NO and NO_2 from roadside sources and comparing results for two environments using novel electrochemical air quality sensors. This study represents the first attempt to characterise high resolution spatial variability of these gaseous species in Lagos, Nigeria.

6.1.2.3. Study Location

A field campaign was conducted on 23rd November, 2010 in Lagos (South West, Nigeria). Two locations within the city were chosen for this study. Site 1 (Victoria Island) is located on an island in the city (fig. 6.9) while Oshodi (site 2) is located in mainland Lagos. At site 1, measurements were taken at a beach (blue track in fig 6.10) for a period of two and a half hours to give background levels after which measurements were made along the streets and major roads in the nearby city centre (red track in fig 6.10) for approximately 45 minutes. Victoria Island is the financial district in Lagos and when Lagos was the capital of Nigeria, major companies had headquarters located in this part of the city [102]. In contrast, site 2 (Oshodi) is the busiest city in mainland Lagos (fig 6.11) and serves as transit point by road for major destinations within Lagos. The areas covered at site 2 (Oshodi) include part of busy expressway (Agege Motor road), quiet roads / streets (e.g. Oshodi Road) mainly used by small vehicles and a flyover (Apapa Oworonshoki Express way) connecting Oshodi to neighbouring towns. The entire deployment lasted approximately three hours which included the morning rush hours. Area of interest in site 2 included Lagos Bus Rapid Transit

system (BRT) bus station, old bus transit parks (which house fleets of second hand midi-buses locally known as *Molue*), side street leading to an open markets and a side road (fig 6.11).

Figure 6.9. Map of Lagos showing the two deployment sites: Victoria Island (site 1) is part of the islands that make up Lagos while Oshodi (site 2) is located in mainland Lagos. Also shown is the relative distance between these sites and the prevailing wind direction. Map courtesy Google Map [81]

Figure 6.10. High resolution map of Victoria Island showing sampling routes for deployment on 23rd November, 2010. Map courtesy Google Map [81]

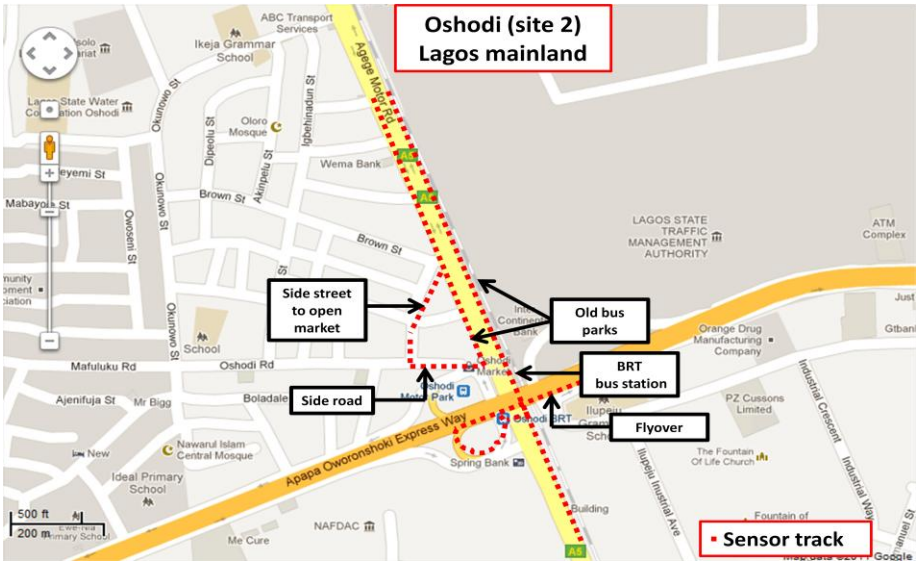

Figure 6.11. High resolution map of Oshodi showing sampling routes for deployment on 23rd November, 2010. Also shown in the map are areas of interest at this test location. Map courtesy Google Map [81]

6.1.2.4. Results and Discussion

Data processing

Two pairs of mobile sensor nodes (S7 & S12 Oshodi and S8 & S10 Victoria Island) measuring CO, NO, NO_2 and temperature were used in this study. Measurements made at the beach in site 1 were used as background reading because this area was far away from traffic sources. The NO data was corrected for baseline-dependent temperature changes using the methodology described in chapter 4. All data presented here are 30 s averaged data in line with the response time (t_{90}) of the sensors which on average is < 30 s. Background mixing ratios of 200 ppb, 8 ppb and 2 ppb [104] were added to the rebased CO, NO and NO_2 data. One of the NO_2 sensors used at the two sites failed during the deployment and only results from one sensor at each site will be shown for this species. All time are reported in UTC, the local time is UTC+1 and the morning rush hour[19] is between 06:00 – 07:00 UTC.

[19] Rush hour is defined as traffic peak period which is between 05:30 to 07:30 UTC (06:30 to 08:30 local time) for the morning period during weekdays in Nigeria.

Reproducibility of measurements

Results of the CO and NO measurements showed good reproducibility for the pair of sensor nodes used in this study. A correlation coefficient (R^2) of 0.99 was recorded for CO and NO in Oshodi (fig. 6.12). Similarly, the R^2 values were 0.99 (CO) and 0.92 (NO) for the measurements made in Victoria Island (fig. 6.13). The significance of these duplicate measurements is seen when peak events are observed. For instance, the high CO mixing ratio (~146 ppm) recorded in Oshodi (at approximately 06:16 UTC) was seen in the measurements of the two sensor nodes (fig. 6.12). This suggests that this event was not an anomaly and must be due to a local source (e.g. vehicular emission). On further analysis it was found that this event was actually due to sampling of the exhaust plume of an old commercial bus which is part of the fleet of commercial vehicles constituting the city's road transport system. Similarly, peak events in NO mixing ratio measurements (~ 08:18 in Oshodi) and (08:50 in Victoria Island) were seen by both sensor nodes deployed at these sites (figures 6.12 and 6.13).

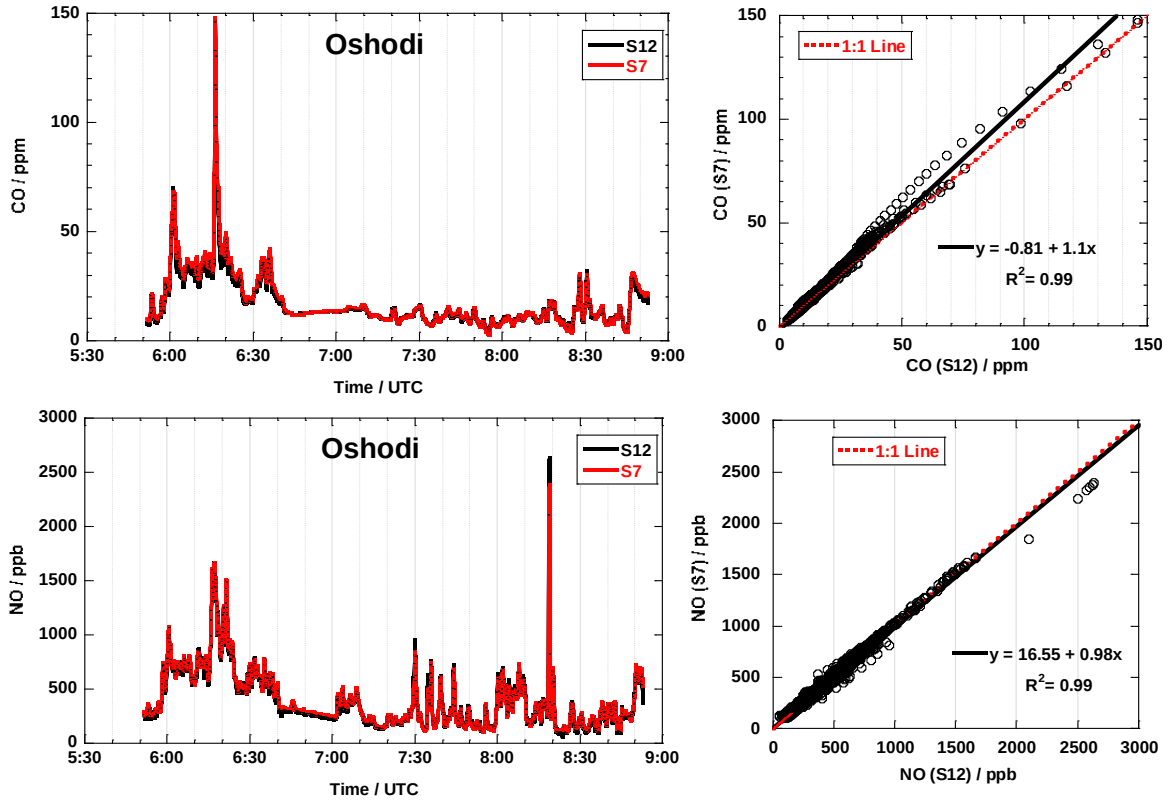

Figure 6.12. Time series and correlation plots for CO (top panels) and NO (bottom panels) for the pair of sensor nodes deployed in Oshodi, Lagos on 23rd November, 2010.

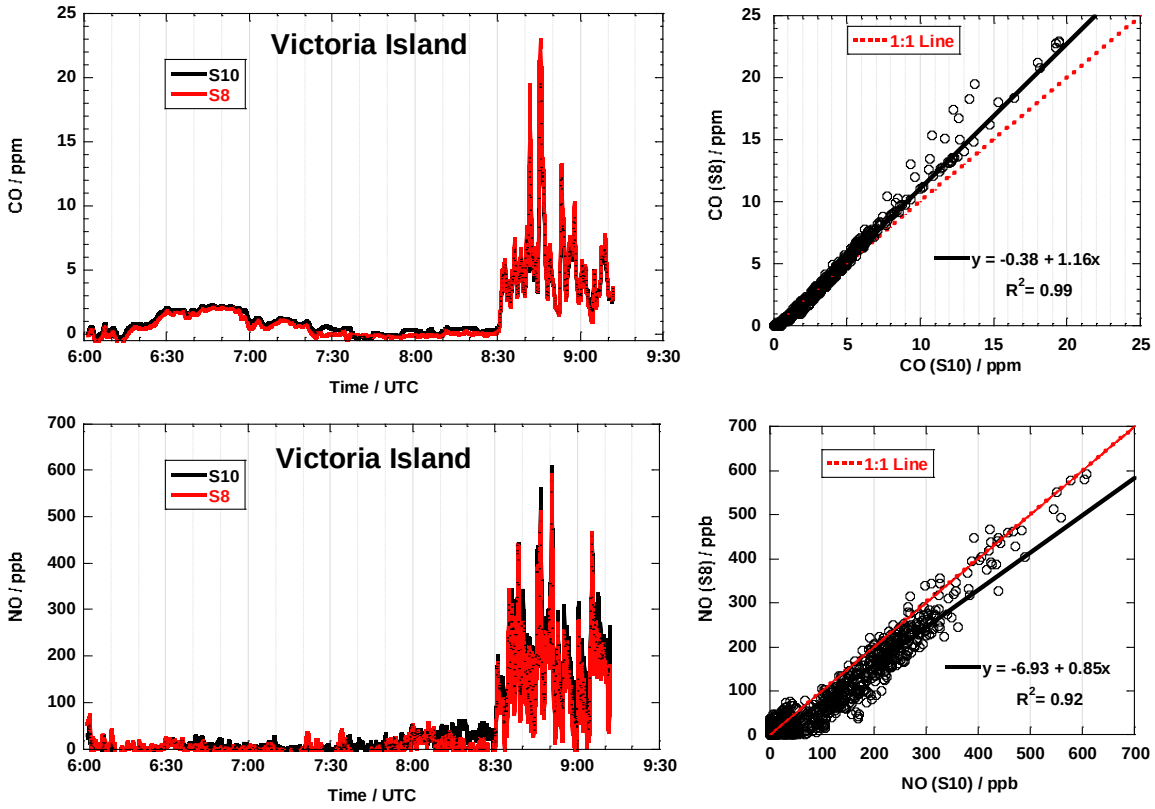

Figure 6.13. Time series and correlation plots for CO (top panels) and NO (bottom panels) for the pair of sensor nodes deployed in Victoria Island, Lagos on 23rd November, 2010.

Overall result: coastal and city centre measurements

The average CO, NO and NO_2 mixing ratios for period (06:00 – 08:30) spent at the beach were 0.80 ppm, 8.0 ppb and 8.0 ppb respectively. In contrast, corresponding mean mixing ratios in the city centre (08:30 – 9:12) in site 1 were 4.80 ppm, 200 ppb and 21.0 ppb. Results from site 1 (Victoria Island) therefore show relatively low mixing ratios at the beach compared to the neighbouring city centre (fig. 6.12). The sudden change in mixing ratio levels noticed after 08:30 coincides with the period when measurements were being made within the city centre. This increase in mixing ratio of all three species is attributed to emissions from road traffic sources an indication of spatial variability of AQ going from clean background (beach) to city centre. This variability is shown in the spatial plot for site 1 (fig. 6.14).

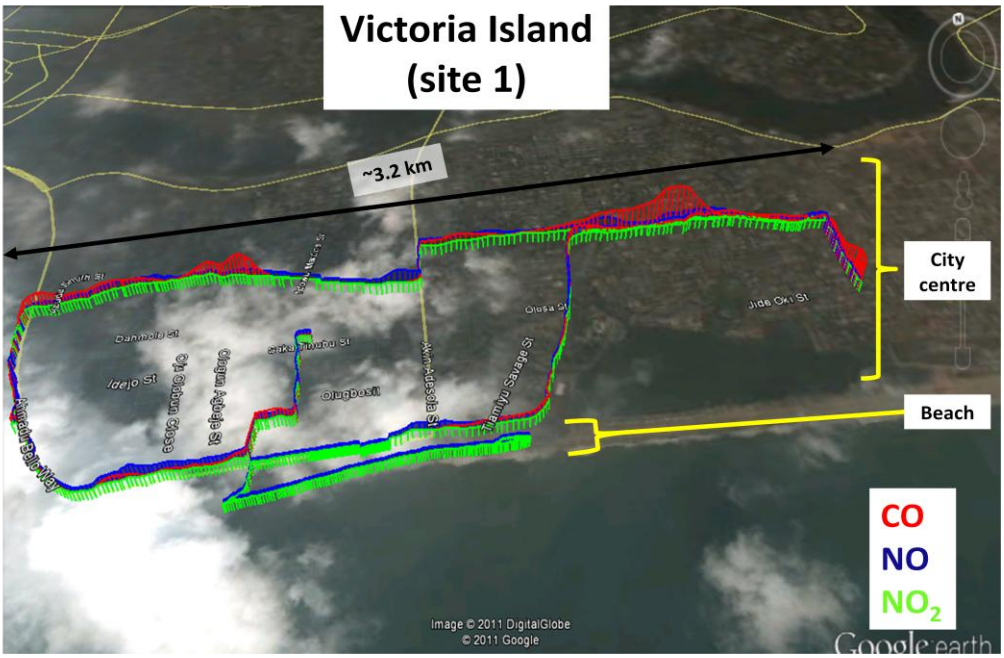

Figure 6.14. Plot showing spatial variability in mixing ratio of CO, NO and NO_2 in Victoria Island, Lagos on 23rd November, 2010. Heights of the trace are proxy for mixing ratios. Map courtesy Google Earth [80].

Although the mixing ratios of CO, NO and NO_2 are spatially variable in Oshodi (site 2) as shown in figure 6.15, the overall mean mixing ratios for these air quality (AQ) gaseous species are higher than those recorded in Victoria Island (site 1). The mean mixing ratios for CO, NO and NO_2 for the entire duration (05:51 – 08:49) of the deployment in this location were found to be 16.7 ppm, 390 ppb and 92 ppb respectively. These mixing ratios gives a broad picture of the relative pollution level in Oshodi, however this does not represent the small scale variability of AQ in Oshodi. A better understanding of the spatial variability of AQ is seen by considering mean mixing ratios at specific locations of interest. The mean mixing ratios for the time spent at the BRT bus station (06:41 – 08:11) were 11.49 ppm, 290 ppb and 120 ppb for CO, NO and NO_2 (fig. 6.15). These were relatively smaller compared to mean mixing ratios recorded at the old bus park (08:12 – 08:21) which were 12.3 ppm (CO), 450 ppb (NO) and 110 ppb (NO_2). A possible reason for this large difference is the different fleets of vehicles present in these two locations. While the BRT station composed of mainly new buses, the old bus park has a mixture of second hand mini buses and commercial vans which are classified as heavy emitters because of their age and poor combustion efficiency. On the side road leading to the motor way (fig. 6.15), the mean CO, NO and NO_2 mixing

ratios were 18.1 ppm, 220 ppb and 71.0 ppb respectively. The lowest mean mixing ratios (CO of 6.8 ppm for CO, 107 ppb for NO and 44.0 ppb for NO_2) were recorded for time spent (08:22 – 08:25) on a side street leading to an open market (fig 6.15). A possible reason for this low mean mixing ratio is that the side road is mainly used by pedestrian and petrol powered motorcycles.

Except for NO_2 (45.0 ppb), the highest mean mixing ratios for CO (29.6 ppm) and NO (680 ppb) were recorded during the morning rush hour (05:51 – 06:40) where the measurement were taken along the Agege Motor Road and on the Flyover (fig 6.15). Although the morning rush hour extends till about 07:30 UTC, between the period 06:41 and 08:11 measurements were made at a specific location (the BRT bus station fig. 6.15) and was therefore not included in the statistical analysis. A detailed temporal and spatial result for the rush hour period is shown in figure 6.16.

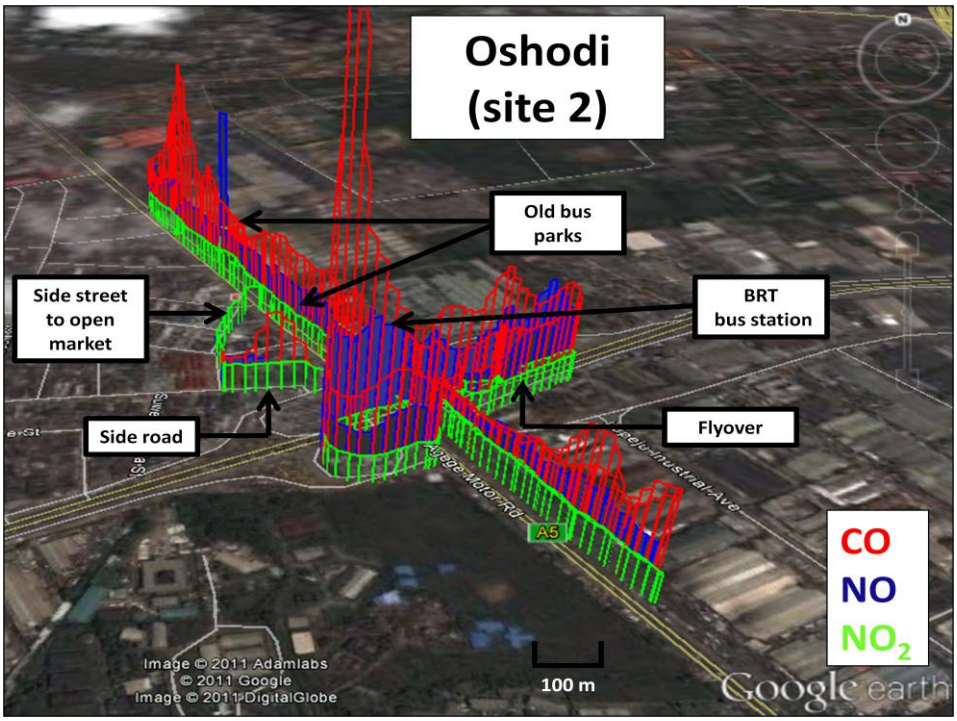

Figure 6.15. Plot showing spatial variability in mixing ratio of CO, NO and NO_2 in Oshodi, Lagos on 23rd November, 2010. Heights of the trace are proxy for mixing ratios. Map courtesy Google Earth [80].

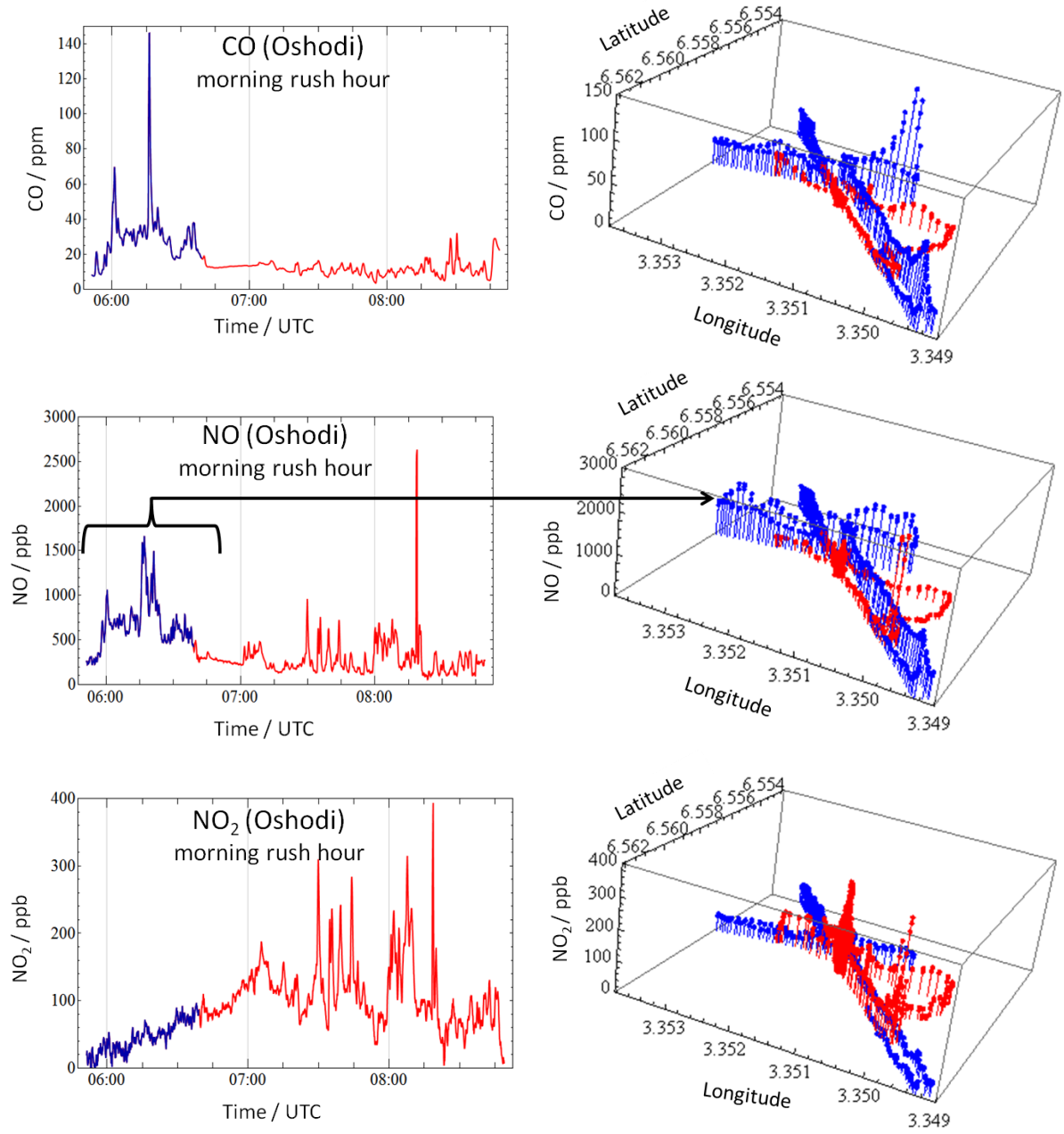

Figure 6.16. Temporal and spatial variability of CO, NO and NO_2 mixing ratios in Oshodi, Lagos during the morning rush hours on 23rd November, 2010. The blue line represents measurements during morning rush hour and the red line shows measurements after this period.

Statistical Comparison between Roadside Victoria Island and Roadside Oshodi.

The statistical comparison of roadside measurements between the two sites was performed using the period when the volunteer was in the city centre in the Victoria Island (08:30 –

09:12) and for the entire deployment period in Oshodi (05:51 – 08:50). The period spent at the beach (site 1) was excluded from this comparison because it does not contain roadside measurements and will otherwise bias the analysis. The distribution patterns of CO and NO_2 centres around high modes (13-14 ppm for CO and 80-90 ppb for NO_2) in Oshodi while in Victoria Island the spread of the mixing ratios were around lower modes (3-4 ppm for CO and 10-20 ppb for NO_2) as shown in the histogram plots (fig. 6.17). Although the mode of NO mixing ratios lies between 200 – 250 ppb at the two locations, a second mode at higher mixing ratio (between 450 – 500 ppb) can be seen in the data from Oshodi (fig. 6.17). Statistics of measured mixing ratios of the three species at these sites in relation to national and international AQ standards are summarised in table 6.2.

While the overall mixing ratio distribution at Victoria Island is lower than Oshodi for all three species, the mean mixing ratio of CO (16.7 ppm) at Oshodi was almost twice the values set by national and some international standards (see table 6.2). Although the averaging time is different for these values in table 6.2 (8 hour averages for the standards compared to 45 min at Victoria Island and 2hrs 45mins at Oshodi), if the modal values were used as a measure of the typical exposure at the two sites, then the mixing ratios of CO at Oshodi (13-14 ppm) will be well above the recommended limits.

These differences in mixing ratios between the two sites and consequently air quality are ascribed to varying vehicle fleet and traffic volumes on the roads in these two locations. Oshodi is a very busy part of Lagos with almost every known vehicle type (diesel buses, petrol cars, petrol and diesel run vans) present on the roads. In contrast, a large numbers of the vehicles on the road in Victoria Island (the financial district in Lagos) are privately owned petrol cars. In addition, there is poor traffic management in Oshodi with a large number of second hand commercial diesel buses on the roads which have inefficient combustion engine and are high emitters of CO evident in the peak event noticed in the CO data (fig. 6.16). This is likely due to better traffic management in Victoria Island compared to Oshodi with restriction on the type of vehicles on the roads with relatively fewer second hand vehicles on the road compared to Oshodi.

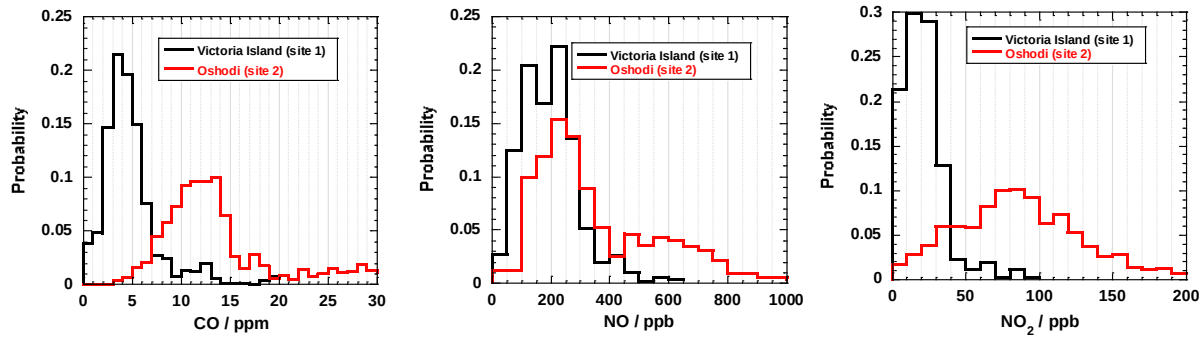

Figure 6.17. Probability distribution ensemble of CO, NO and NO_2 of roadside measurements in Victoria Island and Oshodi (mainland Lagos).

Table 6.2. Statistical summary for the roadside exposure levels at the two study sites (Oshodi and Victoria Island) in Lagos, Nigeria compared to some international AQ standards.

	CO / ppm		NO / ppb		NO_2 / ppb	
	Mean	Max	Mean	Max	Mean	Max
Roadside Victoria Island	4.8 (40 min)	19.5	200 (40 min)	0.61×10^3	21.0 (40 min)	90.0
Roadside Oshodi	16.7 (3 hr)	140	390 (3 hr)	2.60×10^3	92.0 (3 hr)	390
FEPA / NESREA [97]	10 (8 hr)	NA	NA†	NA†	100 (1 hr)	NA
WHO[20] [16, 33]	10 (8 hr) 25 (1 hr)	NA	NA†	NA†	105 (1 hr)	NA
EU / UK [35, 46]	8.7 (8 hr)	NA	NA†	NA†	105 (1 hr)	NA
NAAQS (US-EPA)[21] [36]	9 (8 hr) 35 (1 hr)	NA	NA†	NA†	100 (1 hr)	NA

NA means not applicable. † There are no standard limits for impact of NO pollution on human health. It is often regulated (as NO_X) for impact on vegetation and ecosystem.

Macro- and Micro-Meteorology

Temperature measurements from the mobile sensor nodes were used as a measure of micro-meteorology during the deployment. Average temperature data were generated from these measurements on the same time scale as measurement from meteorology station at the Murtala Muhammed international airport (DNMM 6.577 N, 3.321 E). The overall trend

[20] World Health Organisation (WHO)
[21] National Ambient Air Quality Standards (United States Environmental Protection Agency)

shows that the temperature measurements from the sensors were always higher (approximately 2.5 – 4.5 ^{o}C higher at the first half of the deployment and 2^{o}C at later half) compared to the macro temperature from met1 (figure 6.18). In addition, wind measurements from the meteorogical station shows that the wind condition was calm (0 ms^{-1}) to moderate breeze (4 ms^{-1}) blowing predominantly from the westerly direction throughout the duration of the deployment as seen in the polar plot in figure 6.18. This mild weather conditions suggests the observed mixing ratios are dominated by roadside sources.

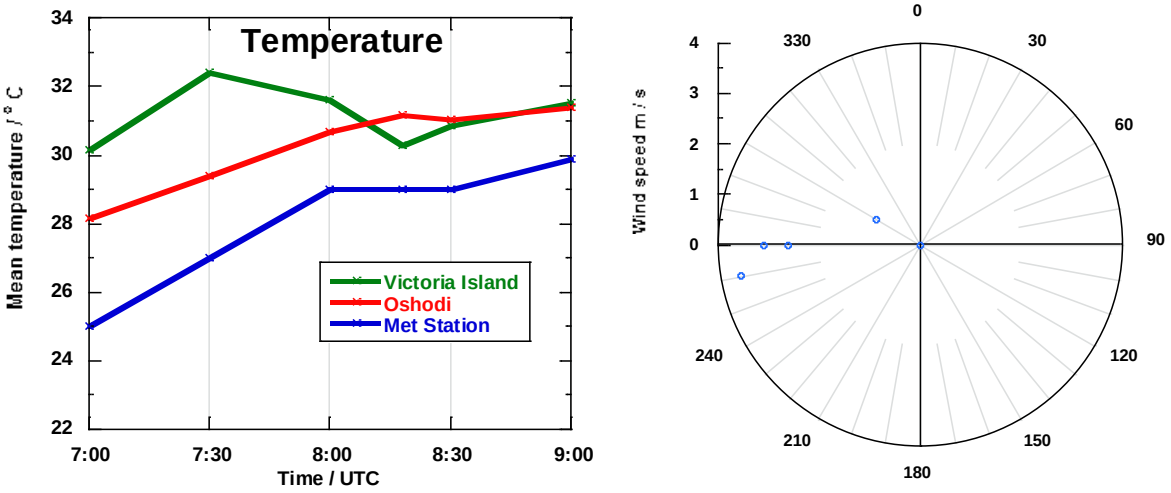

Figure 6.18. Plots showing time series of mean macro- and micro-temperature measurements and polar plot during the deployment. Individual points in the polar plots represent half hourly wind measurements.

Conclusions

This is the first deployment utilising low-cost mobile electrochemical sensor nodes for air quality studies in Lagos, Nigeria. The test areas were coastal site on an island (Victoria Island) and the busiest mainland city centre in Lagos (Oshodi). Comparison of results from the two sites shows that mixing ratios of CO, NO and NO_2 were higher in Oshodi compared to Victoria Island. In addition, the overall mean mixing ratio of CO at Oshodi was well above the recommended national and some international standards. Results from meteorological data shows that wind condition during the deployment was mild hence long range transport effect is negligible. Consequently, measurements were characteristic of local AQ which is dominated by local transport sources.

In conclusion, results from this campaign show how air quality is highly variable both in space and time within the city. This variability is likely to due to traffic volume, vehicle type and proximity to pollution source. It also shows that the CO level in Oshodi, Lagos exceeds both national and international standards.

6.2. Long-term measurement of CO and NO in Cambridge, 2010

The previous section in this chapter has focused on short-term deployment of mobile sensor nodes in urban environments. In this section, the long-term measurements using these sensor nodes will be discussed. The influence of meteorology and how wind parameters (like wind speed and wind direction) are used for source attribution will also be discussed.

6.2.1. Deployment area

As discussed in chapter five, a pair of electrochemical sensor nodes was deployed for a period of about six months between February and December, 2010 at Gonville Place Local Air Quality Network (LAQN) station in Cambridge, UK (52.199957 N, 0.127719 E). The LAQN is situated close to a cross road linking four busy roads in the city centre (Hills Road, Gonville Place, Regent Street and Lensfield Road) as shown in figure 6.19.

Figure 6.19. Location of the LAQN station at Gonville Place in Cambridge, UK where long-term measurements of CO and NO species were undertaken. Inset is the co–location of two electrochemical sensor nodes (housed in weather proof enclosures) with the chemiluminescence unit at the LAQN station. Image courtesy Cambridge City Council. Map courtesy Google Map [81].

Although the electrochemical sensor nodes measured three species (CO, NO and NO_2), only results from the CO and NO will be presented in this section. This is because the NO_2 measurements from these prototype mobile sensor nodes were very noisy. The Cambridge City Council Environmental Department has a chemiluminescence NO and NO_2 instrument at this site which makes it possible to compare NO measurements.

6.2.2. Data processing

The NO measurements for this deployment have been temperature corrected as discussed in chapter five and hourly averaged data were generated for both the CO and NO data. Local meteorological data were obtained from the Digital Technology Group (DTG) Weather Station in the Computer Laboratory Department, University of Cambridge.

Data analysis was done using openair, an air pollution analysis package written in the R programming language [105]. It is an open-source tool developed specifically for air pollution data analysis and it has the advantage that it utilises meteorology parameters like wind speed and direction to generate plots that can help identify long-range or local pollution sources. One very informative plot is the bivariate polar plot which shows the variation of pollution mixing ratio with wind speed and direction. Wind speed is represented by concentric circles where increasing speed is represented by increasing circumference as shown in fig. 6.22. In addition, time series can be generated as daily, weekly or monthly averages. This can be used to investigate weekend effect[22] on pollution mixing ratios.

6.2.3. Results and discussion

The CO and NO measurements from one of the electrochemical sensor for the entire duration of the deployment are shown in the time series in figure 6.20. Similarly, figure 6.21 shows high resolution plot of part of the deployment (2-29 September) for the pollution data (CO and NO) and some meteorology measurements.

In chapter 5, it was shown that a good correlation existed between the NO measurements from temperature-corrected electrochemical sensor and the chemiluminescence instrument. This agreement is also seen in the bivariate polar plot of the NO measurements from these two instruments (figure 6.22). High mixing ratio measurements (> 35 ppb) at low

[22] Weekend effect is defined as reduction in traffic volume due to less number of vehicles on the road compared to official working days of the week (or workweek) which is from Monday till Friday in the UK.

wind speed (< 5 ms^{-1}) from the south-east direction can be seen in both instruments. This suggests the presence of a local source when the wind is blowing from the SE direction relative to the LAQN station. Figure 6.23 shows the CO and NO bivariate polar plots from the electrochemical sensor and interestingly the elevated pollution from a source in the SE direction at low wind speed is seen in both gas species (> 500 ppb for CO and > 35 ppb for NO). This was attributed to pollution venting from Hills Road (see fig 6.19) which is located SE to the sensor location. Similarly, high mixing ratio events (500-550 ppb CO and 25-30 ppb NO), although relatively lower to that from the SE direction, were observed both in the CO and NO plots from the westerly and close to South-South Westerly (SSW) direction (figure 6.23). The former was attributed to pollution from the road westerly to the LAQN site (Regent Street) and the latter to Lensfield Road which is SSW relative to the monitoring station (figure 6.19). The contribution from these sources can also be characterised using days of the week as shown in figure 6.24. Interestingly, contribution from the SE becomes less noticeable on Sunday probably due to weekend effect relating to low traffic volume. The bus time table for Cambridge city show smaller overall journey time on weekends compared to weekday [106]. Weekday and weekend effects were further investigated by comparing several time series averaged over different timescales.

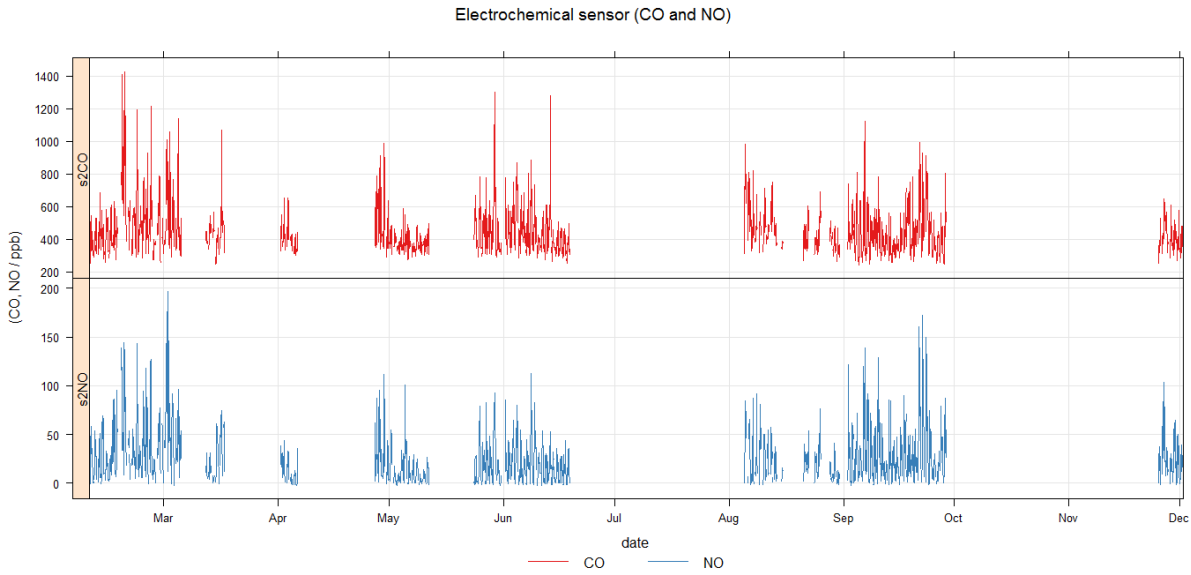

Figure 6.20. Time series of hourly mean CO and NO measurements of an electrochemical sensor at the LAQN in Gonville Place, Cambridge (February-December, 2010). Gaps in plot are periods when the electrochemical AQ sensors were not deployed.

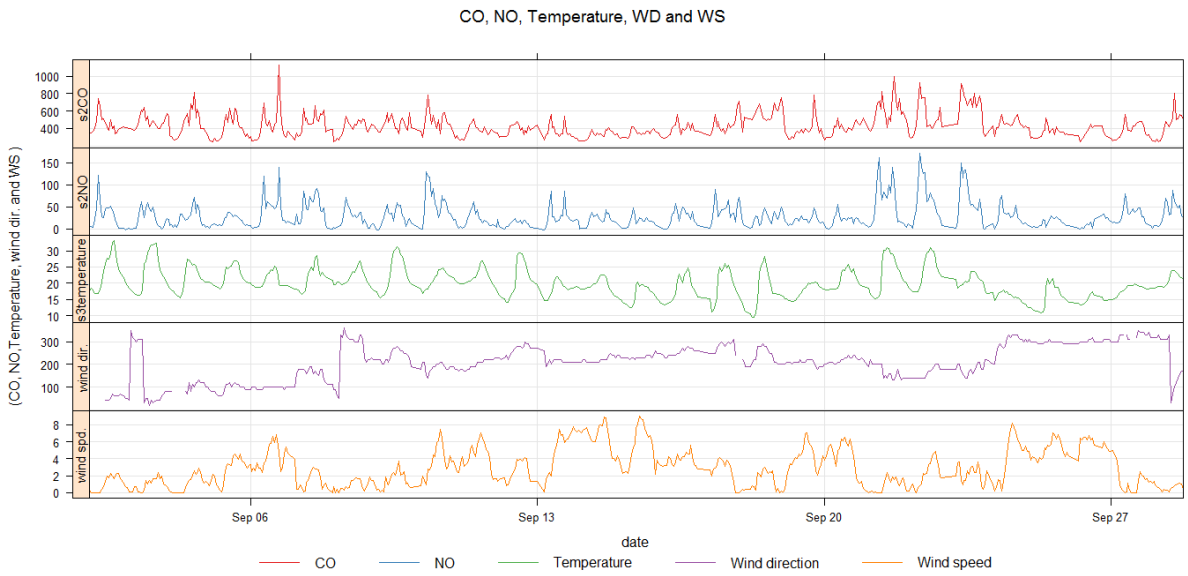

Figure 6.21. Time series of hourly mean CO, NO, temperature, wind direction and wind speed at the LAQN station in Gonville Place, Cambridge (2-29 September, 2010). Note the gaps in the wind direction plot correspond to values of very low wind speed when wind direction is therefore very difficult to measure.

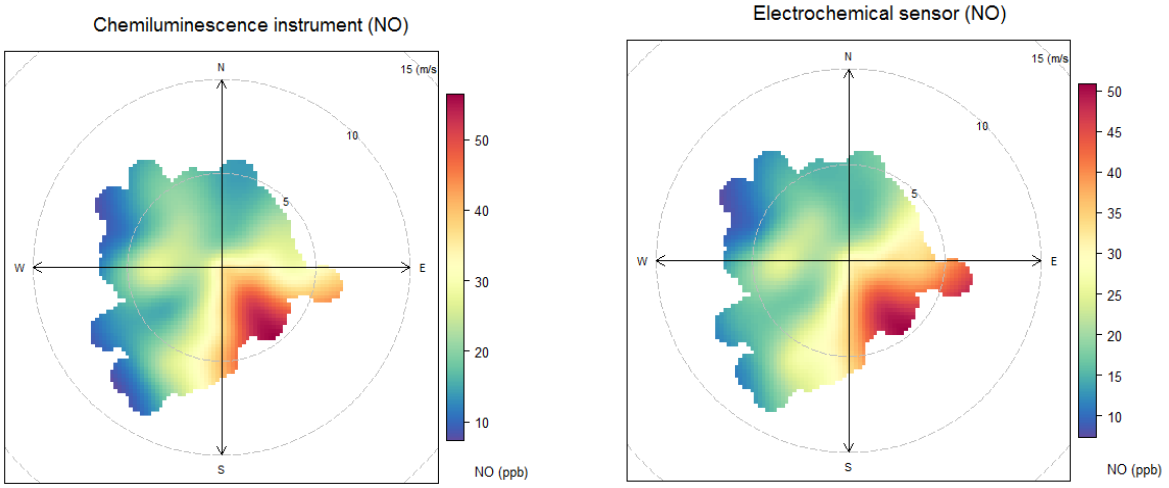

Figure 6.22. Bivariate polar plot comparing long-term hourly mean NO measurements between chemiluminescence and electrochemical sensor node at the LAQN station in Gonville Place, Cambridge (February-December, 2010).

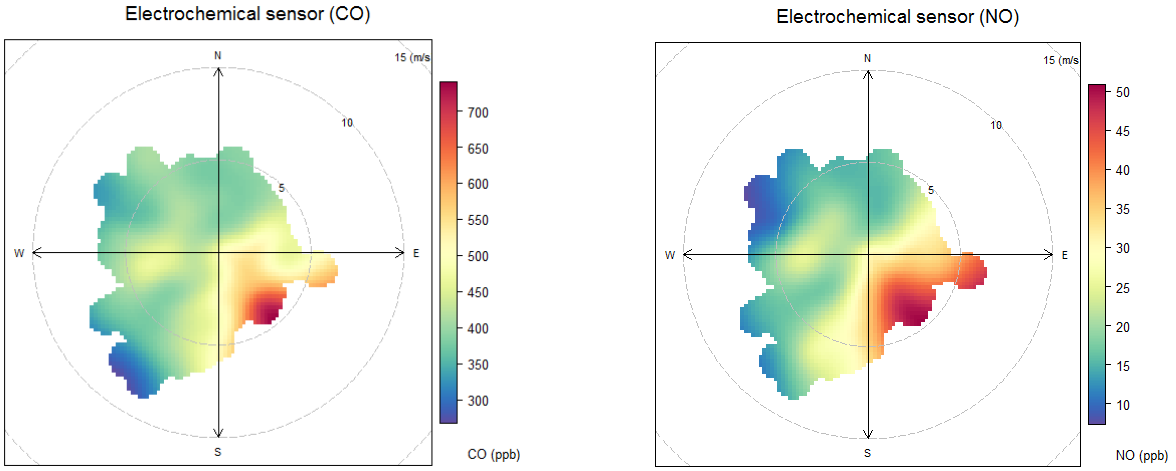

Figure 6.23. Bivariate polar plot of long-term hourly mean CO and NO measurements of an electrochemical sensor node at the LAQN station in Gonville Place, Cambridge (February-December, 2010).

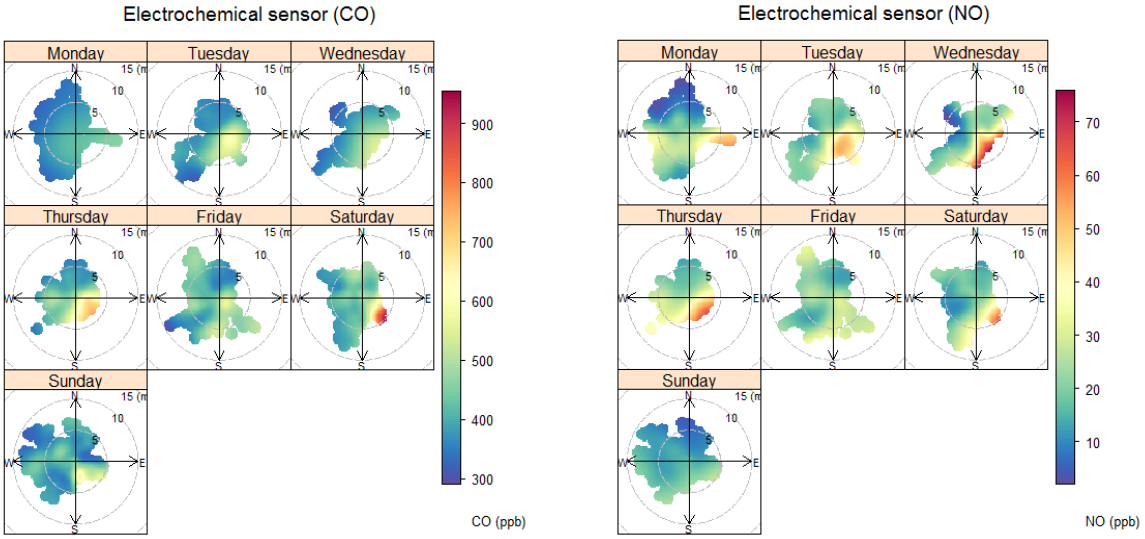

Figure 6.24. Bivariate polar plot by days of the week of long-term hourly mean CO and NO measurements of an electrochemical sensor node at the LAQN station in Gonville Place, Cambridge (February-December, 2010).

Figure 6.25 shows four unique time series comparing the NO measurements from the electrochemical sensor node and the chemiluminescence instrument. Time averages used are: (a) day of the week hourly averages for the entire deployment (fig 6.25 i), (b) overall hourly average for 24 hr for the entire deployment (fig 6.25 ii), (c) monthly averages for whole time period (fig 6.25 iii) and (d) mean daily mixing ratios for the whole time series (fig 6.25 iv).

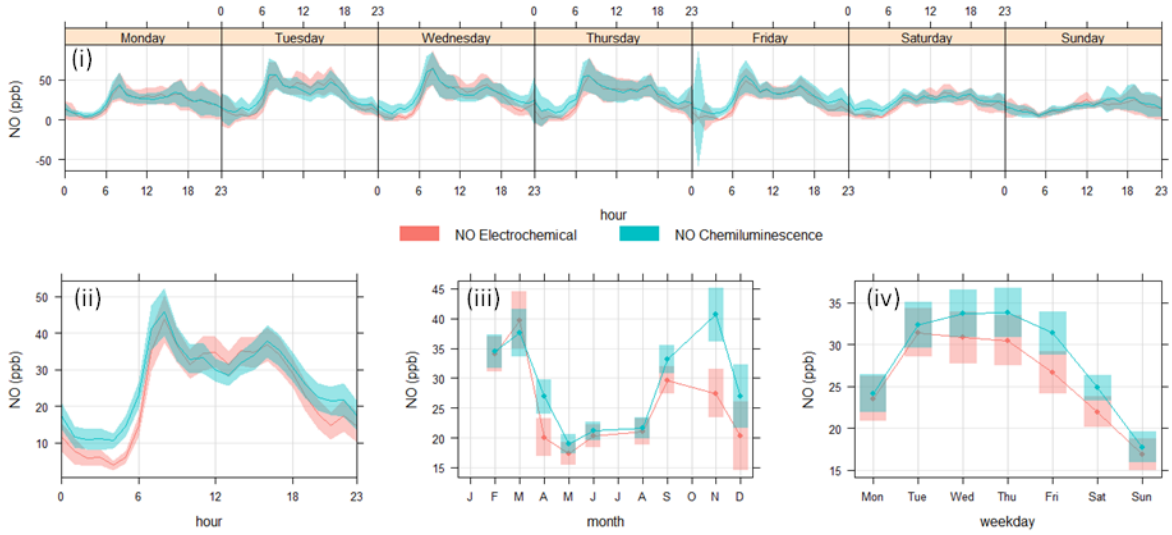

Figure 6.25. Four time series averaged over different time scales comparing the hourly NO mixing ratios between electrochemical and chemiluminescence instruments at the LAQN station in Gonville Place, Cambridge (February–December 2010). Note the shading represents 95 % confidence interval about the mean for each plot.

Except for the months of April and November in fig 6.25 iii, there is good agreement between the two techniques for the NO measurement irrespective of the averaging time. One possible reason for this slight deviation in these months is because there were fewer data gathered during these periods (figure 6.20) which affects the mean and associated error for this period. In spite of this, the overall trend is similar for NO measurements between the two instruments. Similar plots were generated for the CO measurements from the electrochemical sensor node. These plots together with those of NO from the electrochemical sensor node were used to characterise the CO and NO observations during the deployment as shown in figure 6.26(a-b). Figure 6.26 has been corrected for changing rush hour period due to daylight saving time (DST). This is important as the rush hour will be one hour earlier in winter compared to summer time in the UK under DST condition (all times shown here are in UTC). This has significant effect on the two peak events associated with the morning (0700 UTC) and the evening rush (1700 UTC) hour periods noticed in figures 6.26a (ii) and 6.26b (ii) which are relatively suppressed in the uncorrected data shown in figures 6.27a (ii) and 6.27b (ii).

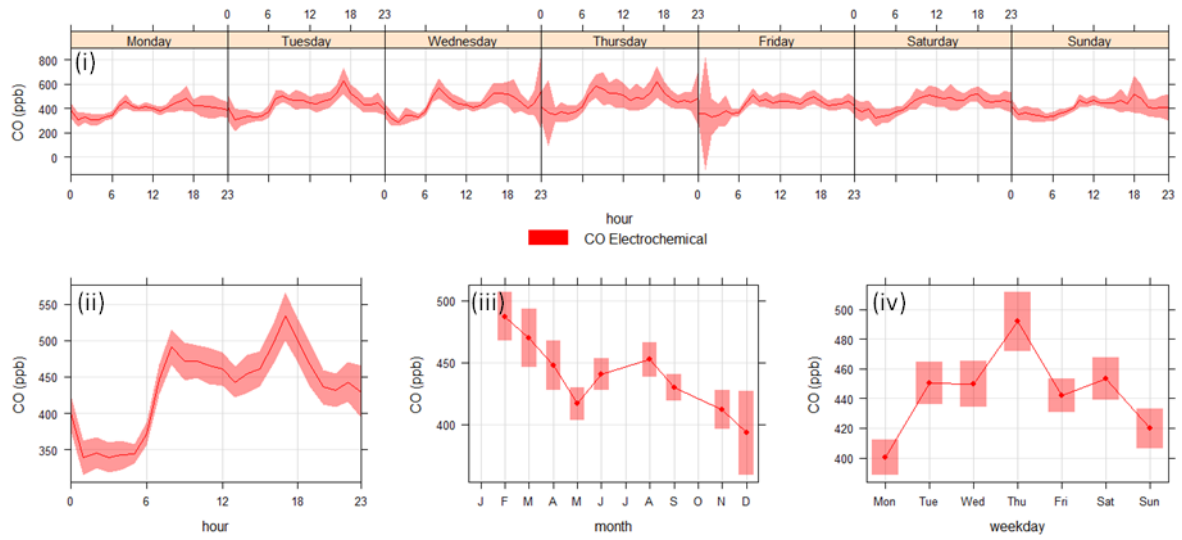

(a)

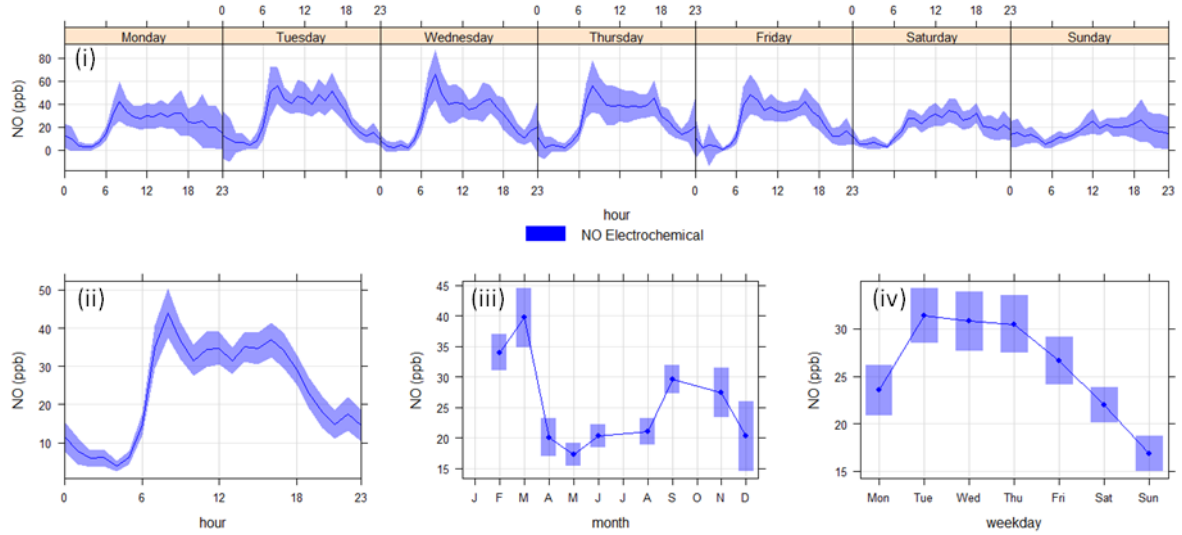

(b)

Figure 6.26. Time series plot corrected for change in rush hour time due to daylight saving time (a) Four time series averaged over different time scales of hourly CO electrochemical sensor mixing ratios at the LAQN station in Gonville Place, Cambridge (February–December 2010). (b) Four time series averaged over different time scales of the hourly NO electrochemical sensor mixing ratios at the LAQN station in Gonville Place, Cambridge (February–December 2010).

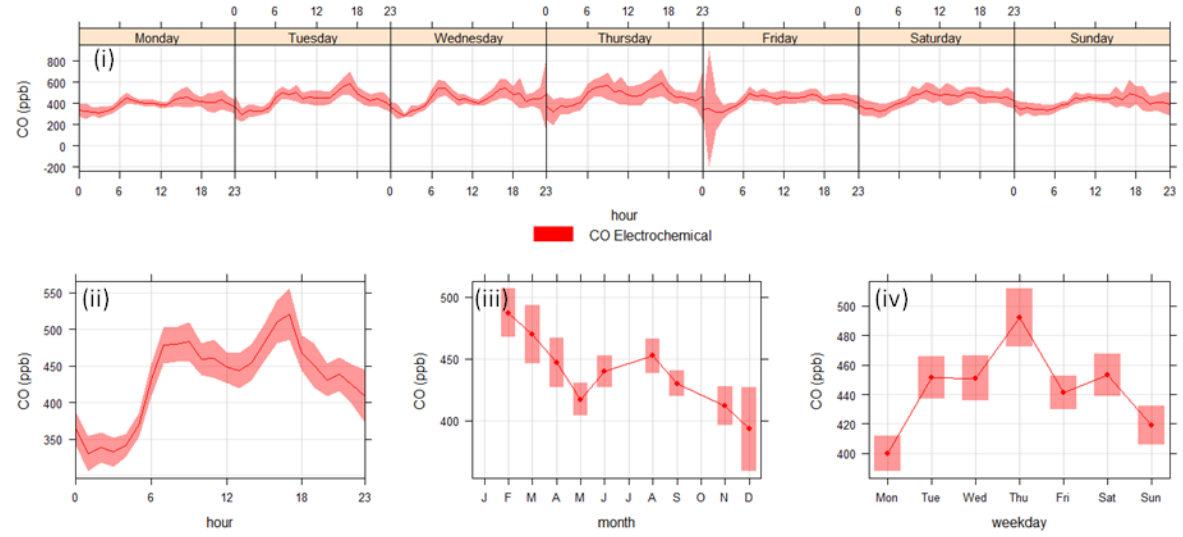

(a)

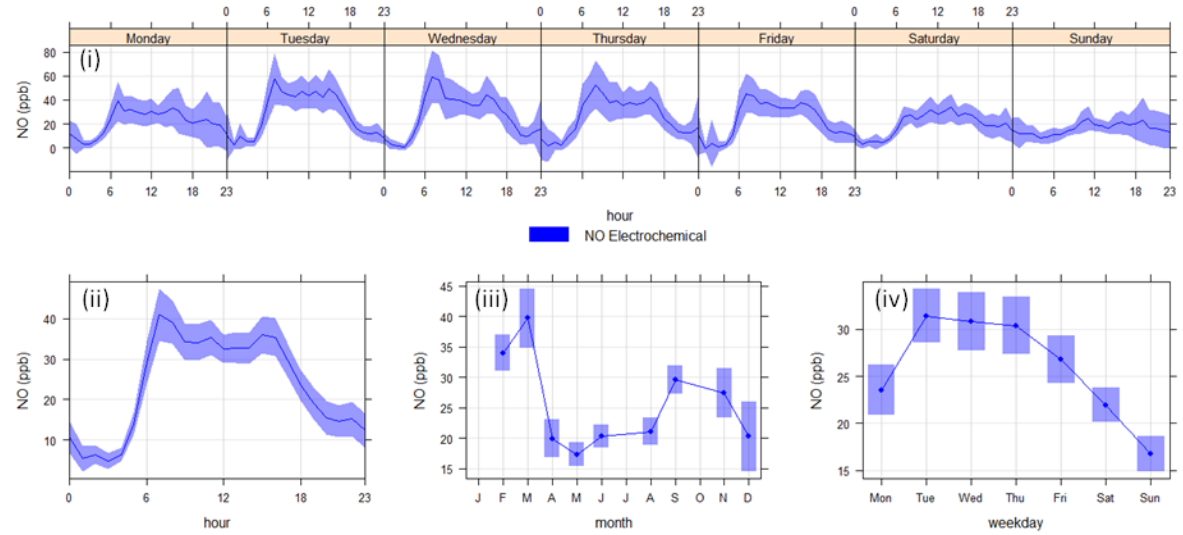

(b)

Figure 6.27. Time series plot uncorrected for change in rush hour time due to daylight saving time (a) Four time series averaged over different time scales of hourly CO electrochemical sensor mixing ratios at the LAQN station in Gonville Place, Cambridge (February–December 2010). (b) Four time series averaged over different time scales of the hourly NO electrochemical sensor mixing ratios at the LAQN station in Gonville Place, Cambridge (February–December 2010).

The weekend effect was observed more in the NO plots compared to CO as seen in figure 6.26b (i and iv). While the lowest CO mixing ratios were recorded on Sundays and Mondays as shown in figure 6.26a (i) and 6.26a (iv). This may be due to combination of reduced

vehicle use at the weekends and a change in frequency of vehicle types from weekdays to weekends. It has been shown earlier (section 6.2) that coaches / buses potentially emit higher NO and the volumes of this type of vehicle decrease during the weekend hence the possible decline in the NO mixing ratios on weekends [107]. While there are a reduced total number of vehicles on weekends, there appear to be no significant reduction in the mean CO mixing ratios on weekends for the duration of this study. Seasonal variabilities were observed in the mixing ratios of the pollutants measured during this deployment especially in the NO species. The low mixing ratios observed during the warmer months in the summer (fig. 6.26b (iii)) were partly due to a more unstable boundary layer which is characterised by rapid mixing which allows dilution of pollution. In contrast, the cold conditions in the winter encourages stable boundary layer with little vertical mixing which in turn leads to trapping of pollution close to the surface of the earth. In addition, the chemistry during summer time is different than in winter due to the prolonged sunlight which encourages production of OH radical a principal oxidant that removes gaseous species during the daytime.

6.2.4. Conclusions

This section has shown the reliability of electrochemical sensors for long-term measurements of CO and NO. In addition, this provides opportunities to better characterise AQ over long-term by combining pollution data with meteorology data.

With the aid of the openair software tool, trends in CO and NO over different timescale are investigated. This makes it possible to detect rush hour period and also weekend effects of pollution measurements. In addition, this tool offers the opportunity to predict road sources from combined wind speed, wind direction and pollution data. For this particular deployment, the major road source was from the SE direction to the monitoring station.

6.3. Measurement of NO and NO_2 from aircraft plume using mobile electrochemical sensor nodes

The small sensors group from the University of Cambridge was involved in two field campaign at Cranfield airport in 2009 and 2011, during which electrochemical sensor nodes were deployed with the aim of detecting aircraft plume by measuring the mixing ratios of NO and NO_2 from the exhaust plume of UK FAAM research aircraft BAe 146.

6.3.1. OMEGA 2009: AETIAQ campaign

The AETIAQ (Aircraft Emission and Their Impact on Air Quality) campaign was part of wider study, the OMEGA (Opportunities for Meeting Environmental challenge of Growth in Aviation) project, which was aimed at quantifying airport pollution. AETIAQ was intended to improve on the existing data for the evolution and emission of aircraft plume during their landing and takeoff (LTO) cycle at airport using variety of ground based instruments. This field campaign was conducted in Cranfield airport on the 17th February, 2009 and it involved a consortium of UK universities measuring varying parameters from the exhaust plume of the UK research aircraft BAe 146. The measurements made included gas species NO and NO_2 using portable electrochemical sensor nodes (University of Cambridge), aerosols using scanning Lidar instrument Manchester Metropolitan University (MMU), particulates using OSIRIS instrument (MMU), tyre smoke from landing gear using an optical counter and analyser SPARCLE (University of Oxford).

6.3.1.1. Measurements of NO and NO_2 mixing ratios in aircraft plume using electrochemical sensor nodes

Flight details and gas sensors deployment

There were eight sorties during the campaign, four in the morning and four in the afternoon. Each sortie consists of a take-off and landing (TOL) circuits, with about 10 s engine burst at full power. The starting weight of the aircraft was the maximum allowed (37 tonnes) decreasing by 450 kg for subsequent sorties. The prevailing wind direction during the morning flights was 300^{o} and this changed to 320^{o} for the afternoon flights at speed of 4 ms^{-1}. Except for sortie 1 where the aircraft was 50 m beyond the displacement threshold ("piano keys[23]"), the aircraft starting position was at the margin of the displacement threshold for the later sorties.

Ten mobile sensor nodes (first generation) monitoring CO, NO and NO_2 gas species were used during the field campaign. They were arranged in two arrays: an array of four sensor nodes in the airfield side of the airport and oriented in an ESE direction parallel to the boundary fence, with the second row of six sensor nodes were arranged along the boundary

[23] This is the black and white lines marking the end of a runway in an airport.

fence of the airport (fig. 6.28). The distance between the two arrays was 50 m and the sensor-to-sensor distance within each arrangement was 10 m. This ESE arrangement was arrived at based on the predicted prevailing wind of 300^{o} for the morning of field trial as this layout provided the best opportunity of detecting the exhaust plume under the influence of strong prevailing ambient wind. The four sensors near airside were secured on angled iron pillars while the sensors along the boundary fence were fastened onto the fence post (inset fig. 6.28) and were all approximately 0.5 m above the ground.

The locations of other instruments during the campaign are shown in figure 6.28. The lidar data were used to generate images for the exhaust plume as it dispersed from the aircraft while the OSIRIS provided measurements for particulate matter as well as local wind speed and direction. The lidar instrument measures the backscatter of particles from the aircraft exhaust plume as a percentage relative to the scatter of the background atmospheric aerosol in ambient air [108].

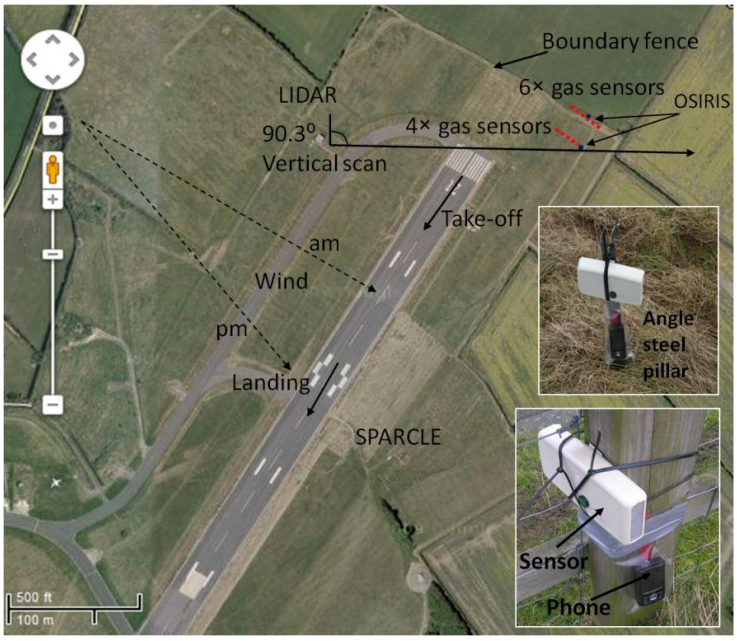

Figure 6.28. Layout of ground based instruments during the AETIAQ extension campaign (17 February, 2009). Inset is pictures of one of the four sensor nodes in the near array (fastened onto a steel pillar) and one of the six sensor nodes in the far array (strapped to a pole along the airport boundary fence). Map courtesy Google Map [109].

6.3.1.2. Results and discussion

Gaseous species (NO and NO_2) measurements

The CO measurements from the sensor nodes are not presented in this chapter because the takeoff and landing circuits were not distinct from background measurements. In contrast, with the exception of A12 (which only had data for the morning sorties) all the sensor nodes captured the peak events in NO and NO_2 for all eight sorties carried out during the campaign. The NO_X measurements relative to the positions of the sensor nodes are shown in fig. 6.29. The peak events coincide with the flight time record shown in table A1 in appendix. The first two sensors in the near array (A02 & A12 in the airfield) detected the plume with NO_2 mixing ratios above 20 ppb. Similarly the first three sensors in the far array (A14, A16 & A17) showed similar NO_2 mixing ratio distribution for sorties 2-8, the NO_2 measurements in sortie 1 were below 20 ppb one possible explanation was that the aircraft was further away (50 m) from the piano key during sortie 1 and as a results the far array sensors will detect relatively aged plume compared to sensor in the near array (figure 6.29). The sensors further right of the two arrays (A13 & A15 in near array and A18, A03 & A04) recorded relatively low mixing ratios of NO and NO_2 (< 20 ppb NO_2 for all eight sorties). This suggests these sensors were at the edge of the plume and this is evident from their relative positions to the runway (figure 6.29). A high resolution plot of the NO_2 time series for third sortie reveals two distribution modes for the peak event.

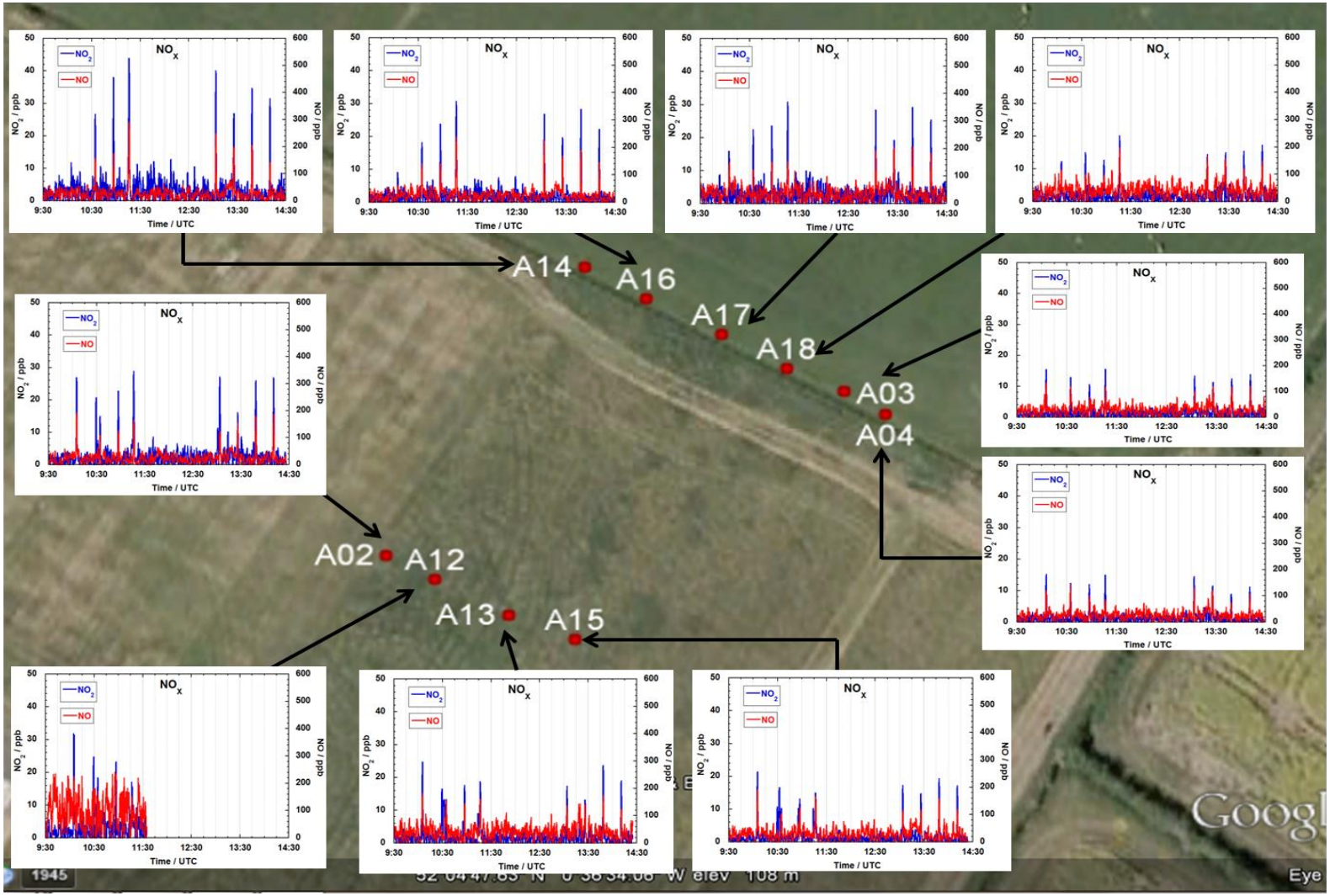

Figure 6.29. Time series showing the mixing ratios of NO_X (NO and NO_2) relative to positions for the sensor nodes deployed at Cranfield airport (1t7h February, 2009). Maps courtesy Google Earth [80]. Individual time series are shown in figure 1A&B in appendix.

The first is centred around 10:56:50 with NO_2 mixing ratios above 20 ppb (sensors A02, A12 near array and sensors A14, A16 & A17 far array) shown by the red plots in figure 6.30 while the other distribution occurred around 10:57:10 with mixing ratio below 20 ppb which correspond to the sensors A13 & A15 (near array) and sensors A18, A03 & A04 (far array) blue plots in figure 6.30. The earlier peaks at around 10:56:50 (red plots fig 6.30) coincides with the period of full power burn (see table 1A in appendix) and the mixing ratios of the sensors to the right in both arrays (blue plots fig 6.30) do not reach a maximum. These sensors however reach a maximum (10:57:10) when the aircraft started rolling for takeoff (see table 1A in appendix) and the exhaust plume will become increasingly influenced by the ambient wind as the aircraft moves away from the sensors for takeoff. This is visible from the tailing off of observed NO mixing ratios as the time lapses with the blue plots mixing ratio rising above those of the red plots (fig 6.30).

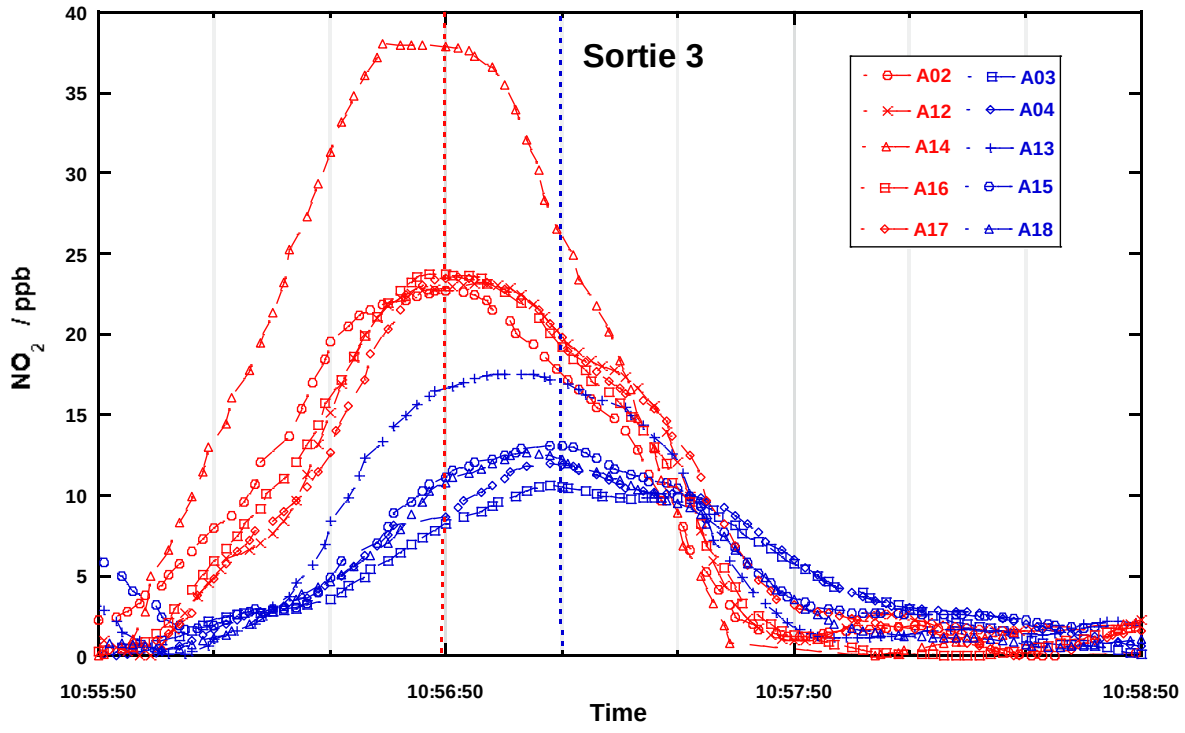

Figure 6.30. High resolution time series of NO_2 mixing ratio for the 3rd sortie showing two distribution modes centred on the maximum mixing ratios. The red lines represent sensors which are closer to the centre of exhaust plume while blue lines show sensors likely at the edge of the plume during full engine burn.

Comparison of NO & NO_2 measurements with OSIRIS and Lidar data.

The OSIRIS instrument was located between sensor A17 and A18 in the morning flight and close to sensor A15 for the afternoon flight, consequently, OSIRIS data were compared with the morning data of sensor A17 and the afternoon data of sensor A15. The wind direction from the OSIRIS data changed abruptly from a steady background reading of 300° to 210° (morning flight see fig 6.31(a)) and 330° to 210° (afternoon flight see figure 6.31(b)) coinciding with the power-up period for each sortie (table 1A appendix), these events also coincide with the peak mixing ratios of NO and NO_2 (fig 6.31), suggesting the enhancements in NO_X mixing ratios were a direct consequence of the takeoff events.

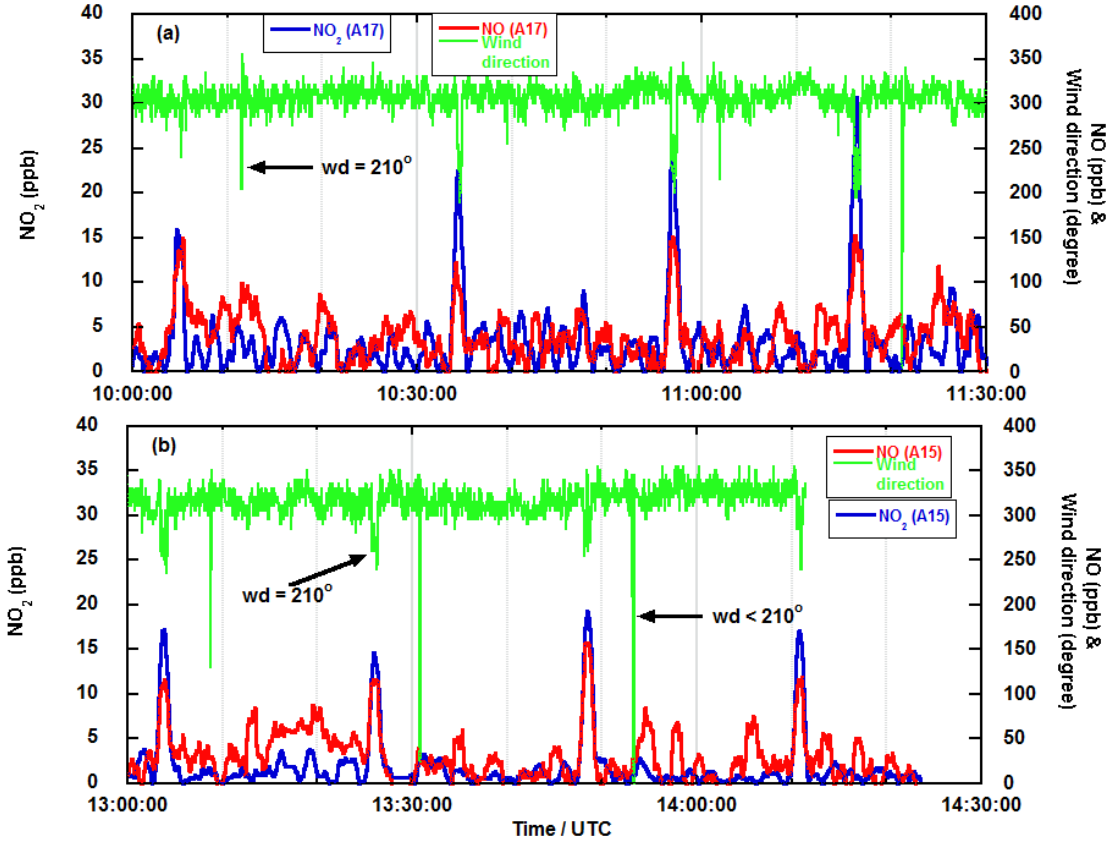

Figure 6.31. Time series of NO & NO_2 mixing ratios and the wind direction from OSIRIS for all eight sorties carried out during the campaign (17th February, 2009). (a) Is the plot of sortie 1-4 when the OSIRIS instrument was located close to sensor A17 and (b) plot of sortie 5-8 when the OSIRIS instrument was located close to sensor A15. OSIRIS data adapted with permission from Simon Christie, Centre for Air Transport and the Environment, Manchester Metropolitan University, UK.

In addition, the direction of the wind (210^{o}) aligns well with runway, indicating the observed reading was due to the excess velocity resulting from the jet exhaust during the full power burn. While the OSIRIS instrument picked up the landing events especially in the afternoon flights as indicated by the wind direction of < 210^{o}, these were not observed in the NO_X measurements as shown in fig. 6.31(b).

Although results of the lidar vertical scan (at 90.3^{o} azimuth fig 6.28) at 14:10:53 during the 8th sortie suggests an elevated plume at the location of the sensors (fig 6.32), all the sensors detected NO_2 from the aircraft plume. The observed NO_2 mixing ratios showed decreasing mixing ratios for sensors closer to the centre of the plume than those nearer the edge of the plume as shown for the final sortie in fig. 6.33.

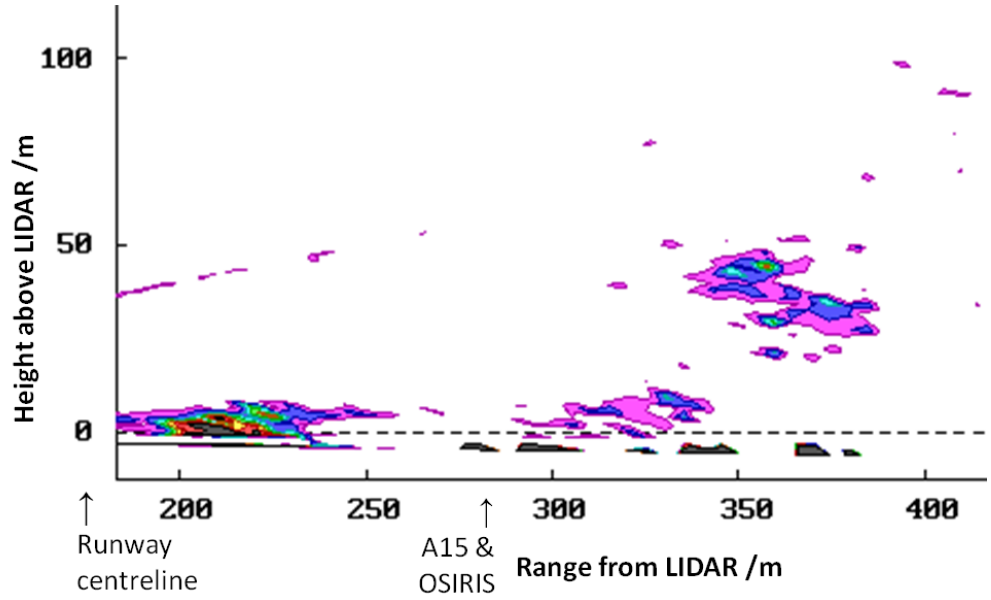

Figure 6.32. Lidar vertical scan plot showing cross section of the exhaust plume at 14:10:53 for the 8th sortie. The vertical axis is the height of the vertical distance relative to Lidar mirror which is 4m above the ground. The lower contour represents an excess back scatter of 4% above ambient and black to an excess of 16%. [Figure from reference[110] , adapted with permission].

However, the NO_2 mixing ratios at the time of lidar scan for all sensors were below 25 ppb as the aircraft was already moving for takeoff during the scan (fig. 6.33). Result of the lidar scan suggests that the instrument could not distinguish between components of the plume and background measurements at the distance of sensor A15. Evidence of exhaust plume at

ground level was drawn from the detection of other components of the plume (in this case NO_2) at significant mixing ratios (20 ppb) by all the gas sensors during the Lidar scan.

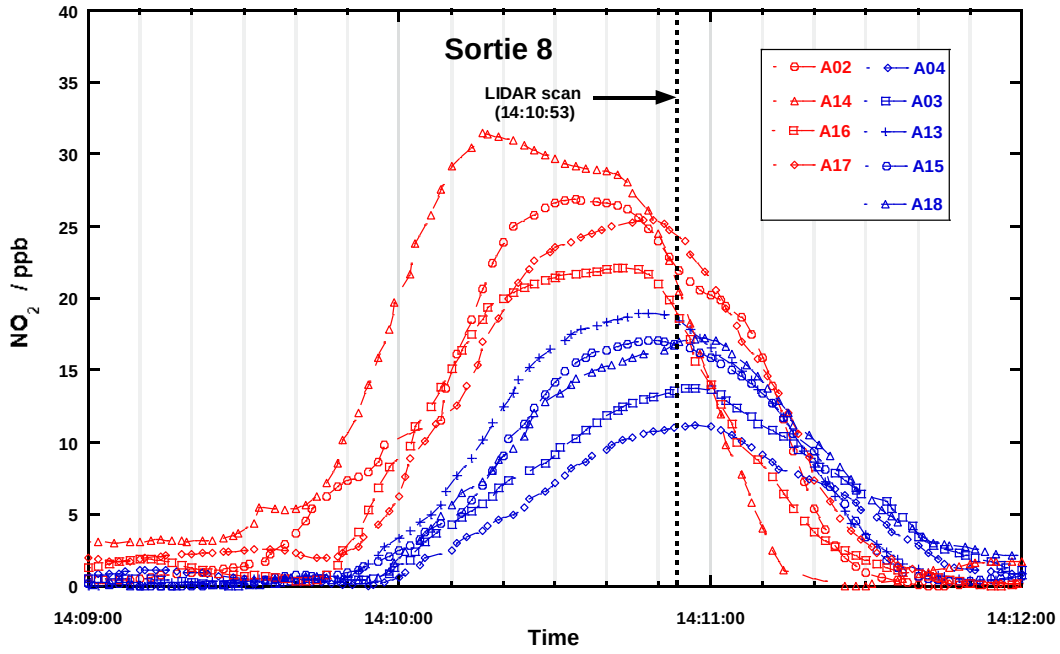

Figure 6.33. High resolution time series of NO_2 mixing ratios for the 8th sortie with the time of Lidar measurement indicated by the dash black line. The red lines represent sensors which are closer to the centre of exhaust plume while blue lines show sensors likely at the edge of the plume during full engine burn.

6.3.1.3. Conclusions

A range of portable low-cost gas sensors have been successfully deployed at Cranfield airport as part of the AETIEQ extension campaign (February, 2009).

Results of the NO and NO_2 mixing ratio measurements showed the capability of this instrument at detecting aircraft plumes during the trial. The fast response of this instrument was also demonstrated during the campaign as peak mixing ratio times coincide with wind direction change measured by another instrument (OSIRIS).

While Lidar is a good remote sensing technique for tracking the broad vertical / horizontal dispersion of the aircraft plume during the field campaign, point measurements using *in situ* techniques like gas sensors deployed in this campaign have shown that some gas phase species characteristic of the aircraft plume were still detectable even when in the absence

of distinguishable aerosols components. This implies that combinations of instruments are required to properly characterise aircraft plume dispersion.

Proper siting of gas sensors will also ensure that more information about the dispersion of aircraft plume is obtained. This is because during this study, the gas sensors were always located in the aircraft plume thus information on the extent of the plume-width downwind was not captured.

6.3.2. Baffles Trial at Cranfield Airport 2011

The baffles trial was a project led by Manchester Metropolitan University (MMU) involving project partners from UK universities (Southampton University, Cranfield University and University of Cambridge). The aim of the project was to investigate the potential of baffles at aiding the uplifting of aircraft exhaust plume. Electrochemical sensors were used to measure NO and NO_2 mixing ratios during the trial.

6.3.2.1. Flight details and setup of instruments

There were twelve sorties over three days (four sorties per day) for the entire duration of campaign. Each sortie involves takeoff and landing circuit with a full engine run lasting over 10 s before each takeoff. The baffles (120 in total) are made up of agricultural windbreak mesh fitted unto a light aluminium frame (figure 6.34). Baffles were arranged in three increasing size arcs (43.2 m, 55.1 m and 66.3 m) behind the runway as depicted in fig. 6.35(a). The baffles were in erect position for the two middle sorties of each day (sorties 2, 3, 6, 7, 10 and 11) and were down for the first and last sorties of each trial day (sorties 1, 4, 5, 8, 9 and 12) with the aim of detecting possible changes in the aircraft plume features for when baffles were up and down.

Figure 6.34. (a) Array showing three rows of baffles (in erect position) at Cranfield airport (September, 2011). (b) View from the last row of baffles during a landing routine during the field trials.

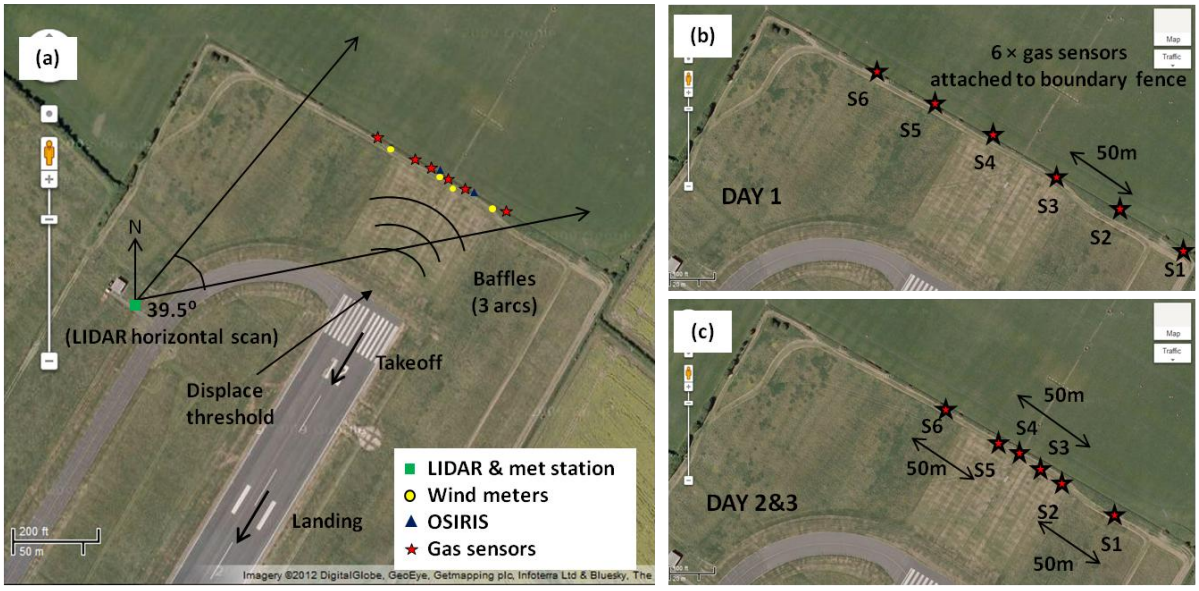

Figure 6.35. (a) Instrumental layout for the baffle trials at Cranfield airport (September, 2011). (b) Layout of six gas sensors on day 1 at Cranfield airport. (c) Layout of six gas sensors on day 2 & 3 at Cranfield airport. Map courtesy Google Map [109].

MMU deployed a scanning lidar which was used to trace aerosol composition in the aircraft plume by doing low-level horizontal scan (at height of 3 m) from an angle of 40° to 79.5° (corresponding to 39.5° sweep) relative to grid North presented in fig 6.35(a). In addition to the lidar instrument, MMU also deployed runs of wind meters (along the boundary fence), meteorology station (co-located with the lidar) and OSIRIS instrument measuring particulate matters (PM_1, $PM_{2.5}$ and PM_{10}) as shown in fig 6.35(a).

Deployment of sensor nodes

Six mobile sensor nodes were deployed in a single array by attaching them to the airport boundary fence as depicted in fig. 6.35(a). Except for the first 4 sorties (day 1), the gas sensors arrangement was the same for sorties 5-12 (day 2 and 3). On day 1, the sensors were spaced apart at distance of about 50 m with the aim of capturing both in-plume and out-plume (background mixing ratios) of NO and NO_2 as shown in fig 6.35(b). However the gas sensors were deployed using different layout for day 2 & 3 because most of the sensors missed the aircraft plume on day 1. This new layout had four sensors (S2, S3, S4 & S5) separated over a distance of 50 m (behind the runway) with the outermost sensors (S1 & S6) at a distance of 50 m from their respective neighbouring sensors as shown in fig 6.35(c).

6.3.2.2. Results and discussion

The NO and NO_2 time series for all the six sensors for sorties 1-4 is shown in fig 6.36. Only three sensors detected an increase in NO mixing ratios (S1, S2 & S3) and two sensors observed increased NO_2 mixing ratios (S2 & S3) for the four landing and takeoff circuits of day 1. This suggests that others (S4, S5 & S6) lie outside the aircraft plume on day 1. Sensor S3 is most likely closer to the centre of the aircraft plume during full engine burn as shown in sortie 3 (11:02:41-11:02:57 see table 1B appendix) where the peak mixing ratio of NO (604 ppb) recorded was more than threefold larger than the maximum NO mixing ratio observed in S2 (177 ppb) over the same period. The peak mixing ratios of NO of 211 ppb observed in S2 at 11:03:12 and 66 ppb for S3 at 11:03:30 (fig. 6.36) were recorded when the aircraft was moving for takeoff. While the aircraft plume resulting from the full engine burn (when the aircraft was stationary) will have a momentum dominated by the engine power, the plume resulting from a moving aircraft will be more susceptible to dispersion by the ambient wind, in this a case moderate breeze (5.7 ms^{-1}) blowing from a direction of 248^{o} as the aircraft taxis for takeoff. S2 also detected the takeoff plume during sortie 3 albeit at lower mixing ratio (fig. 6.36). This mixing ratio distribution pattern was observed in the NO and NO_2 measurements for all four sorties in day 1.

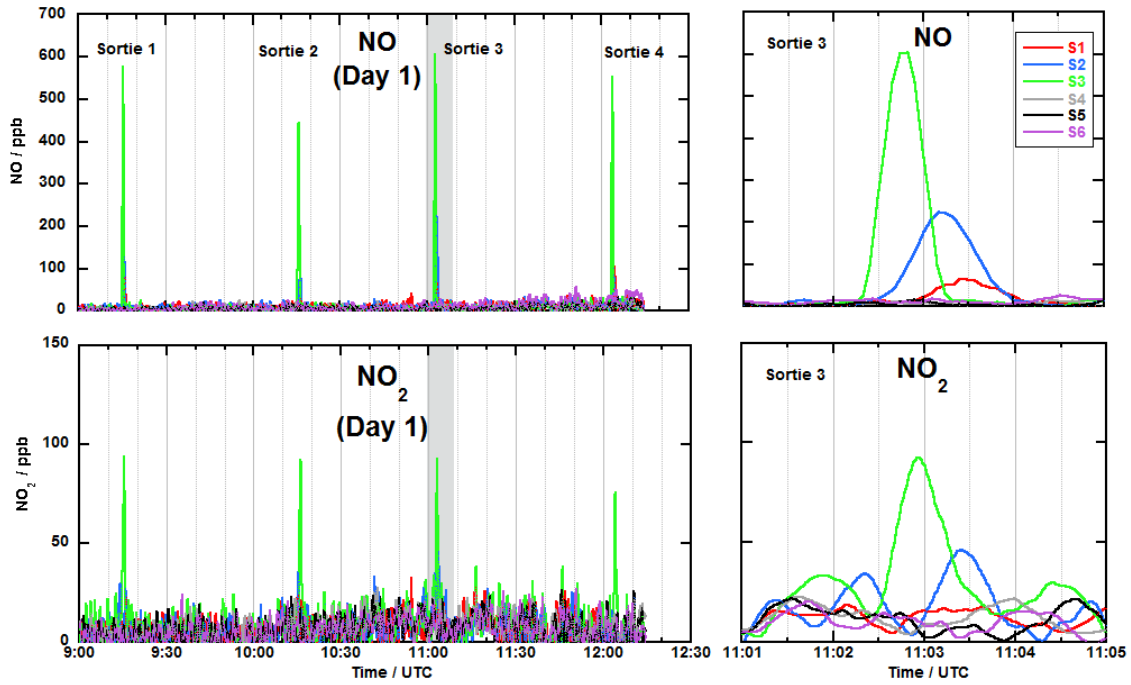

Figure 6.36. Time series of NO and NO_2 mixing ratios for sorties 1-4 (left panels). Note shown in the right panels are the high resolution plots of the grey areas (sortie 3) for the four sorties on day 1.

As described earlier, the gas sensors were arranged differently along the fence for sorties 5-12 (fig. 6.35(c)) and this reflected on the mixing ratio distribution of the NO and NO_2 for the six sensors during day 2 and day 3 trials. As expected, more sensors were able to detect the LTO circuits (S2, S3, S4 & S5 for day 2 and S1, S2, S3 & S4 for day 3 see fig. 6.37) compared to day 1 when S2 & S3 detected most of the LTO circuits (fig. 6.36).

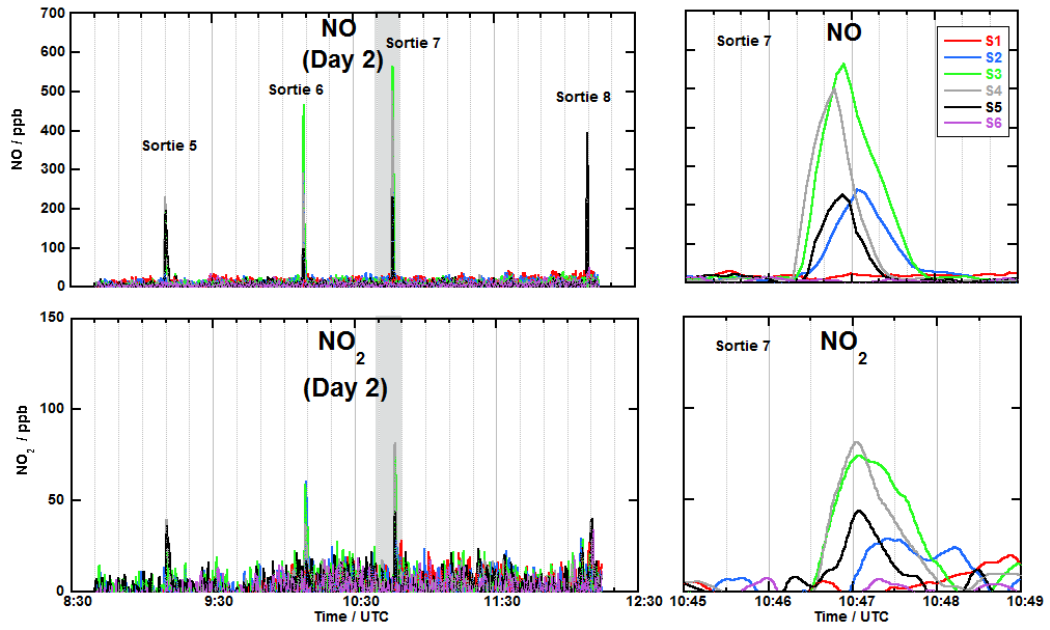

(a)

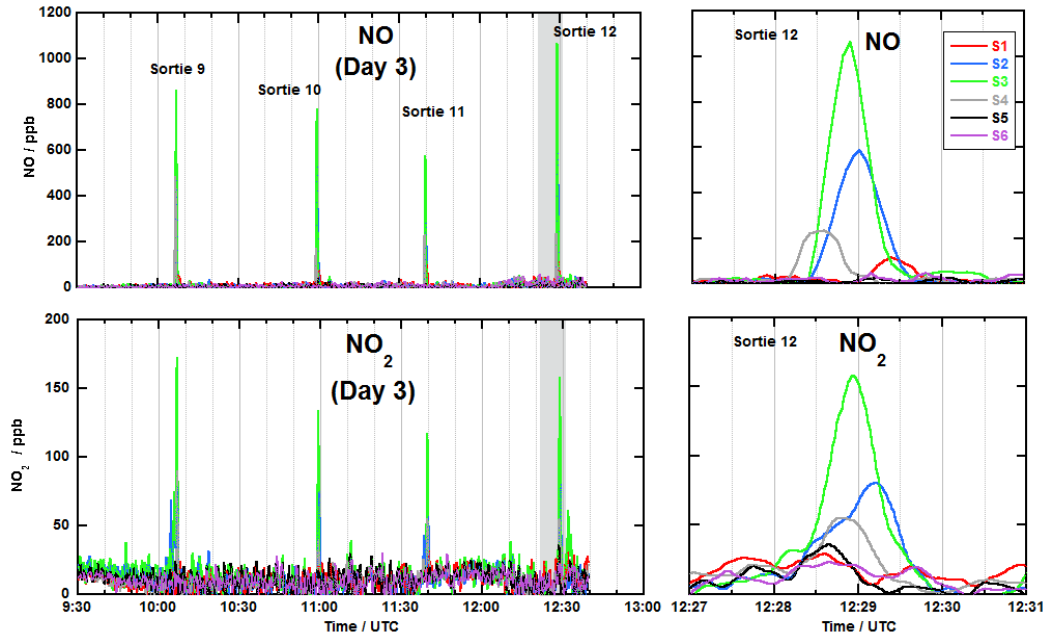

(b)

Figure 6.37. (a)Time series of NO and NO_2 mixing ratios for sorties 5-8 (left panels) and the high resolution plots of the grey areas (sorties 7) are shown in the right panels. (b)Time series of NO and NO_2 mixing ratios for sorties 9-12 (left panels) and the high resolution plots of the grey areas (sorties 12) are shown in the right panels.

Results from the horizontal Lidar scan [110] were used to track the dispersion of the plume during the trial. These were further used to interpret the observed NO distribution patterns in the time series shown in figure 6.36-6.37. For instance, during sortie 7 the time series of the NO species shows only four sensors (S2, S3, S4 and S5) detecting the takeoff event (fig. 6.38). This was consistent with the results from two low-level horizontal lidar scans (at 10:46:51 and 10:47:00) were the plume dispersed over the same four sensors (fig. 6.38). Similarly, the scans shows S1 and S6 lie outside the plume which was consistent with the observations in the NO measurements of these two sensors where the takeoff event was not detected.

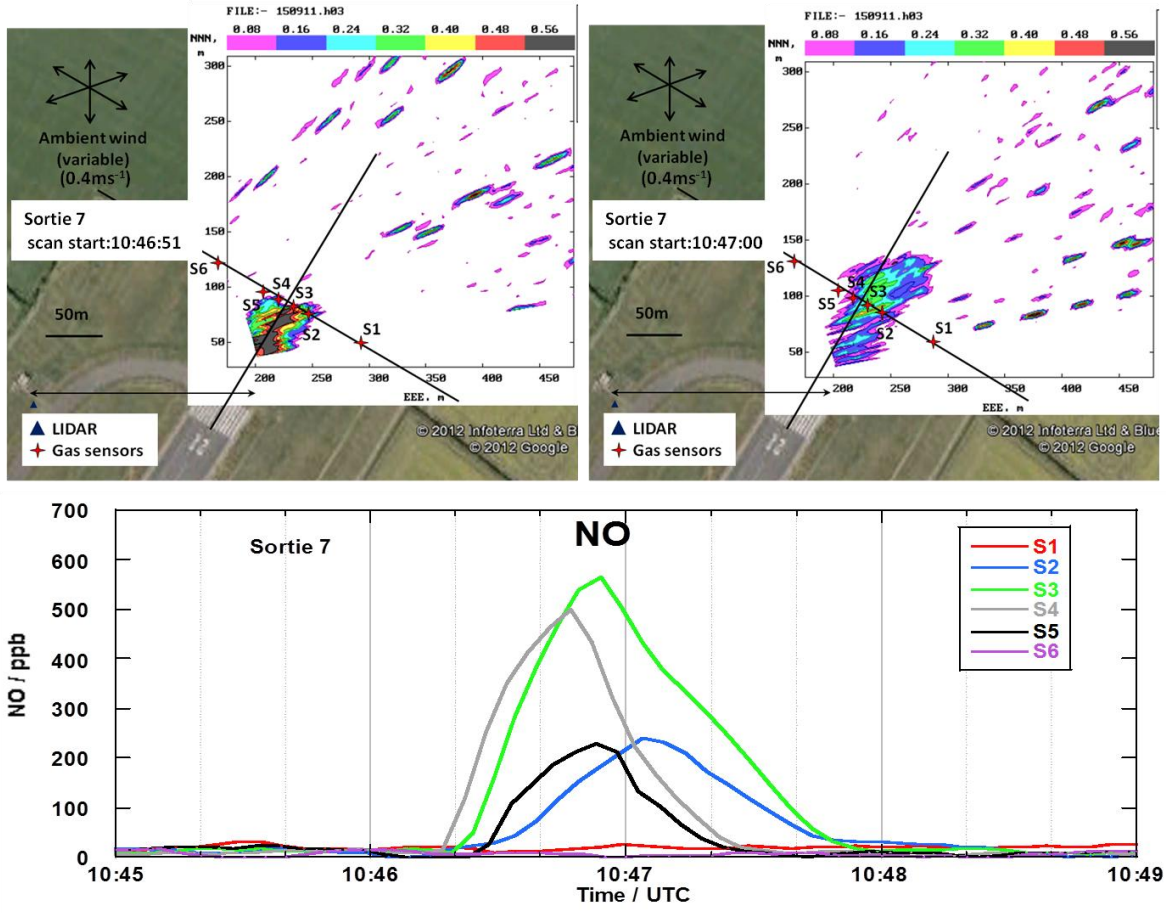

Figure 6.38. Low elevation horizontal scan for two different time period (top panel) and a high resolution plot of NO mixing ratios for sortie 7 (bottom panel). The lower contour in Lidar scan represents an excess back scatter of 10% above ambient and brown to an excess of 70% while vertical axis of the Lidar plot represents northerly distance from Lidar position and the horizontal axis is the easterly distance in meters. [Lidar data from reference [110], adapted with permission]. Map courtesy Google Map [109].

Effect of Baffles

Results of the NO and NO_2 measurements show that the gas sensors were able to detect takeoff events both for periods when the baffles were up (sorties 2, 3, 6, 7, 10 and 11) and down (sorties 1, 4, 5, 8, 9 and 12) as shown in figures 6.36-6.37. This was consistent with the lidar results as scans for sorties when baffles were up and down show the detection of the aircraft plume at ground level beyond the baffles (fig. 6.39). For instance, fig. 6.39(a) shows the lidar scans for sorties 11 (baffles up) and sorties 12 (baffles down) with corresponding NO time series and tables of the integral NO mixing ratios for each sensor for each of these two sorties shown in figure 6.39(b). The integral NO mixing ratios were calculated by integrating the area between the curves for each sensor over same time window of three minutes which corresponds to 11:38:30-11:41:30 for sortie 11 and 12:27:30-12:03:30 for sortie 12. While the lidar plot shows that the plume is detectable beyond the baffles when the baffles were up in sortie 11 (fig. 6.39(b)), a significant reduction in sum total NO mixing ratio of about 50 % was noticed when the baffles were up (total integral NO was 82,753.13 ppbs when baffles were down (sortie 12) compared to 43,021.14 ppbs when baffles were up during sortie 11). This result shows that while the aircraft plume was detectable whether the baffles were up or down, there was significant reduction in total NO mixing ratios when the baffles were up. It appears that baffles encouraged uplifting of part of the aircraft plume thereby allowing dispersion at elevated height downwind of the plume. Although these are preliminary results of the data analysis from the trial, further analysis will be needed in order to prove the potential of applying this technology to improve air quality around airports.

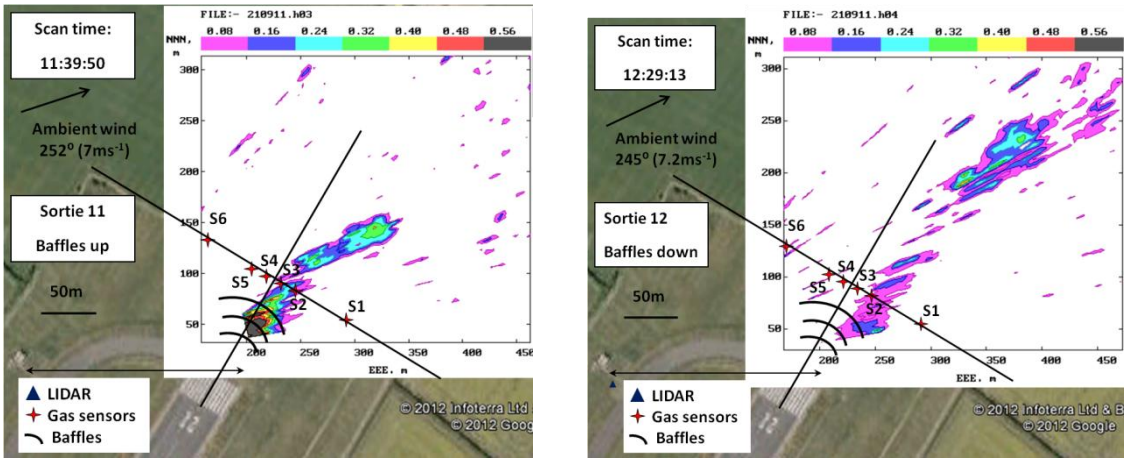

(a)

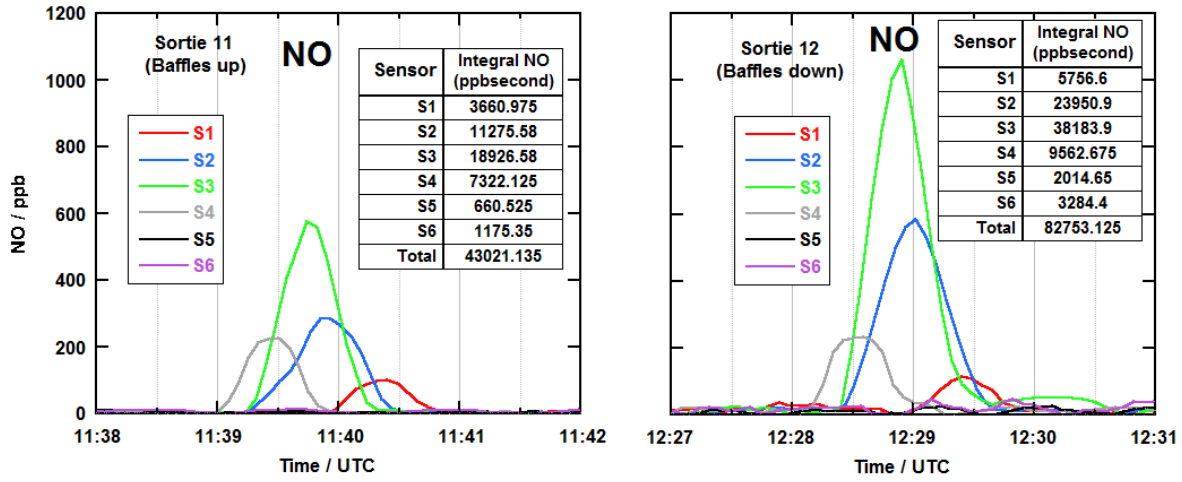

(b)

Figure 6.39. (a) Low elevation horizontal Lidar scan for sortie 11 baffles up (at 11:39:50) and sortie 12 baffles down (at 12:29:13). The lower contour in LIDAR scan represents an excess back scatter of 10 % above ambient and brown to an excess of 70 %. The vertical axis of the LIDAR plot represents northerly distance from Lidar position and the horizontal axis is the easterly distance in meters. (b) High resolution plot of NO mixing ratios for sortie 11 and sortie 12. Also shown (inset) are tables of the total NO mixing ratios (in ppbsecond) for all sensors and the corresponding sum total NO mixing ratios for these two sorties. [Lidar data from reference [110], adapted with permission]. Map courtesy Google Map [109].

6.3.2.3. Conclusions

Results from the twelve sorties of the aerodynamics baffles trials at Cranfield airport has demonstrated that an array of electrochemical sensors can be used to resolve aircraft NO and NO_2 both is space and time.

The horizontal scans from the Lidar instrument were used to trace the dispersion of the aircraft plume and to explain the distribution pattern observed in the NO and NO_2 measurements.

Although the aim of this trial was to see if the baffles will aid vertical uplift of the aircraft plume during takeoff, results of the study indicated that the baffles did not totally encourage the uplift of the plume as all sensors were able to detect the plume but with significant reduction (about 50%) in total gaseous components (NO mixing ratios). Based on the last two sorties (sortie 11 and 12), the baffles seem to reduce the total NO mixing ratios at the distance of the pollution sensors. This result was only observed in the final two sorties but not in the previous 10 sorties.

This field trial has further demonstrated the capability of electrochemical sensors in detecting aircraft plume during takeoff as observed earlier during the AETIAQ campaign.

6.4. Summary and conclusions

Field performance of the mobile electrochemical sensors has been demonstrated for both short-term and long-term deployment. The ease of deploying the sensor instruments makes it possible to simultaneously quantify air quality at different locations within a city (Lagos deployment) albeit a snapshot which will depend on local meteorology. It has been shown that CO mixing ratios elevated above recommended standards occurred in the very busy parts of Lagos (Nigeria).

In addition the sensor instruments can be used to identify individual pollution sources (unique to particular vehicle) while long-term pollution measurements combined with meteorological data can be used to identify major road sources. The stability of the sensor performance over a long-term also makes it possible to investigate weekday and weekend effects using long-term data.

The successful deployment of the sensor instruments during two aircraft plume studies at Cranfield airport in 2009 and 2011 have also shown the potential application of this technique in air quality studies at airport. Results of the baffles trial at Cranfield showed that baffles may help decrease total NO_X exposures at ground level. However further analysis is needed to further prove the potential application of baffles for air quality improvement around airports.

Chapter 7 Network Deployments of Mobile and Static AQ Sensors[24]

Chapter Summary

This section discusses deployment of network of AQ sensors on both short-term (a few hours using mobile sensor nodes) and long-term (2-3 months using static sensor nodes) basis with the aim of characterising road transport related pollutions in urban centre. These were achieved owing to the portability, reliability and reproducibility of measurements from the AQ sensor instruments.

7.1. Mobile AQ Sensor Network

A number of network deployments involving the use of mobile AQ sensors were carried out in urban centres of two cities in the UK and also in Valencia, Spain. In addition comparison of pollution measurements made in Cambridge, London, Valencia and Lagos will be discussed.

7.1.1. London Deployment 2009

As part of the MESSAGE Project Demonstration Day [111] hosted at Imperial College, London on June 30th 2009, a network of six mobile AQ sensors were deployed in South Kensington, London for about one hour forty minutes (13:30-15:10 UTC). Volunteers with the sensor instruments walked on kerbside along selected routes including busy road (Cromwell Road), semi-busy roads (Queen's Gate, Exhibition Road, Kensington Road) and quiet road (Imperial College and Prince Consort Roads) covering an area of about 80 m × 100 m as shown in figure 7.1. Local pollution data (in this case ratified 15 minutes average data [112]) were obtained from the AURN/LAQN roadside station managed by the Royal Borough of Kensington and Chelsea, London.

[24] AQ sensors in this chapter imply the electrochemical based sensor nodes / instruments described in chapters 3.

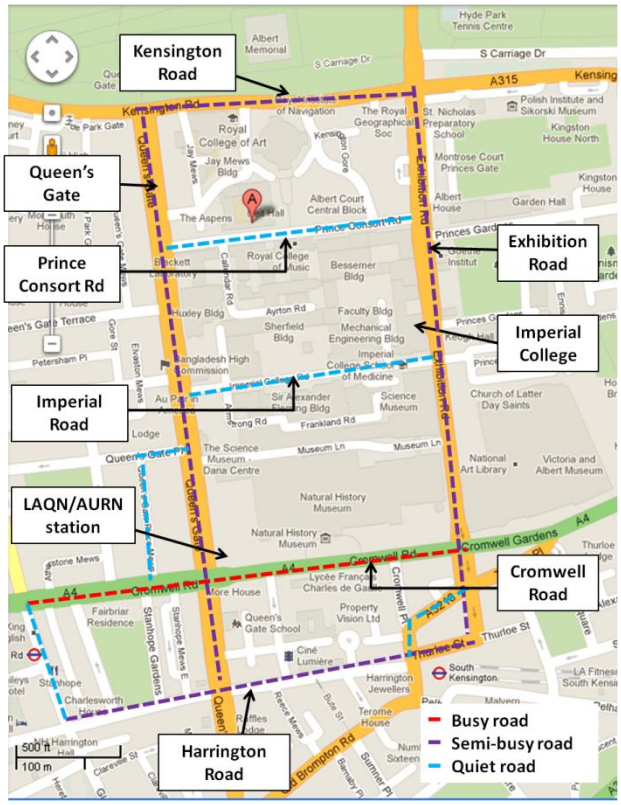

Figure 7.1. Map of deployment route around London on 30th June, 2009. Routes are colour coded to indicate traffic density. Map courtesy Google Map (Tele Atlas, 2012) [81].

7.1.1.2. Results and Discussion

Figure 7.2 shows example of temporal variation of CO, NO and NO_2 mixing ratios measured by three arbitrarily selected AQ sensors during the deployment. From the plot, pollution events related to road transport sources were observed in the CO, NO and NO_2 species. For instance, elevated mixing ratios were recorded in sensor 6 around 14:40 and similar events were also observed in sensor 5. Interestingly, the observed mixing ratios during peak events in sensor 1 were not as high as in the other two sensors. One possible explanation is the proximity of these two sensors to the road during the deployment. A distance of tens of centimetres can affect the level of peak mixing ratios observed as shown in height study earlier discussed in chapter 6.

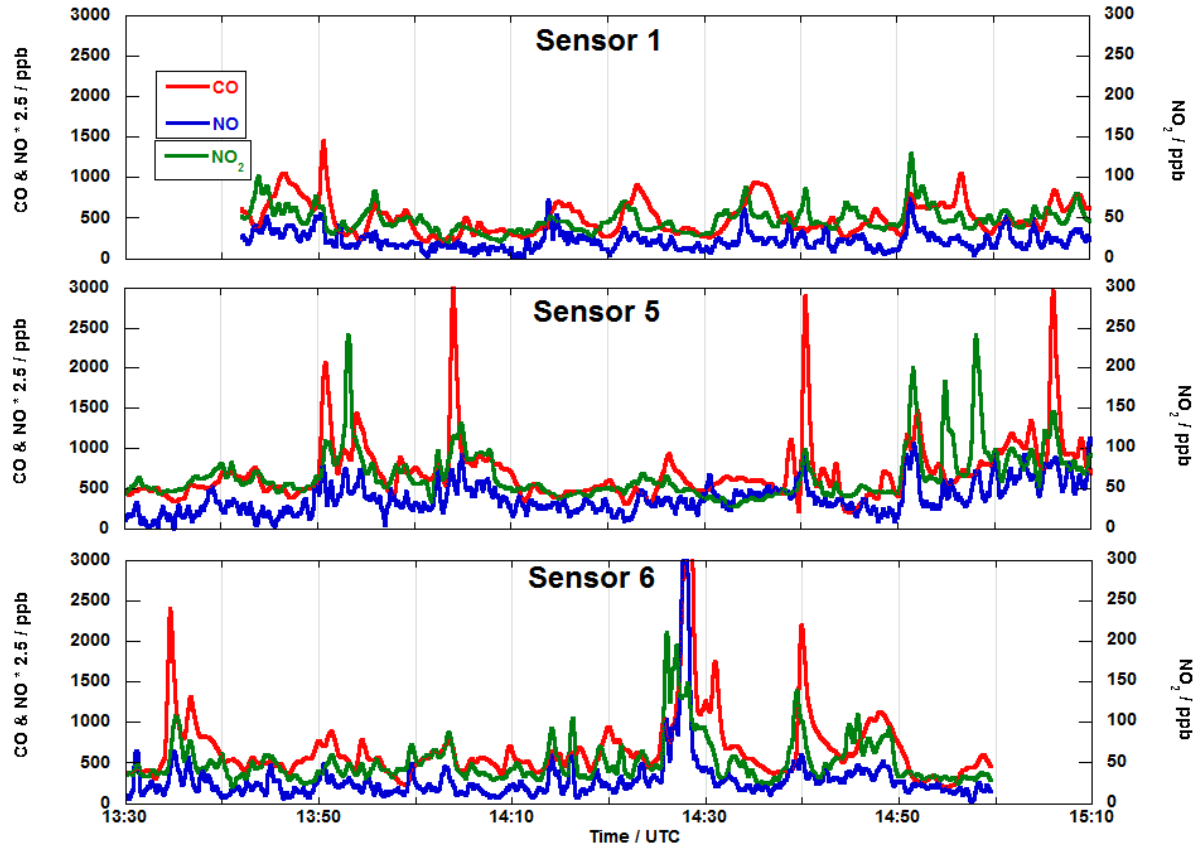

Figure 7.2. Time series of CO, NO and NO_2 mixing ratios for three mobile AQ sensors during the network deployment in London, UK (June 30th 2009). Note mixing ratios of NO have been multiplied by a factor of 2.5.

Data from all six mobile AQ sensors deployed were used to generate grid plots showing mixing ratio distribution during the deployment. Mean mixing ratios of CO, NO and NO_2 in 10 m × 10 m grid boxes were calculated as shown in figure 7.3. From figure 7.3, high mean mixing ratios were observed along the Cromwell Road for the three gas species being measured. Similarly, elevated mean mixing ratios were also observed at traffic junctions especially for those between Cromwell Road-Queen's Gate and Cromwell Road-Exhibition Road (> 1.20 ppm for CO, > 200 ppb for NO and > 100 ppb for NO_2) as shown in figure 7.3. These are considered significant giving the number of data points (> 50 points) recorded at these junctions. This network deployment highlighted pollution hotspots in the area covered during the deployment at an ultra-high spatial resolution (10 × 10 m) which is easily achieved by utilising portable mobile AQ instruments.

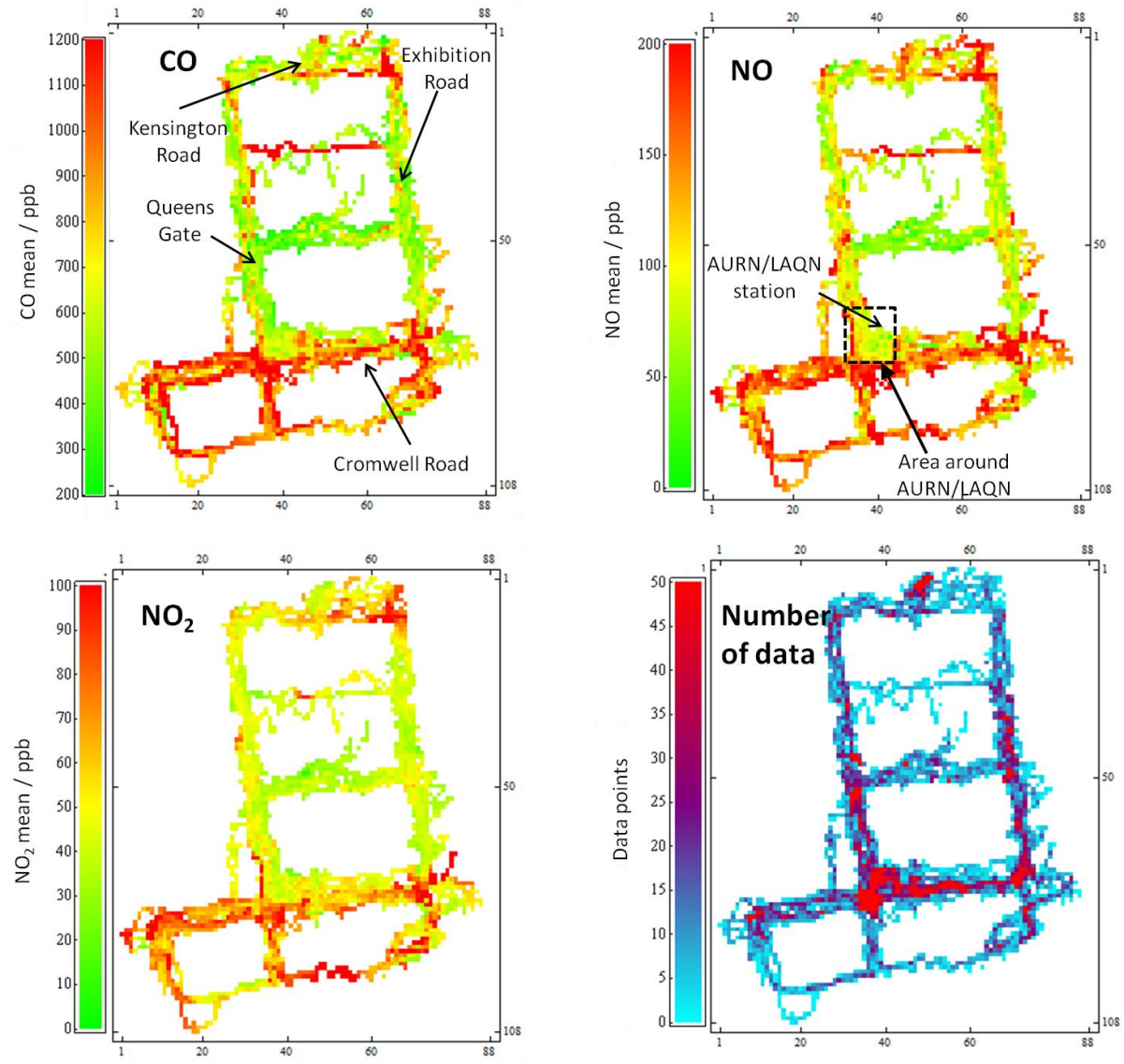

Figure 7.3. Grid plots (10 × 10 m boxes) during the mobile AQ sensors deployment in London, UK (30th June, 2009). Shown are the mean mixing ratios of CO, NO and NO_2 as well as corresponding number density of measurement points across the deployment area.

The overall mean mixing ratios for CO, NO and NO_2 for all sensors deployed were 790 ppb, 130 ppb and 58 ppb respectively. Table 7.1 shows a summary of the statistics for all sensors deployed in London on the 30th June, 2009. Maximum mixing ratios for all three species were recorded at junctions between two busy roads: maximum CO mixing ratio of 4.80 ppm was observed at the Exhibition-Cromwell Road junction while maximum in NO at 1.50 ppm and NO_2 at 0.70 ppm mixing ratios were recorded at the Queen's Gate-Cromwell Road junction.

Mean mixing ratios calculated from ratified LAQN/AURN data indicated roadside mean mixing ratios of 220 ± 44.0 ppb (CO), 47.0 ± 6.40 ppb (NO) and 56.0 ± 4.20 ppb (NO_2) compared to mean values of 650 ± 0.09 ppb (CO), 105 ± 0.05 ppb (NO) and 51.0 ± 0.02 ppb (NO_2) calculated from the mobile AQ sensor instruments (see table 7.2). While there is close agreement in the mean NO_2 mixing ratios, the mean CO and NO mixing ratios observed by the mobile AQ sensors within the vicinity of the AURN site are higher than those from the AURN station by factors of approximately three for CO and two NO. Similar results have been reported for CO measurements using fixed and portable analysers in Boston, USA and Helsinki, Finland [113, 114].This implies that AQ parameters (in this case CO and NO species) are highly heterogeneous in space and spatially limited fixed measurements do not adequately characterise this variation.

Table 7.1. Statistics of CO, NO and NO_2 mixing ratios for entire deployment of network of mobile sensor instruments in London, UK (30th June, 2009).

	CO	**NO**	**NO_2**
Mean / ppb	790	130	58.0
Max / ppb	4.80×10^3	1.50×10^3	0.70×10^3
Standard error of mean / ppb	2.30	0.50	0.20

Table 7.2. Statistics table comparing AURN/LAQN and mobile AQ measurements for CO, NO and NO_2 in London, UK (30th June, 2009).* LAQN/AURN statistics were calculated using 15 minutes ratified data between 13:30-15:15 (spanning duration of deployment) while the mobile AQ data was calculated from 1 Hz data collected in the region around the LAQN site (see NO plot in figure 7.3).

		CO	**NO**	**NO_2**
LAQN/AURN*	Mean / ppb	220	47.0	56.0
	Standard error of mean / ppb	44.0	6.40	4.20
Mobile AQ sensors*	Mean / ppb	650	105	51.0
	Standard error of mean / ppb	0.09	0.05	0.02

7.1.2. Cambridge Deployment 2009

7.1.2.1. Overview of deployment

Following the successful demonstration of network deployment of mobile AQ sensors as part of MESSAGE Project Demonstration Day in London (30th June, 2009), a wider network deployment was carried out in Cambridge, UK in August 2009. This involved deploying forty mobile AQ sensors using three different platforms (pedestrian, cycles and vehicles) to map Cambridge over a period of two hours (13:00-15:00 UTC).

Cambridge was divided into zones covering the Cambridge centre, North-, South-, East- and West-Cambridge. Except for Cambridge centre, these zones were all mapped with mobile AQ sensors mounted on cycles. Cambridge centre was further subdivided into smaller zones which were mapped using sensors on mixed platforms of vehicles, pedestrians and cyclist. The outer motorway (M11) and carriageway (A14) were covered by sensors mounted on vehicles. The deployment was planned to map an area of about 10 × 13 km as shown in figure 7.4. Sensors mounted on vehicles were secured onto the dashboard on the passenger side in the front seat with the vehicle windows half-way down to ensure air circulation, while cyclists and pedestrians had sensor instruments at waist height with the aid of secure straps.

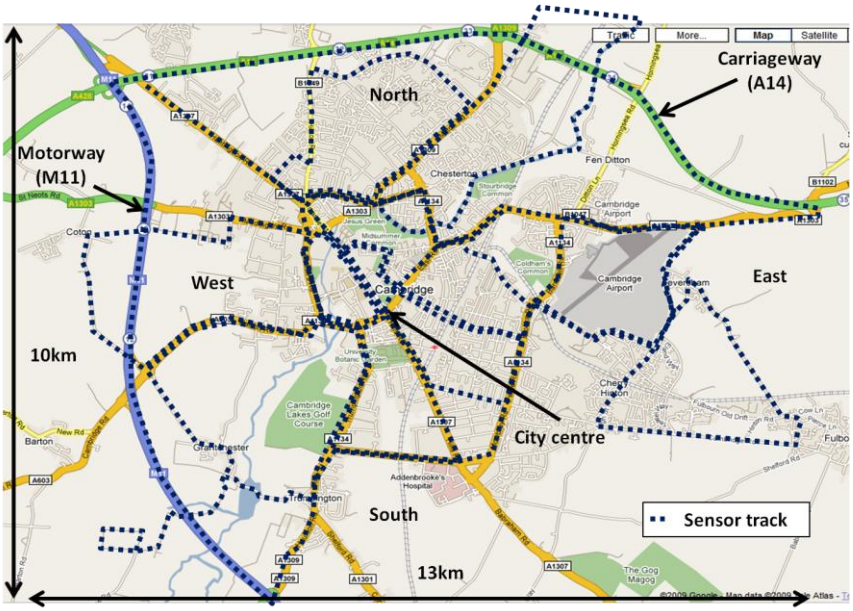

Figure 7.4. Map of Cambridge, UK showing zones mapped during the mobile AQ sensor network deployment 12th August, 2009. Map courtesy Google Map (Tele Atlas, 2012) [81].

Data collected were transmitted to a web server and were viewed live on a display monitor in the Chemistry Department, University of Cambridge. This web interface was also used to monitor failure in the sensor network and effect contingency plan put in place for such event as described in chapter 3.

7.1.2.2. Results and discussion

Although some failures were recorded during the deployment, the number of measurements made was sufficient to cover the area originally planned as shown in figure 7.5. Data presented have been processed to remove periods when sensors were indoors or for periods when vehicles were idle in car parks. In addition, time coverage varied between different sensors as some instruments were started earlier than others. Figure 7.6 shows example of time series corresponding to three different platforms used during the campaign. Gaps in the data are due to failure during data transmission. From figure 7.5 elevated NO and NO_2 mixing ratios can be seen in the city centre compared to other regions during the campaign.

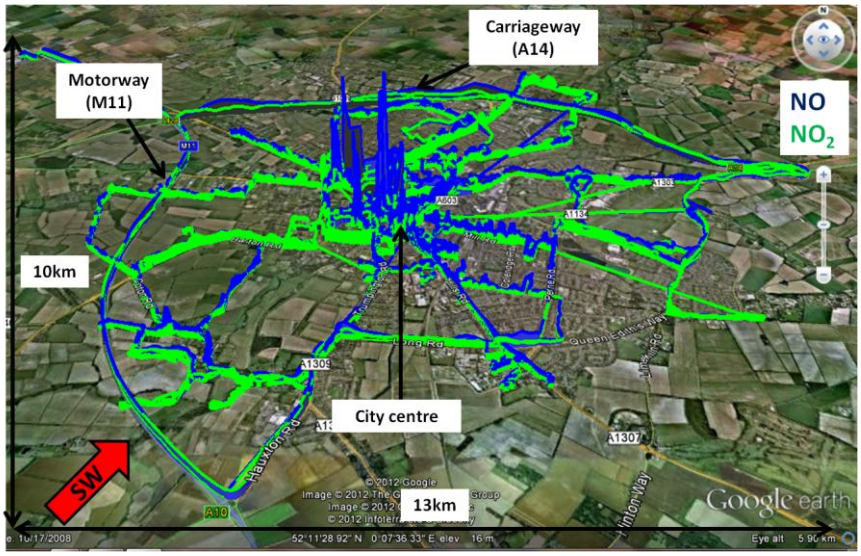

Figure 7.5. Plot showing coverage area and spatial variability of NO and NO_2 across Cambridge, UK during the mobile AQ sensor network deployment 12th August, 2009. The heights of the trace are proxy for mixing ratios of the gas species. Map courtesy Google Earth [80].

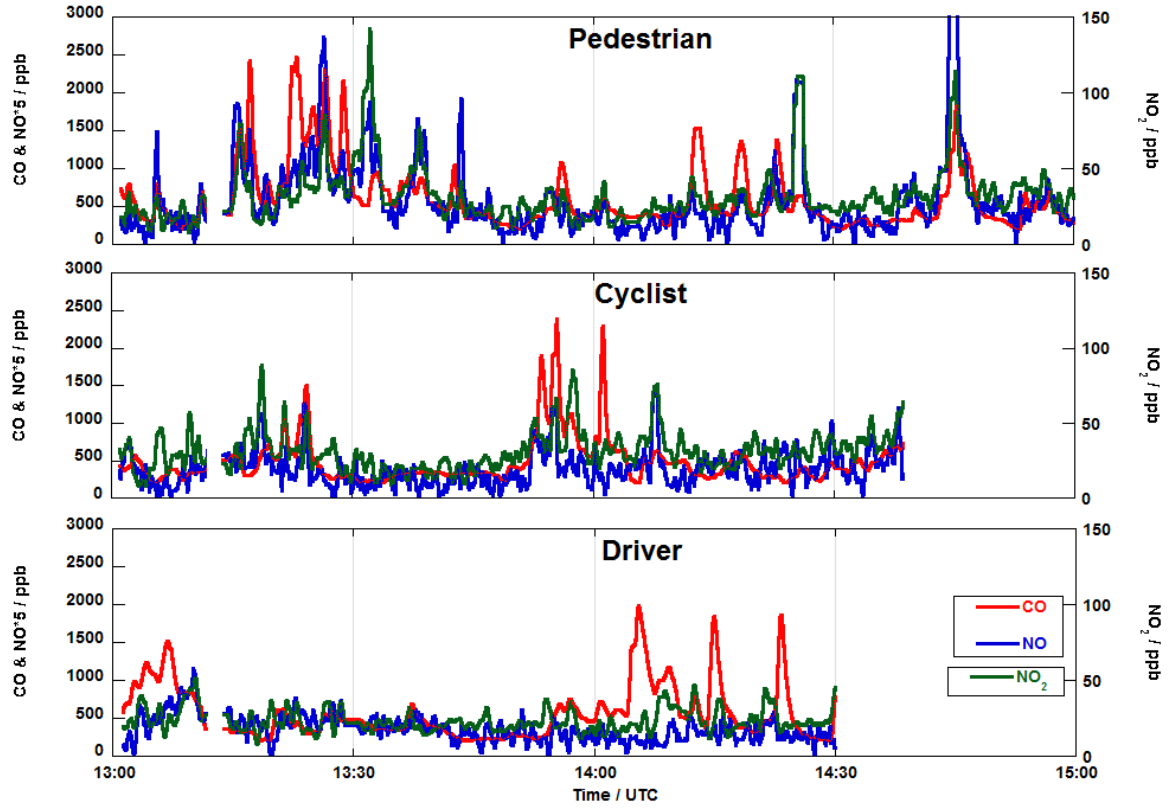

Figure 7.6. Time series of CO, NO and NO_2 mixing ratios for pedestrian, cyclist and driver during the deployment in Cambridge (12th August, 2009). Note the NO mixing ratios have been multiplied by a factor of 5 for clarity.

Figure 7.7 shows the grid plot (100 × 100 m) of mean mixing ratios of CO, NO and NO_2 and the number of data points during the deployment. This figure shows for the first time the significant variation in mean mixing ratios of these three major pollutants across Cambridge based on high resolution measurements. The significance of this variability becomes even more apparent given that there are only five continuous AQ monitoring stations [115] spanning an area of about 1.5 × 1.5 km in the city centre for the entire Cambridge City area. These stations are located within the air quality management area (AQMA) declared for the city in 2004 in response to predictions that national objective for NO_2 limits will not be achieved for the city [115]. Although additional spatial measurements for NO and NO_2 are obtained within the AQMA using diffusion tubes, temporal resolution is lost as the data only gives monthly mean mixing ratios. However, from the result shown in figure 7.7, it is evident that to properly characterise the spatial variability of road traffic related pollution, a high resolution AQ network is required. The highest mean mixing ratios in the grid plot for all three species (> 600 ppb for CO, > 200 ppb for NO and > 60 ppb for NO_2) were mostly

recorded along the motorway, carriageway and at few locations in the city centre. Although these events are relatively rare in the city centre, the fact that the grid size is relatively large (100 × 100 m) strongly suggests the significance of the spatial coverage of these events. Elevated mean CO mixing ratios were also observed in the South and North of Cambridge compared to measurements in the East and West of Cambridge (figure 7.7). This is attributed to the differences in traffic intensity along these routes.

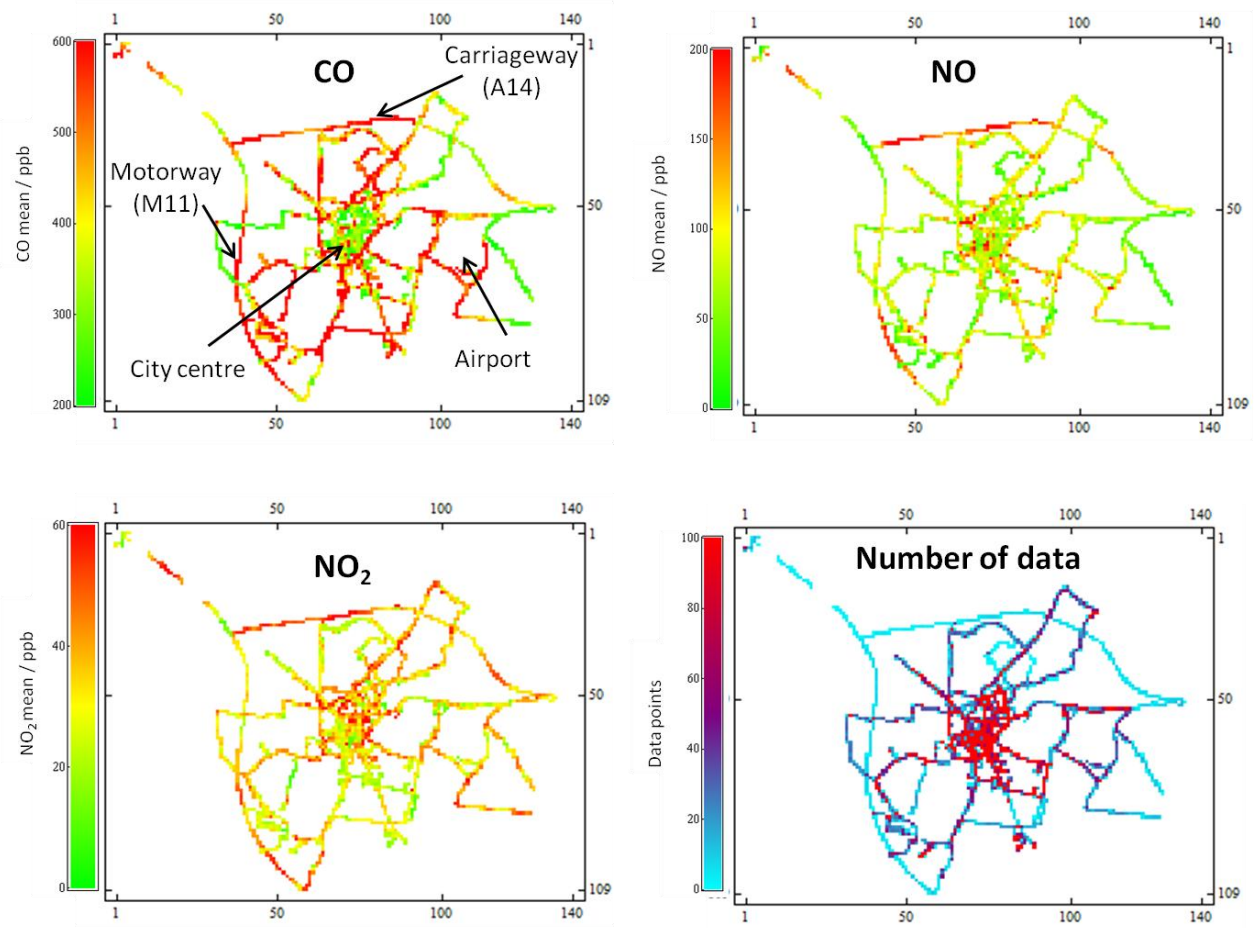

Figure 7.7. Grid plots (100 × 100 m boxes) during the mobile AQ sensors deployment in Cambridge, UK (12th August, 2009). Shown are the mean mixing ratios of CO, NO and NO_2 as well as corresponding number density of measurement points the deployment area.

Table 7.3 shows the summary of the statistics for CO, NO and NO_2 based on mode of transport for the entire deployment. Note the cyclist and driver data are binned to include only measurements within the regions covered by the pedestrians. This helps remove any statistical bias resulting from sampling by cars and cyclists along highly polluted regions for instance along the motorways which will affect the comparison between the different modes of transport. For all three species, the mean mixing ratio is smallest for pedestrian

compared to cyclist and drivers. A possible explanation is while measurements for cyclist and drivers are made along the road, pedestrians can only sample along kerbsides. This small distance away from primary road sources can affect the overall statistical comparison between the three modes of transport. Except for NO species (105 ± 0.60 ppb for driver compared to 110 ± 0.80 ppb cyclist), the driver experienced higher mean mixing ratios (570 ± 5.00 ppb for CO and 40.0 ± 0.17 ppb for NO_2) compared to the cyclist (520 ± 3.40 ppb for CO and 35.0 ± 0.14 ppb for NO_2) as shown in table 7.3. Other studies have also shown elevated CO mixing ratios inside cars compared to ambient measurements made from other mode of transport [116, 117]. Maximum mixing ratios observed during the deployment were 6.80 ppm (CO), 2.00 ppm (NO) and 0.30 ppm (NO_2). These were observed in sensors carried by pedestrian and interestingly, the maximum NO mixing ratio occurred around the bus station likely due to sampling of the exhaust plume of a bus similar to earlier observation shown in section 6.1.1.2 in chapter 6.

Table 7.3. Summary of statistics for CO, NO and NO_2 based on modes of transport.

	Species	**Pedestrian**	**Cyclist**	**Driver**	**All transport modes**
Mean / ppb	CO	480	520	570	450
	NO	100	110	105	85.0
	NO_2	35.0	35.0	40.0	30.0
Max / ppb	CO	6.80×10^3	3.70×10^3	5.80×10^3	6.80×10^3
	NO	2.00×10^3	1.20×10^3	0.50×10^3	2.00×10^3
	NO_2	0.30×10^3	0.12×10^3	0.13×10^3	0.30×10^3
Standard error of mean / ppb	CO	1.60	3.40	5.00	1.03
	NO	0.50	0.80	0.60	0.24
	NO_2	0.09	0.14	0.17	0.05
Number of data		46840	10627	12011	69478

A probability ensemble plot of CO, NO and NO_2 for the three modes of transport is shown in figure 7.8. The most likely exposure mixing ratios for CO were found to be between 200-300 ppb (pedestrian), 300-350 ppb (cyclist and drivers). Meanwhile, a second higher modal mixing ratio range (400-450 ppb) can be seen in the CO plot for the cyclist. From figure 7.8,

the most likely exposure mixing ratios observed for NO species in decreasing order is 80-100 ppb (cyclist) > 60-80 ppb (driver) > 40-60 ppb (pedestrian). In addition to cyclist experiencing the highest likely mixing ratios, there was high probability they will experience elevated mixing ratios above 100 ppb compared to other modes of transport. The cyclists were most likely to be exposed to higher NO_2 mixing ratios in the range of 35-40 ppb compared to 20-25 ppb experienced by pedestrians and drivers. However, drivers have higher probability of exposure to mixing ratios greater than 50 ppb compared to cyclist and pedestrians. During this deployment, it was discovered that cyclists are more likely to experience higher mixing ratios for all three gaseous species compared to the pedestrian and drivers. A possible explanation is that the cyclists quite often find themselves behind vehicles at traffic junctions and will easily be exposed to elevated mixing ratios from the vehicle exhaust compared to pedestrians on kerbsides or drivers who are relatively protected inside their vehicles.

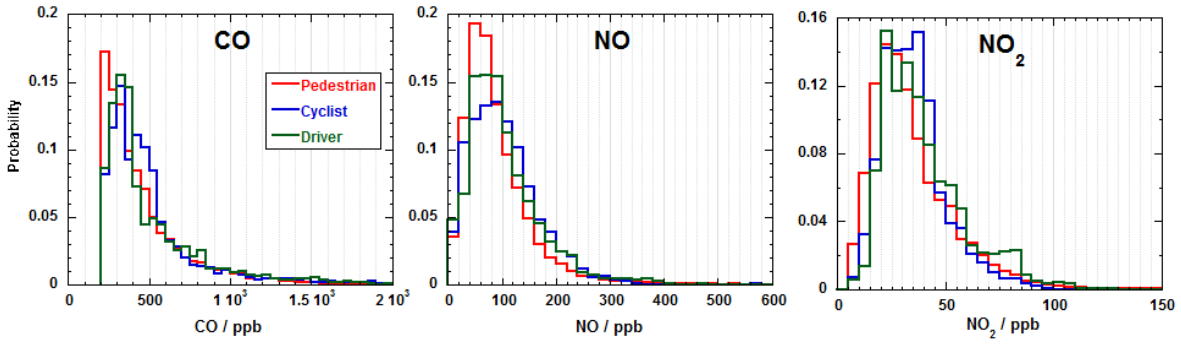

Figure 7.8. Probability ensemble plot of CO, NO and NO_2 mixing ratios showing distribution pattern and exposure levels experienced by pedestrian, cyclist and drivers during the mobile AQ sensor deployment in Cambridge, UK (12th August, 2009).

7.1.3. Valencia Deployment 2009

7.1.3.1. Overview of deployment

A network of eight mobile AQ sensors was deployed in Valencia, Spain on 3rd April, 2009. This deployment lasted approximately three hours (17:00-21:00 UTC) and was designed to cover an area of approximately 1.8 km × 2.1 km. Three gaseous species CO, NO and NO_2 were measured during the deployment. It is the first network deployment of portable AQ sensor instruments in the city. This was also the first major deployment when the Python

programme software was used in the mobile phone. Prior to this, the Symbian mobile operating platform had been used as the communication protocol between the phone and the first generation mobile AQ instruments. However due to a license issue, this was replaced with the Python programme. Although the current Python code used in the mobile phones is very robust, it is worth pointing out that the developmental version was used during this deployment. Data from the mobile network of AQ sensors were compared with measurements from two local monitoring stations: (a) RVVCCA-Valencia Vivers (39.47945 N, 0.369444 W) which was the only monitoring station located within the deployment zone and (b) RVVCCA – Pista de Silla station (39.458056 N, 0.376667 W), a roadside station located about 0.5 km from the deployment zone [118].

7.1.3.2. Results and discussion

Figure 7.9 shows the area covered during the deployment and also the spatial variability of the measured gas species. Shown in figure 7.10 are time series from three sensors for the entire duration of the deployment. The missing gaps in the data set are due to loss of connection between the sensor and the mobile phone caused by failure of the Python code. Sensors had to be frequently re-connected with the phones during the deployment.

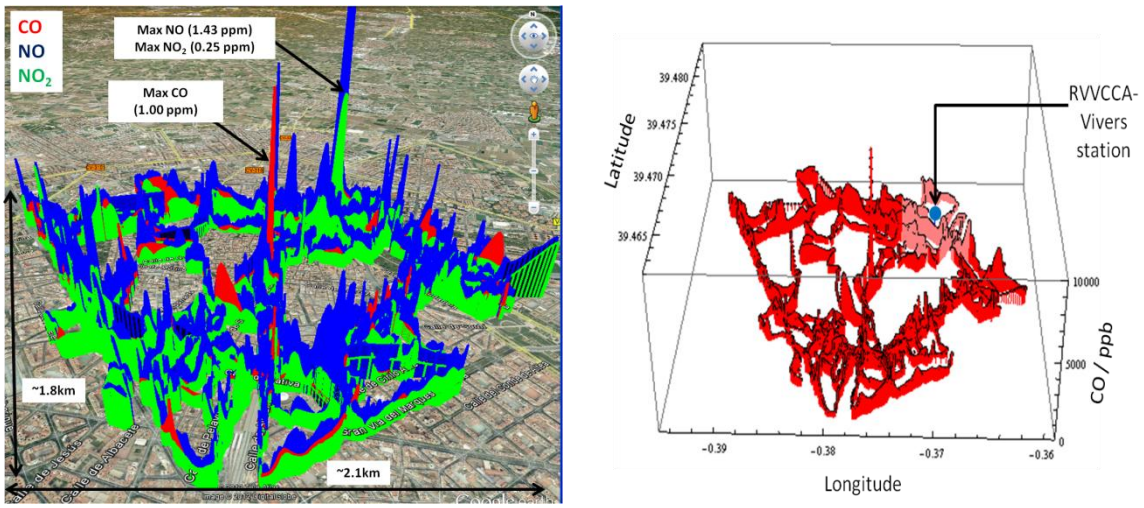

Figure 7.9. Plots showing spatial variation of gas species during the network deployment in Valencia (3rd April, 2009). The left panel shows spatial plot of CO, NO and NO_2 with the heights of the trace representing mixing ratios (see text for absolute magnitudes of the mixing ratios in the instruments of ppb). The right plot depicts spatial variation of CO mixing ratios (in red) with the region around the monitoring station shown in pink. Map courtesy Google Earth [80].

The maximum NO (1.40 ppm) and NO_2 (0.25 ppm) mixing ratios were observed at a junction between two roads while the maximum CO mixing ratio (10.0 ppm) was recorded along a major road. The total mean mixing ratios of CO, NO and NO_2 during the deployment were 810 ± 3 ppb, 104 ± 0.5 ppb and 41.0 ± 0.10 ppb respectively. Table 7.4 summarises some basic statistics for the network of sensors for the entire deployment.

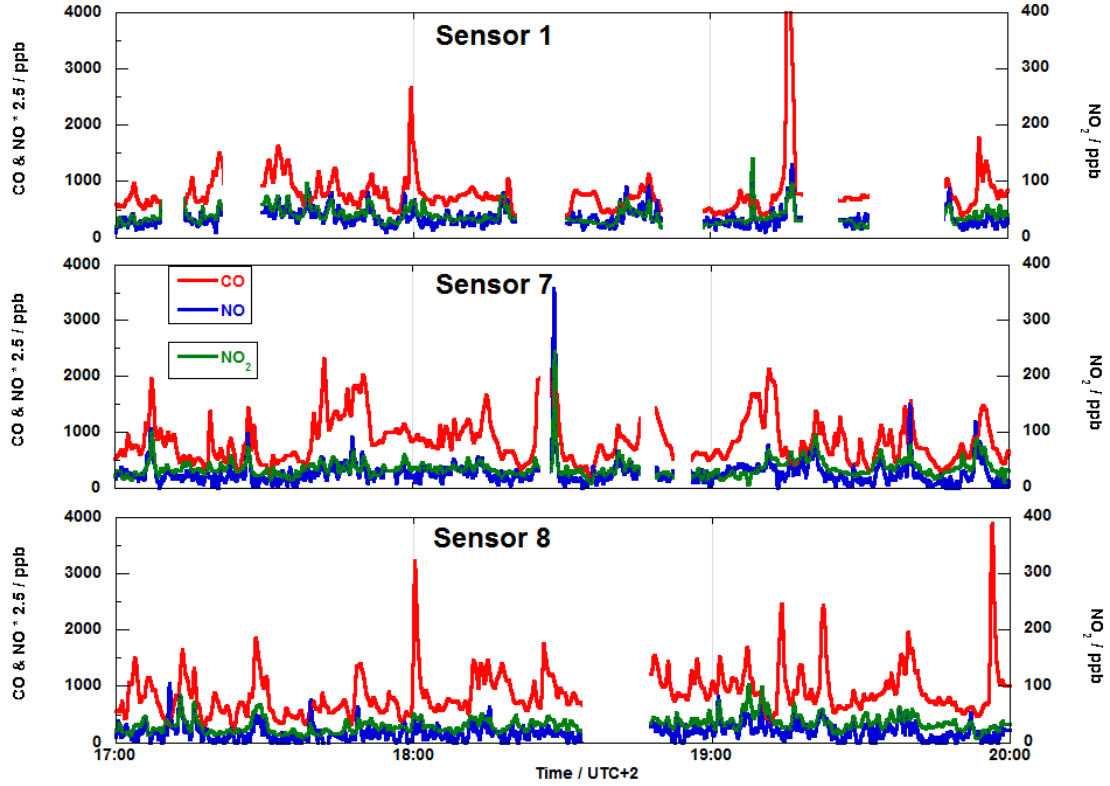

Figure 7.10. Time series of three sensors from the network deployment of mobile AQ sensors in Valencia, Spain (3rd April, 2009). Note the NO mixing ratios have been multiplied by a factor of 2.5 for clarity.

Mean mixing ratios of CO (260 ppb), NO (10.0 ± 0.70 ppb) and NO_2 (23.0 ± 2.80 ppb) calculated from the hourly mean data from the local monitoring station (RVVCCA – Vivers station) were all lower than the values calculated from the mobile AQ sensors CO (835 ± 0.20 ppb), NO (114 ± 0.05 ppb) and NO_2 (43.0 ± 0.01 ppb) located in the proximity of the monitoring site (see table 7.5). The RVVCCA – Vivers station is located in a residential zone and cannot be classified as a roadside station which possibly explains the lower mean mixing ratios recorded at this site. In contrast, RVVCCA-Pista de Silla station is a roadside station (although not within the deployment zone) has total mean NO_2 mixing ratio (41.0 ± 4.8 ppb) similar to that from the network of mobile sensors (41.0 ± 0.10 ppb see table 7.5). The mean

CO (290 ± 30 ppb) and NO (25.0 ± 3.50 ppb) mixing ratios from this site were however lower than mean values from the network of mobile sensors for the entire duration of deployment (810 ± 3.00 ppb for CO and 104 ± 0.50 ppb for NO). This shows that while the mean NO_2 mixing ratios observed at fixed sites can be fairly representative of the overall NO_2 mixing ratio in the area of the deployment, this is not true for highly variable species like CO and NO. These results further emphasis that more spatial measurements are required to characterise the mean mixing ratios over the spatial scale of this deployment.

Table 7.4. Statistics table for the entire duration of the deployment in Valencia for all AQ sensors deployed.

	CO	**NO**	**NO_2**
Mean / ppb	810	104	41.0
Max / ppb	10.0×10^3	1.40×10^3	0.25×10^3
Standard error of mean / ppb	3.00	0.50	0.10

Table 7.5. Statistics table comparing local monitoring stations (RVVCCA- Valencia Vivers and* Pista de Silla *[118]) and mobile AQ measurements for CO, NO and NO_2 in London, UK (3rd April, 2009).* RVVCCA statistics were calculated using hourly mean data between 17:00-20:00 (covering duration of deployment) while the mobile AQ data were calculated from 1s data collected in the region around the station (see right side of figure 7.9).† Statistics based on data from all mobile AQ sensors for the entire duration of deployment.

	CO mean / ppb	**NO mean / ppb**	**NO_2 mean / ppb**
RVVCCA – Vivers station*	260	10.0 ± 0.70	23.0 ± 2.80
Mobile AQ sensors*	835 ± 0.20	114 ± 0.05	43.0 ± 0.01
RVVCCA – Pista de Silla station	290 ± 30	25.0 ±3.50	41.0 ± 4.80
Mobile AQ sensors†	810 ± 3.00	104 ± 0.50	41.0 ± 0.10

7.1.4. Comparison of short-term roadside air quality in different cities

In the previous sections, results of field studies using mobile AQ sensors have been discussed. In this section however, comparison of the pollution measurements between these cities and Lagos, Nigeria will be discussed. This comparison is based only on measurements made by pedestrians in the different cities. Figure 7.11 shows the distribution plots for CO, NO and NO_2 mixing ratios for roadside measurement in Lagos, Valencia, Cambridge and London. The plots have been normalized to the most likely exposure level (modal mixing ratios).

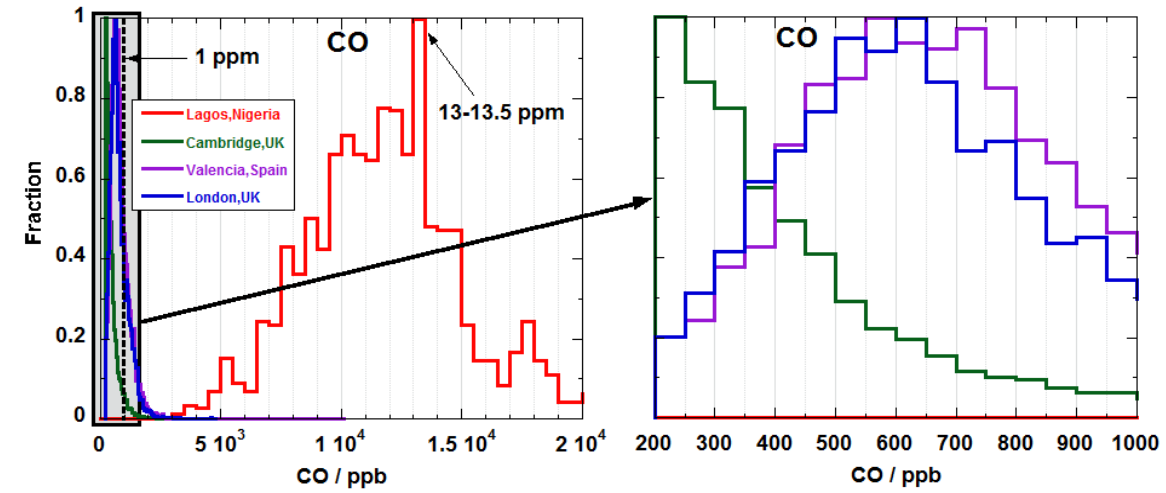

(a)

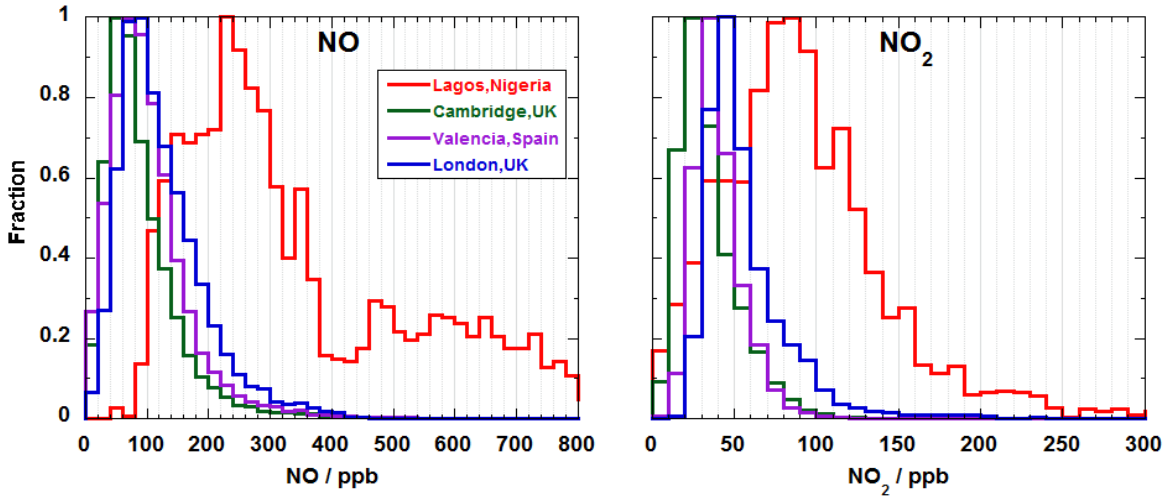

(b)

Figure 7.11. Distribution ensemble of CO, NO and NO_2 mixing ratios in four different cities (Cambridge, London, Valencia and Lagos). (a) Is the CO distribution plot with high resolution plot shown on the right. (b) The NO and NO_2 mixing ratio distribution plots.

Lagos has the highest most likely exposure level for CO of 13-13.5 ppm compared to the other cities as shown in Fig. 7.11(a). The high resolution plot of the CO mixing ratio distribution is shown in the right panel in figure 7.11(a). Cambridge has the lowest CO mixing ratio exposure level (200-250ppb) while the most likely exposure mixing ratio was 550-600 ppb in Valencia and 600-650 ppb in London. The distribution pattern is similar for NO and NO_2 with the highest likely exposure levels recorded in Lagos (200-240 ppb and 80-90 ppb for NO and NO_2 respectively), followed by London (80-100 ppb and 40-50 ppb for NO and NO_2 respectively) then Valencia (60-80 ppb and 30-40 ppb for NO and NO_2 respectively) with the lowest exposure level observed in Cambridge (40-60 ppb and 20-30 ppb for NO and NO_2 respectively).

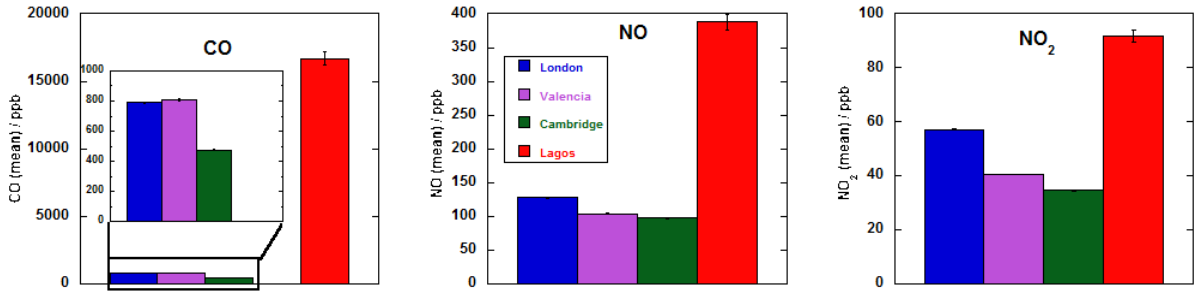

Figure 7.12. Bar chart of the total mean mixing ratios (± 95% confidence interval) for CO, NO and NO_2 in the four cities (Cambridge, London, Valencia and Lagos).

Figure 7.12 show the bar chart of the total mean mixing ratios for CO, NO and NO_2 in the four cities. Lagos has the highest mean mixing ratios for all three species with CO (16.7×10^3 ± 0.5×10^3 ppb), NO (390 ± 12.0 ppb) and NO_2 (92.0 ± 2.00 ppb). Except for CO (810 ± 6.00 ppb in Valencia, 790 ± 4.50 ppb in London and 480 ± 28.5 ppb in Cambridge) the next highest mean mixing ratios were recorded in London, followed by Valencia and finally Cambridge i.e. NO mixing ratios of 130 ± 1.00 ppb (London), 104 ± 1.00 ppb (Valencia) & 100 ± 1.10 ppb (Cambridge) while NO_2 mixing ratios of 58.0 ± 0.30 ppb (London), 41.0 ± 0.20 ppb (Valencia) & 35.0 ± 0.20 ppb (Cambridge) as depicted in fig. 7.12.

If the distribution pattern and the mean mixing ratios measurements are used to judge the outdoor air quality, then the order of decreasing air quality in the four cities are Cambridge > Valencia > London > Lagos. Several factors are responsible for these observed patterns including air quality management and control (poor in Lagos, Nigeria), traffic density (high in

London and Lagos compared to Cambridge), type of fuel (mostly petrol engines in Nigeria compared to diesel in Europe) and traffic management (poor in Lagos [101]). Another possible reason for the difference in AQ between the cities could be linked to meteorological conditions during the deployments.

The weather conditions during these short-term deployments in these cities were markedly different as shown in table 7.6. While it was relative calm in Lagos, London and Cambridge with mean wind speeds of less than 1.5 ms^{-1}, a light breeze (2.3 ms^{-1}) was experience during the deployment in Valencia. Although the deployments in London and Cambridge were carried out in summer months, the average temperatures were 27^{o}C and 19^{o}C respectively.

Table 7.6. Summary of some meteorological parameters during the short-term deployment of AQ sensors in four different cities.

	Lagos	Valencia	London	Cambridge
Mean temperature (^{o} C)	27	17	27	19
Mean RH (%)	84	54	31	91
Mean wind direction (degrees)	253	242	282	252
Mean wind speed (ms^{-1})	1.5	2.25	1.0	1.2
Mean rainfall (mm)	0	0	0	5.7

One reason for this difference was the heavy rain experienced in Cambridge with mean rainfall of 5.7 mm compared to dry conditions in the other three cities. The lowest mean temperature of 17^{o}C was recorded during the spring deployment in Valencia while the high mean temperature of 27^{o}C observed in Lagos was typical of tropical weather conditions. In all four cities, the mean wind directions were between the WSW and the NW for the duration of the deployments. The relative humidity observed during the campaigns range from high in Lagos and Cambridge (84% and 91% respectively) through moderate in Valencia (54%) and relatively low in London (31%). Although there are noticeable differences in meteorological conditions between the cities, nevertheless, the marked differences in mixing ratios of pollutants between Lagos and the other three cities are likely to be an indication of the higher general levels of pollution in Lagos.

7.3. Static AQ Sensor Network

In the previous sections of this chapter, the need for high spatial resolution, *in situ* measurements of AQ pollutants have been shown. In this section, a long-term deployment of AQ sensors (about three months) monitoring CO, NO, NO_2, relative humidity (RH) and temperature within Cambridge will be described.

7.3.1. Deployment area

The experience gathered from the short-term network deployment in Cambridge using mobile AQ sensors helped in designing the deployment area for this study. Sensors were located in a number of different environments such as urban centre, semi urban centre, bus station, residential area and quiet zones. Other areas of interests include semi-rural and rural area in Cambridge. The deployment lasted for about three months between March and May, 2010. Sensors were secured onto lamppost with the aid of brackets at height of about three metres above ground to avoid vandalism and also to meet the city council safety regulation. The sensors sampled every 10 s and transmitted packets of data every two hours to an online database. The online tool described in chapter 3 was used for daily monitoring of the network performance. A total of forty six static AQ sensors were deployed during the campaign covering an area of approximately 10 × 10 km. Twenty one instruments were located in the city centre while the rest were deployed in the outer zones of the city as shown in figure 7.13. One reason for installing a large number of sensors around the city centre is the need to cover a large area within the Air Quality Management Area (AQMA) for the city of Cambridge. Five of these sensors were installed on lampposts close to the five monitoring stations (one AURN and four LAQN stations [115]) in the city centre. The city centre is classified as urban and semi-urban sites. Zones of interest in the city centre include the bus stations, busy roads and crossroads, quiet streets and residential area. In outer Cambridge, sensors were installed in rural roadside locations e.g. in Coton in West Cambridge and Cow Lane in East Cambridge. There were also sensors installed in residential areas both in the North and East of Cambridge.

Figure 7.13. Map showing network of static AQ sensors deployed in Cambridge between March and June 2010. On the right is picture of two installations of the sensors instruments on a lamppost in the city centre. Map courtesy Google Map (Tele Atlas, 2012) [81].

7.3.2 Meteorology conditions during campaign

Macro-scale meteorology data for the duration of the deployment were obtained from the DTG Weather Station at the Computer Laboratory Department (52.210907 N and 0.092225 E), University of Cambridge. Relative to the AQ sensor network, this station was categorised as part of outer Cambridge. The station is about 14 meters above ground level. Macro-temperature measurements from the weather station were compared with the micro-temperature measurements from the sensors instruments.

The large number of AQ sensors involved in the network coupled with the diverse environment covered during the deployment offered a good opportunity to investigate the atmospheric phenomenon – urban heat island (UHI). Densely populated urban centres tend to have higher temperature than neighbouring rural environments which is described as urban heat island [119]. There are two types of urban heat island: the surface urban heat island and the atmospheric urban heat island [120]. The former is detected by using surface temperature measurements which is achieved by remote sensing. In contrast, atmospheric UHI can be studied with the aid of weather stations or making ambient temperature measurements at a few metres above the ground level. As stated earlier, the AQ sensors

were installed at heights of 3 m above ground level, as a result, temperature measurements from the network were used to study possible evidence of atmospheric UHI in Cambridge. Higher temperatures, a consequence of UHI, can have a direct impact on air quality in urban areas by enhancing some reactions in the troposphere that lead to formation pollutants. For instance, an increase in temperature can result in elevated ground level ozone mixing ratios by enhancing its production from photochemical reactions of NO_X with VOCs [120, 121].

7.3.3. Application of openair tool for pollution data analysis

Openair, an open source pollution analysis tool [105] was used in analysis of pollution data by combining the sensor measurements with meteorology data from the weather station in Cambridge. Although the sensor data have high temporal resolution (10 s), for the purpose of this analysis 10 minutes or hourly mean data were sufficient for the openair analysis. For analysis involving comparison with AURN/LAQN data, the time resolution is limited by the hourly measurements from these sites; hence, hourly mean AQ pollution data were employed for those analyses. All other analysis employed 10 min mean AQ pollution data. Although there are several functions available in the openair tool package for analysing pollution data, in this chapter only three functions were utilised. These functions include windRose, polarPlots, timeVariation functions [105] which generate wind rose plots, bivariate polar plots and time series averaged over different time windows.

7.3.4. Results and Discussion

7.3.4.1. Overall result

Figure 7.14 compares the percentage data capture between the database and onboard memory for the period of deployment. Although the sensors were deployed for a period of three months (12 March-24 June, 2010), the maximum data recovered from the onboard storage device was equivalent to two and half months. This resulted from reaching the maximum storage capacity of the onboard memory (16 M byte). The limitation of memory capacity was unknown until the end of the deployment and the problem has been addressed in the latest version of static AQ sensors which have much larger external memory (8 G byte). The percentage data capture (onboard and database) were therefore calculated based on a maximum storage period of two and a half months. Figure 7.14 shows a good data capture for both onboard (≅80%) and online data, although the latter is about

6% less than the former. Note data from the online storage for all 46 sensors were never 100%; this is because lines of data acquired during the transmission routine (see section 3.2.2 in chapter 3) are not sent online although they are stored onboard. One of the benefits of having this dual storage capability is to minimise data loss during the deployment. In addition, the online transmission of data served as a quick diagnosis tool for the network performance. If a sensor unit stops sending data, the installation is physically inspected, if there are signs of damage it is replaced depending on availability of spare sensor instruments. In situations where there were no replacements available, it was assumed that if the failure was due to GPRS module, then data would still be stored onboard as was the case for sensors S6 and S40 which respectively had 55% and less than 1% data capture online compared with 100% and 41% data capture onboard.

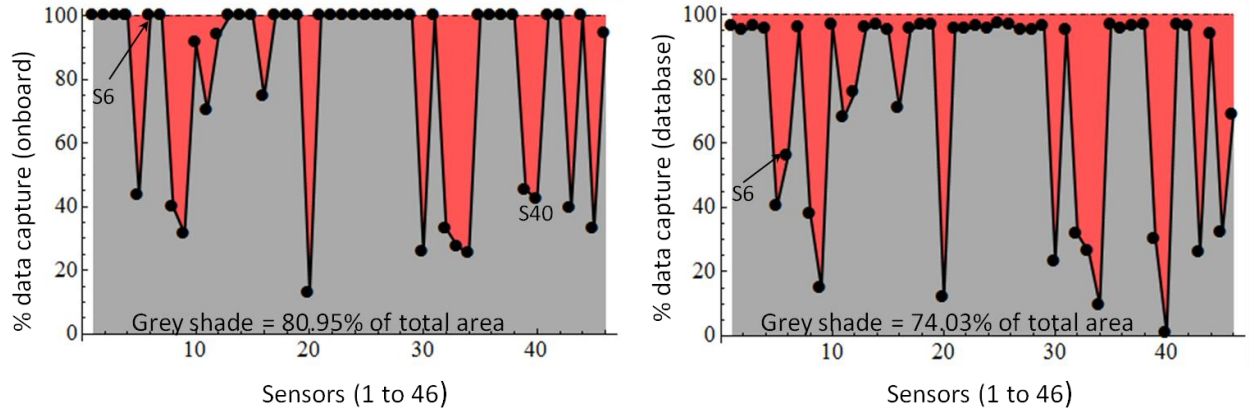

Figure 7.14. Percentage data capture during the network deployment in Cambridge, UK (12 March – 23 May, 2010). Left panel shows percentage data stored onboard while the right plot depicts percentage capture from the database.

Results of the NO_2 measurements will not be presented for this deployment because the electrochemical sensors used were still under development by the manufacturer, and results obtained from the network revealed highly digitised measurements. Ignoring NO_2 measurements, a total of about 91,570,176 measurements (stored onboard) were made across the network which included measurements of two gas species (CO and NO), temperature and relative humidity.

An example of high temporal resolution NO mixing ratio measurement from a sensor unit in the network is shown in figure 7.15. Both the temperature corrected and uncorrected data

are shown in the plots. Pollution events can be seen in the high resolution plot against the background mixing ratios (bottom plot in fig. 7.15). All the CO and NO data presented in this section have also been temperature corrected and a background mixing ratio of 200 ppb added to the temperature corrected CO measurements.

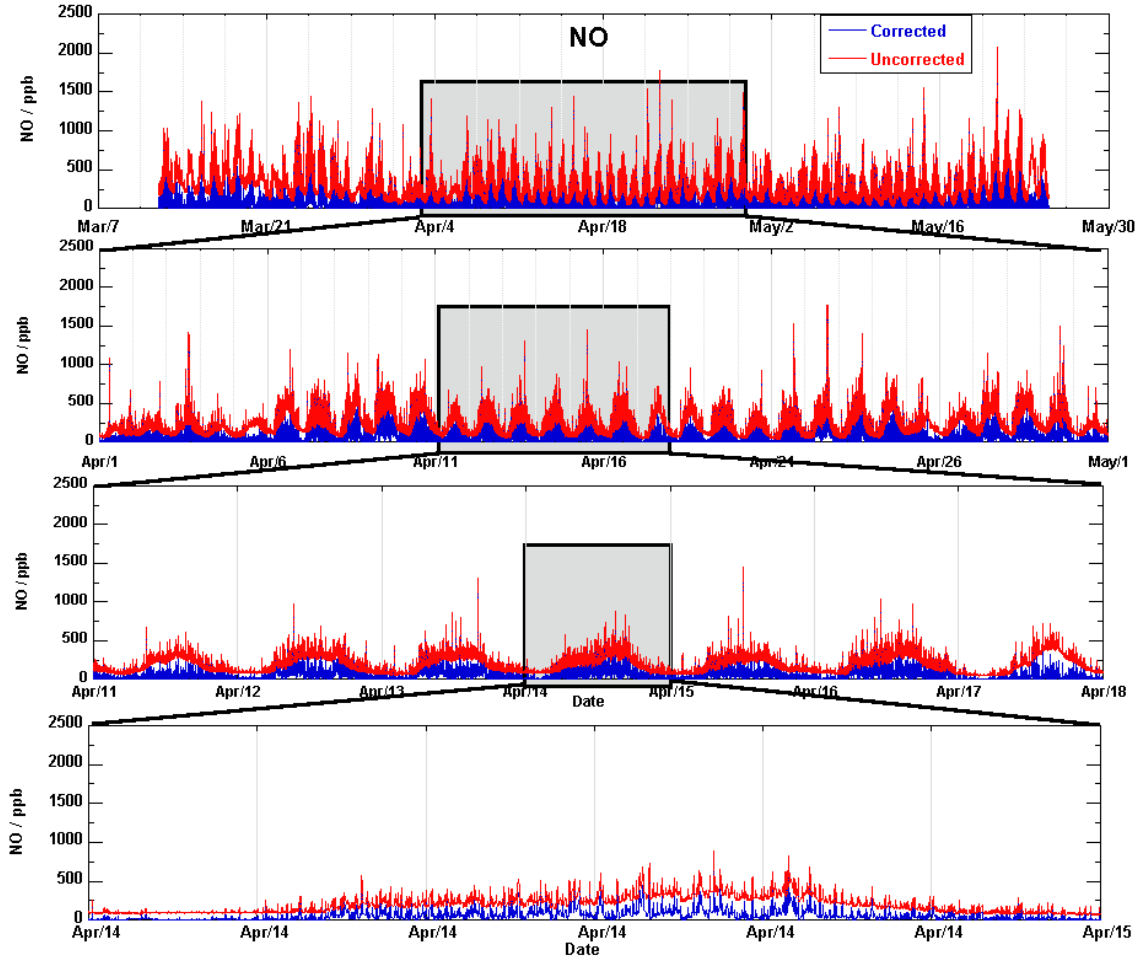

Figure 7.15. Time series of temperature corrected (blue) and uncorrected (red) NO mixing ratios (30 s averaged data) from a static AQ sensor unit located in Cambridge City centre. Top panel shows data for the entire deployment, second from top depicts a month data, third panel from top represents data for one week and the bottom panel shows data for a twenty four hour time window.

7.3.4.2. Comparison of CO and NO measurements from different sites across the AQ network

As described in section 7.3.1, the network covered a variety of ambient environments. In this section results from five sensors representing different environments will be discussed.

The sensors were chosen to span urban environments (crossroad, bus station and roadside) and rural environment (rural roadside and rural residential) as shown in map in figure 7.16. Ten minutes mean average plots for the month of April shown in figure 7.17 indicates that the frequency of peak pollution events recorded in the CO and NO measurements vary with the locations. Note there are no data before 8th April for the AQ sensor at Coton (bottom panel fig 7.17). The original unit failed a few days after installation and was only replaced when a spare sensor unit became available in April. This late installation meant that the unit had data up till 15th June, 2010 compared to other instruments which had data till 23rd May, 2010. There are frequently high mixing ratio events for CO and NO in AQ sensors located in the urban centre as seen in panels 1 and 4 from the top in fig. 7.17. High mixing ratio events were also observed in NO measurements (greater than 100 ppb) at the bus station (2nd panel from top fig. 7.17) in the city centre but the CO measurements were relatively of low mixing ratios compared to the other two sensors in the city centre. In contrast, the pollution patterns at rural stations shows elevated CO mixing ratios with relatively low NO mixing ratios at less than 100 ppb (plots 3 and 5 from top fig. 7.17).

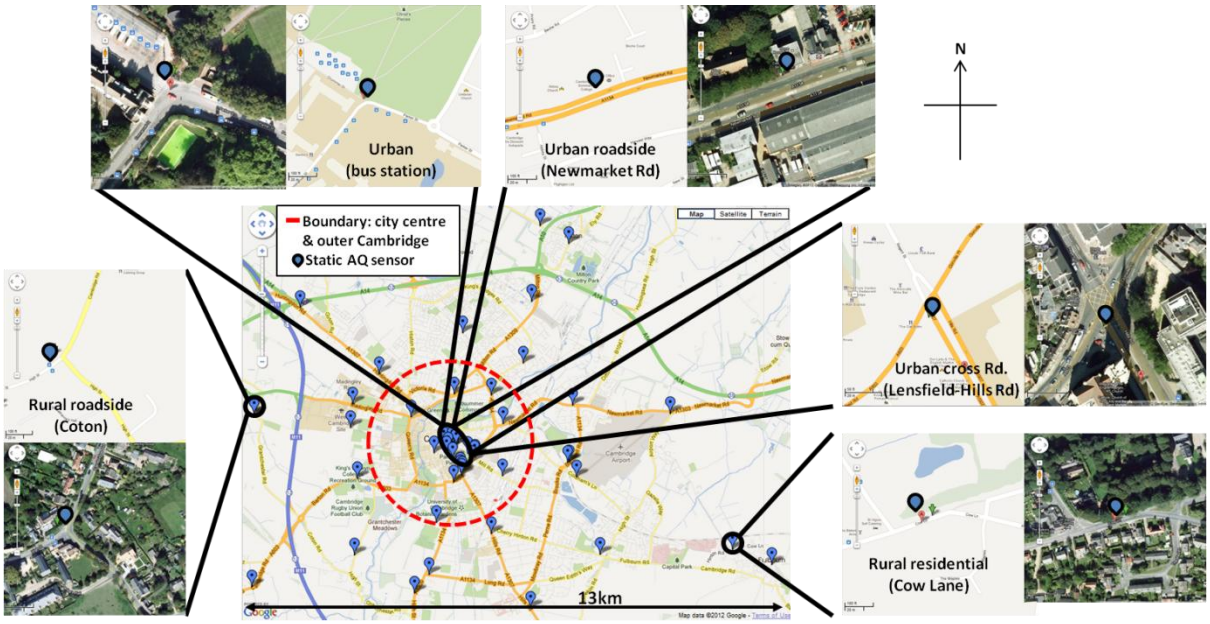

Figure 7.16. High resolution map showing locations of five AQ sensors within the static AQ network (three inside the city centre and two outside the city centre).

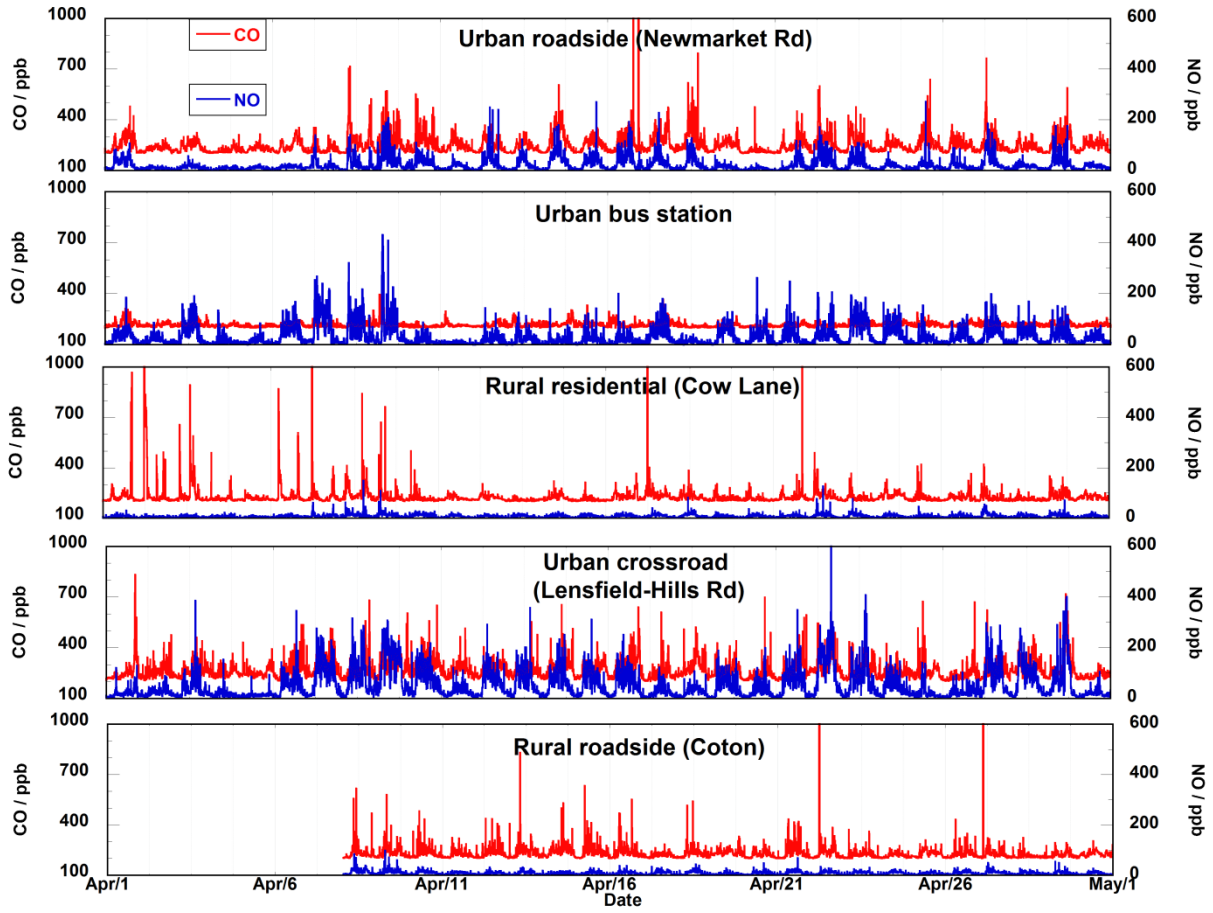

Figure 7.17. Time series (April 2010) showing 10 minutes mean CO and NO mixing ratios of five AQ sensors (see figure 7.16) within the static AQ network.

To characterise the observations across these sites, the mean of the ratio between (CO-$CO_{background}$) and NO mixing ratios were determined and are shown in figure 7.18(a). For the sensors considered in this analysis, mean ratios > 4 shows a rural environment, while values between 2 and 4 is characteristic of busy urban roadside as shown in fig. 7.18(a). Mean ratio < 2 might suggest urban bus station as there were elevated NO mixing ratios compared to CO measurements at this site as shown in fig. 7.18(a). This is not a general rule because sensors located at quiet urban roadside can have mean ratio values > 4. For instance, the AQ sensor located at Regent Terrace a quiet street in the city centre (S18 next to S17 in figure 7.18(b)) has mean ratio 4.75 ± 0.19.

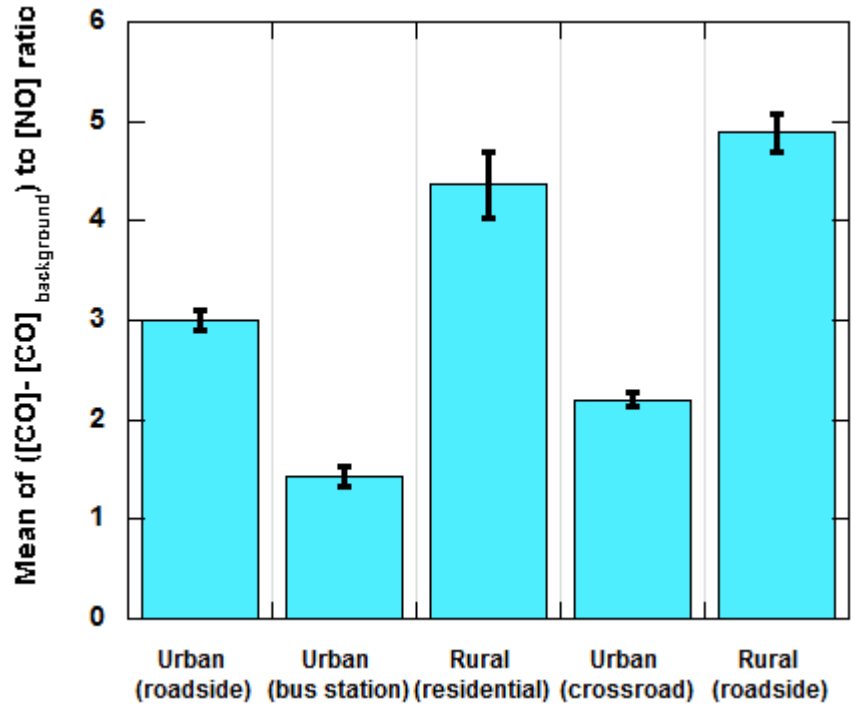

(a)

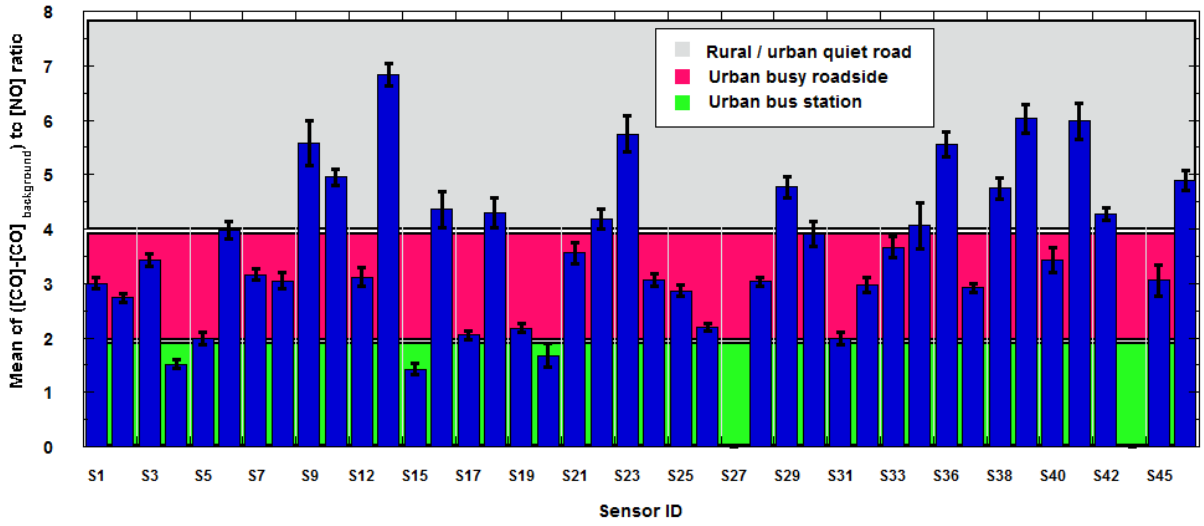

(b)

Figure 7.18. Bar chart showing the ratio of mean (CO-CO $_{background}$) to NO mixing ratios (± 95% confidence interval). (a) Shows five AQ sensors (see figure 7.16) within the static AQ network. (b) All other sensors in the network. Note S27 and S43 are excluded from plot 7.18 (b) because the NO sensors failed during the deployment.

Characteristics of the CO and NO mixing ratio measurements at the five different locations were further investigated by considering the probability distribution (figure 7.19). The right

panels in figure 7.19 depict the high resolution plot of the high mixing ratio regions. The distribution pattern is different among the five locations. The most likely exposure mixing ratios for CO were 210-220 ppb (urban roadside) and 240-250 ppb (urban crossroad). In contrast, the modal mixing ratio range for the rural sites and bus station was 200-210 ppb. The order of decreasing probability of exposure to CO mixing ratios greater than 240 ppb was urban crossroad > urban roadside > rural roadside > rural residential > urban bus station (fig 7.19). Unlike CO species, the distribution pattern for NO mixing ratio was similar for all five locations with the most likely exposure mixing ratio of 0-10 ppb. However the order of decreasing probability of exposure to high mixing ratio is slightly different for NO compared to CO species.

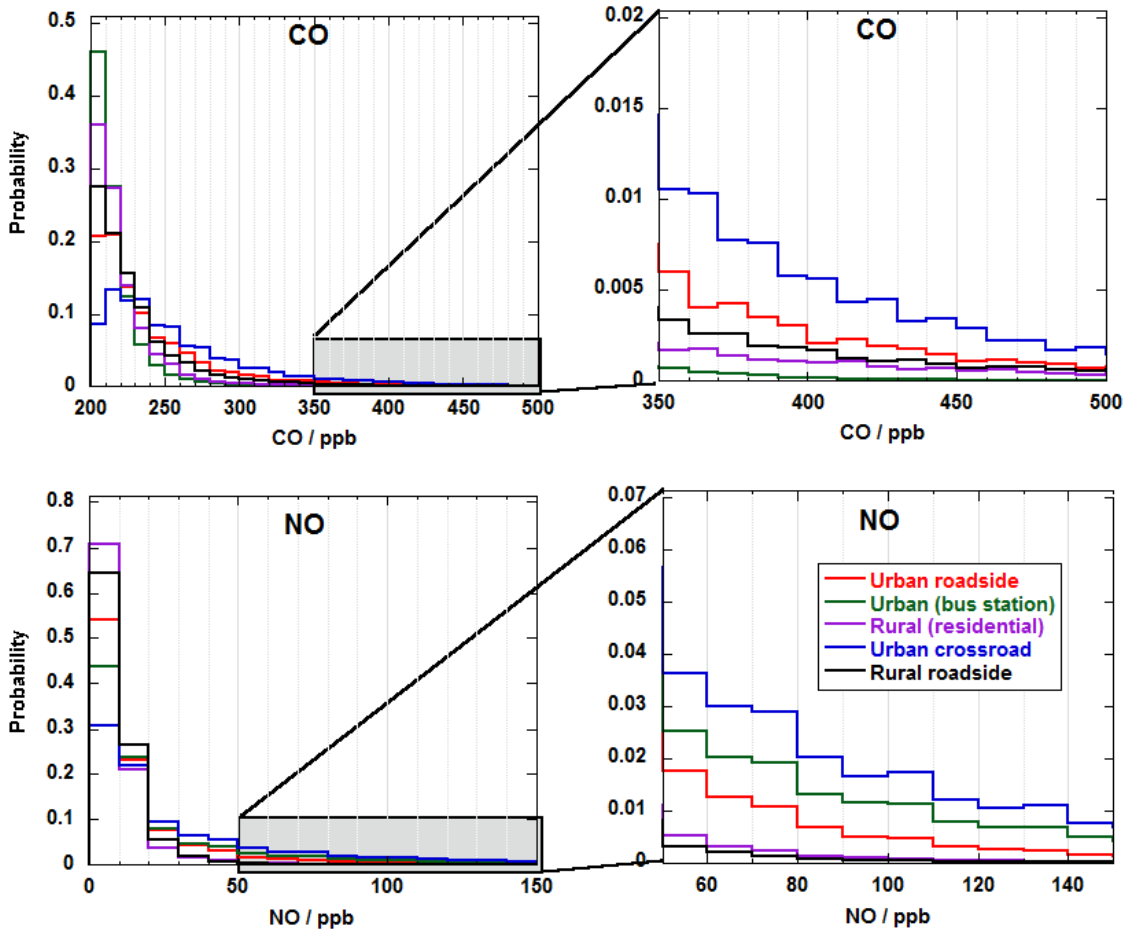

Figure 7.19. Probability distribution plots of CO and NO mixing ratios of five AQ sensors (see figure 7.16) within the static AQ network.

From fig 7.19, the order of decreasing likelihood of exposure to NO mixing ratios greater than 20 ppb were urban crossroad > urban bus station > urban roadside > rural residential >

rural roadside. Just like the result from the mean CO / NO ratio analysis (fig. 7.18), elevated NO mixing ratios were associated with the bus station. One possible reason for the elevated mixing ratios at the crossroad is traffic intensity at this location. This site connects the major road leading to the bus station (Regent Street) with three other roads that lead to north-east (Gonville Place), south-west (Lensfield Road) and south east (Hills Road) of the city centre as shown in the top two maps in right hand panel in fig. 7.16.

7.3.4.3. Attribution of road traffic related pollution sources

Results presented in this section were obtained by utilising the openair pollution analysis tool (see section 7.3.3). Figure 7.20 shows the wind rose plot for two different periods. The left plot represents the wind conditions for most of the AQ sensors (forty four) while the right plot shows the wind conditions for the AQ sensor unit installed at much later time in Coton. In fig 7.20, wind speeds are represented by “paddles” with scales shown at the bottom of each plot. The grey concentric circles depict the frequency (in percents) of the measurement and the wind directions are in bins of 30 degrees. In both plots, the most frequent wind direction is from the SSE which is dominated by wind speeds of 0-2 ms^{-1}. The highest frequency of strong wind events (wind speeds > 6 ms-1) was observed when the wind was blowing from the South, SSW & WSW direction (left plot fig. 7.20) and from North & NNW direction (right plot in fig. 7.20).

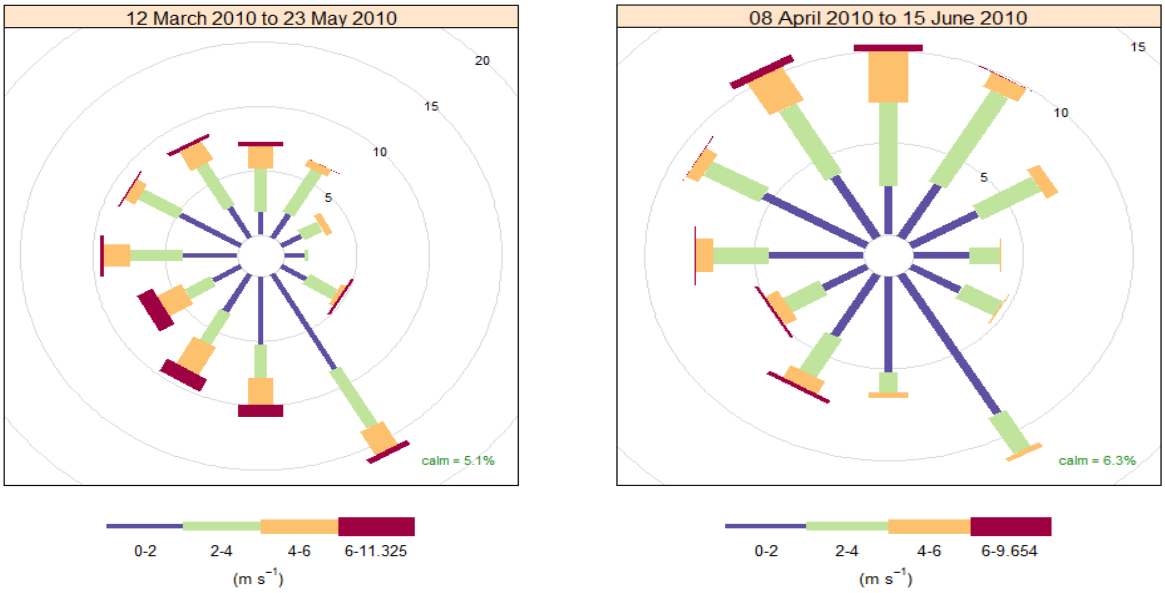

Figure 7.20. Wind rose plots relating wind speed and wind direction during the deployment. The left plot represents measurements from 12th March-23rd May, 2010 while the right plot data from 8th April- 15th June, 2010. Calm represent the percentage of the wind data where the wind speed is zero and are therefore assigned Northerly wind direction [105].

Bivariate polar plots were used to identify pollution sources at the five different environments shown in fig. 7.16. These plots show the relationship between three variables: pollution data (CO / NO measurements), wind speed and wind direction. This plot can be generated on different time scales either as a single plot utilising all data measurements or as 24 hr plots with data sorted by hour of the day. From the top panels in fig. 7.21(a) high mixing ratios in CO (> 280 ppb) and NO (> 35 ppb) were observed along the NE and SW directions. This suggests there is a local source in this direction relative to the sensor location. Figure 7.16 shows that the sensor is actually located to the north of Newmarket Road which runs in the NE direction. High pollution events recorded are due to this road and is observed at both low wind speed < 5ms^{-1} and high wind speed 5-10 ms^{-1}. The hourly plots depicted in the bottom panel fig 7.21(a) also confirm this observation in addition to providing information on how the traffic builds up from the morning at about 0600hrs to peak activity in both CO and NO mixing ratios at 0700 hrs in the SW direction. A similar result was observed for the sensor located in the middle of a crossroad (Lensfield Rd-Hills Rd-Regent Street-Gonville Place) in the urban centre (fig. 7.16). Relative to the sensor

positions Regent Street was located to the NW, Gonville Place to the NE, Hills Rd to the SE and Lensfield Rd to SW. Hills Road accounted for the highest pollution events both in CO and NO measurements (top panel fig. 7.21(b)) which occurred during the evening traffic hours (1600-1700 hrs) as shown in the bottom panel in fig 7.21(b). Bivariate polar plot of the sensor located at the bus station suggests a high CO pollution source when the wind is blowing from the SW direction (top left panel fig. 7.21(c)) which coincides with Emmanuel Road located in the SW direction to the sensor location. In contrast, elevated NO mixing ratios from the SE direction (top right panel fig. 7.21(c)) were attributed to Parker Street which located SE to the sensor position (fig 7.16). Note that between the North and East quadrant in the bivariate polar plots, low mixing ratios were observed for both CO (< 210 ppb) and NO (< 20 ppb). This was attributed to absence of road in that section of the sensor location. This section is actually next to a green park as seen in fig. 7.16 top left two plots. The polar plots for sensors located in the rural sites (fig. 7.16) suggests the highest pollution events were due to local roads in relation to sensor position at each site as seen in fig. 7.21(d) and fig. 7.21(e).

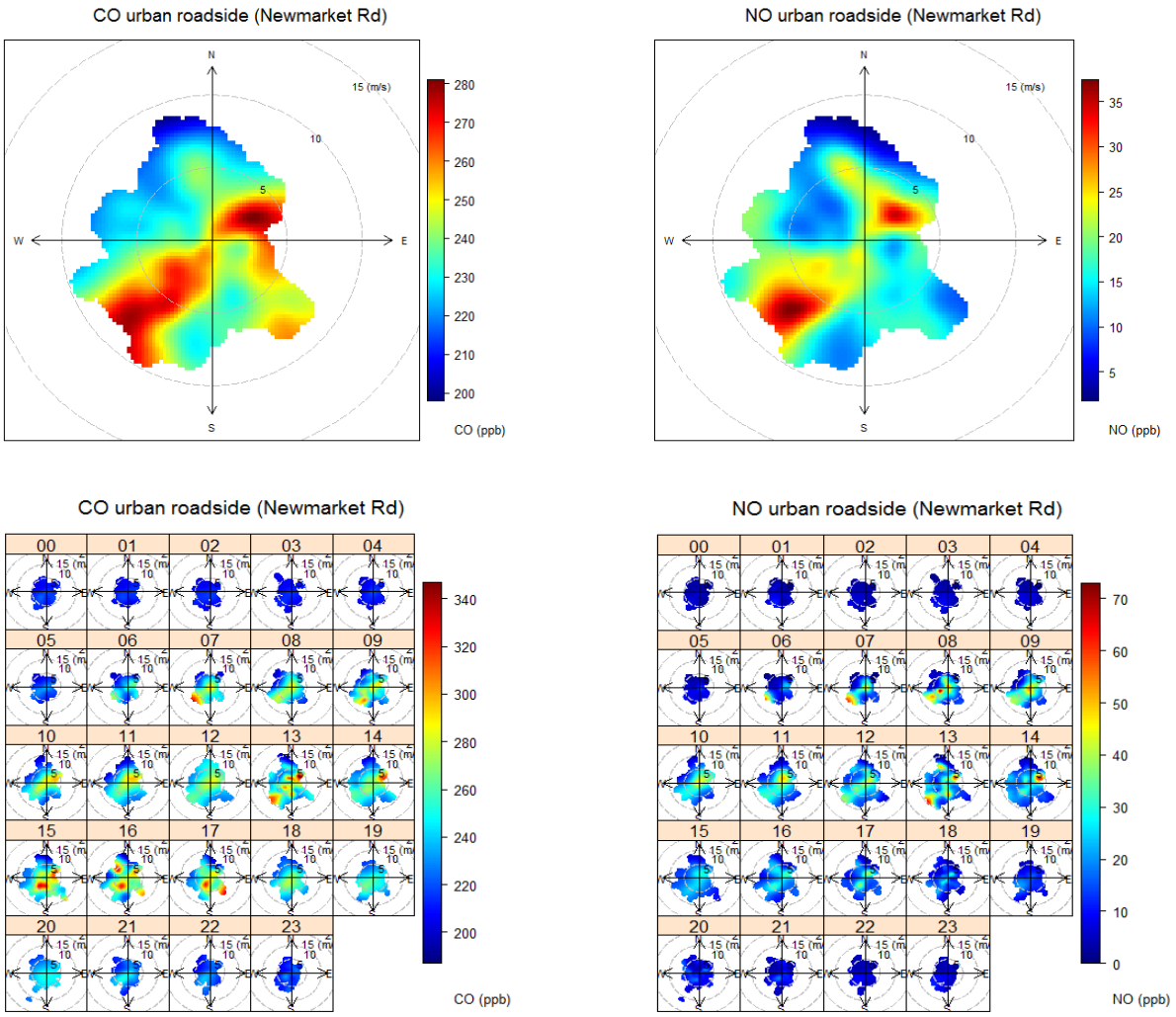

Figure 7.21 (a). Bivariate polar plot of CO and NO measurements from an AQ unit located at urban roadside at Newmarket Road in Cambridge, UK for the three-month AQ network deployment in 2010. The top are generated from all data capture without sorting by time while the bottom plots shows the polar plots by hours of the day.

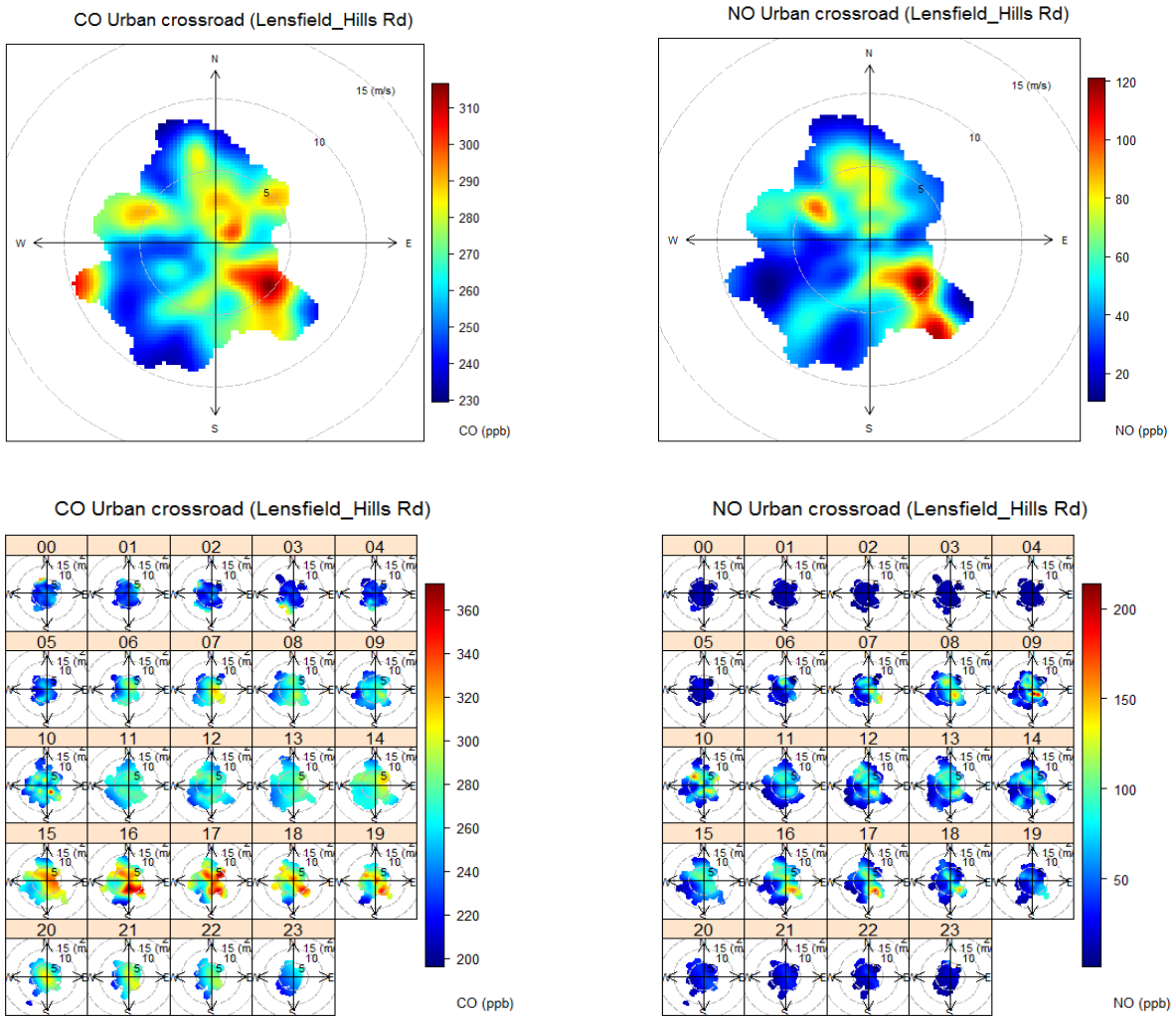

Figure 7.21 (b). Bivariate polar plot of CO and NO measurements from an AQ unit located at urban crossroad between Lensfield Rd, Hills Rd, Regent Street and Gonville Place in Cambridge, UK for the three-month AQ network deployment in 2010. The top are generated from all data capture without sorting by time while the bottom plots shows the polar plots by hours of the day.

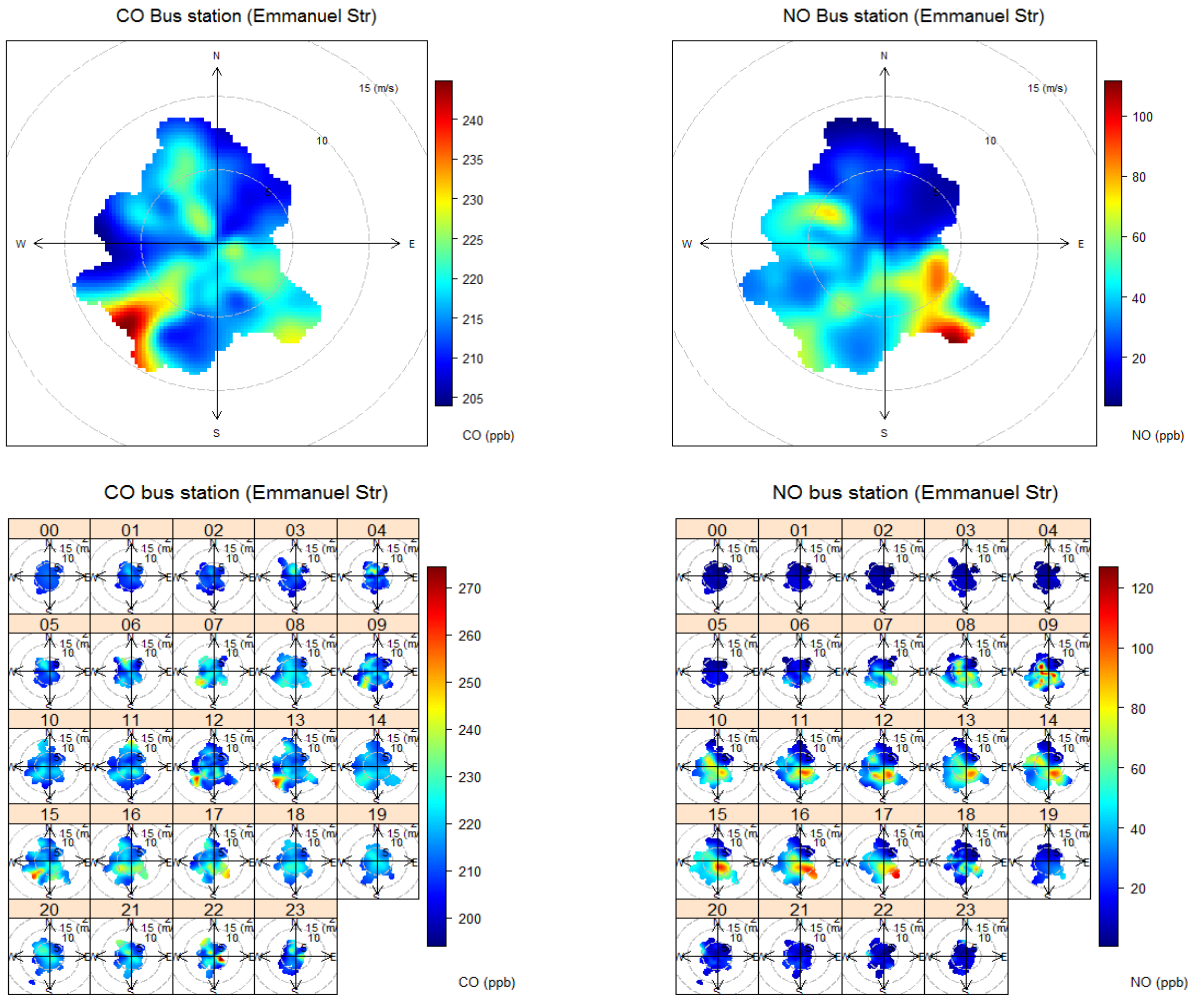

Figure 7.21 (c). Bivariate polar plot of CO and NO measurements from an AQ unit located at urban bus station at Emmanuel Road in Cambridge, UK for the three-month AQ network deployment in 2010. The top are generated from all data capture without sorting by time while the bottom plots shows the polar plots by hours of the day.

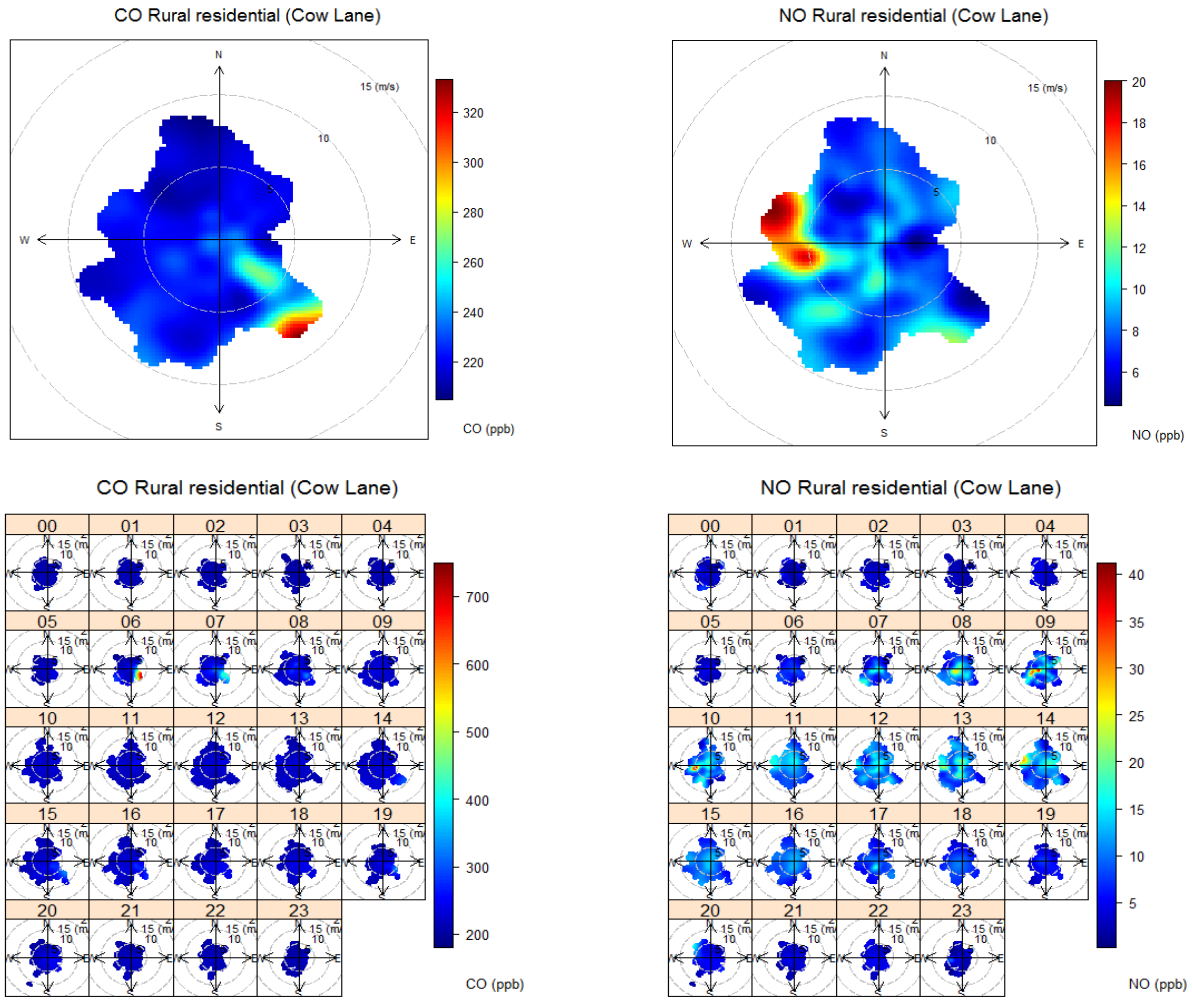

Figure 7.21 (d). Bivariate polar plot of CO and NO measurements from an AQ unit located at rural residential at Cow Lane in Cambridge, UK for the three-month AQ network deployment in 2010. The top are generated from all data capture without sorting by time while the bottom plots shows the polar plots by hours of the day.

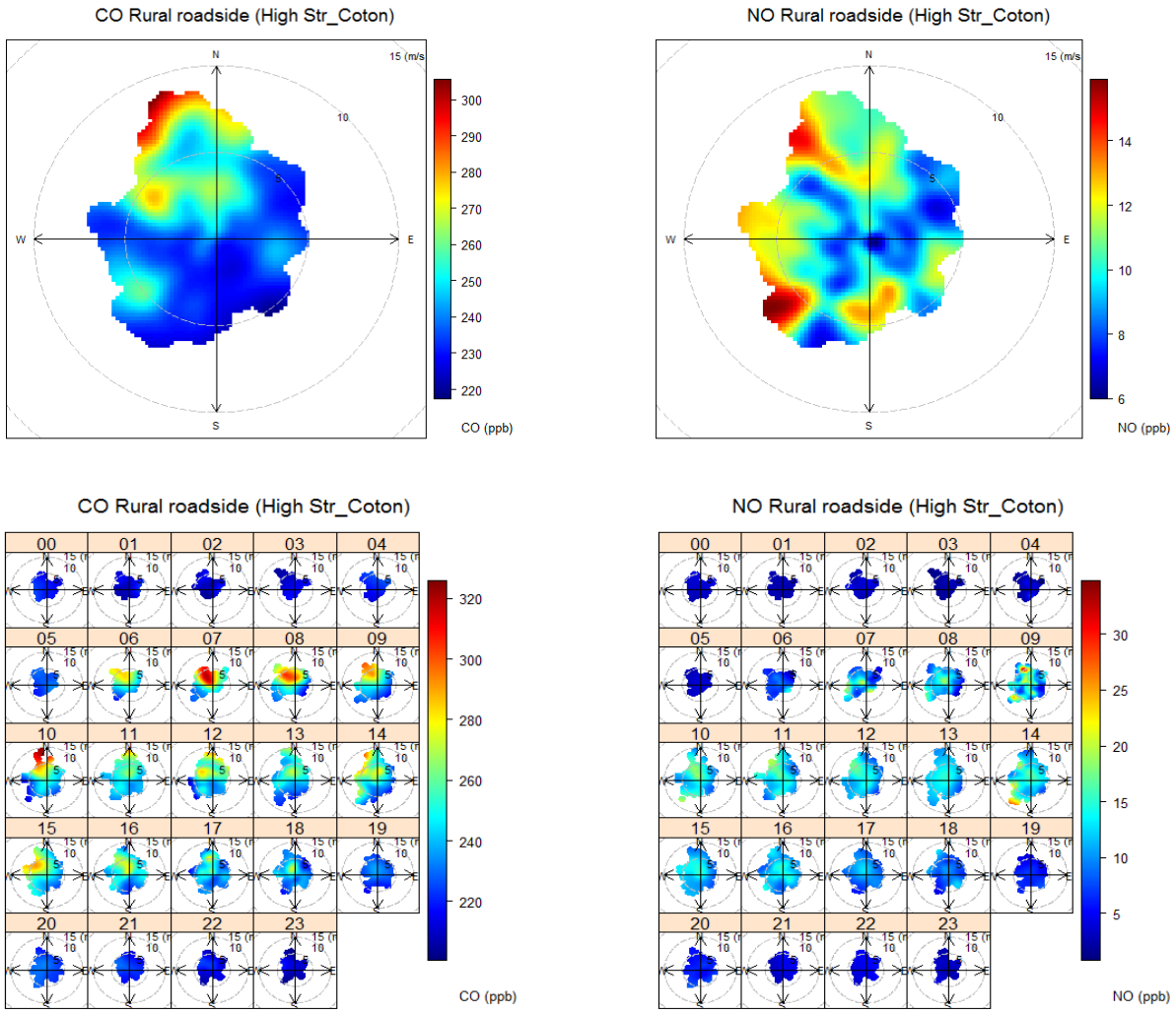

Figure 7.21 (e). Bivariate polar plot of CO and NO measurements from an AQ unit located at rural roadside at High Street Coton in Cambridge, UK for the three-month AQ network deployment in 2010. The top are generated from all data capture without sorting by time while the bottom plots shows the polar plots by hours of the day.

7.3.4.4. Trends in CO and NO mixing ratios during the deployment

Time series averaged over different time scales were used to assess trends in CO and NO mixing ratios during the deployment. Time averages used are: (i) day of the week hourly averages for the entire deployment, (ii) overall hourly average for 24 hr for the entire deployment, (iii) monthly averages for whole time period and (iv) mean daily mixing ratios for the whole time series as shown in plots (a) and (b) in figures 7.22-7.24. Data used for this analysis have been corrected for changing rush hour[25] period due to daylight saving time

[25] Rush hour is defined as period when there is increased in traffic congestion in the city which occurs both in the morning (06:00-10:00 UTC) and evening hours (15:30-18:00 UTC).

(DST). This is important as the rush hour will be one hour earlier in winter compared to summer time in the UK under DST condition (all times are in UTC). In plots (i) and (ii) in both the CO and NO plots of figure 7.22 and 7.23, evidence of morning and evening rush hour can be seen. In contrast, these peak activities were only evident in the CO mixing ratio plot for the rural residential site as shown in plots (i) and (ii) in figure 7.24(a). CO mixing ratio trends downward at the three locations considered in this analysis as shown in plot (iii) in figures 7.22(a)-7.24(a). Except for sensor located at the cross road (figure 7.22) where there is an increase monthly mean NO mixing ratio from March to April then a decrease in May, there was a general downward trend in the other two locations (figures 7.23-7.24). These monthly mean trends in CO mixing ratios are not highly significant as the range is < 5 ppb in all the three locations. However the downward trend in monthly mean NO mixing ratio at the bus station (figure 7.23(b) iii) is significant as there was about 50 % reduction between March and May. “Weekend effect” occurs when there is reduced road traffic pollution mixing ratio on weekends relative to weekdays. This is often related to reduction in traffic volume during weekends compared to workdays. This effect was clearly visible in the CO and NO mixing ratio plots from all three sites as seen in plots (i) & (iv) in figures 7.22-7.24. There was significant reduction (40 – 50 ppb) in mean NO mixing ratios especially on Sunday at the urban sites (crossroad and bus station) compared to measurements during the weekdays as shown in fig. 7.22(b) iv and 7.23(b) iv.

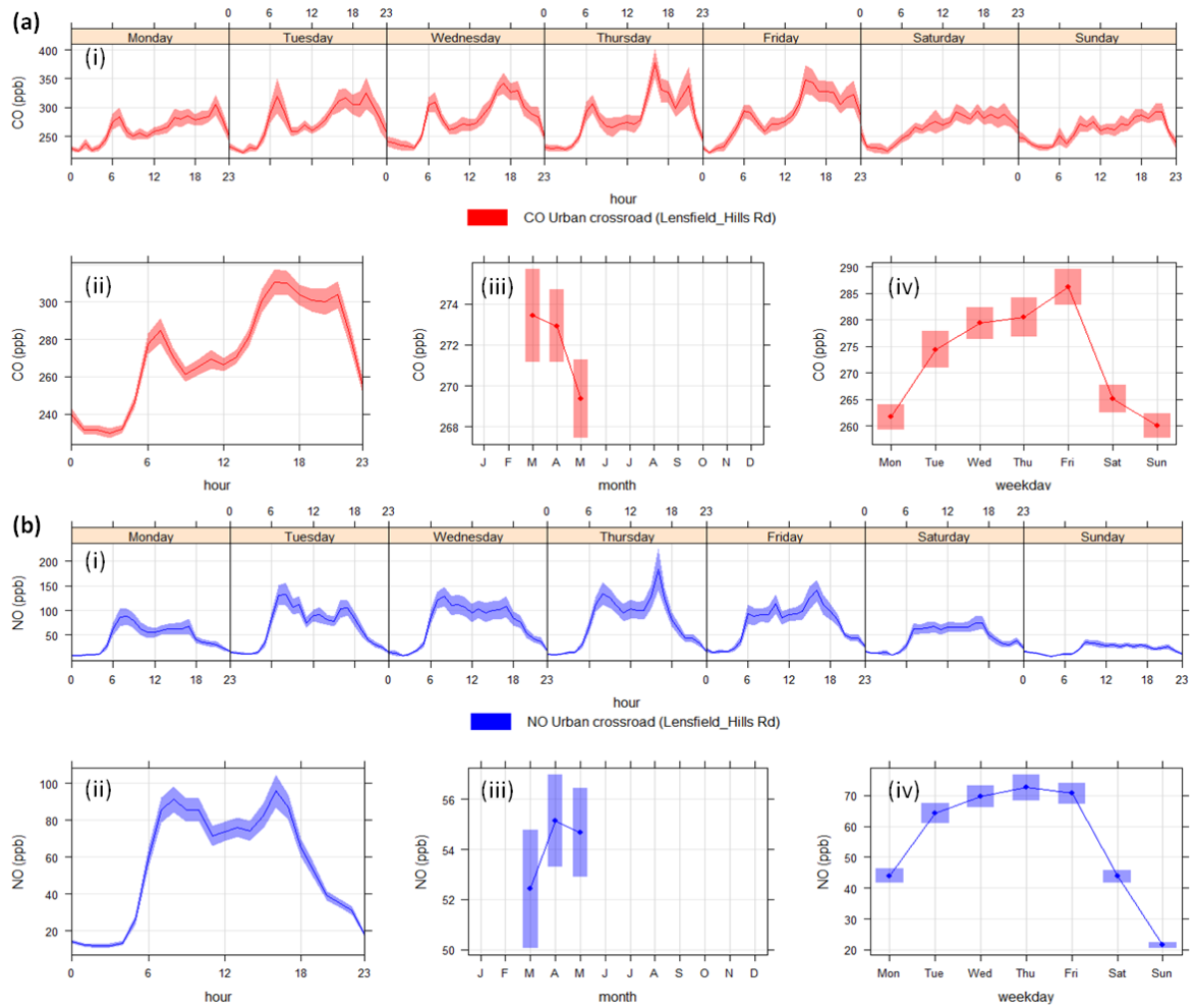

Figure 7.22. Time series corrected for change in rush hour time due to daylight saving time (a) Four time series (i-iv) averaged over different time scales of 10 minutes averaged CO mixing ratios at Lensfield Road, Hills Road, Gonville Place and Regent Street crossroad, Cambridge (12th March-23rd May, 2010). (b) Four time series (i-iv) averaged over different time scales of 10 minutes averaged NO mixing ratios at Lensfield Road, Hills Road, Gonville Place and Regent Street crossroad, Cambridge (12th March-23rd May, 2010). Note the shading represents 95% confidence interval about the mean for each plot.

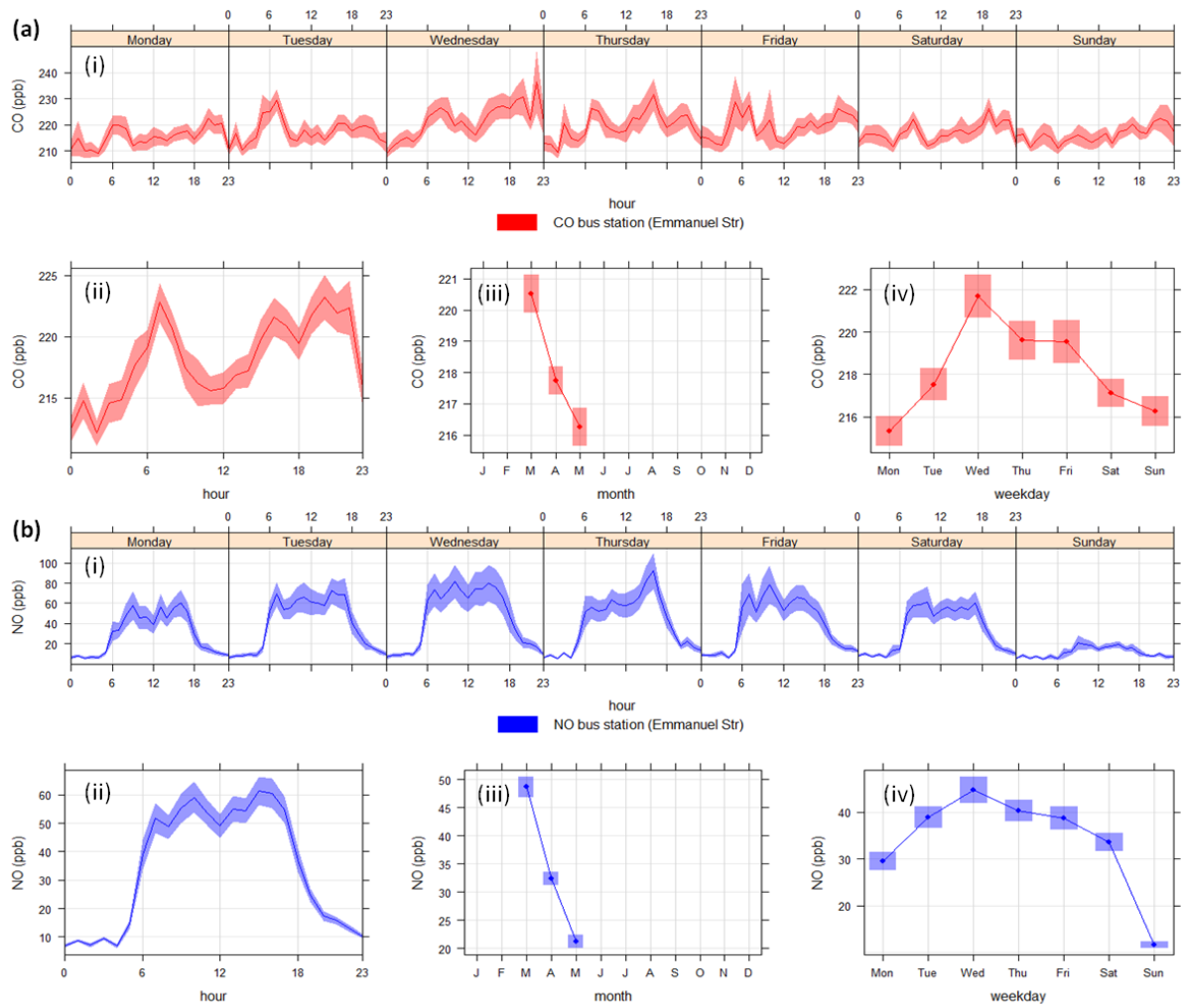

Figure 7.23. Time series corrected for change in rush hour time due to daylight saving time (a) Four time series (i-iv) averaged over different time scales of 10 minutes averaged CO mixing ratios at urban bus station Emmanuel Road, Cambridge (12th March-23rd May, 2010). (b) Four time series (i-iv) averaged over different time scales of 10 minutes averaged NO mixing ratios at urban bus station Emmanuel Road, Cambridge (12th March-23rd May, 2010).

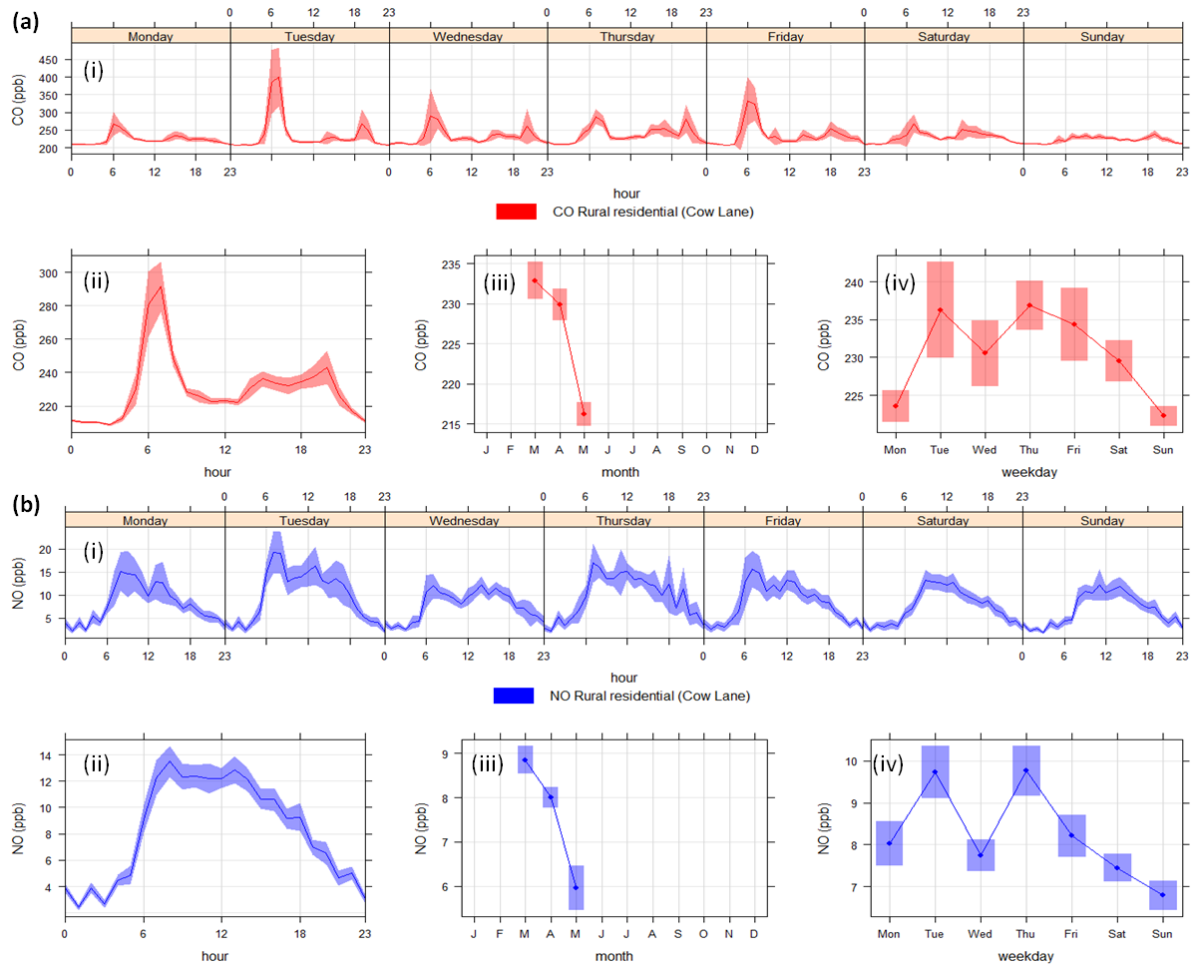

Figure 7.24. Time series corrected for change in rush hour time due to daylight saving time (a) Four time series (i-iv) averaged over different time scales of 10 minutes averaged CO mixing ratios at rural residential site Cow Lane, Cambridge (12th March-23rd May, 2010). (b) Four time series (i-iv) averaged over different time scales of 10 minutes averaged NO mixing ratios at rural residential site Cow Lane, Cambridge (12th March-23rd May, 2010).

7.3.4.5. Evidence of street canyon effects

The AQ sensor located in Regent Street opposite the AURN station provided a unique layout to study street canyon effect. This is possible because the instruments (the AQ unit and the AURN station) were located on either side of the street as depicted in fig. 7.25. Regent Street runs North Westerly relative to the AURN site and a crosswind blowing from the North-easterly direction (fig. 7.25) will result in an idealised street canyon effect as depicted in figure 7.26. Although the two sensors were not closely co-located, they were in a similar environment and as a result pollution measurements from the two instruments were expected to show similar trends. The time series of NO mixing ratio shows that the two

measurements track each other well for periods when the wind direction lies outside 0^o to 90^o (from the northerly, north-easterly and easterly directions) as shown in fig. 7.27. As stated earlier, wind blowing between 0-90 degrees will result in a perfect crosswind leading to street canyon effect that results in high mixing ratios upwind of the re-circulated air (at the AQ site) and low mixing ratios downwind of the re-circulated air (at the AURN site) as shown in fig. 7.26. Bivariate polar plot is useful in the quick identification of the street canyon effects. This phenomenon is spotted in a plot when high mixing ratios are observed when wind is blowing away from the sensor location. Figure 7.28 shows the bivariate polar plot for NO and NO_2 measurements at the AURN station. High mixing ratio events (> 40 ppb for NO and > 25 ppb NO_2) along the SE and NW direction are attributed to Regent Street which runs along this direction as shown in fig. 7.25. Note the low mixing ratios in NO and NO_2 observed from the NE direction. Similarly the bivariate polar plot of the CO and NO measurements from the AQ sensor show elevated CO (240-255 ppb) and NO (40-60 ppb) mixing ratios when the wind direction is parallel to Regent Street as depicted in fig. 7.29. However the highest mixing ratio events for CO (> 260 ppb) and NO (> 120 ppb) occurred when the wind is blowing away from the sensor (from the NE direction) as shown in fig. 7.29. This shows that for this wind condition, the AQ sensor recorded elevated gas pollutant mixing ratios compared to the monitor at the AURN site (see figures 7.27 and 7.30). When the wind conditions were reversed, in this case when wind was blowing from the SW direction, the street canyon effect was still observed but with the reversed re-circulation in the canyon resulting in elevated mixing ratios at the AURN site compared to low mixing ratios at the location of static AQ sensor. This can be seen in figure 7.30 where NO mixing ratio > 40 ppb were observed at the AURN station compared with values < 35 ppb recorded at the AQ site for winds blowing from the SW direction.

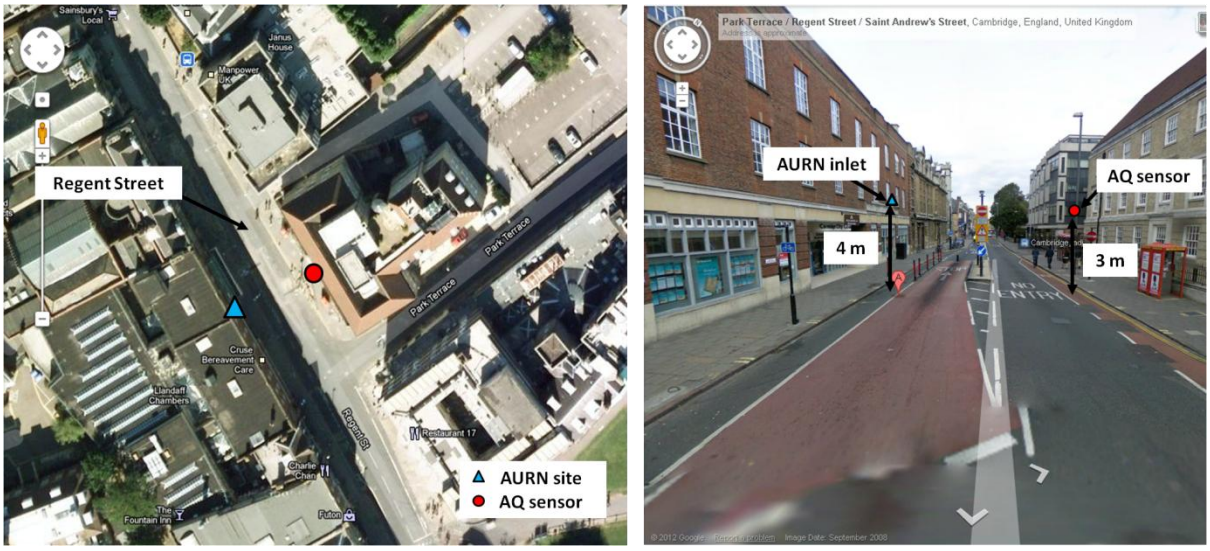

Figure 7.25. Map showing locations of static AQ unit and AURN site relative to Regent Street in Cambridge, UK. Map courtesy Google Map (Tele Atlas, 2012) [109].

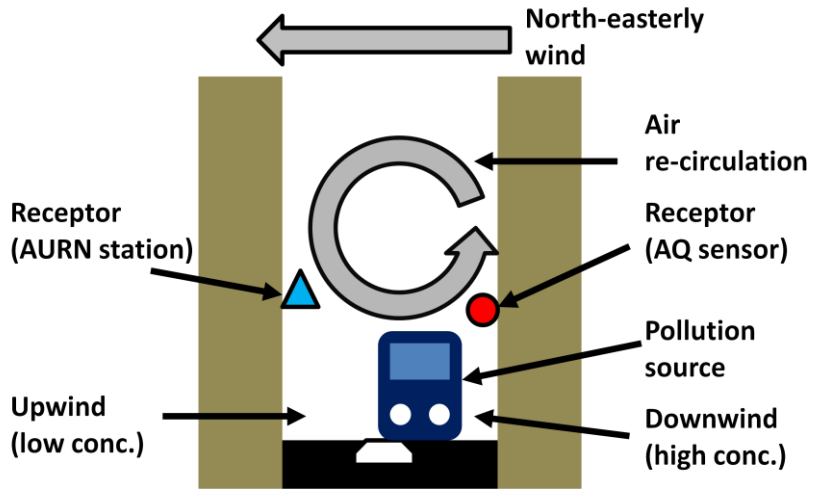

Figure 7.26. Conceptualised street canyon effect in Regent Street, Cambridge showing air re-circulation for a north-easterly crosswind.

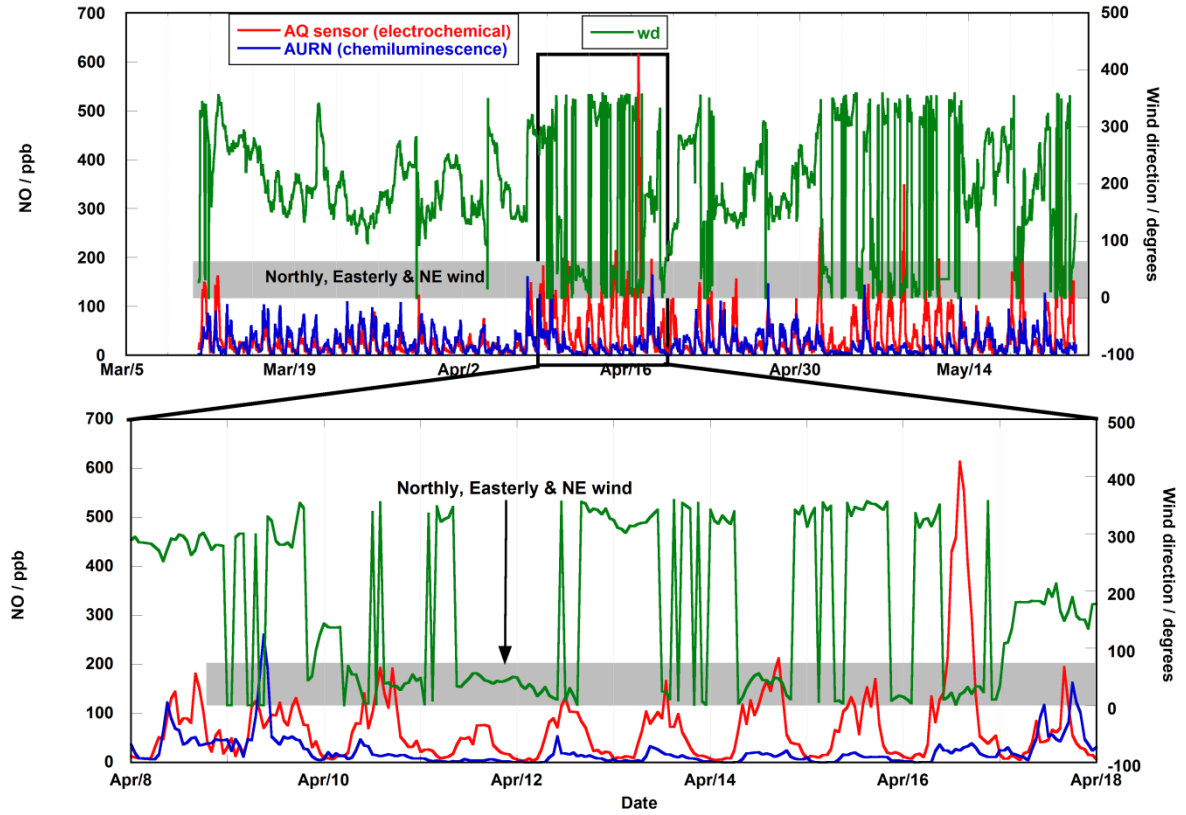

Figure 7.27. Time series of hourly mean wind direction and NO measurements from the AURN (chemiluminescence instrument) and AQ (electrochemical) sensor in Regent Street, Cambridge. The top plot shows data measurement between 12th March-23rd May, 2010 while the bottom plots show a measurement between 8th April-18th April highlighting the large difference in NO mixing ratios between the two instruments.

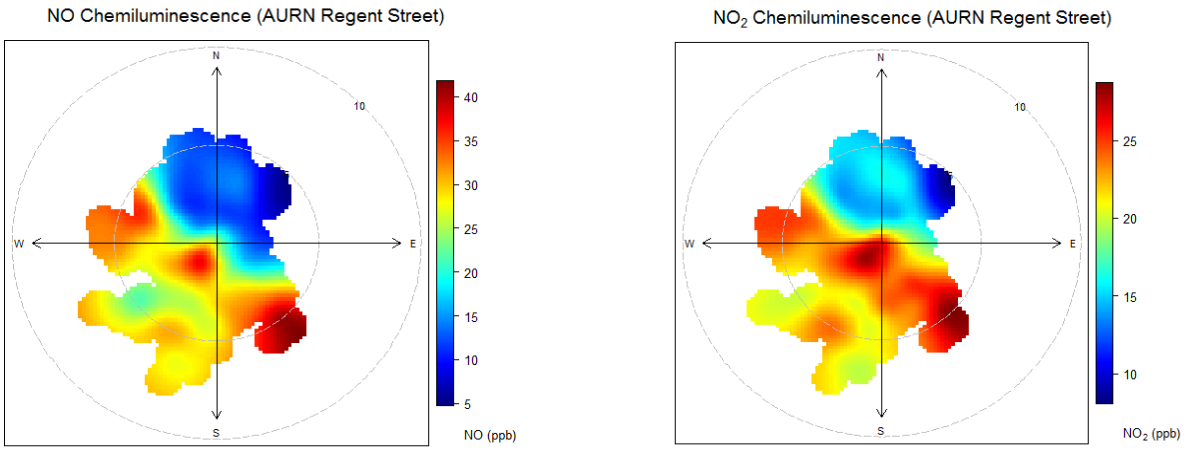

Figure 7.28. Bivariate polar plots of NO and NO_2 measurements from the chemiluminescence instrument at the AURN station in Regent Street, Cambridge.

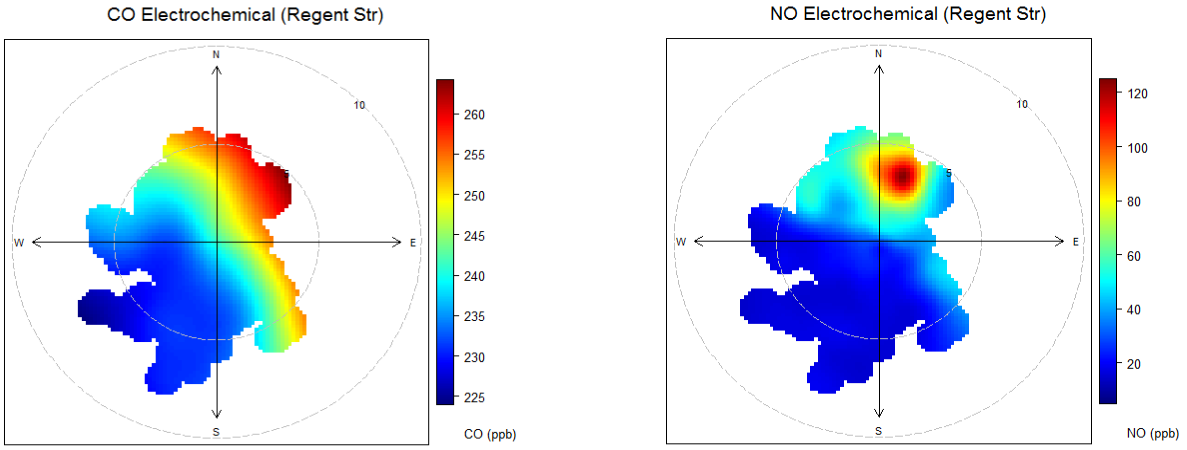

Figure 7.29. Bivariate polar plots of CO and NO measurements from the electrochemical AQ sensor instrument on Regent Street, Cambridge.

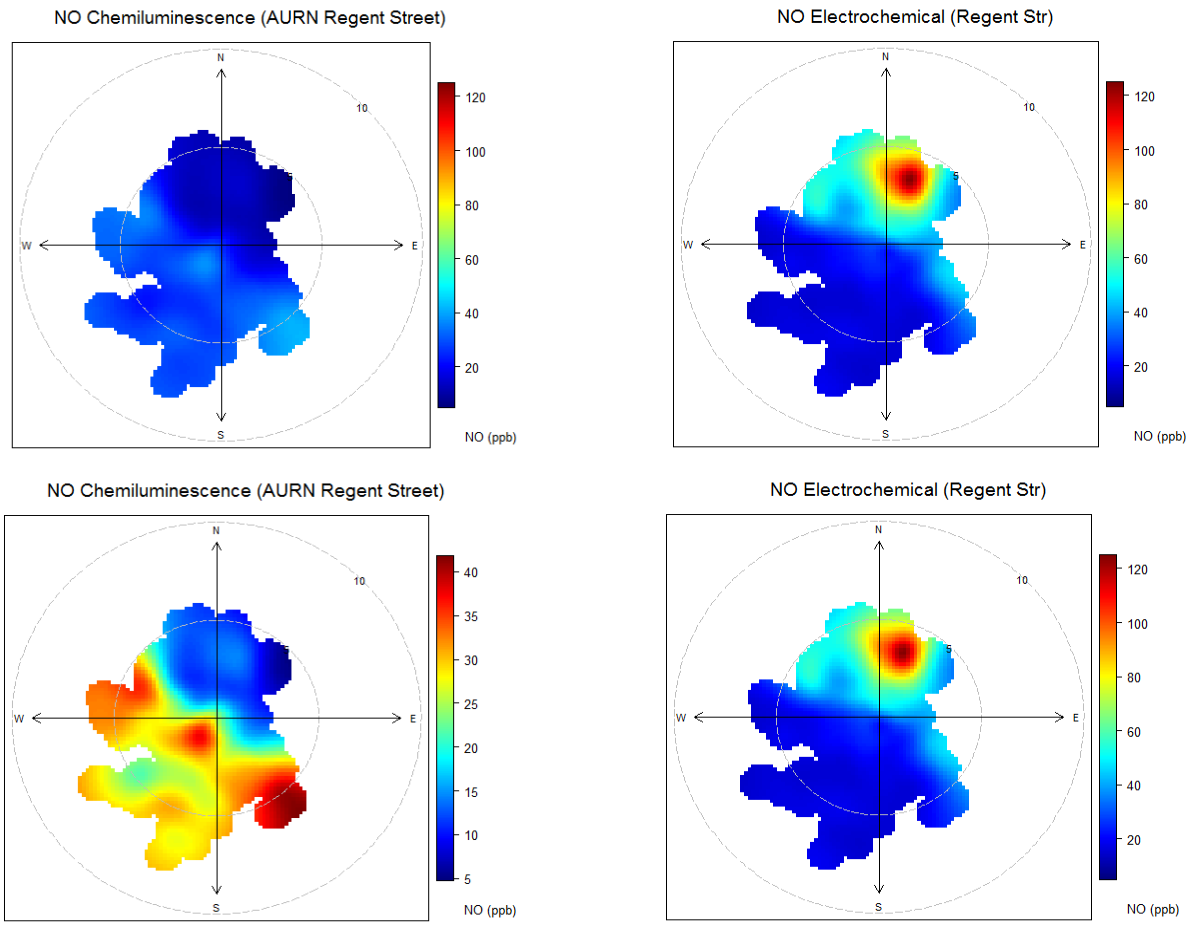

Figure 7.30. Bivariate polar plots of NO measurements comparing measurements between the AURN station and the AQ sensor in Regent Street, Cambridge. Top panel show plots with the same mixing ratio scale, while the bottom panel represent plots with different scales to highlight pollution events.

7.3.4.6. Comparison between AQ sensors and LAQN stations

In the previous section NO measurements between the AURN station and the nearest static (electrochemical) AQ sensor was considered. It was shown that the measurements are correlated under certain wind conditions. In this section NO mixing ratio from two LAQN stations will be compared with measurements from the electrochemical AQ sensors nearest to these stations. The monitoring stations considered include the site in Parker Street (close to the bus station) and the one in Newmarket Road (see fig. 7.31).

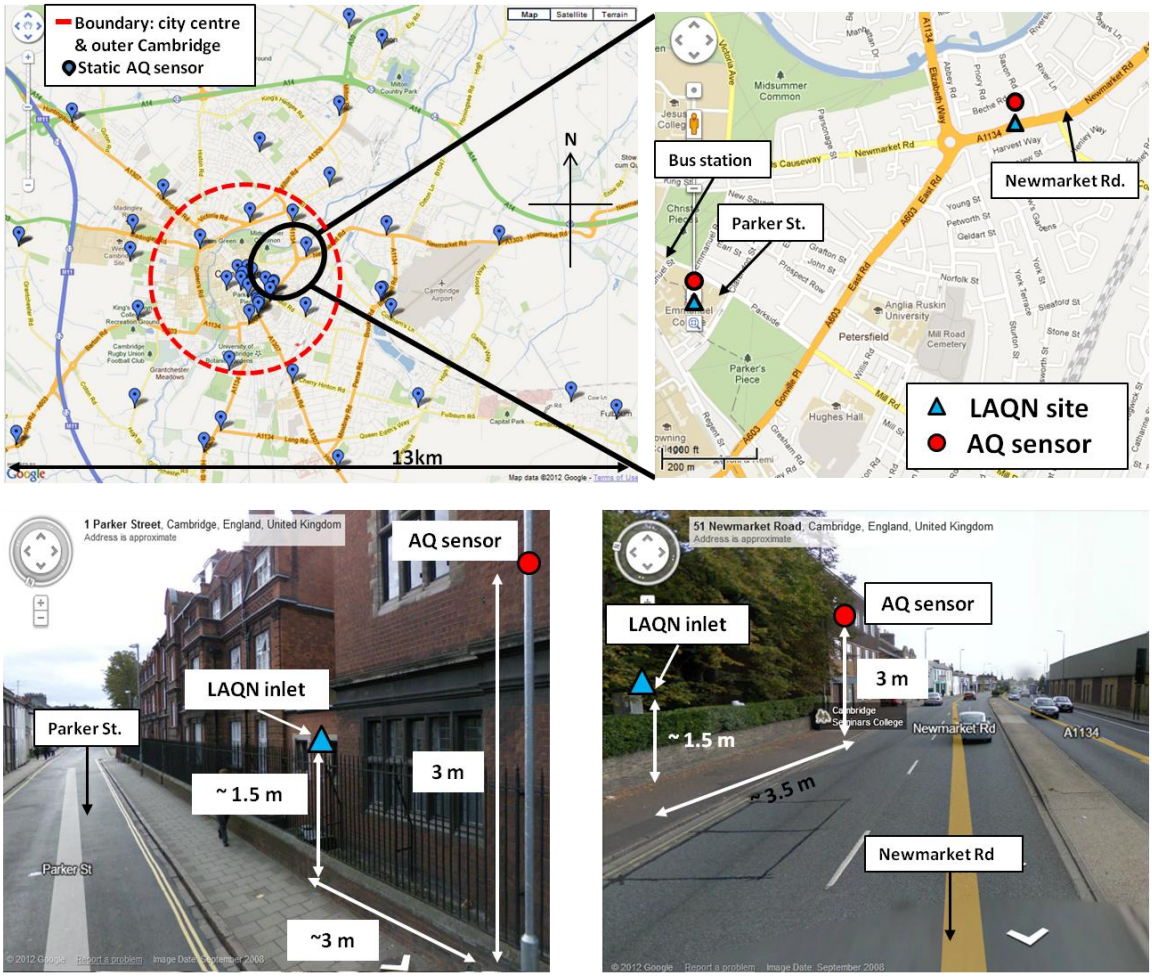

Figure 7.31. Maps showing locations of static AQ sensor instruments relative to positions of the LAQN stations on Parker Street and Newmarket Road in Cambridge, UK. Map courtesy Google Map (Tele Atlas, 2012) [109].

These LAQN sites only monitor NO and NO_2 gas species using the chemiluminescence instrument. As earlier stated only CO and NO measurements from the AQ sensor network are reported for this deployment, hence the NO measurements were used for the intercomparison study. Unlike the AQ sensor which was installed opposite to the AURN site in Regent Street, the AQ sensors at Newmarket Road and Parker Street were both installed on lamppost on the same side of the road as the monitoring station (see fig. 7.31). However the AQ sensors were approximately 1.5 meters higher than the sampling inlet at these two stations as shown in fig. 7.31. Time series and correlation plot for the site in Parker Street show good agreement for the NO measurements from the two instruments as depicted in fig. 7.32. A correlation coefficient of 0.7 was observed for the measurements between the two systems with a gradient of 0.87 (fig 7.32). This is a good agreement between the two

instruments given they are sampling at different heights and a small horizontal distance (~3 m) from each other (bottom panel fig 7.31). Although the two instruments (the chemiluminescence and electrochemical AQ sensor) were located in a street which has tall buildings on either side that can result in canyon effect, any weather anomaly will affect the two instruments in a similar way. The slight deviation from the 1:1 line is expected given that the two instruments were not closely co-located.

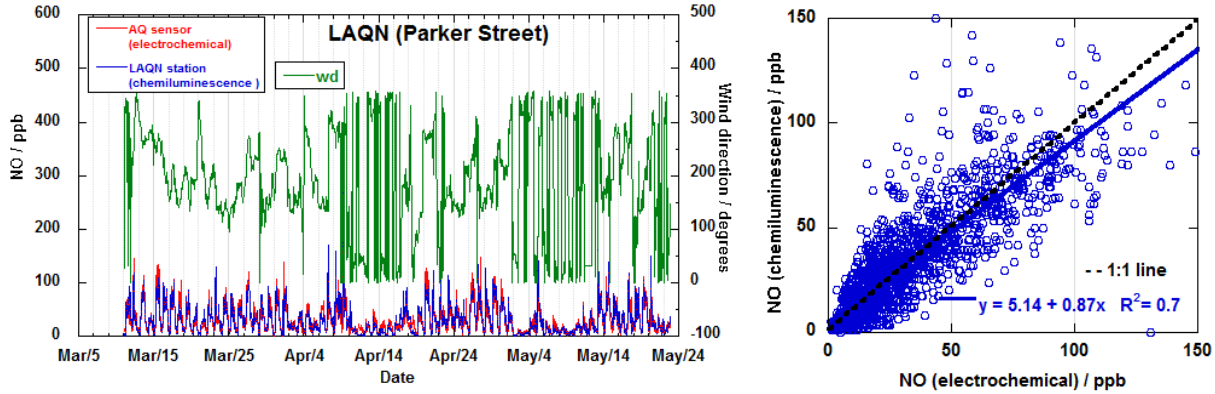

Figure 7.32. Time series and correlation plots of hourly mean NO measurements from the LAQN (chemiluminescence instrument) and AQ (electrochemical) sensor at Parker Street, Cambridge for data between March-23rd May, 2010.

However results of the comparison study in Newmarket Road show poor agreement even though the two instruments were located on the same side of the road. A correlation coefficient of 0.36 was observed for the NO measurements between the LAQN station and the AQ static sensor (right plot top panel figure 7.33). Careful inspection of the time series shows that there were large differences in the NO mixing ratios between the two instruments when the wind is blowing between 0 to 60 degrees (top panel fig 7.33). This was also observed in the bivariate polar plots of NO mixing ratios for the two instruments (fig. 7.34). The fact that the AQ sensor unit was detecting elevated NO mixing ratios when the wind is blowing along Newmarket Road in both directions (NE and SW directions) while LAQN is experiencing similar pollution event only from the SW direction suggests that there is structural obstruction to the air when it was blowing from the NE direction. Figure 7.31 shows that the LAQN station is actually located to the south of the building nearest to the lamppost onto which the AQ sensor is installed. When NO measurements corresponding to wind directions between 0 to 60 degrees were removed from the comparison data,

improved correlation was observed between the two measurements with R^2 = 0.52 (bottom plot fig. 7.33). The correlation coefficient still suggests some differences between the NO mixing ratios from the two instruments and this was partly attributed to the fact that the two instruments were not closely co-located as shown in figure 7.31.

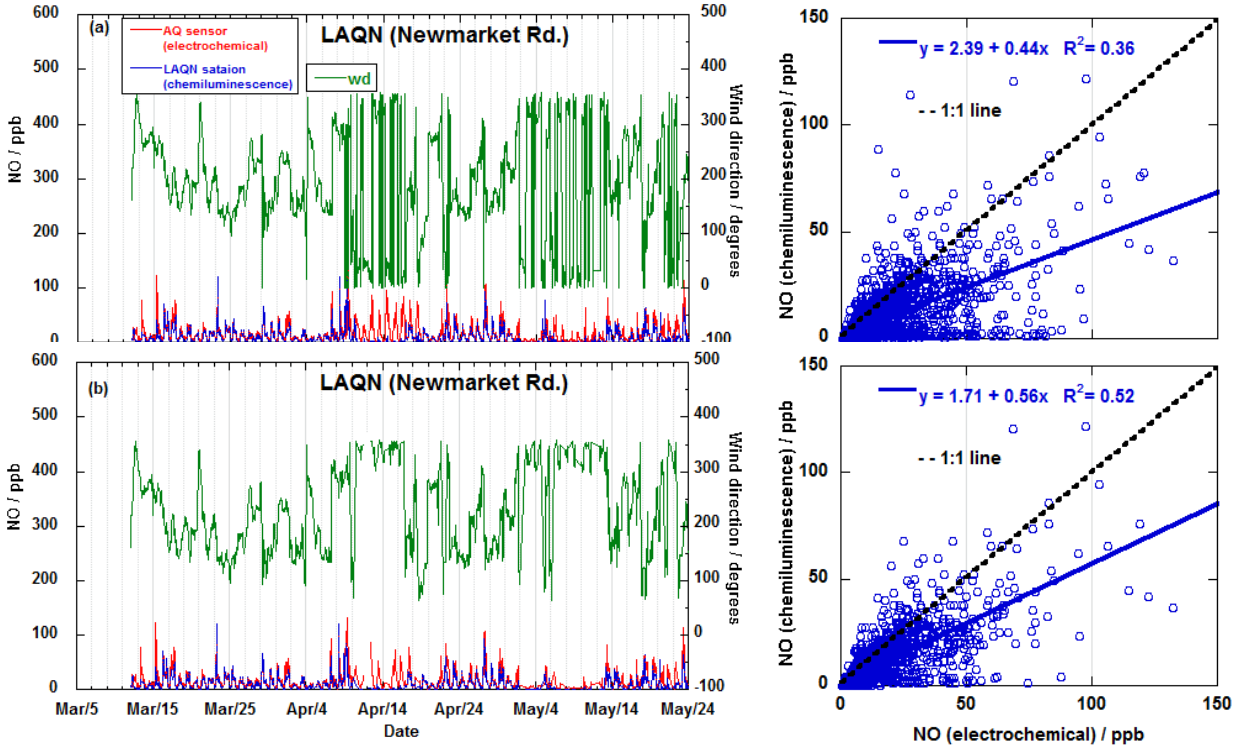

Figure 7.33. Time series and correlation plots of hourly mean NO measurements from the LAQN (chemiluminescence instrument) and AQ (electrochemical) sensor at Newmarket Road, Cambridge for data between March-23rd May, 2010. (a) Represents all data collected during the deployment. (b) Shows plot for all data except when the wind was blowing between 0-60^o directions.

Similar pollution pattern were observed in the polar plots (fig. 7.35) of the other gas species measured at this site. These species include NO_2 (monitored at the LAQN site using chemiluminescence technique) and CO (measured by the static electrochemical AQ sensor unit). Note the pollution events from the SE direction in fig. 7.34 and fig. 7.35 correspond to SE crosswind which transports pollution from Newmarket Road to the monitoring instruments. Measurements for periods when the wind direction is between 0-60 degrees accounts for approximately 16% of the total data collected for the duration of the campaign. These results show that while pollution measurements from the AQ sensor were truly

representative of roadside pollution for this site, the LAQN station only show similar results for situations in which the wind was not blowing from NE direction (in this case only 84% of the LAQN data truly represent roadside measurements).

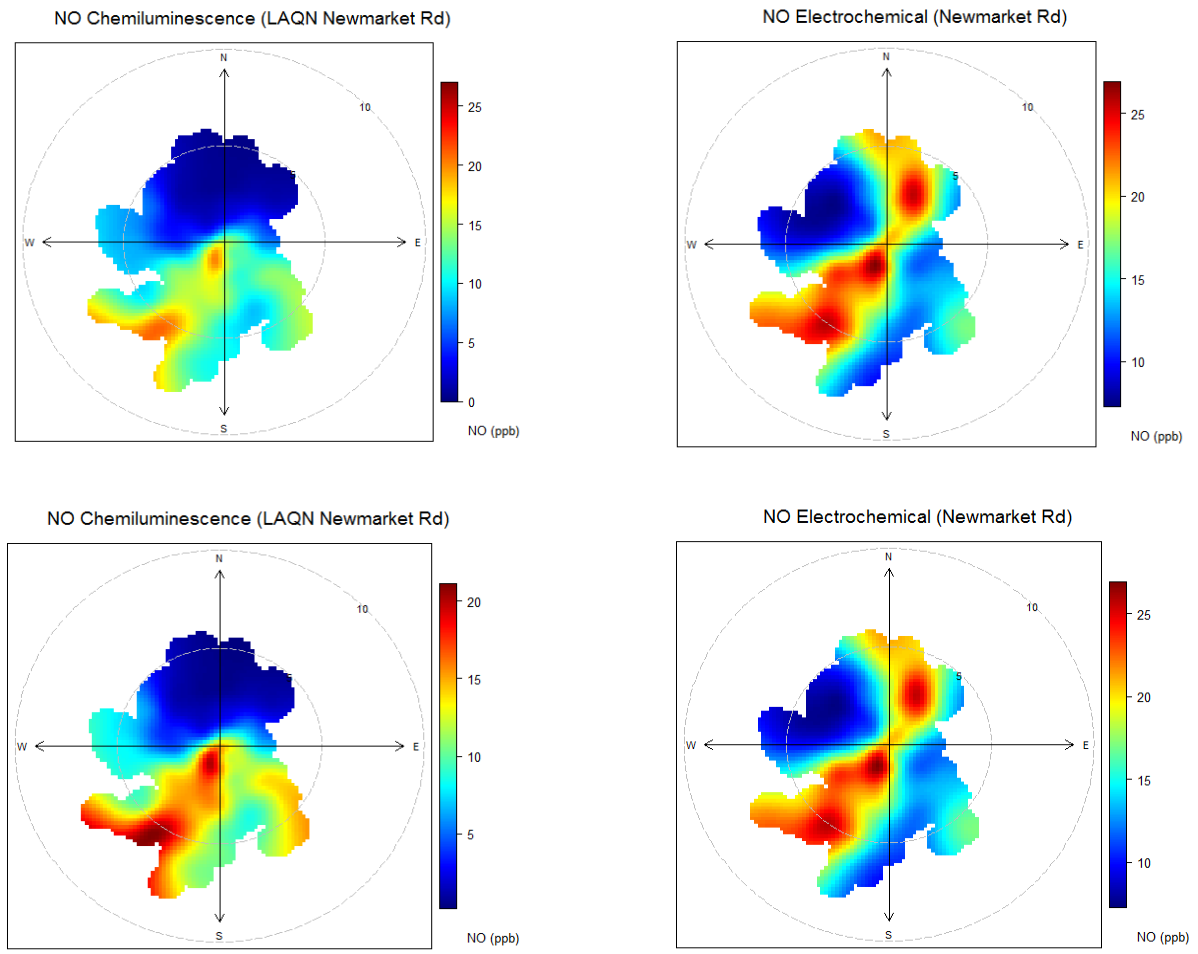

Figure 7.34. Bivariate polar plots of NO data comparing measurements between the LAQN station and the AQ sensor in Newmarket Road, Cambridge. Top panel shows plots with same mixing ratio scale, while the bottom panel represents plots with different scales to highlight pollution events.

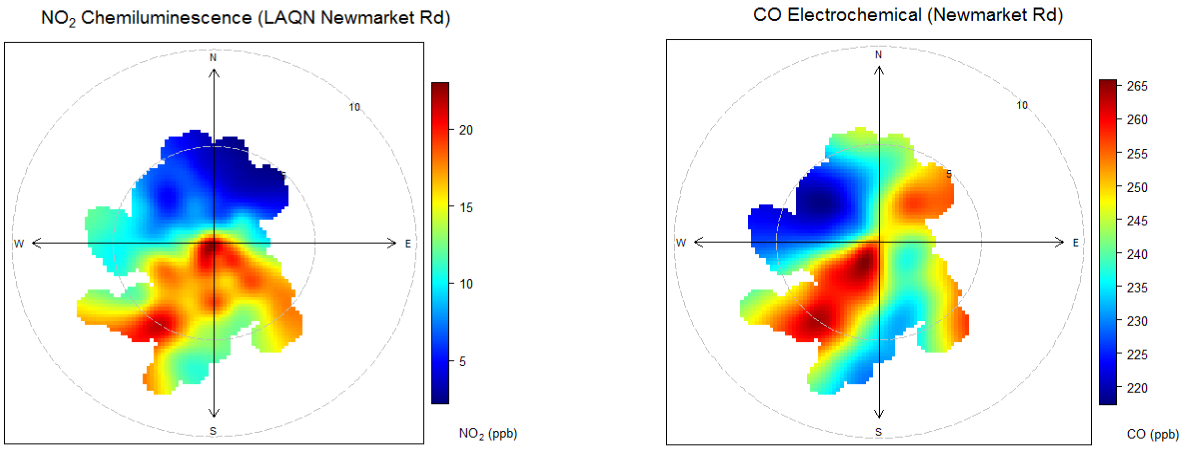

Figure 7.35. Bivariate polar plots of NO and CO mixing ratios (electrochemical using chemiluminescence instrument (LAQN station) and electrochemical AQ sensor unit respectively in Newmarket Road, Cambridge.

7.3.4.7. Investigating the possible atmospheric urban heat island (UHI) phenomenon in Cambridge, UK

While not part of the AQ studies, it also proved possible to explore atmospheric UHI using temperature measurements from the AQ network. The network was divided as urban and rural / semi-urban sites based on their locations relative to the city centre as shown in figure 7.36.

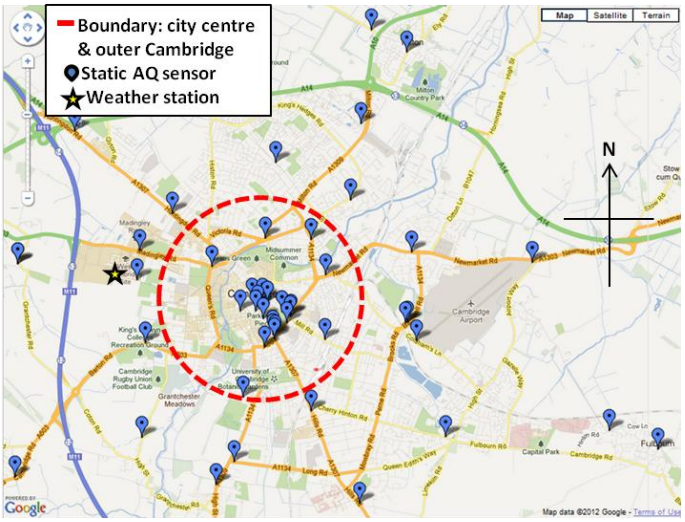

Figure 7.36. Map showing network of static AQ sensors deployed in Cambridge between March and June 2010. Also shown is the location of the weather station. Map courtesy Google Map (Tele Atlas, 2012) [81].

Urban site represents all AQ instruments within the boundary shown in figure 7.36 with the rest of the AQ instruments classified as semi-urban / rural site. Figure 7.37 shows typical plots of hourly mean temperature measurements from the weather station and one AQ instruments located in the urban site. Note the measurements from the weather station were consistently below that from the AQ unit possibly because of the different heights these measurements were made. The weather station is located at approximately 14 m above the ground level compared to the AQ instruments which were at a height of 3 m. The hottest days during the deployment were in May as shown in fig. 7.37. As a result, temperature measurements from the month of May 2010 were used for generating the twenty-four hour mean temperature measurements for sensors located in the urban and semi-urban / rural sites (fig. 7.38). Although the temperature profile of the semi-urban / rural sites was consistently higher than that of the urban site during day time, the pattern is reversed after sunset. This type of temperature profile is characteristic of atmospheric UHI as reported by Oke T.R. [119]. Higher temperature at the rural / semi-urban site during the day time was due to a faster rate of warming of the air at this environment compared to urban area. The difference in temperature between the two sites (black line fig. 7.38) is a measure of the heat island intensity. It has been reported that on a clear and calm night, the heat island intensity starts increasing after mid-day and reaches a maximum just after sunset as shown in left panel in fig. 7.39. Both the idealised and real UHI represented in figure 7.39 both show similar diurnal temperature profile for the urban and rural environment. This type of temperature evolution is characteristic of atmospheric urban heat island [119]. Although there is evidence of atmospheric UHI in Cambridge city centre during this deployment, the strength of atmospheric UHI in terms of temperature difference is small with a maximum of 0.93^{o} C (figure 7.39 right panel).

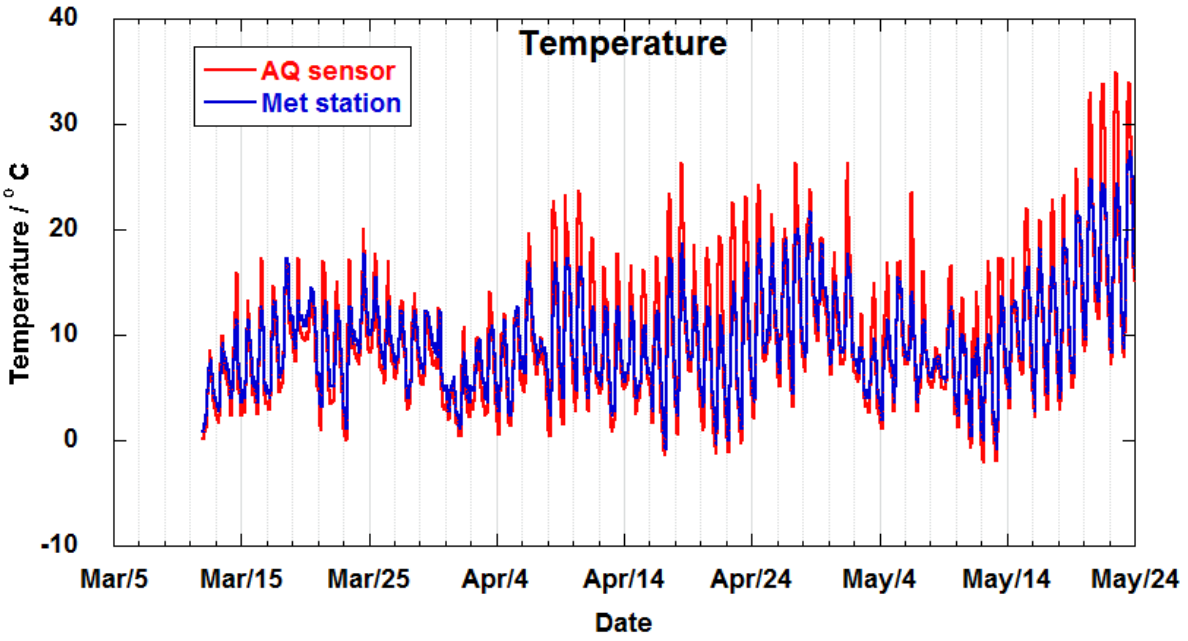

Figure 7.37. Time series showing hourly mean temperature measurements from one AQ unit and the weather station in Cambridge, UK (March-23rd May, 2010).

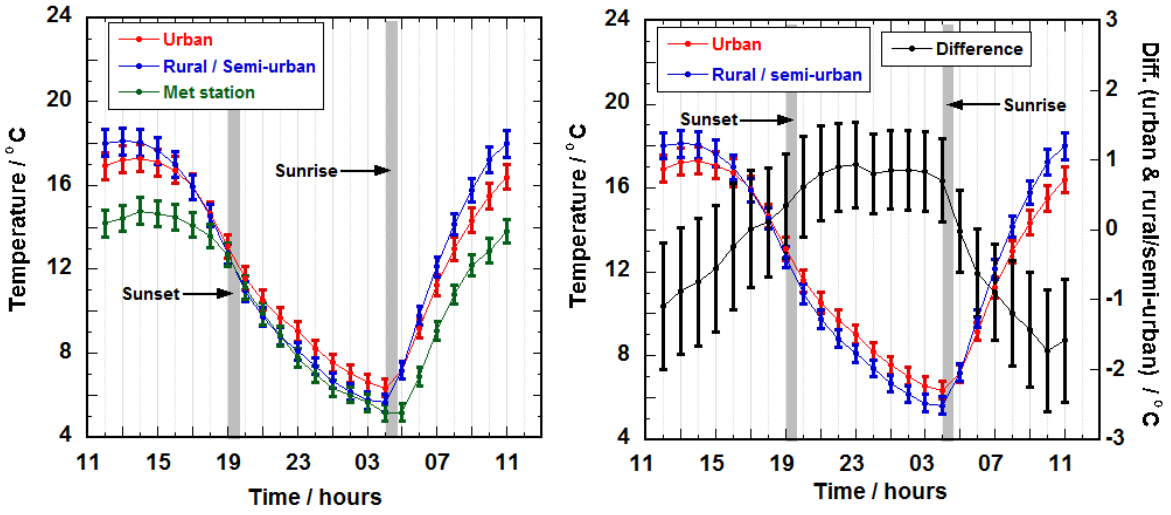

Figure 7.38. Twenty four hour mean temperature (± 95% confidence interval) profile of the hottest month (4th-23rd May, 2010) during the AQ network deployment. These data are on the hour mean averages of hourly mean temperature measurements. The left plot shows temperature data from two environments (urban and rural/semi-urban areas) relative to measurements from the meteorology station. The right plot shows both the mean temperature measurements from the two sites and the corresponding mean temperature differences (black line).

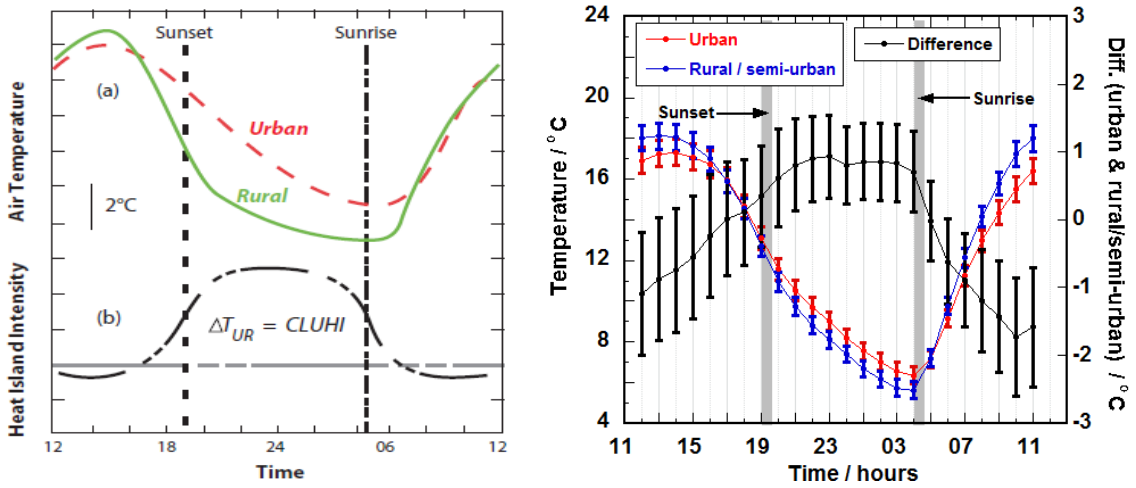

Figure 7.39. Twenty-four temperature profile of rural and urban sites due to atmospheric urban heat island. Left panel is conceptual depiction of typical atmospheric urban heat island under calm and clear air conditions. Right panel shows actual temperature profile between urban and rural / semi-urban locations in Cambridge, UK (4th-23rd May, 2010). Left plot was reproduced from [120] which was modified from [119].

7.4. Summary and Conclusions

The successful deployments of both mobile and static electrochemical sensors have been shown in this chapter. Results from the mobile AQ network study showed that while the NO_2 measurements from static AURN/ LAQN stations can help provide estimates of pollution exposure within the vicinity of the station, large spatial variations (over distances as small as 10 m) were observed in the CO and NO measurements. The ease of deploying multiple mobile air quality sensors has offered the opportunity to compare pollution measurement between different cities over short time scales (few hours). This gave a snapshot of air quality in these different locations. Based on these studies, outdoor air quality was relatively better in Cambridge (UK) compared to Valencia (Spain). On the other hand, air quality in terms of NO and NO_2 mixing ratios show that Valencia was better than London (UK) while in all cases Lagos (Nigeria) had the poorest air quality among the four cities studied.

The static AQ network deployment offered the opportunity of comparing traffic related pollution in different environments in Cambridge, UK. In general, low mixing ratios of NO (below 200 ppb) were observed in rural and semi-rural areas compare to urban sites.

Elevated CO and NO (above 100 ppb) mixing ratios were recorded at busy roads and crossroads within the city centre. However, elevated mixing ratios were observed only in NO at the bus station in the city centre. This network deployment also offered the opportunity of studying atmospheric phenomena like street canyon effects and atmospheric urban heat island. For instance by utilising the openair tool, street canyon effect was detected around the AURN site on Regent Street in Cambridge under certain wind conditions. Results from the network study also showed that the location of a monitoring station (micro siting) is important as underestimation of pollution mixing ratios can occur under certain wind conditions as was discovered at the LAQN in Newmarket Road. Meanwhile, analysis of temperature measurements across the AQ network revealed evidence of atmospheric UHI in Cambridge albeit with low heat island intensity.

This chapter has shown that electrochemical AQ sensors can be integrated into the existing monitoring system to better characterise air quality in urban environments. These can be achieved with little personnel and at relatively low-cost with good temporal and spatial resolutions as well as significantly improved sensitivity and precision.

Chapter 8 Summary and Future Work

8.1. Summary and conclusions

Recent advances in miniature electrochemical gas sensors have led to improved sensitivity to the target gas at mixing ratios similar to levels present in ambient environments. Suitably configured, electrochemical based gas sensors can provide cost effective, indicative measurements of air quality gas species in the environment. One of the challenges in air quality assessment is the lack of adequate spatial measurements of pollutants due to the limitations associated with high cost of the standard measurement techniques. In addition, factors like size, safety, specialist operator and power demand have limited the establishment of more spatial AQ monitoring network based on the traditional techniques.

The work presented in this thesis shows that AQ sensors based on low-cost technology like electrochemical gas sensors have a niche in the existing AQ monitoring network. This thesis describes the development of electrochemical based AQ sensor instrument measuring CO, NO and NO_2 in addition to temperature and relative humidity. Practical applications of these instruments were demonstrated in field deployments under multiple atmospheric environments including urban roadside, airport and remote coastal location.

The key conclusions of this thesis can be categorised into two parts: technical conclusions of electrochemical sensor node studies (development and characterisation) and urban air quality studies using electrochemical sensor nodes.

8.1.1. Technical conclusions of electrochemical sensor nodes studies

- Electrochemical based sensors (including CO, NO and NO_2) have been developed with characteristic fast response (< 20 s), good sensor-to-sensor agreement (both in the laboratory and outdoor conditions) and good accuracy (to ± 2 ppb at ppb levels of CO (0-160 ppb), ± 1 ppb NO_2 (0-70 ppb) and ± 2 ppb at ppb levels of NO (0-130 ppb) under laboratory conditions).
- Intercomparison studies between electrochemical sensors and chemiluminescence instruments under ambient conditions showed agreement to within < 5% for NO and < 20% for O_3 corrected NO_2 at typical ambient mixing ratios of ppb.

- Though not exhaustive, the sensors appear stable over ≈ 1 year. For example, the gain of a temperature-corrected NO electrochemical sensor showed no statistically significant change over a year. It also revealed that there were no significant effects of meteorological parameters (pressure, RH and temperature) on sensitivity of the instrument during the deployment.

8.1.2. Urban air quality studies

- Mobile electrochemical sensor nodes measuring CO, NO and NO_2 were used for personal exposure studies at four different cities. Results from these studies showed that these pollutants were highly spatially and temporally variable. In addition, results from human height exposure studies showed a significant difference in mean exposure level of CO & NO (≈ 10%) between waist and shoulder heights over a period of 1 hr 20 min although there was negligible difference in the case of NO_2.
- The portability of the mobile sensor nodes made it possible to establish a mobile air quality network for air quality assessment for short periods (few hours). This facilitated some indicative study of the impact of modes of transport (walking, cycling and driving) on the level of pollution experienced in urban environment. More studies are required to establish the robustness of the differences observed during this study.
- The fast time response (< 20 s) of the sensors has shown their potential application in the dynamic evaluation of aircraft plumes. Results from this kind of study can be used in validating models used for aircraft plume simulation and plume dispersion more generally.
- A long-term network deployment (≈ 3 months) of static electrochemical sensor nodes in Cambridge city made it possible to identify different pollution environments within the city, including areas affected by street canyon effects within the city. These findings demonstrate the role of these devices can play in improving both sophisticated research models (like Large Eddy Simulation, LES) and those used for air quality (ADMS, Atmospheric Dispersion Model System).
- Results from the long-term study also revealed that the siting of the current fixed monitoring stations can fail to represent the actual air quality distribution and may therefore be unrepresentative. Comparison of NO mixing ratio between the static

nodes and the AURN/LAQN stations revealed large differences in measurements under certain wind conditions. For instance, the large underestimations observed at the LAQN station in Newmarket Road represented approximately 17% of the data gathered over the 3 month deployment.

- Temperature measurements during the long-term study, even though not using standard meteorology calibration procedures, revealed that the atmospheric urban heat island effect can be investigated with the static sensor nodes.

8.2. Future work

The work presented in this thesis has shown the potential of applying electrochemical based AQ sensors for both personal exposure / mobile network studies and for continuous assessment of ambient AQ in different urban environments. Further studies involving exposure assessment for the purpose of providing the necessary pollution data for epidemiological studies will be done using the mobile AQ instruments. These studies will help in quantitative assessment of pollutants in relation to observed health effect due to short-term or long-term exposure to traffic related pollutions.

Other future directions of the current research involving the static AQ sensors will focus on incorporating more species including O_3, sulphur dioxide (SO_2), total VOC (using photo-ionization detectors), CO_2 (using miniature NDIR sensors) and size-speciated aerosol which will cover particles with size range of 1 µm to 20 µm (using optical particle counter OPC, instrument). This new instrument will also include a sonic anemometer for wind data (wind speed and wind direction). In addition, the electrochemical sensors measuring ambient CO, NO, NO_2, SO_2 and O_3 will have a self compensating temperature electrode which eliminates the need for temperature correction of the data. Other meteorological parameters like temperature and RH will be included with GPS (providing real-time and location) and GPRS for live data transmission. First deployment of these modified instruments will be during the London Heathrow project. This is a three-year project involving deployment of a network of approximately fifty AQ sensors in and around Heathrow Airport for a period of twelve months. This project is in conjunction with other UK Universities including University of Cambridge (UCAM), Imperial College London (IMP), University of Manchester (UM) and University of Hertfordshire (UH). Other partners include the National Physics Laboratory

(NPL), Cambridge Environmental Research Consultants (CERC) and British Airports Authority (BAA). Some of the objectives of this project include:

- deployment of pilot AQ sensor network in and around London Heathrow Airport measuring CO, NO, NO_2, SO_2, O_3, total VOC, speciated aerosols, wind data, temperature and RH. See figure 8.1 and 8.2 (UCAM & UH)
- pollution source attribution outputs for London Heathrow based on the sensor network data and data collected from emission source activities during the deployment. (UCAM,UH & BAA)
- generation of calibrated, high spatial and temporal data for the pollutants above for use in scientific and policy studies. (UCAM, UH & NPL)
- evaluation of sensor data against bottom-up emission inventories and dispersion model with aim of improving both. (CERC, UCAM, BAA & UH)
- development of novel software tools for network calibration, analysis, data mining and visualisation. (UCAM & IMP)

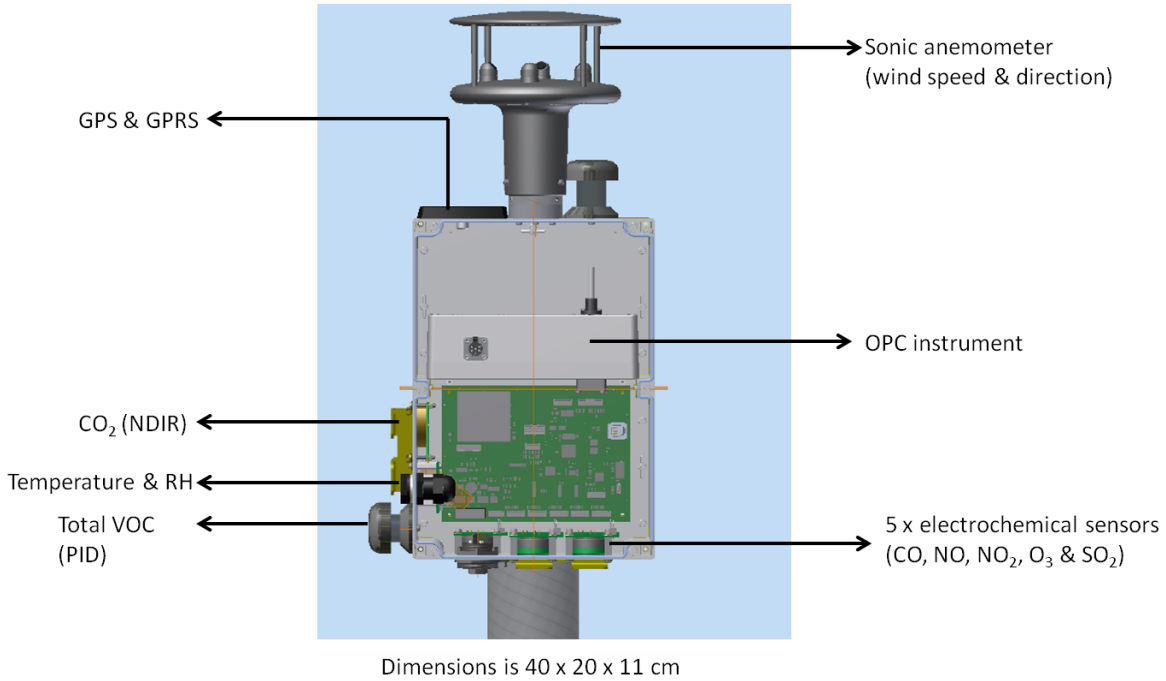

Figure 8.1. Schematic diagram of the new static AQ sensor showing details of internal components and species being measured.

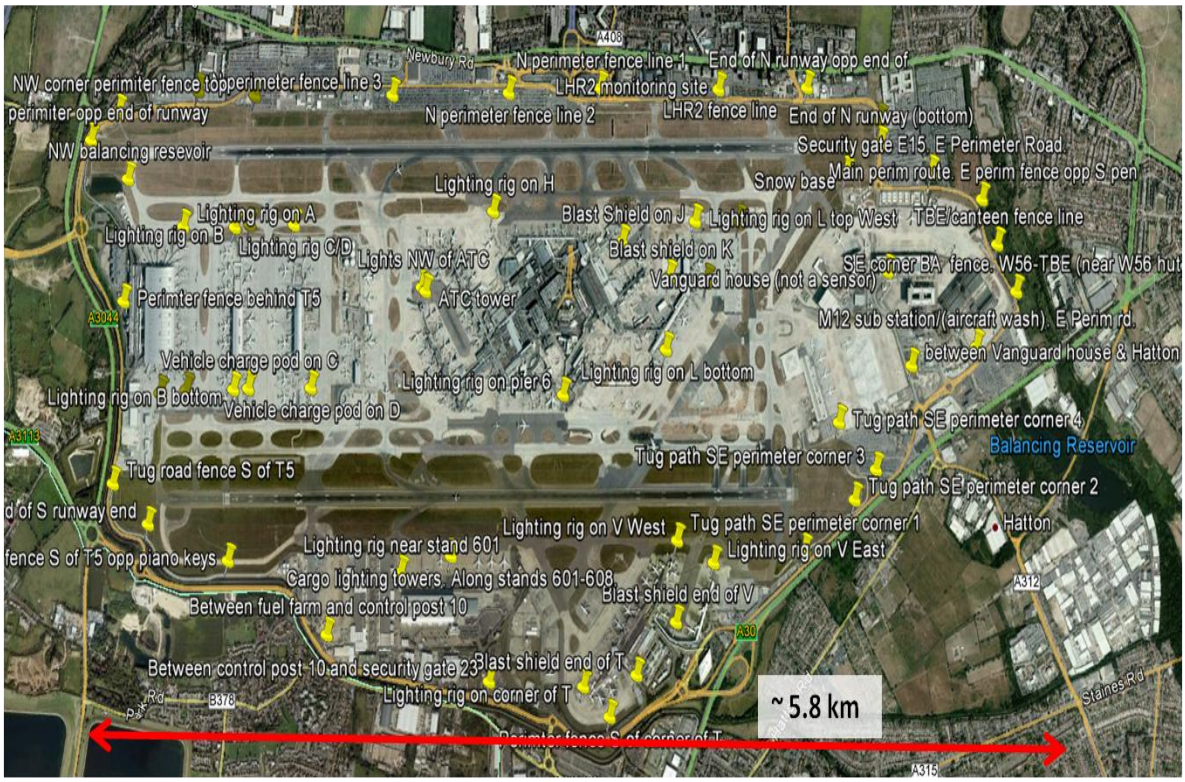

Figure 8.2. Layout showing proposed locations of network of static AQ sensors in and around London Heathrow Airport. Maps courtesy Google Earth [80].

Appendix

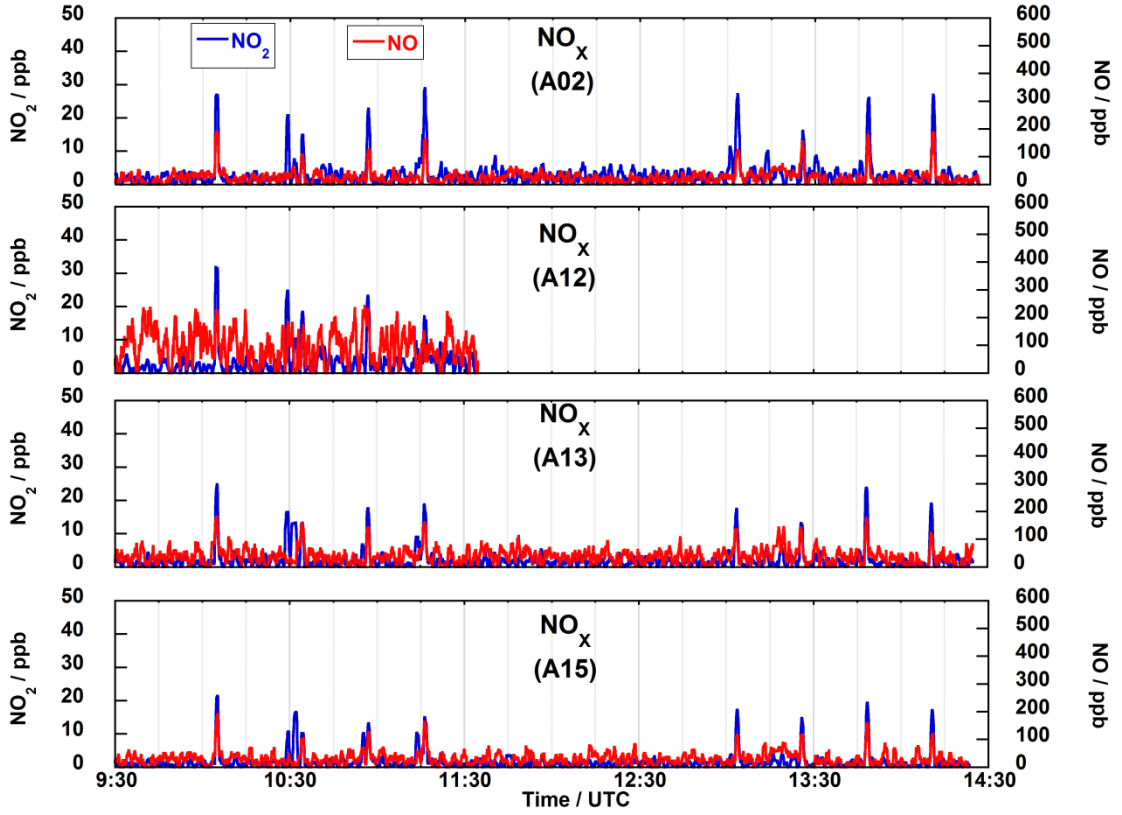

Figure 1A. Time series of NO and NO_2 mixing ratios of sensors in front array during the field trial at Cranfield airport (17th February, 2009).

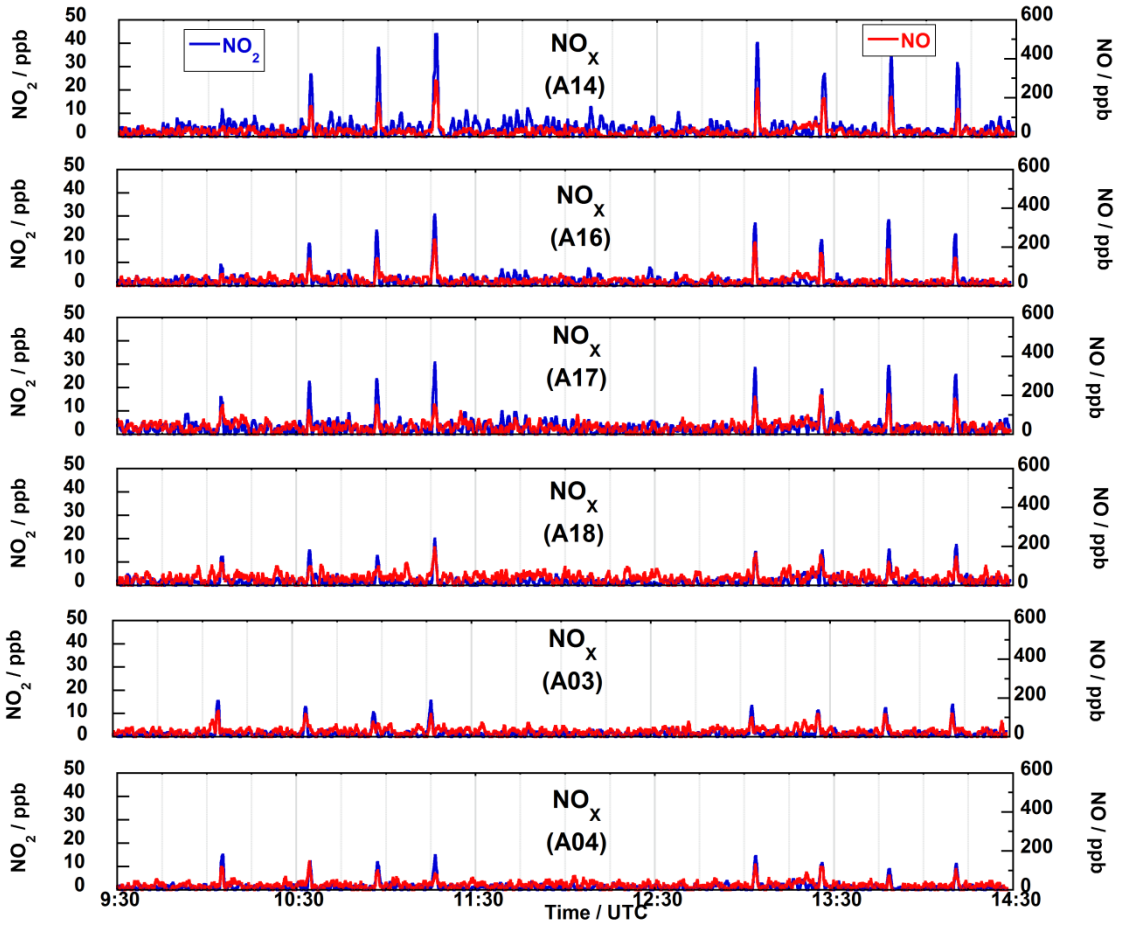

Figure 1B. Time series of NO and NO_2 mixing ratios of sensors in back array during the field trial at Cranfield airport (17th February, 2009).

Table 1A. Flight time details of the eight sorties for the AETIAQ campaign at Cranfield airport on 17 February, 2009. Note the start of stroll indicate the moment aircraft start moving after ~10 s full power engine run.

Time of day	Sortie	Full power (UTC)	Start of roll (UTC)	Take-off (UTC)	Landing (UTC)
am	1	10:04:59	10:05:01	10:05:37	10:11:25
	2	10:34:10	10:34:26	10:34:53	10:39:23
	3	10:56:44	10:57:00	10:57:30	11:01:45
	4	11:16:04	11:16:29	11:16:54	11:20:57
pm	5	13:03:19	13:03:37	13:04:05	13:08:20
	6	13:25:38	13:25:52	13:26:25	13:30:20
	7	13:47:58	13:48:17	13:48:44	13:52:53
	8	14:10:27	14:10:43	14:11:09	14:15:10

Table 1B. Flight time details of the twelve sorties for the aerodynamics baffles trials at Cranfield airport on September, 2011. Note the wind values are one minute average after the start of full engine burn.

Sortie	Trial day	Start time of full burn (UTC)	Time on full power (s)	Time of start of roll (UTC)	Distance from threshold (m)	Mean wind speed (m/s)	Mean wind direction (degrees)
1		09:15:22	13.8	09:15:36	35	5.7	259
2		10:15:45	14.3	10:15:59	35	6.3	250
3	Day 1	11:02:41	15.8	11:02:57	70	5.7	248
4		12:03:39	12	12:03:51	60	4.8	252
5		09:10:01	2.6	09:10:04	121	0.6	256
6		10:08:50	7.4	10:08:57	118	0.9	187
7	Day 2	10:46:49	4.9	10:46:54	73	0.4	Variable
8		12:09:39	5.7	12:09:45	73	1	73
9		10:06:54	9.1	10:07:03	57	7.1	239
10		10:59:16	10.9	10:59:27	57	5.4	250
11	Day 3	11:39:43	11.1	11:39:54	24	7	252
12		12:28:54	8.8	12:29:03	38	7.2	245

References

1. Seinfeld, H.J., Pandis, S.N., *Atmospheric Chemistry and Physics: From Air Pollution to Climate Change*. 2nd ed. 2006, Hoboken, New Jersey: John Wiley & Sons, Inc.
2. Wayne, R.P., *Chemistry of the Atmosphere*. 3rd ed. 2006, New York: Oxford University Press.
3. U.S. EPA, *Air Quality Criteria for Ozone and Related Photochemical Oxidants*. Vol. 2. 2006, Washington DC: Office of Research and Development. U.S. Environmental Protection Agency. EPA 600/R-05/004bF, February 2006.
4. Hinc, N., *Air Pollution.* Journal of Chemical Education, 1969. **46**(2): p. 93-95.
5. Baxter, J., *Human impacts of volcanoes*, in *Volcanoes and the environment*, J. Martin, Ernst, G.G.J., Editor. 2005, Cambridge University Press: Cambridge,UK; New York.
6. Thordarson, T., Self, S., *Atmospheric and environmental effects of the 1783-1784 Laki eruption: A review and reassessment.* Journal of Geophysical Research-Atmospheres, 2003. **108**(D1).
7. Prata, A.J., Tupper, A., *Aviation hazards from volcanoes: the state of the science.* Natural Hazards, 2009. **51**(2): p. 239-244.
8. Bell, M.L., Davis, D. L., *Reassessment of the lethal London fog of 1952: Novel indicators of acute and chronic consequences of acute exposure to air pollution.* Environmental Health Perspectives, 2001. **109**: p. 389-394.
9. Ministry of Health, *Mortality and morbidity during the London fog of December 1952*, in *Reports on Public Health and Medical Subjects 95*: London: HMSO, 1954.
10. Met Office. *Case Study-Smog: The Great Smog of 1952*. [cited 2012, March 27]; Available from: http://www.metoffice.gov.uk/education/teens/case-studies/great-smog.
11. *Department for Environment, Food and Rural Affairs (DEFRA), UK*. [cited 2012, March 27]; Brief history: air pollution, UK]. Available from: http://uk-air.defra.gov.uk/networks/brief-history.
12. Finlayson-Pitts, B.J., Pitts Jr., J. N., *Chemistry of the Upper and Lower Atmosphere*. 2000, San Diego, California, USA; London, UK: Academic Press.
13. USEPA. *Clear Air Act (CCA)*. Available from: http://www.epa.gov/air/caa/.
14. *WHO Air quality guidelines for particulate matter, ozone, nitrogen dioxide and sulfur dioxide. Global update 2005. Summary of risk assessment*. 2006b, World Health Organisation. WHO/SDE/PHE/OEH/06.02.
15. *Ambient Air Pollution: Carbon monoxide. Position Paper-draft version 5.2*. 1999 [cited 2012, March 27]; Available from: http://ec.europa.eu/environment/air/pdf/pp_co.pdf.

16. WHO, *Air Quality Guidelines for Europe*. 2nd ed. 2000, Copenhagen: World Health Organisation: Regional Office for Europe.
17. Alberts, W.M., *Indoor Air-Pollution: NO, NO2, CO and CO2.* Journal of Allergy and Clinical Immunology, 1994. **94**(2): p. 289-295.
18. U.S. EPA, *Air Quality Criteria for Carbon Monoxide*. 2000, Washington DC: Office of Research and Development. U.S. Environmental Protection Agency. EPA 600/P-99/001F, June 2000.
19. Laties, V.G., Merigan, W. H., *Behavioral-Effects of Carbon-Monoxide on Animals and Man.* Annual Review of Pharmacology and Toxicology, 1979. **19**: p. 357-392.
20. Bunnell, D.E., Horvath, S. M., *Interactive Effects of Physical Work and Carbon-Monoxide on Cognitive Task-Performance.* Aviation Space and Environmental Medicine, 1988. **59**(12): p. 1133-1138.
21. Longo, L.D., *Biological Effects of Carbon-Monoxide on Pregnant Woman, Fetus, and Newborn-Infant.* American Journal of Obstetrics and Gynecology, 1977. **129**(1): p. 69-103.
22. Morello-Frosch, R., Jesdale, B. M., Sadd, J. L., Pastor, M., *Ambient air pollution exposure and full-term birth weight in California.* Environmental Health, 2010. **9**: p. 44.
23. Working Group on Nitrogen Dioxide. *Position paper on Air Quality: nitrogen dioxide*. 1997 [cited 2012, March 27]; Available from: http://ec.europa.eu/environment/air/pdf/pp_no2.pdf.
24. U.S. EPA, *Air Quality Criteria for oxides of nitrogen (Final, 1993)*. Vol. 3. 1993, Washington DC: Office of Research and Development. U.S. Environmental Protection Agency. EPA600/8-91/049cF, August 1993.
25. Parkhurst, W.J., Humphreys, M. P., Harper, J. P., Spengler, J. D., *Influence of Indoor Combustion Sources on Indoor Air-Quality.* Environmental Progress, 1988. **7**(4): p. 257-261.
26. Clark, N.A., Demers, P. A., Karr, C. J., Koehoorn, M., Lencar, C., Tamburic, L., Brauer, M., *Effect of Early Life Exposure to Air Pollution on Development of Childhood Asthma.* Environmental Health Perspectives, 2010. **118**(2): p. 284-290.
27. Hwang, B.F., Lee, Y. L., *Air Pollution and Prevalence of Bronchitic Symptoms Among Children in Taiwan.* Chest, 2010. **138**(4): p. 956-964.
28. Wallace, J., Nair, P., Kanaroglou, P., *Atmospheric remote sensing to detect effects of temperature inversions on sputum cell counts in airway diseases.* Environmental research, 2010. **110**(6): p. 624-632.
29. Nitta, H., Sato, T., Nakai, S., Maeda, K., Aoki, S., Ono, M., *Respiratory Health Associated with Exposure to Automobile Exhaust .1. Results of Cross-Sectional Studies in 1979, 1982, and 1983.* Archives of Environmental Health, 1993. **48**(1): p. 53-58.

30. U.S. EPA, *Air Quality Criteria for Ozone and Related Photochemical Oxidants*. Vol. 1. 2006, Washington DC: Office of Research and Development. U.S. Environmental Protection Agency. EPA 600/R-05/004aF, February 2006.
31. U.S. EPA, *Air Quality Criteria for Ozone and Related Photochemical Oxidants*. Vol. 3. 2006, Washington DC: Office of Research and Development. U.S. Environmental Protection Agency. EPA 600/R-05/004cF, February 2006.
32. U.S. EPA, *Air Quality Criteria for oxides of nitrogen (Final, 1993)*. Vol. 2. 1993, Washington DC: Office of Research and Development. U.S. Environmental Protection Agency. EPA600/8-91/049bF, August 1993.
33. *WHO Air quality guidelines for particulate matter, ozone, nitrogen dioxide and sulfur dioxide. Global update 2005. Summary of risk assessment,*. 2006b, World Health Organisation.
34. Krzyzanowski, M., *WHO air quality guidelines for Europe.* Journal of Toxicology and Environmental Health-Part a-Current Issues, 2008. **71**(1-2): p. 47-50.
35. *DIRECTIVE 2008/50/EC OF THE EUROPEAN PARLIAMENT AND OF THE COUNCIL.* Official Journal of the European Union, 2008. **L152**.
36. USEPA, *National Ambient Air Quality Standards (NAAQS)*. 2011, United States Environmental Protection Agency (USEPA).
37. *History of the Pollutant Reports*. Air Quality: EPA's Integrated Science Assessments (ISAs) [cited 2012, April 6]; Available from: http://www.epa.gov/ncea/isa/basicinfo.htm.
38. *NIST Chemical Kinetics Database*. [cited 2012, April 2]; Available from: http://kinetics.nist.gov/kinetics/index.jsp.
39. Bruinen de Bruin, Y., Hänninen, O., Kephalopoulos, S., Kotzjas, D., Carrer, P., Moroni, M., Cavallo, D., Jantunen, M., *Exposure of an Urban Adult Population to Carbon Monoxide. Direct and Indirect Exposure Assessment Methods. Determinants and Sources. Final Report*. 2005, Luxembourg: Office for Official Publication of the European Communities.
40. Dignon, J., Ando, T., Brenninkmeijer, C., Conny, J., Granier, C., Khalil, A., King, G., King, S., Law, K., Levine, J. S., and T. Röckmann, Stedman, D., Yung, Y., Zafiriou, O. *Carbon monoxide sources and sinks: working group summary report*. in *Atmospheric carbon monoxide and its environmental effects*. 1998. Portland, Oregon. Washington, DC: U.S. Environmental Protection Agency; report no. EPA/600/R-98/047; pp. 359-374.
41. U.S. EPA, *Air Quality Criteria for oxides of nitrogen (Final, 1993)*. Vol. 1. 1993, Washington DC: Office of Research and Development. U.S. Environmental Protection Agency. EPA600/8-91/049aF, August 1993.

42. AQEG, *Trends in Primary Nitrogen Dioxide in the UK.* 2007, Report prepared by Air Quality Group for the Department for Environment, Food and Rural Affairs;Scottish Executive; Welsh Assembly Government; and Department of the Environment in Northern Ireland.
43. Carslaw, D.C., *Evidence of an increasing NO2/NOX emissions ratio from road traffic emissions.* Atmospheric Environment, 2005. **39**(26): p. 4793-4802.
44. Intergovernmental Panel on Climate Change (IPCC), *Climate Change 2001: The Scientific Basis*. 2001, Cambridge, UK: Cambridge University Press.
45. *Environment Act 1995*. [cited 2012 April 4]; Available from: http://www.legislation.gov.uk/ukpga/1995/25/part/IV.
46. DEFRA, *The Air Quality Strategy for England, Scotland, Wales and Northern Ireland.* 2007. **1**.
47. DEFRA, *Air Pollution in the UK 2010. A report prepared by AEA for Defra and the Devolved Administrations.* 2010, London: Department for Environment, Food and Rural Affairs, September 2011.
48. House of Commons Environmental Audit Committee, *Air Quality, Fifth Report of Session 2009–10*. Vol. 1. 2010, London:The Stationery Office Limited.
49. Carslaw, D., Beevers, S., Westmoreland, E.,Williams, M., Tate, J., Murrells, T., Stedman, J., Li,Y., Grice, S., Kent, A.,Tsagatakis, I., *Trends in NOx and NO2 emissions and ambient measurements in the UK*. 2011, Report prepared for Defra version 18th July 2011.
50. *Department for Environment, Food and Rural Affairs (DEFRA), UK*. [cited 2012, May 31]; Emissions of Carbon monoxide by source: 1970-2007]. Available from: http://archive.defra.gov.uk/evidence/statistics/environment/airqual/aqemco.htm.
51. *DIRECTIVE 98/69/EC OF THE EUROPEAN PARLIAMENT AND OF THE COUNCIL of 13 October 1998 relating to measures to be taken against air pollution by emissions from motor vehicles and amending Council Directive 70/220/EEC.* Official Journal of the European Union, 1998. **L 350**: p. 1.
52. Williams, M.L., Carslaw, D. C., *New Directions: Science and policy - Out of step on NOx and NO_2?* Atmospheric Environment, 2011. **45**(23): p. 3911-3912.
53. Carslaw, D.C., Beevers, S. D., Tate, J. E.,Westmoreland, E. J., Williams, M. L., *Recent evidence concerning higher NOx emissions from passenger cars and light duty vehicles.* Atmospheric Environment, 2011. **45**(39): p. 7053-7063.
54. *DIRECTIVE 2009/28/EC OF THE EUROPEAN PARLIAMENT AND OF THE COUNCIL of 23 April 2009 on the promotion of the use of energy from renewable sources and amending and subsequently repealing Directives 2001/77/EC and 2003/30/EC.* Official Journal of the European Union, 2009. **L140**: p. 16.

55. AIR QUALITY EXPERT GROUP, *ROAD TRANSPORT BIOFUELS: IMPACT ON UK AIR QUALITY. Advice note prepared by AQEG for The Department for Environment, Food and Rural Affairs, Welsh Assembly Government, the Scottish Executive and the Department of the Environment for Northern Ireland*. 2011.

56. Navas, M.J., Jimenez, A. M., Galan, G., *Air analysis: Determination of nitrogen compounds by chemiluminescence.* Atmospheric Environment, 1997. **31**(21): p. 3603-3608.

57. Jimenez, A.M., Navas, M. J., Galan, G., *Air analysis: Determination of ozone by chemiluminescence.* Applied Spectroscopy Reviews, 1997. **32**(1-2): p. 141-149.

58. Skoog, D.A., Leary, J.J., *Principles of Instrumental Analysis*. 4th ed. 1992, Fort Worth; Philadephia; San Deigo; New York; Orlando; Austin;USA: London; UK: Saunders College Publishing; A Harcourt Brace Jovanonich College.

59. Schiff, H.I., Mackay, G. I., Bechara, J., *The Use of Tunable Diode-Laser Absorption-Spectroscopy for Atmospheric Measurements.* Research on Chemical Intermediates, 1994. **20**(3-5): p. 525-556.

60. U.S. EPA, *Air Quality Criteria for Ozone and Related Photochemical Oxidants*. Vol. 1. 1996, Washington DC: Office of Research and Development. U.S. Environmental Protection Agency. EPA 600/P-93/004aF, July 1996.

61. Papayannis, A., Ancellet, G., Pelon, J. and G. Megie, *Multiwavelength Lidar for Ozone Measurements in the Troposphere and the Lower Stratosphere.* Applied Optics, 1990. **29**(4): p. 467-476.

62. Roscoe, H.K., Clemitshaw, K. C., *Measurement techniques in gas-phase tropospheric chemistry: A selective view of the past, present, and future.* Science, 1997. **276**(5315): p. 1065-1072.

63. Stetter, J.R., Li, J., *Amperometric gas sensors-A Review.* Chem Rev, 2008. **108**(2): p. 352-66.

64. DEFRA, *Local Air Quality Management.Technical Guidance LAQM.TG(09)*, in *Part IV of the Environment Act 1995, Environment (Northern Ireland) Order 2002 Part III*. 2009. p. A1.

65. Atimtay, A.T., Emri, S., Bagci, T., Demir A.U., *Urban CO exposure and its health effects on traffic policemen in Ankara.* Environmental Research, 2000. **82**: p. 222-230.

66. Chan, L.Y., Lau, W.L., Zou, S.C., Cao, Z.X., Lai, S.C., *Exposure level of carbon monoxide and respirable suspended particulate in public transportation modes while commuting in urban area of Guangzhou, China.* Atmospheric Environment, 2002. **36**: p. 5831– 5840.

67. Duci, A., Chaloulakou, A., Spyrellis, N., *Exposure to carbon monoxide in the Athens urban area during commuting.* Science of the Total Environment, 2003. **309**: p. 47– 58.

68. Neasham, J.A., Sharif, B.S., Blythe, P.T., Bell, M.C., *A pervasive sensor network for environmental and traffic monitoring*, in *1st Smart Environment Interest Group Conference*. 2007: London, UK.

69. Blythe, P.T., Sharif, B., Watson, P., Bell, M.C., Edwards, S., Neasham, J., Suresh, V., Wagner, J., Bryan, H., *An environmental sensor system for pervasively monitoring road networks*, in *IET - Road Transport Information and Control.* 2008: Manchester, UK.

70. Popoola, O.A.M., Mead, M., Stewart, G., Hodgson, T., McLeod, M., Baldovi, B., Landshoff, P., Hayes, M., Calleja, M., Jones, R., *Low-Cost Sensor Units for Measuring Urban Air Quality*, in *Sensor Systems for Environmental Monitoring, AAMG - RSC Conference* 2010: London, UK.

71. Liu, C.C., *Electrochemical Sensors. The Biomedical Engineering Handbook: Second Edition*, J.D. Bronzino, Editor. 2000, Boca Ration:CRC Press LLC.

72. Kissinger, P.T., Heineman W. R. , *Laboratory Techniques in Electroanalytical Chemistry*. Second ed. 1996, New York: Marcel Dekker, Inc.

73. Liu, C.C., *Electrochemical Sensors.*, in *The Biomedical Engineering Handbook: Second Edition*, J.D. Bronzino, Editor, Boca Ration:CRC Press LLC, 2000.

74. Bard, A.J., Faulkner, L.R., *Electrochemical Method: Fundamentals and Application*. 2nd ed. 2001, New York: John Wiley & Sons.

75. *Alphasense Application Note: How Electrochemical Gas Sensors Work*. 2005. p. 1-4.

76. *Mobile Environmental Sensing System Across Grid Environments: MESSAGE Project*. 2012 [cited 2012 February 14]; Available from: http://bioinf.ncl.ac.uk/message/.

77. *Python Programming Language*. Available from: http://www.python.org/.

78. *Apache HTTP Server 2.2 Official Document*. 2012 [cited 1-4; Available from: http://www.apache.org/dist/httpd/docs/httpd-docs-2.2.14.en.pdf.

79. *PostgreSQL*. 2012 [cited 2012 16 February, 2012]; Available from: http://www.postgresql.org/.

80. *Google Earth: Tele Atlas, Infoterra Ltd & BlueSky, Getmapping plc, The GeoInformation Group (2012).*

81. *Tele Atlas (2012). Google Maps*. [cited 2012 28 February]; Available from: http://maps.google.co.uk/.

82. Alphasense. *NO2-A1 Nitrogen Dioxide Sensor. Application Note Alphasense*. February, 2009 [cited 2011 October 5th]; Available from: http://www.alphasense.com/pdf/NO2A1.pdf.

83. DEFRA, *Local Air Quality Management.Technical Guidance LAQM.TG(09)*, in *Part IV of the Environment Act 1995, Environment (Northern Ireland) Order 2002 Part III*. 2009. p. A1-31,1-12.

84. *MESSAGE Project*. [cited 2011 May 31]; Available from: http://bioinf.ncl.ac.uk/message/.

85. *DUVAS Technologies Ltd*. 2008 [cited 2011 October 3rd]; DUVAS Technology LTD]. Available from: http://www.duvastechnologies.com/index.php.

86. *London Air: Kensington and Chelsea - Cromwell Road AURN/LAQN station*. [cited 2011, October 3rd]; Available from: http://www.londonair.org.uk/london/asp/publicdetails.asp?region=0&site=KC2&bulletin=daily&la_id=20&bulletindate=23/06/2009&postcode.

87. Ki-Hyun, K., Min-Young K., *Comparison of an open path differential optical absorption spectroscopy system and a conventional in situ monitoring system on the basis of long-term measurements of SO_2, NO_2 and O_3.* Atmospheric Environment, 2001. **35**: p. 4059–4072.

88. Alphasense. *INTERFERING GASES.Application Note Alphasense. AAN 109-02*. 2009 [cited 2011 October 5th]; Available from: http://www.alphasense.com/pdf/AAN_109-02.pdf.

89. Grant, A., Stanley, K. F., Henshaw, S. J., Shallcross, D. E., O'Doherty, S., *High-frequency urban measurements of molecular hydrogen and carbon monoxide in the United Kingdom.* Atmospheric Chemistry and Physics, 2010. **10**(10): p. 4715-4724.

90. Fahey, D.W., Eubank, C. S., Hubler, G., Fehsenfeld, F. C., *Evaluation of a Catalytic Reduction Technique for the Measurement of Total Reactive Odd-Nitrogen Noy in the Atmosphere.* Journal of Atmospheric Chemistry, 1985. **3**(4): p. 435-468.

91. Chang, C.T., Liu, T. H., Jeng, F. T., *Atmospheric concentrations of the Cl atom, ClO radical, and HO radical in the coastal marine boundary layer.* Environmental research, 2004. **94**(1): p. 67-74.

92. *Scotland 1971–2000 averages*. [cited 2011 November 1]; Available from: http://www.metoffice.gov.uk/climate/uk/averages/19712000/areal/scotland.html.

93. *England 1971–2000 averages*. [cited 2011 November 1]; Available from: http://www.metoffice.gov.uk/climate/uk/averages/19712000/areal/england.html.

94. Hitchman, M.L., Cade, N. J., Gibbs, T. K., Hedley, N. J. M., *Study of the factors affecting mass transport in electrochemical gas sensors.* Analyst, 1997. **122**(11): p. 1411-1417.

95. Hitchman, M.L., *Measurement of Dissolved Oxygen*. 1978, New York: Wiley.

96. DEFRA, *QA/QC Procedures for the UK Automatic Urban and Rural Air Quality Monitoring Network (AURN)*. 2009. p. 5,21.

97. *National Environmental Standards and Regulations Enforcement Agency (Establishment) Act, 2007*. Federal Republic of Nigeria Official Gazette. Vol. 94. 31 July 2007, The Federal Government Printer: Lagos, Nigeria.

98. Taiwo, O., *Carbon dioxide emission management in Nigerian megacities: the case of Lagos.* 2005, Lagos Metropolitan Management Authority (LAMATA).

99. Abam, F.I. and G.O. Unachukwu, *Vehicular Emissions and Air Quality Standards in Nigeria.* European Journal of Scientific Research, 2009. **34**(4): p. 550-560.

100. Osuntogun, B.A. and C.A. Koku, *Environmental-Impacts of Road Transportation in South-Western States of Nigeria.* Applied Sciences, 2007. **7**(16): p. 2536-2360.

101. Mobereola, D., *Strengtening Urban Transport Institutions. A Case Study of Lagos State*, in *Sub-Saharan Africa Transport Policy Program*. 2006.

102. Bashiru, A.R., Waziri, O.O., *Analysis of intra-urban traffic problems in Nigeria: a study of Lagos metropolis.* Indonesian Journal of Geography, 2008. **40**(1): p. 31-51.

103. *Lagos Overview: Population*. [cited 2012, April 13]; Available from: http://www.lagosstate.gov.ng/index.php?page=subpage&spid=12&mnu=null.

104. Bright, V., W. Bloss, and X. Cai, *Modelling atmospheric composition in urban street canyons.* Weather, 2011. **66**(4): p. 106-110.

105. Carslaw, D.C., Ropkins K., *openair: Open-source tools for the analysis of air pollution data. R package version 0.3-15.* 2011, Environmental Research Group, King's College London, 21st Januray 2011.

106. *Cambridgeshire Bus. Timetables by Location*. [cited 2012, April 13]; Available from: http://www.cambridgeshire.gov.uk/transport/around/buses/Bustimetabbusno.htm.

107. Bacon, J., Bejan, A., Beresford, A. R., Evans, D., Gibbens, R., Moody K., *Using Real-Time Road Traffic Data to Evaluate Congestion*, in *Dependable and Historic Computing*, C. Jones, Lloyd, John, Editor. 2011, Springer Berlin / Heidelberg. p. 93-117.

108. Bennett, M., et al., *Composition of Smoke Generated by Landing Aircraft.* Environmental Science & Technology, 2011. **45**(8): p. 3533-3538.

109. *Google Map: DigitalGlobe, GeoGlobe, GeoEye, Getmapping plc, Infoterra Ltd & BlueSky, The GeoInformation Group, Map data (2012).* [cited 2012 28 February]; Available from: http://maps.google.co.uk/maps.

110. *Personal communication with Michael Bennet, Centre for Air Transport and Environment, Manchester Metropolitan University*. January 2012.

111. *MESSAGE Project: Demonstration Day June 2009*. [cited 2012 February 23]; Available from: http://bioinf.ncl.ac.uk/message/?q=node/2.

112. *London Air: Kensington and Chelsea - Cromwell Road AURN/LAQN station*. [cited 2012 23rd February]; Available from:

http://www.londonair.org.uk/london/asp/publicdetails.asp?region=0&site=KC2&bulletin=daily&la_id=20&bulletindate=23/06/2009&postcode.

113. Cortese, A.D. and J.D. Spengler, *Ability of Fixed Monitoring Stations to Represent Personal Carbon-Monoxide Exposure.* Journal of the Air Pollution Control Association, 1976. **26**(12): p. 1144-1150.

114. Alm, S., Reponen, A., Mukala, K., Pasanen, P., Tuomisto, J., Jantunen, M. J., *Personal Exposures of Preschool-Children to Carbon-Monoxide - Roles of Ambient Air-Quality and Gas Stoves.* Atmospheric Environment, 1994. **28**(22): p. 3577-3580.

115. Dicks, J., Lewis, A., *2011 Air Quality Progress Report for Cambridge City Council*. 2011, Cambridge City Council: Cambridge.

116. Ott, W.R., Mage, D. T., Thomas, J., *Comparison of Microenvironmental CO Concentrations in two Cities for Human Exposure Modeling.* Journal of Exposure Analysis and Environmental Epidemiology, 1992. **2**(2): p. 249-267.

117. Fernandez-Bremauntz, A.A., Ashmore, M. R., *Exposure of Commuters to Carbon-Monoxide in Mexico-City .1. Measurement of in-Vehicle Concentrations.* Atmospheric Environment, 1995. **29**(4): p. 525-532.

118. *Valencia Network Monitoring and Control of Atmospheric Pollution: RVVCCA Valencia-Vivers station*. 27 February, 2012]; Available from: http://www.cma.gva.es/web/indice.aspx?nodo=27&idioma=C.

119. Oke, T.R., *Boundary layer climates*. 2nd ed. 1987, London and New York: Routledge.

120. EPA. *Reducing Urban Heat Islands: Compendium of Strategies. Urban Heat Island Basics*. Available from: http://www.epa.gov/hiri/resources/pdf/BasicsCompendium.pdf.

121. Stathopoulou, E., Mihalakakou, G.,Santamouris, M.,Bagiorgas, H. S., *On the impact of temperature on tropospheric ozone concentration levels in urban environments.* Journal of Earth System Science, 2008. **117**(3): p. 227-236.